

Molecular level understanding of supramolecular gels



Susana Campos e Menezes Jorge Ramalhete

University of East Anglia
Faculty of Science
School of Pharmacy

This thesis was submitted to the School of Pharmacy, University of East Anglia, in fulfilment of the requirements for the degree of *Philosophiæ Doctor* (PhD).

September 2017

Dedicated to my family and friends

This copy of the thesis has been supplied on condition that anyone who consults it is understood to recognise that its copyright rests with the author and that use of any information derived there from must be in accordance with current UK Copyright Law. In addition, any quotation or extract must include full attribution.

Acknowledgements

There are several people whom I would like to acknowledge for their abiding support during the last four years, without which my PhD thesis would not have been possible.

I am sincerely grateful to my supervisory team, Prof. Yaroslav Khimyak and Dr. Jesús Angulo, for giving me the opportunity to undertake this challenging PhD project. A very special thanks goes to Prof. Yaroslav for constantly challenging me, for helping me grow as a researcher and for supporting me on grey days (which there were quite a few of during this last week of writing). Yaroslav is an exemplary researcher and PhD supervisor, because of how close he is with his team and his determination in moving mountains to help his students. All those sophisticated curry and large glass of red wine nights will not be forgotten. Jesús is probably the most passionate person about research and science in general that I have encountered. The analogies he uses to explain difficult quantum mechanics concepts were simply brilliant (as the supervisors in rotating chairs). His enthusiasm always rubbed off on NMR socials with the most original NMR or physics related jokes. I will always remember with gratitude his kindness and emotional support. I feel blessed for having had the opportunity to work alongside such talented people who were, quite often, life coaches.

I believe the conduction of successful NMR experiments would not have been possible without the continued support of Dr. Colin Macdonald, who was always there to calm down any temperamental equipment, and sometimes even a temperamental PhD student (me). His patience was key in solving unsolvable spectrometer issues and in managing to resolve complex situations as “Error message: No error”. I would also like to thank Dr. Bertrand Lézé for his assistance with PXRD and SEM and Dr. Dinu Iuga for his experimental advice on NMR pulse sequences. I would like to acknowledge the University of East Anglia for the PhD scholarship, and the UK 850 MHz Solid-State NMR Facility at the Warwick University.

Several extraordinary people have passed through this amazing NMR basement (eh, I am sorry) office. In there, our NMR family has shared exquisite red wine tasting (in mugs), heavenly pizza with mayonnaise (I apologise to all Italians on behalf of Domino’s) and managed to somehow keep ourselves sane in an office without windows. Sincere thanks go to Lucy, Valeria, Fabiana, Khaled and Franco for being part of the best memories

formed in the last four years. I consider myself very lucky to have had the chance to meet and work alongside many great people at the Schools of Chemistry and Pharmacy.

A special paragraph is reserved for Karol and Serena. Karol has been a mentor, a critical-thinking promoter, a good friend, and above all, a super-argumentative annoying older brother. I have appreciated all the help with my research, NMR experiments and thesis corrections. Serena, in whom I have found eternal friendship, my deepest thanks for creating a better version of myself and shaping me into a yoga-practising nature-connected market-buying city person who is now able to distinguish between different vegetables.

I am eternally grateful to my parents, who are truly the ones who made this dream come true. I owe to them my academic success and personal development, as they helped shape me into who I am today. I want to recognise their patience for the last four years and for all those phone and Skype calls. To my sister, whose ambition and success make me aim higher in life, who continues being a role model and a superwoman who juggles a successful career with a balanced and happy family. I am very grateful to my brother(-in-law) who continuously develops my critical thinking skills and is an inspiring and kind human being.

My deepest gratitude goes to Pedro, my boyfriend and partner in crime, who has been by my side the most in the last few years. I would like to thank him for his understanding and patience for all those weekends in which research forced me to go to the university or abroad for a week, and, now, throughout the endless days and nights of writing my thesis. I am very grateful for the hours he spent hearing me rambling about the challenges of the PhD project and complaining about undergraduate students. Doing a PhD is an emotionally draining task but Pedro has been my rock and held me afloat, by constantly reminding me of my ability to excel in it. Thank you for your continued support throughout my entire PhD and for sharing the greatest moments of my life in last few years.

Some equally important people who have made all the difference with small gestures are my very close friends in Portugal, who have constantly reminded me of their love, despite the distance, and have always found the time to make new memories with me whenever I was back home.

Abstract

Supramolecular gels are complex materials which have an expanding scope of industrial and biomedical applications, due to their unique viscoelastic properties, high biocompatibility and possibility of functionalisation. The hierarchical structure of molecular materials combines domains with drastically different degrees of ordering and molecular mobility. This makes their full characterisation a significant methodological and experimental challenge. The focus of this work was therefore the understanding of a variety of supramolecular semicrystalline gels in which very rigid solid components co-exist with a dynamic and highly mobile solution phase. Using the examples of amino acid and urea-derivatives gelators, control of the self-assembly processes was successfully gained and tuning of the mechanical properties of the resulting materials by incorporating molecular structure modifications or introducing a variety of structurally diverse additives was achieved. Modification of the structure of the gel fibres was observed, which modulated the dynamic properties of the gel/solution interfaces and dictated the overall behaviour of the system, an aspect which is not commonly investigated in molecular gels.

The resulting single and multi-component gels were used as model materials for the development of an NMR-based general strategy capable of probing the several hierarchical levels present. The multiphasic character of molecular gels required the combined use of solid, solution-state and HR-MAS NMR methods. This project has expanded the understanding of saturation transfer difference NMR experiments, with special focus in their applicability and limitations for the study of supramolecular soft systems. This approach was validated using complementary techniques, more specifically, rheology, microscopy, X-ray diffraction and computational methods. By combining molecular level understanding and measurements of the bulk properties, a methodology which can be applied to other soft materials used in pharmaceutical, biomedical and food science applications was developed. Moreover, this approach might have a generic impact in different fields of science and technology, enabling one to direct the recognition and host-guest properties of soft solids, which is essential for their targeted applications.

List of publications originated from individual and collaborative projects published throughout the PhD studies

- ◆ Courtenay, J. C.; Ramalhete, S. M.; Skuze, W. J.; Soni, R.; Khimyak, Y. Z.; Edler, K. J.; Scott, J. L., Unravelling cationic cellulose nanofibril hydrogel structure: NMR spectroscopy and small angle neutron scattering analyses. *Soft Matter* **2018**, *14*, 255-263.
- ◆ Ramalhete, S.; Foster, J. S.; Green, H. R.; Nartowski, K. P.; Heinrich, M.; Martin, P.; Khimyak, Y. Z.; Lloyd, G. O., FDHALO17: Halogen effects on the solid-state packing of phenylalanine derivatives and the resulting gelation properties. *Faraday Discussions* **2017**, *203*, 423-439.
- ◆ Nartowski, K. P.; Ramalhete, S. M.; Martin, P. C.; Foster, J. S.; Heinrich, M.; Eddleston, M. D.; Hayley, G. R.; Day, G. M.; Khimyak, Y. Z.; Lloyd, G. O., The plot thickens: gelation by phenylalanine in water and dimethyl sulfoxide. *Crystal Growth & Design*, **2017**, *17* (8), 4100-4109.
- ◆ Ramalhete, S. M.; Nartowski, K. P.; Sarathchandra, N.; Foster, J. S.; Round, A. N.; Angulo, J.; Lloyd, G. O.; Khimyak, Y. Z., Supramolecular amino acid based hydrogels: probing the contribution of additive molecules using NMR spectroscopy. *Chemistry-A European Journal* **2017**, *23* (33), 8014-8024.
- ◆ Piana, F.; Case, D. H.; Ramalhete, S. M.; Pileio, G.; Facciotti, M.; Day, G. M.; Khimyak, Y. Z.; Angulo, J.; Brown, R. C.; Gale, P. A., Substituent interference on supramolecular assembly in urea gelators: synthesis, structure prediction and NMR. *Soft matter* **2016**, *12* (17), 4034-4043.
- ◆ Courtney, J. M.; Ramalhete, S. M.; Shannon, N.; Buttress, J. P.; Simmons, T.; Lawrence, E. L.; Bennet, E. J.; Blagg, R. J.; Khimyak, Y. Z.; Wildgoose, G. G., Supercapacitive polymers built from N-pyrrolyl-*bis*-(perhalogenatedaryl)boranes (manuscript in preparation, patent pending: "Conductive Polymers" UK 1711058.6).
- ◆ Debnath, S.; Roy, S.; Frederix, P. W. J. M. Ramalhete, Hirst, A. R.; Javid, N.; Hunt, N. T.; Kelly, S.; Angulo, J.; Khimyak, Y. Z.; Ulijn, R. V., Tunable supramolecular gels by varying thermal history, *Chemical Science* (manuscript in preparation).

- ◆ Ramalhete, S. M.; Green, H. G.; Nikkhah, K.; Iuga, D.; Angulo, J.; Fábián, L.; Lloyd, G. O.; Khimyak, Y. Z., Investigation of isostructural multiple gelator supramolecular hydrogels (manuscript in preparation).

Awards and presentations at conferences

- ◆ Best Oral Presentation award at the 8th GeRMN / 5th Iberian Nuclear Magnetic Resonance Biennial Meeting, 27th – 29th June 2016, oral and poster presentations titled “Understanding nanoscale organisation of tailored supramolecular hydrogels using NMR spectroscopy”.
- ◆ Best Oral Presentation award at the 9th Nuclear Magnetic Resonance Discussion Group Postgraduate Meeting, 23rd June 2016, oral presentation titled “Understanding nanoscale organisation of tailored supramolecular hydrogels using NMR spectroscopy”.
- ◆ School of Pharmacy Research Colloquium of the University of East Anglia, 15th June 2016, oral presentation titled “Understanding nanoscale organisation of tailored supramolecular hydrogels using NMR spectroscopy”.
- ◆ 6th Academy of Pharmaceutical Sciences International PharmSci, 7th – 9th September 2015, oral and poster presentations titled “Understanding nanoscale organisation of tailored supramolecular hydrogels using NMR spectroscopy”.

List of abbreviations and acronyms

AFM	Atomic force microscopy
BABA	Back-to-back
CGC	Critical gelation concentration
COSY	Homonuclear correlation spectroscopy
CP/MAS	Cross-polarisation at magic-angle spinning
CSA	Chemical shift anisotropy
DOSY	Diffusion ordered spectroscopy
DQ	Double-quantum
DSS	4,4-dimethyl-4-silapentane-1-sulfonic acid
Fmoc	Fluorenylmethyloxycarbonyl chloride
FTIR	Fourier transform infrared spectroscopy
FWHM	Full peak width at half maximum
G'	Storage modulus
G''	Loss modulus
HMB	Hexamethylbenzene
HOESY	Heteronuclear nuclear Overhauser effect spectroscopy
HR-MAS	High-resolution magic-angle spinning
HSM	Hot stage microscopy
HSQC	Heteronuclear single quantum correlation
J	Dipole-dipole coupling
LMWG	Low molecular weight gelator
NMR	Nuclear magnetic resonance
nOe	Nuclear Overhauser effect
NOESY	Nuclear Overhauser effect spectroscopy

PFG	Pulsed-field gradient
ppm	Parts per million
PTFE	Polytetrafluoroethylene
PXRD	Powder X-ray diffraction
r.f.	Radiofrequency
r.t.	Room temperature
SAFiN	Self-assembled fibrillar network
SEM	Scanning electron microscopy
SQ	Single-quantum
STD	Saturation transfer difference
T_1	Longitudinal relaxation time, in the laboratory frame of reference
T_2	Transverse relaxation time, in the laboratory frame of reference
TEM	Transmission electron microscopy
T_{gel}	Gel-to-solution transition temperature
TMS	Tetramethylsilane
VT	Variable temperature
w/v	Weight per volume
B_0	External magnetic field
δ	Chemical shift in NMR studies and phase angle in rheology measurements
τ_c	Correlation time
τ_m	Mixing time
ω_0	Larmor frequency

Table of Contents

Chapter 1	28
1. Introduction	28
1.1. A historical overview	28
1.2. Definition of gel	29
1.3. Advantages and disadvantages of gel systems	31
1.4. Classification of gels	32
1.4.1. Chemical gels	32
1.4.2. Physical gels	33
1.4.3. Stimuli responsiveness of <i>smart materials</i>	34
1.5. Supramolecular gels	36
1.5.1. Biomedical applications of supramolecular gels	37
1.5.2. Classification of supramolecular gels	38
1.5.3. Low molecular weight gelators	38
1.5.4. Amino acids, small peptides and peptidomimetics	39
1.5.5. Self-assembly of low molecular weight gelators	41
1.5.6. Gelation <i>vs.</i> crystallisation	42
1.5.7. Other gelation theories	47
1.5.8. Gel aging	47
1.5.9. The importance of self-assembly pathways	48
1.5.10. The role of solvent	48
1.5.11. Multi-component gel systems	49
Chapter 2	86
2. Characterisation techniques	86
2.1. Rheology	86
2.2. Elastic scattering techniques	87
2.2.1. Wide-angle scattering and X-ray crystallography	88
2.3. Nuclear magnetic resonance spectroscopy	89
2.3.1. Basic NMR principles	89
2.3.2. Hamiltonian operators	90
2.3.3. Zeeman interaction Hamiltonian	91
2.3.4. Bulk magnetisation vector	92
2.3.5. Larmor precession	93
2.3.6. Pulsed NMR	93
2.3.7. Laboratory and rotating frames of reference	94
2.3.8. Transition probability equations	95
2.3.9. Spectral density function	97
2.3.10. Nuclear relaxation	98
2.3.10.1. Longitudinal relaxation time	99
2.3.10.2. Transverse relaxation time	100
2.3.10.3. Comparison between T_1 and T_2 relaxation processes	101
2.3.11. Dipolar coupling	102
2.3.11.1. Homonuclear dipolar coupling	102
2.3.11.2. Heteronuclear dipolar coupling	103
2.3.12. Chemical shielding	104
2.3.13. Chemical shift anisotropy	105
2.3.14. Solid-state NMR spectroscopy	106

2.3.14.1. Magic-angle spinning	106
2.3.14.2. Heteronuclear dipolar decoupling	107
2.3.14.3. Cross-polarisation magic-angle spinning	108
2.3.15. High-resolution magic-angle spinning	110
2.3.15.1. Pulsed-field gradient experiments	111
2.3.16. Solution-state NMR spectroscopy	113
2.3.16.1. The nuclear Overhauser effect	113
2.3.16.2. Cross-relaxation rate	114
2.3.16.3. NOESY experiments	116
2.3.16.4. Saturation transfer difference NMR	117
2.3.16.5. The STD experiment	118
Chapter 3	120
3. Experimental section	120
3.1. Materials	120
3.2. Preparation of gels	120
3.3. Vial inversion test	121
3.4. Gel-to-solution transition temperature	121
3.5. Differential scanning calorimetry	121
3.6. Polarised light microscopy coupled to a hot stage unit	121
3.7. Scanning electron microscopy	121
3.8. Atomic force microscopy	122
3.9. Rheology	122
3.10. Powder X-Ray diffraction	123
3.11. NMR Spectroscopy	123
3.11.1. Solid-state NMR spectroscopy	123
3.11.1.1. One-dimensional magic-angle spinning	124
3.11.1.2. Single pulse ^{13}C with high-power ^1H decoupling	125
3.11.1.3. ^1H - ^{13}C , ^1H - ^{15}N , ^{19}F - ^{13}C and ^1H - ^{19}F CP/MAS	125
3.11.1.4. ^1H - ^{19}F - ^{13}C Double CP/MAS	126
3.11.1.5. 1D ^{19}F - ^1H HOESY	127
3.11.2. HR-MAS NMR spectroscopy	128
3.11.2.1. One-dimensional experiments	128
3.11.2.2. ^1H PFG HR-MAS	128
3.11.3. Solution-state NMR spectroscopy	130
3.11.3.1. One-dimensional experiments	130
3.11.3.2. Solvent suppression	130
3.11.3.3. Longitudinal relaxation time	131
3.11.3.4. 2D ^1H - ^1H NOESY	132
3.11.3.5. 2D ^1H - ^1H COSY	133
3.11.3.6. 2D ^1H - ^{13}C HSQC	133
3.11.3.7. STD NMR	134
3.11.4. Two-dimensional experiments	136
3.11.5. Variable temperature	136
3.11.6. Data processing	137
Chapter 4	138

4. Literature review on the structural motifs and self-assembly processes of phenylalanine	138
4.1. Introduction	138
4.2. Investigating early stages of self-assembly of Phe	139
4.3. Exploring gelation properties of Phe	144
4.4. Structural motifs of Phe gel fibres	146
4.5. Aims of the project	147
Chapter 5	148
5. Gel-crystallisation of Phe: structure, dynamics and molecular-level characterisation	148
5.1. Introduction	148
5.2. Results	149
5.2.1. Macroscopic and mechanical properties of Phe hydrogels	149
5.2.2. Morphology of the gel-crystals	151
5.2.3. Computational modelling of structure of Phe fibres	154
5.2.4. Structural studies using NMR spectroscopy	157
5.2.5. Monitoring self-assembly of Phe in water using NMR	158
5.3. Concluding remarks	163
Chapter 6	164
6. Supramolecular amino acid based hydrogels: probing the contribution of additive molecules using NMR spectroscopy	164
6.1. Introduction	164
6.2. Results	165
6.2.1. Macroscopic observations and fibre morphology determination	165
6.2.2. Resistance of gel fibres to deformation	166
6.2.3. Structural characterisation of the fibrous network	167
6.2.4. Investigation of semi-solid components by PFG HR-MAS NMR	171
6.2.5. Dynamics of molecules in solution assessed by ^1H NMR spectra	173
6.2.6. Identifying spatial correlations using 2D ^1H - ^1H NOESY NMR	176
6.2.7. Characterisation of gel/solution dynamics of exchange using ^1H T_1 measurements	178
6.2.8. Investigation of binding processes to the fibrous network by STD NMR	179
6.3. Concluding remarks	184
Chapter 7	186
7. Investigating halogen effect on the solid-state packing of phenylalanine and the properties of the resulting multiple gelator hydrogels	186
7.1. Introduction	187
7.2. Results and discussion	188
7.3. Part I – Halogenated derivatives of Phe	188
7.3.1. Macro and microscopic characterisation of hydrogels	188
7.3.2. Viscoelastic properties of hydrogels	190
7.3.3. Structural characterisation of the rigid fibres	191
7.3.4. Concluding remarks	193

7.4. Part II – Multiple gelator hydrogels of Phe and F-Phe	194
7.4.1. Characterisation of morphologic and viscoelastic properties	194
7.4.2. Structural characterisation of the rigid fibres	195
7.4.3. Investigation of gel/solution interfaces using HR-MAS	205
7.4.4. Dynamics of gelator molecules in solution	207
7.4.5. Monitoring exchange phenomena at the interfaces	214
7.5. Concluding remarks	217
Chapter 8	219
8.1. Introduction	219
8.2. Results and Discussion	220
8.2.1. Macroscopic and morphologic characterisation of hydrogels	220
8.2.2. Mechanical properties of hydrogels	223
8.2.3. Determination of the structure of the gel fibres	223
8.2.4. Investigation of intermolecular interactions responsible for aggregation and network disruption	231
8.2.5. Characterisation of dynamics of disruption and gel formation	235
8.3. Concluding remarks and future work	243
Chapter 9	246
9. Substituent interference on supramolecular assembly of urea gelators: synthesis, structure prediction and NMR	246
9.1. Introduction	246
9.2. Results and Discussion	247
9.2.1. Gelation studies	247
9.2.2. Investigating the effects of the addition of head groups by molecular modelling	249
9.2.3. Determination of the packing motifs of the gel fibres	254
9.2.4. Assessment of the local environments of rigid components of gels by NMR	255
9.2.5. Investigation of the local environments of mobile components of gels by NMR	261
9.2.6. Identification of spatial connectivities in the gel state	262
9.3. Concluding remarks	264
Chapter 10	266
10. General discussion and conclusions	266
10.1. Structure and dynamics of gel-crystallisation of Phe	266
10.2. The effects of structural modifications of Phe	267
10.3. Multi-component hydrogels of Phe	269
10.4. Tuning of rheological properties by preparation of multi-component hydrogels	270
10.5. Modulation of the structure of the gel fibres and of interfacial dynamics in multiple gelator hydrogels	271
10.6. General strategy for the characterisation of supramolecular gels	273
10.7. Interpretation of ^1H T_1 measurements in supramolecular gels	276
10.8. Probing dynamic processes at the interfaces – the role of STD NMR	277
10.8.1. Proposed mechanism of transfer of saturation in molecular gels	279
10.9. Overall conclusions	280
11. References	282

List of Figures

Figure 1.1. Number of publications per year under the research topic of "hydrogel" in the Web of Science™ between 1965 and 2016. Adapted and updated from ³ .	29
Figure 1.2. Human-shaped hydrogel of nanocellulose showing gels mouldability.	31
Figure 1.3. Classification of gels by the nature of interactions (physical and chemical) sub-divided according to the nature of the solid phase (gelator), with some common examples.	32
Figure 1.4. Chemical (black) and physical (red) stimuli. ³²	34
Figure 1.5. Chemical structures of precursors of hydrogelators of Dex-FFFK(Taxol/HCPT)E. ²⁶	36
Figure 1.6. Molecular structures of 1) the first supramolecular gelator dibenzoyl-L-cystine ⁴¹ developed, 2) the fastest gelating aroyl-L-cystine derivative ⁴³ and 3) the smallest gelator N,N'-dimethylurea ⁴⁴ .	37
Figure 1.7. Representation of a) a gel, b) an aerogel and c) a xerogel. ⁸	38
Figure 1.8. Process of hierarchical self-assembly of LMW gelators into larger complex supramolecular structures. ¹⁷	42
Figure 1.9. a) Formation of a fibre network based on the nucleation-growth-fibre branching mechanism. b) Fibre growth is usually followed by branching at the surface of parent fibre tips, which occurs due to crystallographic mismatch branching. ^{12, 28, 73}	44
Figure 1.10. Free energy diagram comparing the gel and crystal states. In this scenario, the crystalline state is considered the thermodynamically most stable product, whereas the gel phase is considered arrested at a metastable state that anticipates crystallisation when quenching thermoreversible gels. Energy of activation (E _a), Gibbs free energy (ΔG). Adapted from references ^{28, 48} .	45
Figure 1.11. Schematic diagram of the free energy of gel and crystal states proposed by Tuttle <i>et al.</i> , showing that fibres can represent the thermodynamic minimum when surrounded by high activation barriers. ¹⁹	46
Figure 1.12. Schematic representation of Hansen solubility parameters (dispersion forces – δ_d , dipolar intermolecular forces – δ_p and hydrogen bonds – δ_h) in the 3D Hansen space and their correlation with gelation outcome. ⁹¹ Dien <i>et al.</i> (2014) noticed a correlation between Hansen solubility parameters and the ability of a sorbitol derived organogelator to gelate in various organic solvents. The results followed a pattern of concentric spheres with the central solubility sphere being surrounded by spherical regions corresponding to slow gelation, instant gelation and insolubility cases. This pattern highlights that gelation requires a balance between solubility and insolubility.	49
Figure 1.13. a) Low molecular weight gelators form complex supramolecular structures through non-covalent interactions. The introduction of additive molecules can either modify the physical properties of the hydrogel (left) or prevent its formation (right). b) Supramolecular co-assembly and self-sorting processes can occur when both molecules are low molecular weight gelators. c) When the additive is a non-gelling molecule, the physical properties of the resulting gel material might be modulated. Adapted from reference ⁵¹ .	50
Figure 1.14. Characterisation techniques able to investigate the hierarchical organisation of supramolecular gels, highlighting the presence of several length scales of organisation.	53
Figure 1.15. Schematic representation of a) parallel plate and b) cone and plate geometry setups. The sample is placed between both surfaces and while the top plate or cone rotates the bottom plate remains stationary. c) Schematic stress response to oscillatory strain deformation for an elastic solid, a viscous fluid and a viscoelastic material, where δ is the phase angle. Adapted from reference ¹⁰¹ .	56
Figure 1.16. a) Factors that determine gel strength, adapted from reference ⁷³ . Raeburn <i>et al.</i> (2013) found that rheological properties were mainly determined by fibre width, degree and distance of fibre branching and degree of fibre interpenetration. b) Transmission electron microscopy image of a freeze-dried sample prepared from a α -manno/p-xylene gel, highlighting the same features in a real fibre. ⁵⁰	57
Figure 1.17. a) Maximum of storage modulus (G'_{\max}) as a function of correlation length (ξ) for N-lauroyl-L-glutamic acid di-n-butylamide gels in isostearyl alcohol. ⁷³ b) Simulation of storage modulus (G') as a function of junction density for N-lauroyl-L-glutamic acid di-n-butylamide gels in isostearyl alcohol. ¹⁰²	58

Figure 1.18. Stress distribution in networks with a) long fibre length (long ξ) and b) short fibre length (short ξ). From red to blue, the stress distribution varies from maximum to minimum, respectively. When the fibre length is long (a) the stress is distributed over a large area, while, whereas when the fibre length is short (b) the stress distribution occurs mainly along several radii. ¹⁰²	58
Figure 1.19. Overview microscopy images of nanocellulose samples acquired using a,d,g) atomic force microscopy, b,e,h) cryo scanning electron microscopy and c,f,i) transmission electron microscopy. ¹⁰⁶	60
Figure 1.20. Powder X-ray diffraction patterns of “gel – sol” (which corresponds to the subtraction of the diffraction pattern of the neat solvent to the diffraction pattern of the wet gel, as described by Weiss ¹¹⁰), wet gel, xerogel, bulk reference solid and simulated pattern from single-crystal data of an imidazole derivative, highlighting the difference between the supramolecular organisation of the gel and the neat crystals. ⁹⁸	62
Figure 1.21. Powder X-ray diffraction patterns of the xerogel, bulk reference solid and simulated from single-crystal data of a secondary ammonium salt, highlighting the similarity between the supramolecular organisation of the gel and crystal structure. ¹¹²	63
Figure 1.22. Pioneering studies on the characterisation of gels using NMR spectroscopy conducted by Schaefer, ¹¹⁶ Child and Pryce, ¹¹⁷ Derbyshire and Duff, ¹¹⁸ Yokota et al., ¹¹⁹ Schmitt et al., ¹²⁰ For et al., ¹²¹ Kobayashi et al., ¹²² Schoonbeek et al., ¹²³ Behanna et al., ¹²⁴ Mahajan et al., ¹²⁵ and Iqbal et al. ¹¹⁵	67
Figure 1.23. Solid-state ^2H NMR spectra acquired on poly (DL-lactide-co-glycolide) 50:50 containing a) 1.17 % of $^2\text{H}_2\text{O}$, b) dried under vacuum and c) dried further under high vacuum, using a 300 MHz solid-state spectrometer. ¹²⁹	69
Figure 1.24. First highly-resolved ^1H - ^{13}C CP/MAS NMR spectrum acquired on CDCl_3 -swollen polystyrene gels using an MAS rate of 4 kHz and a 25 MHz solid-state spectrometer (^{13}C line widths < 15 Hz). ¹²¹	70
Figure 1.25. First ^1H - ^{13}C CP/MAS NMR spectrum acquired on a wet supramolecular gel of a 1,2-bis-urea derivative toluene- d_8 , using an MAS rate of 1.8 kHz and a 400 MHz solid-state spectrometer. ¹²³	71
Figure 1.26. ^1H HR-MAS NMR spectra acquired on supramolecular gels a) with a 50 % diffusion filter and b) without a diffusion filter, using an MAS rate of 4 kHz and a 500 MHz spectrometer. ¹¹⁵	72
Figure 1.27. Distinction between observable and non-observable species on the different solution-state NMR time scales. ¹⁴⁷	77
Figure 1.28. Proposed mechanism for transfer of saturation in STD NMR experiments performed with supramolecular hydrogels. Gelator molecules forming the network (bound state, left) are in fast exchange with those in the bulk solution phase (free state, right), allowing accumulation and detection of saturation in solution.	80
Figure 1.29. Schematic representation of the application of NMR methods to probe different time scales of motions and self-organisation in supramolecular materials at variable length scales.	81
Figure 1.30. Complimentary techniques used in NMR crystallography studies of supramolecular gels, adapted from references ^{132, 137} . Reitveld refinement consists of performing small variations of the atomic coordinates in order to provide the best match to powder diffraction patterns. ¹³⁷	83
Figure 2.1. Schematic stress response to oscillatory strain deformation for an elastic solid, a viscous fluid and a viscoelastic material, where δ is the phase angle. Adapted from reference ¹⁰¹ .	87
Figure 2.2. Geometry for interference of a scattered wave, needed to derive Bragg’s Law. The dashed lines are parallel to the crests of the incidents and diffracted wavefronts. The angle on incidence of the two parallel rays is θ . The interplanar spacing, d , sets the difference in path length for the ray scattered from the top plane and the ray scattered from the bottom plane. This difference in path lengths is $2ds\sin\theta$. Constructive wave interference (and hence strong diffraction) occurs when the difference in path length for the top and bottom rays is equal to one wavelength (λ), $2ds\sin\theta = n\lambda$ (Bragg’s law). Adapted from reference ¹⁶⁶ .	89
Figure 2.3. Relative nuclear energy levels of α and β -states of a spin $1/2$ caused by an external magnetic field (B_0), designated as Zeeman splitting. Adapted from reference ¹⁷¹ .	92
Figure 2.4. The external static magnetic field causes nuclear spins to precess around the z -axis, represented as a vector moving on the surface of a cone (left). Vector model of bulk magnetisation for spin $1/2$ nuclei,	

where the excess in populations of spins in the α -state states give rise to bulk magnetisation (M_0) aligned along the external magnetic field (B_0). Adapted from reference ¹⁷¹ .	93
Figure 2.5. Representation of laboratory and rotating frames of references. ¹⁷¹	94
Figure 2.6. Energy levels for a two-spin system in equilibrium. Adapted from reference ¹⁶⁸ .	96
Figure 2.7. Spectral density function ($J(\omega)$) as a function of frequency of molecular motions for different correlation times (τ_c). The area under the curve is independent of τ_c . Adapted from reference ¹⁶⁸ .	98
Figure 2.8. Process of loss of z -magnetisation via T_1 relaxation. Adapted from reference ¹⁷¹ .	99
Figure 2.9. Process of loss of coherence in the transverse xy -plane via T_2 relaxation, leading to zero net magnetisation. Adapted from reference ¹⁷¹ .	100
Figure 2.10. Motional dependence of longitudinal (T_1) and transverse (T_2) relaxation times. The T_1 minimum occurs when $\omega_0 \tau_c = 1$. Adapted from reference ¹⁷¹ .	101
Figure 2.11. Energy conserving “flip-flop” interaction between two like spins occurs since $\omega I_1 = \omega I_2$. ¹⁷¹	103
Figure 2.12. Energy conserving “flip-flop” transitions cannot occur between two unlike spins since $\omega I \gg \omega S$. ¹⁷¹	104
Figure 2.13. Representation of preferential orientation of the ellipsoidal electron cloud of a carbonyl carbon with respect with the external magnetic field, with the corresponding values of chemical shift tensors, a) δ_{11} , b) δ_{22} and c) δ_{33} . Adapted from reference ¹⁷⁴ .	106
Figure 2.14. Representation of a rotor spun at the magic-angle spinning ($\theta = 54.74^\circ$). ¹⁷⁷	107
Figure 2.15. Energy differences between the transitions of the I and the S spins can be made equal in a doubly rotating frame when the nutation frequencies on both spins are equal ($\omega I = \omega S$). ¹⁷⁴	109
Figure 2.16. HR-MAS stator with a magic-angle gradient (GMAS) along the rotor spinning axis. ¹³⁵	111
Figure 2.17. a) Representation of the gradient produced along the magic-angle of the rotor. b) Typical decay of 1H -peak intensity with increasing gradient strength in a PFG HR-MAS experiment. ¹³⁵	112
Figure 2.18. Energy levels for a two-spin system upon saturation of spin S . Adapted from reference ¹⁶⁸ .	114
Figure 2.19. Example of 1D NOESY difference spectrum. When spin S is irradiated (as indicated by the negative peak intensity), peak intensity of spin I is increased due to cross-relaxation from spin S , which is more evident in the difference (Δ) spectrum. It has been assumed that the cross-relaxation rate is positive, so the nOe enhancement is positive. Adapted from reference ¹⁶⁸ .	114
Figure 2.20. Dependence of nOe peak intensity and signal with correlation time (τ_c). The cross-over point is characteristic of medium-sized molecules and corresponds to the absence of nOe enhancement (occurs when $\omega_0 \tau_c = 1.12$). Adapted from reference ¹⁶⁸ .	115
Figure 2.21. Evolution of nOe enhancement with mixing time (τ_m). The nOe grows linearly initially, reaches a maximum and then decreases back to equilibrium as the equilibrium population differences are restored through relaxation. Adapted from reference ¹⁷¹ .	117
Figure 2.22. Schematic representation of an STD NMR experiment. a) Protein-ligand complex. b) Off-resonance (STD_{off}) and on-resonance (STD_{on}) spectra, and the STD difference spectrum resulting from the subtraction of STD_{on} to STD_{off} . ¹⁹³	119
Figure 3.1. Schematic representation of parallel plate and cone and plate geometry setups, with the gel being placed between both surfaces, adapted from reference ¹⁰¹ .	123
Figure 3.2. Representation of a single pulse experiment. The $\pi/2$ pulse converts equilibrium magnetisation of the I nuclei into transverse magnetisation. During the acquisition time, chemical shifts and spin-spin couplings develop in the x,y -plane. ¹⁷²	124
Figure 3.3. Representation of a single pulse experiment pulse sequence using high-power decoupling of the I spins during acquisition of the S spins.	125
Figure 3.4. Representation of an I - S CP/MAS NMR pulse sequence. The first $\pi/2$ pulse brings equilibrium magnetisation of the I nuclei along the x,y -plane. This magnetisation is locked by a ramped spin lock pulse on I , in which the spin lock power is changed from 70 to 100 % during the spin lock time. Under MAS, the Hartmann-Hahn condition splits into a set of matching sidebands. With a ramped contact pulse, the Hartmann-Hahn is swept over these possible match conditions and becomes insensitive to minor miss-	

settings, instrumental instabilities or different MAS rates. Simultaneously, a spin lock pulse on S assures the same precession frequency for the S spins, to satisfy the Hartmann-Hahn condition (described in Chapter 2, section 2.3.14.3, page 110). During this CP period, I and S spins can exchange energy in their respective rotating frames, which transfers polarisation to the S spins from the large energy bath of the abundant I . High-power decoupling of the I spins is applied during acquisition of the S spins. The repetition time of the pulse sequence is governed by I relaxation.^{172, 174} 125

Figure 3.5. Representation of an ^1H - ^{19}F - ^{13}C double CP/MAS NMR pulse sequence. The experiment uses two consecutive cross-polarisation steps that involve the sequential transfer of polarisation among three spins.^{168, 198} 127

Figure 3.6. Representation of a 1D ^{19}F - ^1H HOESY NMR pulse sequence. The first $\pi/2$ pulse creates ^{19}F magnetisation on the x,y -plane. In the evolution period, a π pulse is located in the middle of t_1 , during which ^{19}F chemical shifts evolve and the π pulse on ^1H eliminates $J(\text{F},\text{H})$ couplings. This creates negative z -magnetisation for ^1H s. Afterwards, the second $\pi/2$ pulse changes ^{19}F transverse magnetisation into the negative z -direction. At the beginning of the mixing time, τ_m , both spins are in the $-z$ -directions so the ^{19}F signal is modulated with this chemical shift information. During the mixing time, the spins undergo cross-relaxation. The final $\pi/2$ pulse realigns the vectors into the x,y -plane and creates ^1H transverse magnetisation. Heteronuclear decoupling of the ^{19}F spins is applied during acquisition of the ^1H spins.^{172, 199} 127

Figure 3.7. Representation of a PFG experiment with stimulated echo and longitudinal eddy current delay diffusion-filtered pulse sequence. Smoothed-square gradients with horizontal stripes correspond to pulsed-field gradients whose strength is varied during the experiment. Field gradients are short periods during which the applied magnetic field is made spatially inhomogeneous. All gradient pulses are trapezoidal shaped to compensate for the inability of instrumentation to generate perfect rectangular gradients. The gradient pairs are applied as bipolar gradients of opposite sign and separated by π r.f. pulses, an approach which reduces gradient artefacts, eddy currents and allows stronger overall gradients. The first $\pi/2$ pulse aligns all I magnetisation into the x,y -plane. The π pulse changes the direction of precession and refocuses chemical shifts, which is important in the presence of chemical exchange or spin diffusion. During the two τ_1 delays, the magnetisation is transverse, and therefore it is subject to T_2 relaxation. The second gradient of equal magnitude cancels the effects of the first and refocuses all spins, provided there was no change of position with respect to the direction of the gradient. During the τ_2 period, the magnetisation is aligned along the z -axis, and thus it is subject to T_1 relaxation. After the second $\pi/2$ pulse, the spins are in the z -axis so additional short gradient pulses, g_{spoil} , are added to destroy transverse magnetisation due to pulse imperfections. Eddy currents are generated in surrounding conducting surfaces by the rapid rise and fall of the gradient pulses. To prevent these effects a delay is necessary between the end of a gradient pulse and the start of spectral acquisition. During this eddy current delay (τ_e), magnetisation is stored in the z -direction and the eddy currents are allowed to decay. This sequence is less prone to T_2 artefacts because during the diffusion time (Δ) the magnetisation is in the z -axis. The stimulated echo sequence is also the method of choice for macromolecules.^{135, 168, 172, 186, 200} 129

Figure 3.8. Representation of an excitation sculpting pulse sequence. It consists of a solvent-selective excitation profile (π pulse) embedded between two pulsed-field gradients. By applying the filter sequence twice with G_1 and G_2 not being correlated to each other, a flat baseline can be obtained.²⁰² 131

Figure 3.9. Representation of an inversion-recovery pulse sequence. The first π pulse inverts the magnetisation so that it lies along $-z$ -axis. Relaxation is then allowed to occur during the delay τ . The $\pi/2$ pulse converts it into transverse magnetisation for detection. During the set of experiments, the delay time τ is varied, which enables the remaining magnetisation to be plotted as a function of time delay.²⁰³ 131

Figure 3.10. Representation of a 2D ^1H - ^1H NOESY NMR pulse sequence using WATERGATE²⁰⁵ 3-9-19 selective spin echo. The first $\pi/2$ pulse aligns all I magnetisation into the x,y -plane. During the evolution period, t_1 , chemical shifts and spin-spin couplings evolve. The second $\pi/2$ pulse aligns the y components of the two vectors, which are now labelled with their individual chemical shifts, into the z -direction. During the

mixing period, τ_m , I spins are allowed to relax, show cross-relaxation and magnetisation is transferred. The final $\pi/2$ pulse realigns the vectors into the x,y -plane and creates transverse magnetisation for detection. WATERGATE²⁰⁵ 3-9-19 is a pulse train of symmetric pulses in the form $3\alpha-\tau-9\alpha-\tau-19\alpha-\tau-19\alpha-\tau-9\alpha-\tau-3\alpha$ with $26\alpha = \pi$ used for solvent suppression. The first sine-shaped gradient dephases all the resonances that have been excited by the first $\pi/2$ pulse. Then, the selective pulses reverse the sense of precession of all the spins of interest but not that of the solvent. The second sine-shaped gradient refocuses the I spins of interest whereas the solvent resonances dephase even further.^{172, 199} 132

Figure 3.11. Representation of a 2D ^1H - ^1H COSY NMR pulse sequence. The $\pi/2$ purge pulse, indicated by the purple square pulse, consists of a long period of spin locking. Magnetisation not aligned along the spin locking axis will precess around the spin locking field and will dephase, as this purge pulse is used to suppress contributions from zero-quantum coherence. The first $\pi/2$ pulse transforms z -magnetisation into transverse magnetisation. The chemical shift and J -coupling develop during the evolution period, t_1 . The chemical shift of the direct dimension, f_2 , is modulated by the J -coupling of the indirect dimension, f_1 . Two gradient pulses of different strengths or durations are applied before and after the second $\pi/2$ pulse to select particular coherence transfer pathways.^{168, 172} 133

Figure 3.12. Representation of a 2D ^1H - ^{13}C HSQC NMR pulse sequence. The sequence starts with an INEPT transfer (insensitive nuclei enhanced by polarisation transfer) from I to S , which results in anti-phase magnetisation of S with respect to I . The editing period has the purpose of attributing different signs to CH and CH_3 , in comparison to CH_2 signals, and it is characterised by G_1 , the π pulse and the τ_1 delays. During the evolution period, t_1 , anti-phase magnetisation develops the S chemical shifts. The π pulse on I in the middle of t_1 applied over a period of time symmetrically distributed eliminates the $J(I,S)$ heteronuclear couplings in the f_1 dimension, when $t_1 = 1/(4J_{1s})$. Afterwards, a reverse INEPT converts S magnetisation into in-phase I magnetisation. Unconventionally, there is the addition of a second reverse INEPT block in order to select both orthogonal components of the magnetisation present during t_1 and improve sensitivity. G_1 and G_2 are gradients for echo/anti-echo selection. Being an echo/anti-echo pulse sequence, the intensity of the refocusing gradient G_2 is inverted on alternated scans to obtain the N- (negative) and P-type (positive) data separately, which allows phase-sensitive spectra to be obtained. Acquisition is conducted with GARP²⁰⁶ decoupling.¹⁷² 134

Figure 3.13. Representation of an STD NMR pulse sequence using WATERGATE²⁰⁵ 3-9-19 selective spin echo. During the saturation time, t_{sat} , I magnetisation is selectively saturated either on (STD_{on}) or off-resonance (STD_{off}) by a train of Gaussian pulses, indicated by the orange Gaussian-shaped pulse in brackets. The band-width of these 50 ms pulses is approximately 20 Hz, applied in a loop with $n = 40$, which results in a narrow-band irradiation. For every set of scans, the pre-irradiation frequency is changed from STD_{on} to STD_{off} (interleave mode) and the two spectra are stored separately. G_1 is a pulsed-field gradient that ensures that only z -magnetisation remains.^{158, 172, 199} 135

Figure 3.14. 2D NMR experiments start with the preparation time, in which the sample is excited. The resulting magnetisation is allowed to evolve during the evolution time, t_1 . During the mixing time, τ_m , there is modulation of magnetisation detected in f_2 by the evolution of the frequency of the second spin, f_1 . Finally, during the detection period, the signal is recorded as a function of the second time variable, t_2 . This pulse sequence is repeated cyclically and an free induction decay is recorded as a function of t_2 for increasing t_1 values.¹⁶⁸ 136

Figure 4.1. a) Electron-diffraction pattern of a single Phe fibril.²⁰⁷ b) Ladder-like structure of Phe aggregates obtained by molecular dynamics simulations conducted at high pH in the presence of counterions (yellow spheres).²⁰⁷ 140

Figure 4.2. a) Monoclinic unit cell of Phe. b) Proposed interactions involved in the stabilisation of Phe fibres, composed of a bilayer of hydrophobic/hydrophilic interactions.⁶⁶ 141

Figure 4.3. a) Lowest energy nanotubular structure ($-8434 \text{ kJ mol}^{-1}$) of Phe proposed by German et al.⁷⁴ and b) crystal structure of Phe monohydrate from reference²¹⁴. Green atoms represent carbon, blue represent nitrogen, red represent oxygen and white represent hydrogen.⁷⁴ 142

Figure 4.4. Representative structures of single, double and tetra-tube models.²⁰⁹ 143

Figure 4.5. Top-view snapshot of a small-scale defect (circled in white) in a DPPC film from molecular dynamics simulations. DPPC molecules are coloured blue with terminal methyl groups coloured yellow. Water molecules are red and white and Phe molecules can be seen by their light blue aromatic rings.²¹⁷ 144

Figure 4.6. *a)* Kinetics of hydrogel formation of Phe from dynamic light scattering studies, with a photograph of a self-supporting gel (300 mM). The initial lag-phase might be due to nucleation events where molecules associate to form productive nucleus for further elongation into mature fibres, or the associated molecules are insensitive to light scattering. *b)* Variation of ¹H chemical shift of aryl protons with concentration of Phe and *c)* rate of change of ¹H chemical shift with respect to change in concentration ($\Delta\delta/\Delta C$) for all Phe protons. *d)* Molecular structure of Phe with assignment.²⁰⁸ 146

Figure 5.1. *a)* Molecular structure of L-phenylalanine, with numbered carbons. *b)* Hydrogel of Phe (303 mM). 150

Figure 5.2. *a)* Frequency sweep and *b)* stress sweep experiments for different concentrations of Phe hydrogels. Lines between points were added to help guide the eye. Hot solutions (ca. 0.5 mL) were pipetted into a 150 μ m gap (cone and plate geometry). All samples were subjected to frequency sweeps in the range of 0.1 to 100 Hz and applied stress of 700 Pa, as well as stress amplitude sweeps in the range of 500 to 10000 Pa. 150

Figure 5.3. *a)* AFM image of the dry hydrogel of Phe, highlighting the entanglement of a fibrous network. *b)* Histogram of measured widths in AFM experiments for the hydrogel of Phe, with an average width of 437 ± 16 nm. 151

Figure 5.4. The determination of the hydrate structure of the hydrogel allows for *a)* the morphology of the fibres by TEM to be confirmed and *b)* the molecular packing in these fibres determined by electron diffraction. Zone axis electron diffraction of the fibres indicates the growing direction to be the [010] crystallographic direction. 152

Figure 5.5. Unit cell of Phe monohydrate shown along the *a* axis (CCDC Number 1532251). The unit cell presented monoclinic metric symmetry, with the following refined parameters: $a = 13.112(14)$ Å, $b = 5.409(5)$ Å, $c = 13.849(14)$ Å, $\beta = 102.985(4)$ Å, ($V = 957.11(17)$ Å³) and $Z = 4$. The space group was assigned as $P2_1$.²¹³ 153

Figure 5.6. *a,b)* BFDH crystal morphology calculation indicated a needle habit of Phe monohydrate. Analysis of the crystal structure indicated that *c)* the electrostatics (shown here as the electrostatic potential Hirshfeld surface) are a significant interaction for the stacking of Phe in this anisotropic manner, with π - π stacking, hydrogen bonding and van der Waals interactions complementing the $+/-/+/-$ stacking in the [010] direction. Figure *c*) shows the structure viewed down [010] and *d*) is shown viewed down the [001] with *b* axis coloured green, *a* axis red and *c* axis blue. 154

Figure 5.7. Calculated energy landscape of Phe. $Z' = 1$ and $Z' = 2$ predicted crystal structures are indicated as grey circles and black diamonds, respectively. The known forms I, II and III, as well as a number of ordered versions of form IV, are indicated. Also highlighted is the structure resulting from *in silico* dehydration of the monohydrate form found in the hydrogel. 156

Figure 5.8. Packing of dimers of Phe shown down the *b* axis, with water molecules removed for clarity. Dimer stacks are interacting with each other except via hydrogen bonding and π - π interactions. What is also clear is that the dimer stacks are anisotropic with the hydrophilic section shorter than the hydrophobic region. 157

Figure 5.9. ¹H-¹³C CP/MAS solid-state NMR spectra of anhydrous Phe and Phe hydrogel acquired with MAS rates of 10.5 or 8 kHz and 2048 or 8192 scans, respectively. All experiments were conducted with a recycle delay of 20 s and $\pi/2$ pulse lengths of 3.2 μ s (¹H) and 3.0 μ s (¹³C), using a 400 MHz solid-state NMR spectrometer. Asterisks represent spinning sidebands. 158

Figure 5.10. Experimental ¹³C chemical shift values for Phe hydrogel derived from the spectra acquired at an MAS rate of 8 kHz vs. calculated chemical shifts for the Phe monohydrate that give best agreement with both NMR and PXRD data from the hydrogel. 158

Figure 5.11. ^1H solution-state NMR spectra of a solution and hydrogel of Phe. The high intensity peak at 4.7 ppm is due to residual water and exchangeable protons. Experiments were conducted with a recycle delay of 2 s, using a 500 MHz solution-state NMR spectrometer. 159

Figure 5.12. **a)** Variation of ^1H NMR chemical shifts (δ) with concentration of Phe in water. **b)** Dependence of ^1H NMR peak intensity on the concentration of Phe in D_2O . Three different stages during the gelation process can be identified based on intensities of the peaks, i.e. solution, supersaturated solution and gel phase. The orange line indicates the NMR-determined CGC. All experiments were conducted with a recycle delay of 10 s, using a 500 MHz solution-state NMR spectrometer. 160

Figure 5.13. Kinetics of gelation of Phe monitored by the acquisition of ^1H solution-state NMR spectra over time, immediately after cooling down a hot solution of Phe (measured at 298 K). All experiments were conducted with a recycle delay of 10 s, using a 500 MHz solution-state NMR spectrometer. 161

Figure 5.14. **a)** Evolution of ^1H solution-state T_1 relaxation times of different regions of Phe as a function of concentration in D_2O . **b)** ^1H T_1 times of hydrogels of Phe (303 mM), recorded from 298 to 353 K. All experiments were conducted with a recycle delay of 10 s, using a 500 MHz solution-state NMR spectrometer. 163

Figure 6.1. Zwitterionic structures of the amino acids in study with the corresponding solubilities in water at 298 K. Tyr is less soluble than Phe since the additional hydroxyl group interacts with nearby hydroxyl and carboxylate groups, resulting in stronger Tyr-Tyr than Tyr-water interactions.²²⁶ 165

Figure 6.2. Storage (G) and loss (G') moduli at **a)** increasing frequency sweeps and **b)** increasing stress sweeps for the hydrogels of Phe, Phe/Ser (5:1), Phe/Leu (5:1), Phe/Trp (5:1) and Phe/Tyr (5:1). Measurements of storage and loss moduli of supramolecular hydrogels were reproducible with an error of 10.7 %. Lines are guides for the eyes. Hot solutions (ca. 1.5 mL) were pipetted into a 300 μm gap (cone and plate geometry). All samples were subjected to frequency sweeps in the range of 0.1 to 100 Hz and applied stress of 700 Pa, as well as stress amplitude sweeps in the range of 500 to 10000 Pa. 167

Figure 6.3. PXRD patterns of the hydrogels of Phe, Phe/Leu (5:1), Phe/Ser (5:1), Phe/Trp (5:1) and Phe/Tyr (5:1) and reference solid powders of the anhydrous form I of Phe and the commercially available Tyr (CSD ref. LTYROS02)²²⁹. 168

Figure 6.4. Polarised light microscopy images of hydrogels of **a)** Phe and **b)** Phe/Tyr (5:1) (303 mM), and **c)** polarised light microscopy images of the commercially available Tyr (CSD ref. LTYROS02)²²⁹. SEM images of the dry hydrogels of **d)** Phe and **e)** Phe/Tyr (5:1) (303 mM). Insoluble white needle-like crystals of Tyr can be seen immersed in a network of entangled thin fibres. 168

Figure 6.5. ^1H - ^{13}C CP/MAS NMR spectra of **a)** wet and **b)** dry hydrogels of Phe, Phe/Leu (5:1), Phe/Ser (5:1), Phe/Trp (5:1) and Phe/Tyr (5:1) acquired with MAS rates of 8.5 kHz and 8192 scans (wet gel samples) or 10 kHz and 2048 scans (dry gel samples); and reference solid powders of the commercially available Trp (CSD ref. QQQBTO03)²²⁹ and Tyr (CSD ref. LTYROS02)²²⁹ acquired with MAS rates of 10.5 kHz and 2048 scans. All experiments were conducted with a recycle delay of 20 s and $\pi/2$ pulse lengths of 3.2 μs (^1H) and 3.0 μs (^{13}C), using a 400 MHz solid-state NMR spectrometer. Rectangles and triangles highlight the presence of rigid elements of Trp and Tyr, respectively. Spectra of reference solid powders of commercially available Leu and Ser are not shown since insoluble components of Leu or Ser were not observed in the mixed materials. Asterisks represent spinning sidebands. 170

Figure 6.6. Evolution of ^1H PFG HR-MAS NMR normalised peak intensity with increasing gradient strength of hydrogels of Phe, Phe/Leu (5:1), Phe/Ser (5:1), Phe/Trp (5:1) and Phe/Tyr (5:1), acquired with MAS rates of 1 kHz at 298 K. Tyr presented poor signal-to-noise, preventing accurate determination of peak intensity. All experiments were conducted with 5 to 95 % of the maximum gradient intensity (G_{\max} = of 49.5 G cm^{-1}), a diffusion delay of 70 ms and a diffusion gradient of 1 ms, using a 400 MHz HR-MAS NMR probe head. 172

Figure 6.7. Kinetics of gelation monitored by the acquisition of ^1H solution-state NMR spectra over time, immediately after cooling down hot solutions of Phe, Phe/Leu (5:1), Phe/Ser (5:1), Phe/Trp (5:1) and Phe/Tyr (5:1) (303 mM) (measured at 298 K). Phe, Trp and Tyr peak ^1H become broader as a consequence of gelation,

whereas Leu and Ser ^1H peaks remained sharp even after the hydrogel is formed. All experiments were conducted with a recycle delay of 10 s, using a 500 MHz solution-state NMR spectrometer. 174

Figure 6.8. ^1H solution-state NMR spectra of hydrogels of Phe, Phe/Leu (5:1), Phe/Ser (5:1), Phe/Trp (5:1) and Phe/Tyr (5:1) acquired 24 h after quenching hot solutions (303 mM) measured at 298 K. Tyr peaks displayed much lower intensities than expected according to the composition, as Tyr precipitates under the experimental conditions. All experiments were conducted with a recycle delay of 10 s, using a 500 MHz solution-state NMR spectrometer. 175

Figure 6.9. 2D ^1H - ^1H NOESY spectra of hydrogels of Phe, Phe/Leu (5:1), Phe/Ser (5:1), Phe/Trp (5:1) and Phe/Tyr (5:1) acquired with a mixing time of 0.5 s (measured at 298 K). Negative $n\text{Oe}$ enhancements (blue), characteristic of large molecules, indicate that free gelator molecules contain properties from the fibrous network. Blue dashed lines highlight intermolecular correlations between Phe and **b**) Leu, **d**) Trp and **e**) Tyr, which are absent in hydrogels of Phe/Ser (c). Positive $n\text{Oe}$ enhancements (green), characteristic of small molecules, are highlighted by green dashed lines and correspond to correlations between Leu molecules in solution (b). All experiments were conducted with a recycle delay of 2 s and 32 scans, using a 500 MHz solution-state NMR spectrometer. 177

Figure 6.10. ^1H solution-state NMR T_1 times of Phe, Leu, Ser, Trp and Tyr in hydrogels of Phe, Phe/Leu (5:1), Phe/Ser (5:1), Phe/Trp (5:1) and Phe/Tyr (5:1), recorded from 298 to 353 K. All experiments were conducted with a recycle delay of 10 s, using a 500 MHz solution-state NMR spectrometer. 179

Figure 6.11. Build-up curves of fractional STD response (η_{STD}) in hydrogels of **a**) Phe measured at 298 K. **b**) Initial slope values recorded from 298 to 338 K upon saturation of the network in the hydrogel of Phe ($\text{STD}_{\text{on}} = 0 \text{ ppm}$ and $\text{STD}_{\text{off}} = 40 \text{ ppm}$). STD parameters in these studies were reproducible with a mean error of 9.6 % as a result of three independent measurements. All experiments were conducted with a total experiment time of 6 s, using a 500 MHz solution-state NMR spectrometer. 181

Figure 6.12. Build-up curves of η_{STD} in hydrogels of Phe/Leu (5:1), Phe/Ser (5:1), Phe/Trp (5:1) and Phe/Tyr (5:1), measured at 298 K ($\text{STD}_{\text{on}} = 0 \text{ ppm}$ and $\text{STD}_{\text{off}} = 40 \text{ ppm}$). 183

Figure 7.1. Molecular structure of the zwitterionic form of Phe with numbering of aromatic carbon atoms and the halogenated derivatives under study. 188

Figure 7.2. Photographs of hydrogels of Phe and its halogenated derivatives. 189

Figure 7.3. SEM images of dry hydrogels of **a**) Phe, **b**) F-Phe, **c**) 2F-Phe, **d**) 5F-Phe, **e**) Cl-Phe and **f**) 2Cl-Phe (100 mM). 190

Figure 7.4. Evolution of storage modulus (G') in frequency sweep experiments for Phe, F-Phe, 2F-Phe, 5F-Phe, Cl-Phe, 2Cl-Phe and Br-Phe. Hot solutions (ca. 1 mL) were pipetted into a 500 μm gap (parallel plate geometry). All samples were subjected to frequency sweeps in the range of 0.1 to 100 Hz and applied stress of 500 Pa. 191

Figure 7.5. Packing motif of the **a**) Phe, **b**) F-Phe, **c**) 2F-Phe and **d**) Cl-Phe fibres. **a**) Packing of dimers of Phe shown down the b axis and with water guests removed for clarity. **b**) A (hydrophobic) and B (hydrophilic) layers are indicated, # is highlighting the dimer formation between the zwitterionic groups. Dimer stacks are not interacting with each other except for some hydrogen bonding and π - π interactions. It is also clear that the dimer stacks are anisotropic with the hydrophilic section shorter than the hydrophobic region. 192

Figure 7.6. Electrostatic potential Hirshfeld surfaces of the **a**) F-Phe and **b**) Cl-Phe derivatives with the asymmetric unit (ASU) of the respective monohydrate crystal structures. Halogenation of the aromatic ring resulted in increased polarisation of the hydrophobic groups and this could be viewed by the blue "hue" of the hydrogen edges of the aromatic groups and the red "hue" of the central carbon rings. The "sigma" hole of the chloro (circular "white" region of the red area) could be viewed in both molecules of the Cl-Phe ASU. Electrostatic potential Hirshfeld surfaces of the **c**) I-Phe and **d**) Br-Phe derivatives. The halogen-halogen interactions are shown clearly with the "sigma hole" indicated by the blue area surrounded by white at the tips of the halogen groups. The sigma hole interacts with the electrostatically negative regions of the halogen groups perpendicularly, as expected for a type II halogen-halogen interaction. 193

Figure 7.7. SEM images of dry hydrogels of **a**) Phe, **b**) Phe/F-Phe (1:1) and **c**) F-Phe (303 mM). 195

Figure 7.8. Evolution of storage (G') and loss (G'') moduli in frequency sweep experiments for Phe, Phe/F-Phe (5:1), Phe/F-Phe (2:1), Phe/F-Phe (1:1), Phe/F-Phe (1:2), Phe/F-Phe (1:5) and F-Phe hydrogels (303 mM). Hot solutions (ca. 1 mL) were pipetted into a 500 μm gap (parallel plate geometry). All samples were subjected to frequency sweeps in the range of 0.1 to 100 Hz and applied stress of 500 Pa. 195

Figure 7.9. PXRD patterns of Phe, Phe/F-Phe (5:1), Phe/F-Phe (2:1), Phe/F-Phe (1:1), Phe/F-Phe (1:2), Phe/F-Phe (1:5) and F-Phe hydrogels. 196

Figure 7.10. Unit cell parameters (normalised to the F-Phe monohydrate phase) determined from the PXRD patterns of Phe, Phe/F-Phe (5:1), Phe/F-Phe (2:1), Phe/F-Phe (1:1), Phe/F-Phe (1:2), Phe/F-Phe (1:5) and F-Phe hydrogels utilising a Pawley fit. The mixtures do not indicate the presence of two components but rather a mixed solid solution with related changes to the unit cells of the structures. 197

Figure 7.11. Overlay of the molecular packing of Phe²¹³ and F-Phe²⁶¹ crystal structures shown along the b axis of the unit cell of the monohydrate forms, which shows their isostructurality. The Phe structure has been transformed to match the F-Phe by moving the origin of the unit cell one half the length of the a axis along the a axis direction. The unit cell of the monohydrate form of Phe (CCDC Number 1532251) presented monoclinic metric symmetry (space group $P2_1$), with the following refined parameters: $a = 13.112(14)$ Å, $b = 5.409(5)$ Å, $c = 13.849(14)$ Å, $\beta = 102.985(4)$ Å, ($V = 957.11(17)$ Å³) and $Z = 4$.²¹³ The unit cell of the monohydrate form of F-Phe presented monoclinic metric symmetry (space group $P2_1$), with the following refined parameters: $a = 13.303(14)$ Å, $b = 5.443(6)$ Å, $c = 14.015(15)$ Å, $\beta = 104.048(5)$ Å, ($V = 988.02(18)$ Å³) and $Z = 4$. 197

Figure 7.12. ^1H - ^{13}C CP/MAS NMR spectra of Phe, Phe/F-Phe (5:1), Phe/F-Phe (2:1), Phe/F-Phe (1:1), Phe/F-Phe (1:2), Phe/F-Phe (1:5) and F-Phe hydrogels (303 mM), acquired with an MAS rate of 8.5 kHz using a 400 MHz solid-state NMR spectrometer. 199

Figure 7.13. Amplification of the aromatic and aliphatic regions of ^1H - ^{13}C CP/MAS NMR spectra of Phe, Phe/F-Phe (5:1), Phe/F-Phe (2:1), Phe/F-Phe (1:1), Phe/F-Phe (1:2), Phe/F-Phe (1:5) and F-Phe dry hydrogels, acquired with an MAS rate of 10 kHz, using a 400 MHz solid-state NMR spectrometer. 199

Figure 7.14. ^{19}F NMR spectra of Phe/F-Phe (5:1), Phe/F-Phe (2:1), Phe/F-Phe (1:1), Phe/F-Phe (1:2), Phe/F-Phe (1:5) and F-Phe wet and dry hydrogels, acquired with MAS rates of 1 or 10 kHz, respectively, using a 400 MHz solid-state NMR spectrometer. Asterisks represent spinning sidebands. 201

Figure 7.15. ^{19}F MAS NMR spectra of Phe, Phe/F-Phe (5:1), Phe/F-Phe (2:1), Phe/F-Phe (1:1), Phe/F-Phe (1:2), Phe/F-Phe (1:5) and F-Phe dry hydrogels (303 mM), acquired with an MAS rate of 20 kHz using an 850 MHz solid-state NMR spectrometer with a 2.5 mm MAS probe head. Asterisks represent spinning sidebands. 202

Figure 7.16. ^1H - ^{19}F CP/MAS NMR spectra of Phe, Phe/F-Phe (5:1), Phe/F-Phe (2:1), Phe/F-Phe (1:1), Phe/F-Phe (1:2), Phe/F-Phe (1:5) and F-Phe dry hydrogels (303 mM), acquired with an MAS rate of 20 kHz using an 850 MHz solid-state NMR spectrometer with a 2.5 mm MAS probe head. Numbers represent chemical shift values given in ppm. Asterisks represent spinning sidebands. 202

Figure 7.17. ^1H - ^{19}F - ^{13}C double CP/MAS spectra of the dry hydrogel of Phe/F-Phe (1:1) performed with a contact time of 2.0 ms using an MAS rate of 20 kHz using an 850 MHz solid-state NMR spectrometer with a 2.5 mm MAS probe head. 203

Figure 7.18. 1D ^{19}F - ^1H HOESY spectra of the wet hydrogel of Phe/F-Phe (1:2) performed under static conditions, acquired using an 850 MHz solid-state NMR spectrometer with a 2.5 mm MAS probe head. 204

Figure 7.19. **a)** ^1H NMR, **b)** 2D ^1H - ^1H BABA and **c)** 2D ^1H - ^1H NOESY spectra of the dry hydrogel of Phe/F-Phe (1:1) performed using an MAS rate of 75 kHz using an 850 MHz solid-state NMR spectrometer with a 1 mm MAS probe head. 205

Figure 7.20. 1H PFG HR-MAS NMR spectra of Phe, Phe/F-Phe (1:1) and F-Phe hydrogels with an effective field of 45.7 G cm⁻¹ (95 % diffusion filter), measured at 298 K and an MAS rate of 1.5 kHz using an 800 MHz HR-MAS NMR probe head. 206

Figure 7.21. Evolution of ^1H PFG HR-MAS NMR normalised peak intensity with increasing gradient strength for Phe and F-Phe in Phe, Phe/F-Phe (1:1) and F-Phe hydrogels measured at 298 K and an MAS rate of 1.5 kHz.	207
Figure 7.22. Kinetics of gelation monitored by the acquisition of ^1H solution-state NMR spectra over time, immediately after cooling down a hot solution of Phe, Phe/F-Phe (1:1) and F-Phe (303 mM) measured at 298 K.	209
Figure 7.23. ^1H solution-state NMR spectra of Phe, Phe/F-Phe (5:1), Phe/F-Phe (2:1), Phe/F-Phe (1:1), Phe/F-Phe (1:2), Phe/F-Phe (1:5) and F-Phe hydrogels (303 mM) measured at 298 K.	210
Figure 7.24. ^1H solution-state NMR peak intensity (f_{abs}) of Phe and F-Phe Arom, C_αH and C_βH_2 sites in Phe, Phe/F-Phe (5:1), Phe/F-Phe (2:1), Phe/F-Phe (1:1), Phe/F-Phe (1:2), Phe/F-Phe (1:5) and F-Phe hydrogels (303 mM) recorded 24 h after quenching hot solutions, measured at 298 K.	210
Figure 7.25. ^1H solution-state T_1 times of Phe and F-Phe Arom, C_αH and C_βH_2 in Phe, Phe/F-Phe (5:1), Phe/F-Phe (1:1), Phe/F-Phe (1:5) and F-Phe hydrogels (303 mM) recorded between 298 and 358 K.	212
Figure 7.26. Comparison of ^1H T_1 times of Phe and F-Phe Arom, C_αH and C_βH_2 in Phe, Phe/F-Phe (5:1), Phe/F-Phe (2:1), Phe/F-Phe (1:1), Phe/F-Phe (1:2), Phe/F-Phe (1:5) and F-Phe hydrogels (303 mM) recorded at 298 K.	212
Figure 7.27. 2D ^1H - ^1H NOESY spectra of the hydrogels of Phe, Phe/F-Phe (1:1) and F-Phe acquired with a mixing time of 0.5 s. The green dashed lines highlight a positive $n\text{Oe}$ enhancement between the aromatic and aliphatic protons of F-Phe molecules.	214
Figure 7.28. Build-up curves of fractional STD response (η_{STD}) in Phe, Phe/F-Phe (5:1), Phe/F-Phe (2:1), Phe/F-Phe (1:1), Phe/F-Phe (1:2), Phe/F-Phe (1:5) and F-Phe hydrogels (303 mM) ($\text{STD}_{\text{on}} = 1$ ppm and $\text{STD}_{\text{off}} = 40$ ppm), measured at 298 K.	216
Figure 7.29. Initial slope values (STD_0) versus [F-Phe] in Phe, Phe/F-Phe (5:1), Phe/F-Phe (2:1), Phe/F-Phe (1:1), Phe/F-Phe (1:2), Phe/F-Phe (1:5) and F-Phe hydrogels (303 mM) ($\text{STD}_{\text{on}} = 1$ ppm and $\text{STD}_{\text{off}} = 40$ ppm), measured at 298 K.	216
Figure 8.1. Molecular structure of zwitterionic $\text{NH}_2\text{-Phe}$.	220
Figure 8.2. Phase diagram of the products obtained depending on the concentration and molar ratio of Phe and $\text{NH}_2\text{-Phe}$ in water. Water solubility of Phe (179 mM) and $\text{NH}_2\text{-Phe}$ (216 mM, experimentally determined) at 298 K are highlighted with black lines.	221
Figure 8.3. Images of hydrogels of a) Phe (303 mM), b) Phe/ $\text{NH}_2\text{-Phe}$ (1:0.05), e) Phe/ $\text{NH}_2\text{-Phe}$ (1:2) and f) $\text{NH}_2\text{-Phe}$ (606 mM), c) suspension of Phe/ $\text{NH}_2\text{-Phe}$ (1:0.4) and d) solution of Phe/ $\text{NH}_2\text{-Phe}$ (1:1). Commercially available $\text{NH}_2\text{-Phe}$ is brown, giving rise to coloured materials.	222
Figure 8.4. SEM images of a) Phe (303 mM), b) Phe/ $\text{NH}_2\text{-Phe}$ (1:2) and c) $\text{NH}_2\text{-Phe}$ (606 mM) dry hydrogels. The average width of the needle-like fibres of $\text{NH}_2\text{-Phe}$ was 25.3 μm (ranging between 2.6 and 47.9 μm).	222
Figure 8.5. Storage (G') and loss (G'') moduli for Phe (303 mM), Phe/ $\text{NH}_2\text{-Phe}$ (1:2) and $\text{NH}_2\text{-Phe}$ (606 mM) hydrogels in frequency sweep experiments. Hot solutions (ca. 1 mL) were pipetted into a 500 μm gap (parallel plate geometry). All samples were subjected to frequency sweeps in the range of 0.1 to 100 Hz and applied stress of 500 Pa.	223
Figure 8.6. Unit cell of $\text{NH}_2\text{-Phe}$ shown along the a axis.	224
Figure 8.7. Experimental ^{13}C chemical shift values for the $\text{NH}_2\text{-Phe}$ (606 mM) dry hydrogel derived from the ^1H - ^{13}C CP/MAS NMR spectrum acquired with an MAS rate of 10 kHz vs. calculated values for the predicted structure. Calculated isotropic chemical shieldings were converted to chemical shifts by matching the calculated and observed chemical shift of the CH_3 carbon.	224
Figure 8.8. ^1H - ^{13}C CP/MAS NMR spectra of Phe (303 mM), Phe/ $\text{NH}_2\text{-Phe}$ (1:0.2), Phe/ $\text{NH}_2\text{-Phe}$ (1:0.4), Phe/ $\text{NH}_2\text{-Phe}$ (1:2) and $\text{NH}_2\text{-Phe}$ (606 mM) hydrogels acquired with an MAS rate of 8.5 kHz and 8192 scans; Phe/ $\text{NH}_2\text{-Phe}$ (1:0.4) dry particles removed from suspension and dried, and Phe and $\text{NH}_2\text{-Phe}$ solid reference powders acquired with an MAS rate of 10 kHz and 8192 scans. All experiments were conducted	224

with a recycle delay of 20 s and $\pi/2$ pulse lengths of 3.2 μ s (^1H) and 3.0 μ s (^{13}C), using a 400 MHz solid-state spectrometer. Asterisks represent spinning sidebands. _____	226
Figure 8.9. PXRD patterns of Phe (303 mM), Phe/NH ₂ -Phe (1:2) and NH ₂ -Phe (606 mM) hydrogels. _____	227
Figure 8.10. Amplification of ^1H - ^{13}C CP/MAS NMR spectra of Phe (303 mM), Phe/NH ₂ -Phe (1:2) and NH ₂ -Phe (606 mM) dry hydrogels acquired with an MAS rate of 10 kHz and 2048 scans. All experiments were conducted with a recycle delay of 20 s, $\pi/2$ pulse lengths of 3.2 μ s (^1H) and 3.0 μ s (^{13}C), using a 400 MHz solid-state spectrometer. Asterisks represent spinning sidebands. _____	228
Figure 8.11. Experimental ^1H - ^{13}C CP/MAS NMR spectra of Phe/NH ₂ -Phe (1:2) dry hydrogel sample and modelled spectra from the superimposition of spectra of pure Phe and NH ₂ -Phe dry hydrogel samples. _____	228
Figure 8.12. ^1H - ^{15}N CP/MAS NMR spectra of ^{15}N -labelled [^{13}C]/[^{15}N]-Phe (303 mM) and [^{13}C]/[^{15}N]-Phe/NH ₂ -Phe dry hydrogel samples, acquired with MAS rates of 10 kHz and 1024 scans. All experiments were conducted with a recycle delay of 20 s and $\pi/2$ pulse lengths of 4.0 μ s (^1H) and 3.0 μ s (^{13}C), using an 850 MHz solid-state NMR spectrometer. _____	230
Figure 8.13. ^1H solution-state NMR spectra of Phe/NH ₂ -Phe (1:0.4) particles removed from suspension, dried and dissolved in DMSO- <i>d</i> ₆ . Experiments were conducted with a recycle delay of 10 s, using a 500 MHz solution-state NMR spectrometer. _____	231
Figure 8.14. 2D ^1H - ^1H NOESY NMR spectrum of Phe/NH ₂ -Phe (1:1) solution, measured with a mixing time 1 s at 298 K. Experiments were conducted with a recycle delay of 2 s and 16 scans, using a 500 MHz solution-state NMR spectrometer. _____	232
Figure 8.15. Chemical shift variation ($\Delta\delta$) in ^1H NMR spectra recorded during dilution studies of the Phe/NH ₂ -Phe (1:0.15) hydrogel, measured at 298 K. _____	233
Figure 8.16. 2D ^1H - ^1H NOESY NMR spectrum of Phe/NH ₂ -Phe (1:0.15) hydrogel with a mixing time 0.5 s, measured at 298 K. _____	234
Figure 8.17. Evolution of normalised cross-peak intensity ($f_{\text{cross-peak norm}}$) with mixing time in 2D ^1H - ^1H NOESY NMR spectra of Phe/NH ₂ -Phe (1:0.15) hydrogel. Colour represents the degree of <i>n</i> Oe enhancement. _____	234
Figure 8.18. Kinetics of gelation monitored by the acquisition of ^1H NMR spectra with time, immediately after cooling down a hot solution of Phe/NH ₂ -Phe (1:0.1) with gradual formation of a hydrogel, measured at 298 K. _____	236
Figure 8.19. ^1H solution-state NMR spectra of Phe (303 mM), Phe/NH ₂ -Phe (1:0.1), Phe/NH ₂ -Phe (1:0.15), Phe/NH ₂ -Phe (1:0.2), Phe/NH ₂ -Phe (1:2) and NH ₂ -Phe (606 mM) hydrogels, Phe/NH ₂ -Phe (1:0.3) suspension and Phe/NH ₂ -Phe (1:1) solution measured at 298 K. _____	236
Figure 8.20. ^1H longitudinal relaxation times (T_1) for Phe Arom, NH ₂ -Phe Arom, C _α H and C _β H ₂ of Phe (303 mM), Phe/NH ₂ -Phe (1:2) and NH ₂ -Phe (606 mM) hydrogels measured between 278 and 328 K. Experiments were conducted with a recycle delay of 10 s, using a 500 MHz solution-state NMR spectrometer. _____	238
Figure 8.21. ^1H solution-state longitudinal relaxation times (T_1) of Phe hydrogels with variable concentration of NH ₂ -Phe, Phe/NH ₂ -Phe (1:2) and NH ₂ -Phe (606 mM) hydrogels, and Phe (100 mM) and NH ₂ -Phe (100 mM) solutions. _____	239
Figure 8.22. Evolution of fractional STD response (η_{STD}) for Phe hydrogels measured at 298 K, using a 500 MHz solution-state NMR spectrometer (STD _{on} = 1 ppm). _____	240
Figure 8.23. Initial slope of build-up curves (STD ₀) of Phe hydrogels with increasing concentrations of NH ₂ -Phe, measured at 298 K, using a 500 MHz solution-state NMR spectrometer (STD _{on} = 1 ppm). _____	241
Figure 8.24. Evolution of fractional STD response (η_{STD}) for Phe/NH ₂ -Phe (1:2) hydrogels measured between 278 and 328 K, using a 500 MHz solution-state NMR spectrometer (STD _{on} = 1 ppm). _____	242
Figure 8.25. Evolution of fractional STD response (η_{STD}) for NH ₂ -Phe hydrogels measured between 278 and 328 K, using a 500 MHz solution-state NMR spectrometer (STD _{on} = 1 ppm). _____	243
Figure 9.1. Schematic representation of the urea tape motif. _____	247
Figure 9.2. Schematic representation of the investigated gelator structures. _____	248

Figure 9.3. Storage (G') and loss (G'') moduli with angular frequency sweeps of organogels 1 and 2 in toluene (20 mg mL ⁻¹). _____	249
Figure 9.4. Environmental SEM images at 500x magnification of xerogels obtained from gels 1 and 2 (20 mg mL ⁻¹) in toluene. _____	249
Figure 9.5. Calculated molecular electrostatic potentials of 1 (a-c) and 2 (d-f). The potentials are plotted on the 0.02 a.u. electronic isodensity surface. The red patches of positive electrostatic potential in b) and e) correspond to the urea hydrogen atom positions. c) and f) show the view down the urea oxygen atom, highlighting its negative electrostatic potential. _____	250
Figure 9.6. Molecular packing in representative low energy predicted crystal structures of 1 (a, b, c) and 2 (d, e, f), with the corresponding calculated lattice energies of each structure. a) and d) are the global minimum energy crystal structures that have been located for each molecule. Hydrogen bonds are shown as dashed blue lines. Hydrogen atoms on the alkyl chains are hidden in (f) for clarity. _____	253
Figure 9.7. PXRD patterns of a) the organogel samples of 1 and 2 in DMSO (30 mg mL ⁻¹), compared to b-g) the simulated diffraction patterns from the six lowest energy predicted crystal structures, all of which contained urea-nitro (N-H···O) hydrogen bonding for 1 and urea-urea hydrogen bonding for 2 . The simulated patterns from the predicted structures are labelled by their calculated lattice energies. _____	255
Figure 9.8. ¹ H- ¹³ C CP/MAS NMR spectra of organogel 1 (30 mg mL ⁻¹ in DMSO- <i>d</i> ₆) acquired a) at 298 K and 1 kHz MAS rate; frozen gel samples acquired at b) 288 K, c) 283 K and d) 278 K and 1 kHz MAS rate; frozen gel samples acquired at 273 K and e) 1 kHz, f) 4 kHz and g) 8 kHz MAS rates; and h) reference solid powder measured at 298 K and 10 kHz MAS rate. All experiments were acquired with a recycle delay of 20 s, 1024 scans and $\pi/2$ pulse lengths of 4.0 μ s (¹ H) and 3.0 μ s (¹³ C), using a 400 MHz solid-state NMR spectrometer. Low-resolution aromatic peaks are highlighted with triangles and spinning sidebands with asterisks. _____	257
Figure 9.9. ¹ H- ¹³ C CP/MAS NMR spectra of organogel 2 (30 mg mL ⁻¹ in DMSO- <i>d</i> ₆) acquired a) at 298 K and 1 kHz MAS rate; frozen gel samples acquired at b) 288 K, c) 283 K and d) 278 K and 1 kHz MAS rate; frozen gel samples acquired at 273 K and e) 1 kHz, f) 4 kHz and g) 8 kHz MAS rates; and h) reference solid powder measured at 298 K and 10 kHz MAS rate. _____	258
Figure 9.10. Experimental ¹³ C chemical shift values (δ) for frozen gels 1 and 2 measured at 298 K and an MAS rate of 8 kHz vs. calculated values for the predicted structures that give best agreement with both NMR and PXRD studies from the gel. Calculated isotropic chemical shieldings were converted to chemical shifts by matching the calculated and observed chemical shift of the CH ₃ carbon in gel. The structures for gelators 1 and 2 correspond to those reported in Figure 9.6a and e, respectively. _____	260
Figure 9.11. 2D ¹ H- ¹ H NOESY spectra of organogels 1 and 2 (30 mg mL ⁻¹ in DMSO- <i>d</i> ₆) measured at 298 K with a mixing time of 0.5 s, a recycle delay of 2 s and 32 scans, using an 800 MHz solution-state NMR spectrometer. Relevant cross-peaks have the corresponding spatial connectivity assigned (coloured lines). _____	263
Figure 9.12. Evolution of normalised <i>n</i> Oe enhancements (<i>I</i> _{1s}) with mixing time (τ_m) for the cross-peaks between H _c -H _d (grey squares) and NH ₂ -H _d (black circles) in organogel 2 , highlighting the characteristic lag time of indirect <i>n</i> Oe enhancements. _____	263
Figure 10.1. The introduction of additive molecules was investigated regarding their effects on the organisation of the 3D network. a) Representation of a single-component hydrogel (Phe) and introduction of a non-interacting additive (Leu). b) Modification of the gel properties resulted from the introduction of a partially disruptive additive (Ser). c) Representation of multi-component (Phe/Trp, Phe/Tyr) and multiple-gelator materials (Phe/F-Phe, Phe/NH ₂ -Phe). d) Gelation could be fully prevented upon the introduction of a disruptive additive (low concentrations of NH ₂ -Phe). _____	270
Figure 10.2. Schematic representation of the NMR methods optimised throughout these studies to probe different length scales of self-organisation and time scales of molecular motions in supramolecular gel materials. _____	274

Figure 10.3. Proposed mechanism for the transfer of saturation in supramolecular gels during STD NMR experiments. Gelator molecules forming the network (bound state, left) are in fast exchange with those in the bulk solution phase (free state, right), allowing accumulation and detection of saturation in solution. 280

List of Tables

Table 2.1. Properties of nuclei spin $I = 1/2$ used throughout the project. ¹⁷¹	90
Table 2.2. Strength of interactions affecting line widths in NMR spectra and their impact in spectra of liquids and solids. ¹⁷²	91
Table 4.1. Crystallographic unit cells of Phe. ²¹⁵	147
Table 5.1. Concentration of Phe in solution and in gel phases based on ^1H NMR peak intensities.	160
Table 6.1. pH values of suspensions of Phe, Phe/Leu (5:1), Phe/Ser (5:1), Phe/Trp (5:1) and Phe/Tyr (5:1), and corresponding dissociation constants ($p\text{K}_a$) and isoelectric points ($p\text{I}$). ²²⁷	166
Table 6.2. Gel-to-solution transition temperatures (T_{gel}) of hydrogels of Phe, Phe/Leu (5:1), Phe/Ser (5:1), Phe/Trp (5:1) and Phe/Tyr (5:1).	166
Table 6.3. ^{13}C chemical shifts from ^1H - ^{13}C CP/MAS NMR spectra of dry hydrogels of Phe, Phe/Leu (5:1), Phe/Ser (5:1), Phe/Trp (5:1) and Phe/Tyr (5:1).	171
Table 6.4. Apparent self-diffusion coefficients (D) calculated from PFG HR-MAS NMR experiments of hydrogels of Phe, Phe/Leu (5:1), Phe/Ser (5:1), Phe/Trp (5:1) and Phe/Tyr (5:1), acquired with MAS rates of 1 kHz at 298 K.	172
Table 6.5. Fraction of ^1H peak intensity (f_{gel}) of spectra acquired 24 h after quenching hot solutions of Phe, Phe/Leu (5:1), Phe/Ser (5:1), Phe/Trp (5:1) and Phe/Tyr (5:1) (303 mM), in comparison with the ^1H peak intensity of spectra acquired immediately (measured at 298 K).	175
Table 6.6. Initial slope values of fractional STD response (STD_0) for the hydrogels of Phe, Phe/Leu (5:1), Phe/Ser (5:1), Phe/Trp (5:1) and Phe/Tyr (5:1), measured at 298 K ($\text{STD}_{\text{on}} = 0$ ppm and $\text{STD}_{\text{off}} = 40$ ppm).	184
<hr/>	
Table 7.1. Gelation results, critical gelation concentration (CGC), water solubility (s_{water}) and molar mass (M) of Phe and its halogenated derivatives at 298 K.	189
Table 7.2. Molar concentrations and ratios of Phe and F-Phe used to prepare single and multiple gelator hydrogels.	194
Table 7.3. ^{13}C chemical shifts from ^1H - ^{13}C CP/MAS NMR spectra of Phe, Phe/F-Phe (5:1), Phe/F-Phe (2:1), Phe/F-Phe (1:1), Phe/F-Phe (1:2), Phe/F-Phe (1:5) and F-Phe dry hydrogels.	200
Table 7.4. Apparent self-diffusion coefficients (D) of Phe and F-Phe molecules determined from variable gradient ^1H PFG HR-MAS NMR experiments of Phe, Phe/F-Phe (1:1) and F-Phe hydrogels were measured at 298 K with an MAS rate of 1.5 kHz.	207
Table 7.5. ^1H solution-state NMR longitudinal relaxation times T_1 for Phe and F-Phe solutions (101 mM) measured at 298 K, with error values in parenthesis.	213
Table 8.1. Molar ratio and concentration of Phe and $\text{NH}_2\text{-Phe}$ in the suspensions and hydrogels under study.	221
Table 8.2. ^{13}C chemical shift values (δ) from ^1H - ^{13}C CP/MAS NMR spectra of Phe and $\text{NH}_2\text{-Phe}$ reference solid powders and Phe (303 mM), Phe/ $\text{NH}_2\text{-Phe}$ (1:0.2), Phe/ $\text{NH}_2\text{-Phe}$ (1:0.2), Phe/ $\text{NH}_2\text{-Phe}$ (1:2) and $\text{NH}_2\text{-Phe}$ (606 mM) dry hydrogel samples.	229
Table 8.3. Interproton distances calculated from 2D ^1H - ^1H NOESY NMR spectrum of Phe/ $\text{NH}_2\text{-Phe}$ (1:0.15) hydrogel with a mixing time 0.01 s, measured at 298 K, using the $\text{H}_{2,6}\text{-H}_{3,5}$ distance from $\text{NH}_2\text{-Phe}$ as reference. Average errors of 7 % were assumed as for fast tumbling molecules in viscous solvents. ²⁷	235
Table 8.4. Concentration of dissolved gelator molecules calculated from ^1H solution-state NMR peak intensity for Phe (303 mM), Phe/ $\text{NH}_2\text{-Phe}$ (1:0.05), Phe/ $\text{NH}_2\text{-Phe}$ (1:0.15), Phe/ $\text{NH}_2\text{-Phe}$ (1:0.2), Phe/ $\text{NH}_2\text{-Phe}$ (1:0.55), Phe/ $\text{NH}_2\text{-Phe}$ (1:2) and $\text{NH}_2\text{-Phe}$ (606 mM) hydrogels, measured at 298 K.	237
Table 8.5. ^1H solution-state NMR longitudinal relaxation times (T_1) for Phe and $\text{NH}_2\text{-Phe}$ solutions (101 mM) measured at 298 K, with error values in parenthesis.	239
Table 9.1. Critical gelation concentration (CGC) values for organogels 1 and 2 .	249
Table 9.2. Experimental ^{13}C chemical shift values (δ) for frozen organogel 1 measured at 298 K and an MAS rate of 8 kHz vs. calculated values for the six lowest energy predicted crystal structures.	259

Table 9.3. Experimental ^{13}C chemical shift values (δ) for frozen organogel 2 measured at 298 K and an MAS rate of 8 kHz vs. calculated values for the six lowest energy predicted crystal structures. _____	260
Table 9.4. Experimental ^{15}N NMR chemical shift values (δ) from 2D ^1H - ^{15}N HSQC experiments for gelators and organogels 1 and 2 (30 mg mL^{-1} in DMSO-d_6) measured at 298 K with a recycle delay of 2 s and 8 scans, using an 800 MHz solution-state NMR spectrometer. _____	261
Table 9.5. Intermolecular distances calculated from initial rates of $n\text{Oe}$ build-up curves with mixing time, using the $\text{H}_c\text{-H}_d$ distance as reference. _____	264
Table 10.1. Gelation results, critical gelation concentration (CGC) and water solubility (s_{water}) of Phe and its derivatives at 298 K, organised in descending order of gelation ability. _____	267

Chapter 1

1. Introduction

Gels are a fascinating class of functional soft materials. They are present in everyday life as contact lenses, food stuff, photography, cosmetics and pharmaceuticals, to name a few.¹ Gels have a recognised potential for a wide range of industries due to their adaptability to the environment.² These are also used for industrial purposes, such as templates for nanofabrication, pollutant removal from waste water and as catalysts for organic reactions. But the growing interest in the research and development of gel materials lies on their wide range of biomedical applications, such as membranes for biosensors, scaffolds for wound healing, self-supporting architectures for cellular growth, networks for tissue engineering and vehicles for advanced drug delivery.^{3,4}

1.1. A historical overview

Hydrogels have drawn the scientific community's attention since 1960. Even though the first reference made to hydrogels was recorded in 1892, it was only in the last two decades that considerable investment was made in the field (Figure 1.1).³ The first paper mentioning these systems for medical applications, published in 1936, introduced hydrogels composed of synthetic poly(2-hydroxyethylmethacrylate), which were later improved by Wichterle and Lim and commercialised as soft contact lenses in 1960.⁵

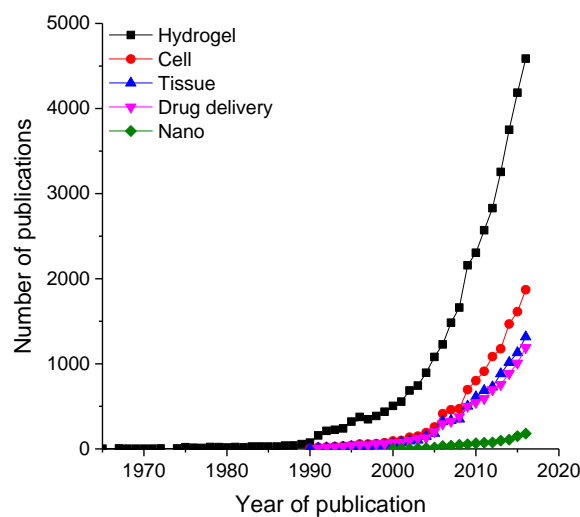


Figure 1.1. Number of publications per year under the research topic of “hydrogel” in the Web of Science™ between 1965 and 2016. Adapted and updated from ³.

There has been a marked increase in the interest in the field of hydrogels since 2000, which is reflected by an exponential growth of the curve. The total number of papers on “hydrogel” was 37681, from which 22 % were on the topic of drug delivery. Gel-based drug delivery systems are currently commercially available for a variety of routes of administration and targets in the human body.⁶ Some examples include solid-moulded forms (e.g. silicone-based contact lenses and intraocular lenses), microparticles (e.g. bioadhesive hydrogels with long-term adhesion for oral application), cationic hydrogels (e.g. pH-sensitive hydrogels with swelling properties for the gastrointestinal tract), solutions (e.g. temperature-sensitive hydrogels for subcutaneous injection) or membranes (e.g. wound dressings and easily interrupted transdermal patches).³

1.2. Definition of gel

A gel is a two-component colloidal dispersion in which a gelator is dispersed (the solid, continuous phase) within a solvent (the liquid, dispersed phase).^{7,8} In this heterogeneous system, the typical particle sizes range from 1 nm to 10^3 nm.^{7,9} The three-dimensional (3D) continuous network is supported by covalent or non-covalent interactions, with high levels of solvent entrapped by capillary forces and surface tension.^{4,10}

Gels are not solids nor liquids, but semi-solid materials. Real soft materials as gels possess the elastic properties of ideal Hookean solids and the viscosity properties of Newtonian

liquids.^{8, 11, 12} It is the co-existence of high contents of solvent with solid structures that distinguishes gel materials from ordinary liquids and solids, being responsible for their unique viscoelastic properties.^{2, 8, 13-15}

The existence of an extremely large interface between the continuous and dispersed phases pre-empts for a thermodynamically unstable system, since a single solid phase would have lower energy.^{9, 16} Hence, gels (and other colloidal materials) represent a state of higher free energy than that of the material in bulk.⁷ In physics, a system will tend to transition to a state of lower free energy spontaneously, unless there is a substantial energy barrier that separates the state of higher free energy (gel) from the lower equilibrium state (solid), called the free energy of activation (E_a).⁷ When the available thermal energy is not sufficient to overcome this activation barrier into a stable lower-energy state, the reaction is under kinetic control, and a gel product is obtained.^{13, 17, 18} The presence of such a barrier traps gels in a state of metastability.⁷ Therefore, the gel state is considered kinetically trapped.¹⁹ Colloid dispersions are not thermodynamically stable, but they are considered to exhibit kinetic stability (depending on the time frame) due to the presence of this energy barrier.^{16, 20} Only an increase in the energy of the system will allow it to overcome this energy barrier.⁷

The presence of long gel fibres results in an excess of interfacial free energy.^{7, 13} The interface affects the global thermodynamic state of the system, as the properties of the interfacial molecules have a different contribution to the thermodynamic properties of the system than those in the bulk phase.⁷ Henceforth, why do these less favourable systems exist? Making a parallel with colloidal materials, according to the DLVO (Derjaguin and Landau, Verwey and Overbeek) theory, the stability of supramolecular gels arises from the combined effect of attractive and repulsive forces at the interfaces between the electrically charged continuous and dispersed phases.^{9, 20} The stabilising structural interactions are the repulsive surface forces, thermal motion of particles and hydrodynamic resistance of the medium.²¹ Contrarily, attractive surface forces encompass the low surface elasticity, gravity and other external destabilising factors.²¹

1.3. Advantages and disadvantages of gel systems

Gels are preferred over conventional systems due to their great resemblance to viscoelastic human tissues, unparalleled by any other class of biomaterials.^{2, 4, 22} These materials present the advantage of confinement to the intended site, overcoming the side effects associated with systemic distribution, due to mouldability (Figure 1.2), adhesiveness and availability in variable dimensions (from nano to macroscales).⁶ Moreover, they have highly tuneable features, with the possibility of functionalisation by the insertion of functional groups, enabling the delivery of drugs to an intended site with optimum pharmacokinetic profiles.²³ More importantly, their responsiveness to their environment is the foundation for their use in targeted and controlled drug delivery, *i.e.* small environmental changes can trigger modifications in the gel's structure.⁶ Not only can these modifications lead to drug release, but also degradation or dissolution of the 3D network, induction of sol-gel transitions or alteration of shape.³ Consequently, a simple phase transition can promote *in situ* gel formation, an unmatched advantage for injectable purposes.⁶

Nonetheless, hydrogels present certain limitations that often condition their development. While ease of application can be problematic for stiff hydrogels, mainly for injectable purposes, soft hydrogels present low mechanical strength that poses significant difficulties in handling.^{2, 24} Sterilisation of hydrogels for intravenous administration is very challenging due to their elevated water content². In addition, the amount of drug loaded in hydrogels may be limited in the case of hydrophobic drugs and the homogeneity of the dispersed drugs is still difficult to guarantee.²⁵



Figure 1.2. Human-shaped hydrogel of nanocellulose showing gels mouldability.

1.4. Classification of gels

Since there is a variety of gel forming molecules with a diverse range of properties, it became important to classify these according to the nature of the cross-links that sustain the network – chemical or physical interactions (Figure 1.3).

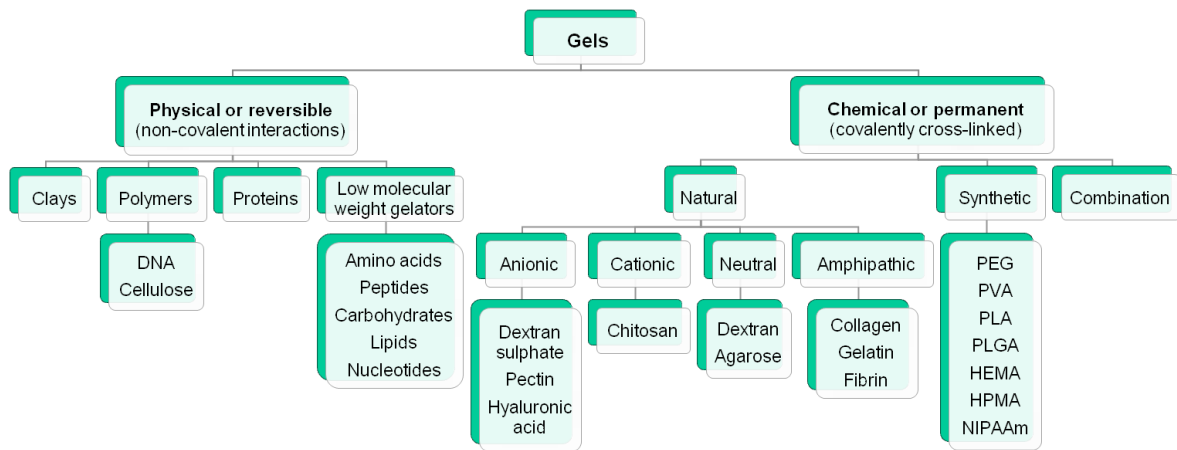


Figure 1.3. Classification of gels by the nature of interactions (physical and chemical) sub-divided according to the nature of the solid phase (gelator), with some common examples.

1.4.1. Chemical gels

Chemical or permanent gels are formed by covalently cross-linked networks, which is behind their strong resistance to external mechanical stress and consequent long-term stability.² These systems are characterised by their capability of absorbing high amounts of solvents and swelling whilst maintaining their shape.²⁶ Their swelling levels are dictated by the cross-linking density.²

These hydrogels can be formed through the addition of small molecules, named cross-linkers, or through polymer-polymer interactions between modified functional groups.²⁵ Small-molecule cross-linkers, as periodate-oxidised sodium alginate, can promote gelation when cross-linked with proteins, such as gelatin, for the delivery of anti-tuberculostatics with minimal cytotoxicity.²⁵ In some cases, the drug itself can act as the cross-linker, as primaquine, which has been cross-linked with periodate-oxidised gum arabic to produce an hydrogel by Nishi and Jayakrishnan (2007).²⁷ Moreover, the active ester form of tartaric acid has been cross-linked with human serum albumin for controlled release of doxorubicin from a tissue adhesive hydrogel.²⁵ Polymers can also be pre-functionalised

with reactive functional groups to prevent the release of potentially toxic small molecules.²⁵ Hyaluronic acid was functionalised with hydrazine bonds to promote a double effect of prolonged-duration local anaesthesia, controlled release of budesonide and tissue plasminogen activator.²⁵ Also, poly(aldehyde guluronate), a functionalised product from oxidised alginic acid, formed an hydrogel with adipic acid dihydrazide and could be used as an injectable matrix for effective delivery of osteoblasts and growth factors.²⁵

Safety, simplicity and cost-effectiveness of this type of hydrogel are very dependent on the type of precursors used. In comparison with physical gels, these systems are less tolerated by the human body, since there is the possibility of release of toxic precursors throughout the administration processes.^{4, 26} Also, their non-reversible interactions are responsible for undesired reduced rates of degradation and clearance times.²⁵

1.4.2. Physical gels

Physical or reversible gels are formed by molecular entanglements and non-covalent interactions induced by aggregation due to the low solubility of the gelator molecules.²⁶ The driving forces (hydrophobic interactions, charge condensation, hydrogen bonding, stereocomplexation or supramolecular chemistry) lead to formation of hydrophobically or ionically-associated domains, contributing to their heterogeneity.^{2, 4, 25}

Even though physically cross-linked hydrogels show lower resistance to mechanical stress, the use of biocompatible and safe precursors grants supramolecular gels a recognised potential in the biomedical field.^{2, 26} These systems can be tailored at the monomer level, which opens specific properties and release profiles that suit the intended application.²⁴ Moreover, their fast degradation rates and ability to alter their shape are important reasons for their continuous application.²⁶ However, the weak nature of such interactions means these gels suffer from rapid erosion and fast release of the entrapped drug, and usually break at lower strains than chemical gels.^{24, 28} Since their mechanical properties are determined by the primary fibre thickness and length, as well as the number and type of entanglement points or cross-links, gels can be manipulated for the intended use according to the type of gelator employed.²⁹

1.4.3. Stimuli responsiveness of *smart materials*

The use of physical gels in targeted and controlled drug delivery is based on their stimuli responsiveness,²³ which enables the introduction of environment-dependent functionalities, therefore receiving the designation of *smart materials*.³⁰ Due to the weak nature of the sustaining interactions, physical gels are capable of responding to physiological (temperature, pH, ionic strength, chemical or biological compounds) and external stimuli (vibration, light, ultrasounds, radiation, magnetic field or electric current).^{4, 31} Some of the stimuli described are shown in Figure 1.4. These triggers may induce changes in the structural and physicochemical properties of smart hydrogels leading to drug release, degradation or dissolution of the 3D network, induction of phase transitions, alteration of shape, melting and/or reforming.^{23, 28}

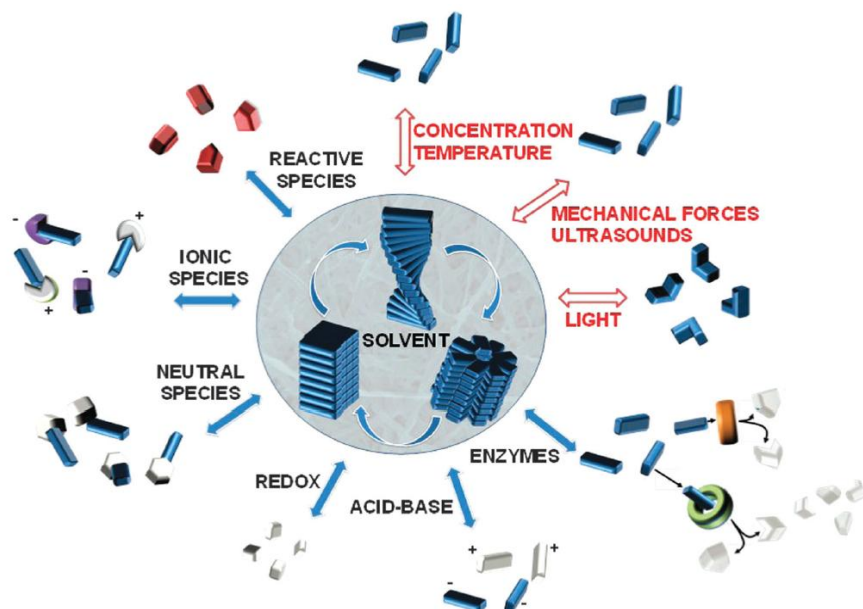


Figure 1.4. Chemical (black) and physical (red) stimuli.³²

Thermoreversible hydrogels are the most developed type of environmentally-responsive systems, due to their ease of preparation.⁴ The majority of natural gelators form hydrogels upon cooling below an upper critical solution temperature.⁴ However, a less common event has been reported for cellulose derivatives, which gelate upon heating above a lower critical solution temperature, gaining the denomination of reverse thermogelators.⁴

Since pH varies considerably inside the human body, it enables a site-specific controlled drug delivery.³¹ pH-sensitive gels result from the presence of ionisable groups (e.g. carboxylic or sulphonic groups) with modifications triggered by differences in ionisation.⁴ pH dependence can be monitored by the addition of glucono-d-lactone (GdL) that hydrolyses slowly to gluconic acid and gradually and uniformly decreases the pH of the solution.³³ This is considered enzyme-assisted self-assembly and allows fine, bottom-up fabrication as gelation is spanned over a period of hours, enabling more homogeneous materials to be obtained.^{27, 33}

Chemical substances (e.g. glucose-responsive systems), ionic species (e.g. calcium-responsive bioerodible systems) or biological compounds (e.g. enzymes, antigen or microbial infection-responsive systems) can also promote structural modifications of the gel networks.⁴ Since certain diseases produce characteristic alterations in their local environment, these modification can be targeted to control and trigger drug release.³¹ Recent biomedical advances discuss the sustained release of anticancer drugs (docetaxel,³⁴ doxorubicin³⁵ and monoclonal antibodies⁶) which release the drug content only when in contact with tumour receptors.⁶ Pinhassi *et al.* (2010) developed an hydrogel based in the natural polysaccharide arabinogalactan conjugated with folic acid and methotrexate, an anticancer anti-folate drug.³⁶ These drugs are released only after the hydrogel contacts with malignant tumour cells, which overexpress folate receptors.³⁶ Upon recognition and penetration into the tumour cells due to the folic acid group, methotrexate finally eliminates them.³⁶ Another fascinating application is the co-delivery hydrogel based on two complementary anticancer drugs, taxol and hydroxycamptothecin (HCPT), developed by Mao *et al.* (2012).³⁷ The hydrogel of Dex-FFFK(Taxol/HCPT)E-ss-EE (Figure 1.5) can be converted to Dex-FFFK(Taxol/HCPT)E by the cleavage of a disulfide bond (black-red). Dexamethasone (Dex) (blue), an anti-inflammatory and immunosuppressant, and tripeptides of phenylalanine (F) (black) were incorporated to promote self-assembly. Diglutamic acid (E) (black) was used to improve the solubility of the precursors of hydrogelators. The stability of the drugs was improved significantly through this formulation and these molecules exhibited a controlled release profile *via* the hydrolysis of the connective ester bonds (pink).³⁷

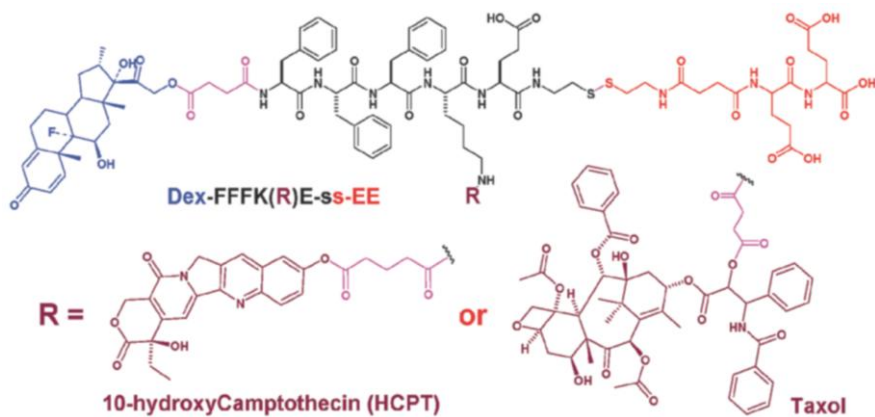


Figure 1.5. Chemical structures of precursors of hydrogelators of Dex-FFFFK(Taxol/HCPT)E.²⁶

1.5. Supramolecular gels

The current project focuses on the smallest molecular building blocks of physical gelation, designed low molecular weight gelators. The resulting supramolecular gels are semi-solid colloidal materials which contain a 3D entangled network with a fine structure that is defined by non-covalent interactions between molecules with a molecular weight up to 2000 Da.^{4, 10, 38} Typically, a very small amount of gelator (*ca.* 0.1 to 10 % (w/v)) is required to entrap large amounts of solvent.^{4, 10}

In 1841, Lipowitz reported a case of failed crystallisation of lithium urate in water. Little did he know he was reporting the first case of supramolecular gelation.³⁹ This case reflected the still commonplace reality of the serendipitous nature of the discovery of new gelator molecules. The first small molecule hydrogelator studied extensively was dibenzoyl-L-cystine (**1**) (Figure 1.6), reported in 1892 by Brenzinger⁴⁰ and found to form strong gels by Hoffman 1921.⁴¹ When advanced experimental methodologies became available (*e.g.*, X-ray crystallography, light and electron microscopy, rheology and calorimetry), Menger (1978) investigated the resulting hydrogels systematically to gain fundamental understanding of the design principles to create effective hydrogelators.⁴² Consequently, Menger's long journey focused on the development of derivatives of aroyl-L-cystines.⁴³ Currently, the fastest gelating molecule with the lowest concentration is the aroyl-L-cystine derivative **2** (Figure 1.6), able to rigidify aqueous solutions at 0.25 mM, *ca.* 0.01 % (w/v), in less than 30 s. To date, *N,N'*-dimethylurea (**3**) (Figure 1.6) is the smallest molecule known to form supramolecular organogels, described in 2005 by Weiss's group.⁴⁴

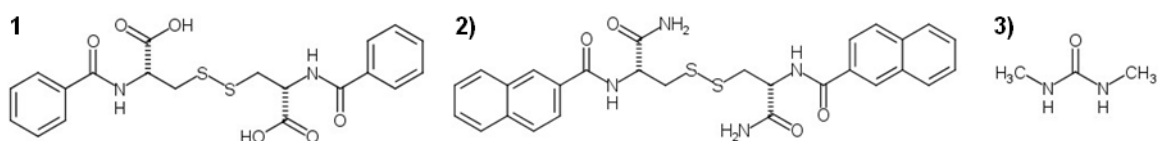


Figure 1.6. Molecular structures of **1)** the first supramolecular gelator dibenzoyl-*L*-cystine⁴¹ developed, **2)** the fastest gelating aroyl-*L*-cystine derivative⁴³ and **3)** the smallest gelator *N,N'*-dimethylurea⁴⁴.

1.5.1. Biomedical applications of supramolecular gels

In 1988, a Nobel Prize was awarded to Cram, Lehn and Pedersen in 1988 for their pioneering work in supramolecular chemistry, which caught the attention of many research groups.⁴⁵ At the moment, molecular gels have more potential applications than proved ones.⁴⁶ The reason behind this is their limited stability at room temperature, as they need to be kept sealed to avoid solvent evaporation and degradation.⁴⁶ Moreover, if used in the human body, they need to be approved by a regulatory health agency, such as Food and Drug Administration or European Medicines Agency.⁴⁶ Despite this, self-assembled supramolecular materials are strong candidates as delivery vehicles as they display many of the criteria required.²⁴

The first supramolecular structures used as drug matrices were lipids and their importance and current popularity as commercially available liposomes and micelles should be acknowledged.²⁴ These hold the leading position for the delivery of hydrophobic drugs.²⁴ Peptide-based hydrogels have also been successfully used as matrices for drug delivery.²⁴ Zhang *et al.* (2006) developed the RADA16 peptide,⁴⁶ later used by Schneider *et al.* to encapsulate and deliver the epidermal growth factor, with the purpose of accelerating cutaneous reepithelialisation for wound repair.⁴⁶ The success of this study granted this peptide a variety of applications, being developed as a vehicle for platelet-derived growth factor BB, stromal cell derived factor-1 and insulin-like growth factor I to the myocardium.²⁴ Other peptides have also demonstrated their capability for encapsulation and delivery of growth factors, with some showing selective hydrogelation according to the surrounding proteins.²⁴

Furthermore, there are several examples of supramolecular gels as tridimensional cell cultures for tissue regeneration.²⁴ One of the most successful examples was a cytocompatible peptide hydrogel, MAX8, developed by Schneider's group, and used as a

matrix to encapsulate mesenchymal stem cells.⁴⁶ Folding and self-assembly was triggered by the addition of cell culture media. This reversible gel possessed shear-thinning and recovery properties, allowing the gel-cell constructs to be delivered with a syringe. The cells remained alive during and after delivery, and the injectable solution remained localised at the injection site.⁴⁶

1.5.2. Classification of supramolecular gels

Depending on the nature of the solvent, these materials are named hydrogels, in which the solvent is water, or organogels, composed of any organic solvent.⁴⁷ Many experimental procedures require the use of dry gel samples. When the solvent is removed by solvent evaporation at room temperature (under vacuum or compression) leading to shrinkage of the network and collapse of the delicate internal structure, a xerogel is obtained (Figure 1.7c). Removal of the solvent by lyophilisation leads to formation of a cryogel, whereas drying under supercritical conditions prevents shrinkage and the solid network remains intact, giving rise to a highly porous material, termed aerogel (Figure 1.7b).^{8, 47}

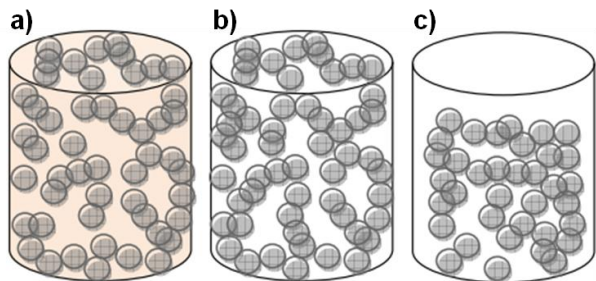


Figure 1.7. Representation of a) a gel, b) an aerogel and c) a xerogel.⁸

1.5.3. Low molecular weight gelators

Low molecular weight gelators (LMWG) are the building blocks of supramolecular gels.³⁸ To rationally design new molecules it is essential to be aware of the several molecular features that make compounds good candidates as building blocks for supramolecular gelation:^{5, 19, 22, 28, 47, 48}

- ◆ The existence of both solvophilic and solvophobic functional groups that impart solubility and stabilisation of solvent molecules, but also prompt aggregation. A delicate balance between the solvophilic and solvophobic regions needs to allow the formation of the nanostructures that remain stabilised within the solvent. A molecule that is too solvophilic will not have a driving force for aggregation and the small aggregates will remain in solution, whereas a molecule that is too solvophobic may precipitate or crystallise.
- ◆ The potential to create non-covalent interactions, such as hydrogen bonds, π - π stacking, electrostatic interactions, hydrophobic forces, van der Waals and dipole-dipole interactions. The combination of different types of non-covalent interactions is the most efficient approach.
- ◆ The presence of anisotropic interactions that favour unidirectional assembly, leading to formation of structures with large surface energy (e.g., fibres, sheets, vesicles), as chiral molecules and molecules with hydrogen bonding potential.

Nowadays there is a huge structural diversity for LMW gelators.⁴⁹ Such molecules include amino acids, peptides, carbohydrates, lipids, nucleotides, dendrimers, urea derivatives and other amphiphilic molecules.^{19, 28, 50, 51} The structures span from very simple motifs, as long alkanes, and very small molecules, as *N,N'*-dimethylurea, to complex and elegantly designed ones.⁴⁶ Hence, the diversity of attractive and repulsive forces that can be formed between gelator and solvent molecules is enormous.⁵² As claimed by Shapiro in 2011, “the spontaneous self-assembly of amphiphilic compounds is a consequence of the synergy of a number of weak forces in a delicate balance”.⁵⁰

1.5.4. Amino acids, small peptides and peptidomimetics

Amino acids are naturally abundant molecules that show great potential for hydrogelation due to their amphiphilic character – the hydrophilic moieties create opportunities for hydrogen bonding and stabilisation of water molecules, whereas the hydrophobic moieties may prompt aggregation.⁵ Weak interactions between complimentary amino acids occur in nature and their importance has been demonstrated in many biological processes, such as protein folding.^{38, 43, 53-55} Amino acids have inherent biocompatibility and biodegradability, and their use in supramolecular gels facilitates

incorporation of bio-functionality.⁵³ Moreover, the abundance of side chains (hydrophobic *vs.* hydrophilic, polar *vs.* apolar, charged *vs.* neutral, aromatic *vs.* aliphatic and linear *vs.* branched) makes available a vast library of functional groups and molecular properties that contribute for the synergism and cooperativity between various non-covalent interactions.⁴⁸

Currently, there is a diverse pool of recognised amino acid based gelators. An excellent review on the topic was recently published by Tomasini and Castelucci (2013).⁴⁷ Fuhrhop *et al.* (1993)⁵⁶ were the first group to report the hydrogelation ability of *L*-lysine. Initially, the development of peptide-based gelator molecules was focused on derivates of *L*-lysine, which became very popular due to its efficiency in hydro and organogelation.⁴⁷ Hydrogelation of phenylalanine also captured some attention recently and some groups focused on understanding the solid, gel and solution states of phenylalanine, as well as early stages of its aggregation. Since this molecule is the core of the project, Chapter 4 (page 138) provides a literature review on this topic.

Nowadays, the bulk of investigation covers amino acid residues and dipeptides coupled to a protective head group. The addition of a bulky aromatic capping group to drive gelation due to the hydrophobic effect and π - π stacking interactions is a common practice when designing new hydrogelator molecules.^{53, 57-59} Despite a variety of groups being available, as anthracene, carbazole, naphthalene, perylene and pyrene, the most popular group is 9-fluorenylmethoxycarbonyl chloride (Fmoc).⁵⁹ The Fmoc residue is very well recognised for its supramolecular hydrogelation ability, with excellent capacity to promote self-assembly by enhancing intermolecular hydrogen bonding of small molecules in water.^{28, 58, 60} Fmoc-phenylalanine derivatives have been extensively studied by Ulijn's group and have recently been proposed as matrices for 3D cell culture⁶¹ and as advanced drug delivery vehicles of a model drug (salicylic acid).⁶² Other successful examples of protected peptides include Boc-Leu-Val-Phe-Phe-Ala-OMe, Py-Phe-Phe-Ala-OMe and Nap-L-Phe-L-Phe-OH.⁴⁷

In solution, peptide molecules naturally attract, repel and accommodate each other. They are able to adopt specific secondary conformations, such as β -sheets, β -hairpins, α -helices and coiled-coil like structural motifs.⁵³ Peptides and peptidomimetics follow a rational conjugation and ordering like Lego® pieces, since amino acid residues are strategically

positioned to create cooperative interactions. This enables the design of gelator molecules with desired structure, properties and chemical function.⁴⁷ The tendency of peptides to self-assemble, the nature of the nanostructures formed and overall properties of the hydrogel are dependent on several factors, such as amino acid sequence, starting peptide concentration, pH and type of electrolyte in the medium.⁶³ The use of peptides with alternating hydrophobic and charged amino acids was pioneered by Zhang *et al.* (2002).⁶⁴ Dipeptides and tripeptides of phenylalanine self-assemble into hollow nanotubes or plate-like nanostructures, respectively, and both show β -sheet conformations.⁶⁵ The importance of this arises from the fact that the majority of amino acid residues in amyloidogenic peptide fragments contain such aromatic groups that promote pathologic amyloid formation.⁶⁶ Recently, Frederix *et al.* (2015) have summarised the rules for self-assembly of tripeptides, in which they covered selection and positioning rules for optimum gelation outcome.⁶⁷

1.5.5. Self-assembly of low molecular weight gelators

Association of small molecules into large tridimensional networks depends on a hierarchical self-assembly process (Figure 1.8).^{17, 53} To understand the relationship between molecular structure and gel properties, the hierarchical process of self-assembly should be broken down according to the length scales present.⁶⁸ The process starts with formation of highly specific, multiple, unidirectional non-covalent interactions that allow molecules to self-assemble into larger supramolecular structures. The nanoscale organisation (angstrom to nanometre scale) is determined by the molecular level recognition events that promote this anisotropic aggregation in one or two dimensions of the gelator molecules.⁶⁸ Hence, molecular interactions control nanostructure.²⁸

The anisotropy of the interactions favours self-assembly in one dimension and leads to the formation of fibrils, which grow, entangle and create nanoscale bundles, referred to as fibres. Microscopic organisation (nano- to micrometer scale) is defined by the morphology of these aggregates, *e.g.* micelles, vesicles, fibres, ribbons, sheets or any structures with a large/high aspect ratio, and it is directly influenced by the molecular structure.^{52, 68}

Elongation of these fibres leads to thicker and longer structures, which interact with each other and entangle. The entanglement of fibres gradually entraps the totality of the

solvent by capillary forces and surface tension to form a self-supporting self-assembled fibrillar network (SAFiN).^{4, 10, 52} The resulting supramolecular network is insoluble in the solvent.¹⁰ At this larger scale, the mesoscopic organisation of the gel (micro- to millimetre scale) involves the interaction of individual fibres. It is the interaction between these structures that is ultimately decisive whether a gel is formed or, instead, fibres precipitate out of solution.⁶⁸

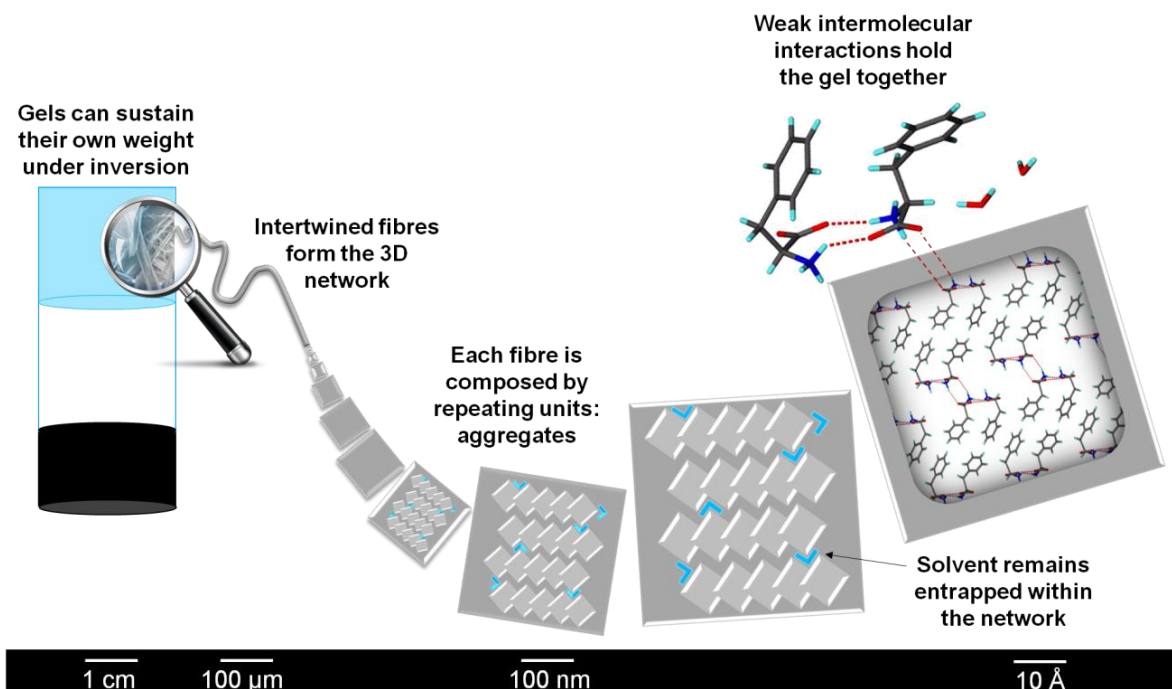


Figure 1.8. Process of hierarchical self-assembly of LMW gelators into larger complex supramolecular structures.¹⁷

1.5.6. Gelation *vs.* crystallisation

Crystallisation and gelation can be viewed as alternative outcomes of the same self-assembly process. These phenomena were broken down to molecular level events for a better understanding of their differences.

When solute molecules are dissolved in a solvent, crystallisation rarely occurs spontaneously, since a driving force is required.¹⁸ A common stimulus is a concentration gradient from the solution to the surface of the growing solute crystal, which occurs under supersaturation conditions, because such solutions are metastable.⁶⁹ Crystals are then formed *via* aggregation-nucleation-growth pathways.⁵² Even though nucleation and

crystal growth occur in parallel, these will be described as consequent events to facilitate understanding.¹⁸

Self-assembly starts with molecular aggregation as a consequence of Brownian encounters, which is followed by a very dynamic supramolecular rearrangement.⁷⁰ Nucleation follows with the generation of the smallest particles of a stable phase capable of growing, formed within the metastable mother phase.¹⁸ Critical nuclei sizes vary from less than ten to several hundred molecules, depending on the substance.¹⁸ Simultaneously, the small crystal surfaces in contact with the supersaturated solution promote crystal growth.¹⁸ Solute molecules or ions diffuse through the solution to the growing crystal. Upon reaching the surface, molecules or ions may be accepted and incorporated into the crystal lattice.¹⁸ Crystal growth happens when the rate of deposition of molecules or ions exceeds the rate of dissolution.¹⁸ Unfortunately, mechanistic understanding of nucleation processes is still limited.⁷¹ Some defend that classical nucleation theory is an oversimplification as there is growing evidence for two-step nucleation processes.^{17, 71} Even though a number of studies support the two-step nucleation theory, this is not a fully validated theory yet.

Gelation resembles crystallisation, having the common starting point in solution of nucleation followed by crystal (fibre) growth (Figure 1.9a).^{49, 72} In contrast to crystallisation, gelation is a unidimensional self-assembly process.²⁸ During the growth of fibres, thermal fluctuations prompt the growth of new layers with a deviated orientation with respect to the surface structure of the parent fibre, designed as crystallographic mismatch branching (CMB).¹² The daughter fibres contain a certain degree of structural mismatch with respect to the crystallographic orientation of the parent fibre (Figure 1.9b).¹² The key mechanism governing crystal network formation is sequential growth, branching and merging.^{12, 28} Fibre branching and merging occur at the junction zones. Crystallographic mismatch nucleation and growth is controlled by thermal fluctuations, thermodynamic driving forces, impurities, kinetics of surface integration and by specific free energy.¹²

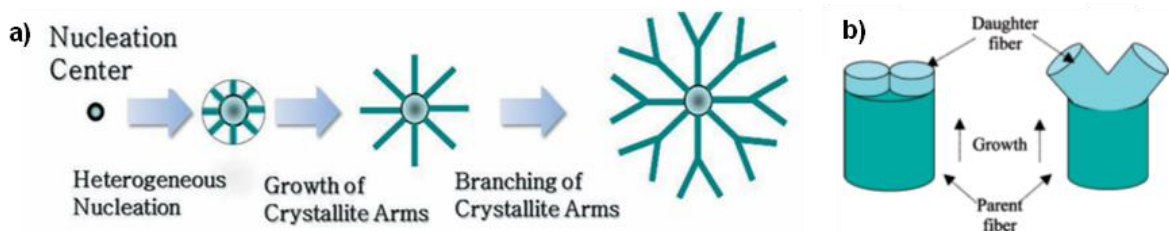


Figure 1.9. a) Formation of a fibre network based on the nucleation-growth-fibre branching mechanism. b) Fibre growth is usually followed by branching at the surface of parent fibre tips, which occurs due to crystallographic mismatch branching.^{12, 28, 73}

Even though gelation is a phenomenon comparable to crystallisation at the molecular level, the resulting products display very different physical properties.^{22, 28, 49, 70} To date, two approaches have been proposed to describe the thermodynamic nature of the gel state.¹⁹

In the first scenario, the crystalline state is considered an organised molecular arrangement over large distances with well-ordered packing and it is the thermodynamically most stable product.^{13, 48} The tridimensional extended structure of crystals is considered more stable as it allows a higher number of stabilising interactions in comparison with the unidimensional structure of the gel fibres.¹⁹ Therefore, the gel state is considered metastable, and the metastability of gel products arises from the presence of long gel fibres which results in an excess of interfacial free energy.¹³

Quenching a hot solution fits into this initial interpretation of gelation. A decrease in temperature produces a condition of reduced solubility with consequent supersaturation and crystal growth.¹⁸ However, rapid cooling does not provide enough time for crystallisation to occur, being anticipated by a gel transition.⁷⁰ This gel phase can hinder the evolution of crystals within the solution.⁷⁰ Gelation is therefore colloquially termed as incomplete or frustrated crystallisation.¹⁷ Formation of such thermoreversible gels follows a multi-step evolutionary process.⁵² As temperature is increased, the energy of the system increases, which promotes Brownian encounters between particles. The solubility of the gelator in the solvent is promoted by raising the temperature, increasing the entropy of the system and culminating with full dissolution of molecules and formation of a clear solution.⁵² Upon cooling of the solution, particles are forced to overcome the solubility boundary and supersaturation drives aggregation *via* stochastic nucleation. During self-

assembly processes, entropy is expected to decrease but quenching overcomes this entropic cost.⁷⁴ Particles start experiencing stronger attractive interactions, which gradually strengthen their attraction and lead to the formation of growing clusters with reduced solubility in the solvent.⁷⁰ Under such conditions, anisotropic driving forces dominate aggregation processes, and preference is given for gel formation over crystallisation.^{13, 22} SAFiNs are therefore formed as a consequence of the delicate balance between crystallisation and solubilisation.⁴⁹ The processes involved in formation of this kinetically trapped phase are represented in Figure 1.10.^{22, 49}

This scenario is supported by the observation of gel-crystal transitions in several systems.⁴⁹ The reversibility of the non-covalent interactions involved can be exploited to maintain the delicate balance of the interfacial tension at the fibre/solvent interface that prevents crystallisation of the metastable gel, or to produce thermodynamically stable crystals.^{28, 75} Depending on the depth of the activation barriers surrounding the gel state, transition to the crystal state can be promoted and has been observed systematically.^{49, 76-80} Some examples include the transition of an organogel of diphenylalanine in toluene into a flower-like microcrystal by introducing ethanol,⁷⁶ and the transition of a hydrogel of a pyridinium derivative into macroscopic crystals over time (hours to days).⁷⁸ With the increasing awareness that gelation can be considered a kinetically-trapped phase, functional groups began to be used as a means to manipulate the solubility parameters of gelators, in an attempt to access this metastable state and take advantage of modified solute-solvent interactions.⁸¹

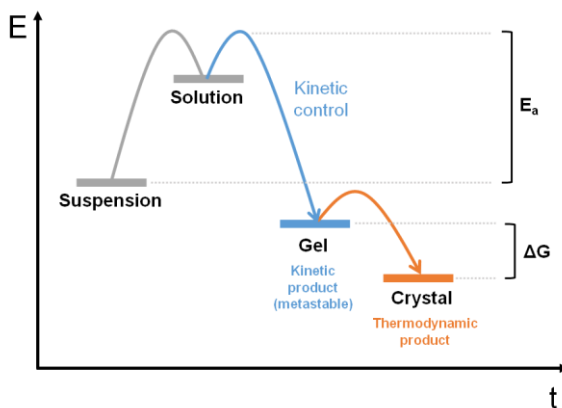


Figure 1.10. Free energy diagram comparing the gel and crystal states. In this scenario, the crystalline state is considered the thermodynamically most stable product, whereas the gel phase is considered arrested at a metastable state that anticipates crystallisation when quenching thermoreversible gels. Energy of activation (E_a), Gibbs free energy (ΔG). Adapted from references ^{28, 48}.

The previous hypothesis is not always valid, and an alternative approach considers the unidimensional structures formed in the gel state as the thermodynamic minimum.^{19, 48} Tuttle *et al.* (2016) argued that such products represent deep local minima surrounded by high activation barriers, severely hindering the access to the global minimum (the crystal state), as illustrated in Figure 1.11.¹⁹ Molecular dynamics studies backed-up their hypothesis, showing preferential formation of 1D nanostructures.¹⁹ Indeed, when molecules have well-defined solvophobic and solvophilic sections, there is preferential formation of unidimensional structures over tridimensional crystals.¹⁹ Recently, they developed a simple packing model that regards amphiphilic hydrogelator molecules (Fmoc-Phe-Phe) as prisms, instead of the conventional spherical representation, and showed that gel fibres did represent the thermodynamic equilibrium.¹⁹ Some examples include the preferred packing of a naphthalene derivative hydrogel into columns, rather than the crystal state, having close energies to the global energy minimum.⁴⁹ According to Tuttle *et al.*, self-healing gels are experimental evidence that gels are at the thermodynamic equilibrium, but they accept also that such systems can represent a state that can be reversibly accessed.¹⁹ Their model is a significant contribution to the molecular understanding of the hierarchical events that lead to formation of a nanofibrous network, as it embraces both scenarios. They concluded that the thermodynamic minimum can be either the gel or the crystal state, depending on the delicate balance between solvophobic and solvophilic forces, the tendency to solubilise or crystallise and the molecular shape.¹⁹

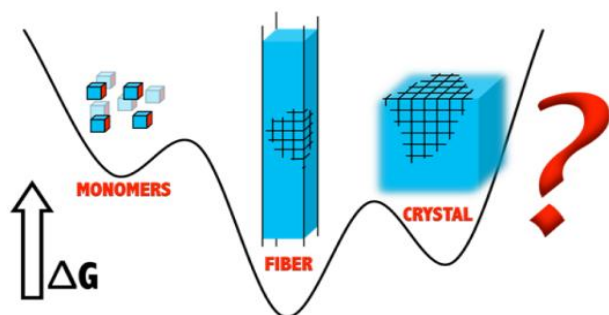


Figure 1.11. Schematic diagram of the free energy of gel and crystal states proposed by Tuttle *et al.*, showing that fibres can represent the thermodynamic minimum when surrounded by high activation barriers.¹⁹

1.5.7. Other gelation theories

Due to the complexity of the processes involved in crystallisation and considering how challenging these are to be probed experimentally, other theories of crystallisation and gelation have been developed.⁷¹ Instead of regarding these processes as sequential, where crystallisation follows gelation, Dixit *et al.* (2003) separate both events in terms of the degree of rearrangement, as an attempt to rationalise the gel-crystal equilibrium in proteins.^{19, 70} They argued that it is the rate of molecular aggregation and dissociation that determines the outcome. When the rearrangement of particles is complete and particles diffuse to locations where their energies are minimised, crystals are formed and the result is an insoluble ordered network.⁷⁰ In contrast to the above, gelation is the product of particles entrapped in non-equilibrium configurations. When the rearrangement of particles is incomplete, instead of acquiring positions where their energy is minimised, particles get trapped in amorphous aggregates or gels.⁷⁰ Clusters of particles trapped in amorphous locations continually aggregate through strong and anisotropic interactions. This is not always valid, as highly crystalline gels, resulting from extended well-ordered interactions, have been frequently reported.^{19, 82}

1.5.8. Gel aging

The metastability of supramolecular gels implies their evolution over time.⁸³ Besides their high interfacial energy, these systems are also unstable due the constant balance between molecular aggregation and the tendency to form solubilising gelator-solvent interactions.⁷⁵ Gel aging can occur *via* a variety of processes.⁸³ Over time, gels can undergo Ostwald ripening, where smaller fibres are lost in preference for larger and more stable structures, leading to a more robust gel, since the gel state is inherently less stable than its macrophase separated state.⁸³ In other cases, gel-crystal transitions can occur, as the gelator molecules crystallise directly from the gel and the network is weakened or collapses completely as a result of the growth of the new crystalline phase.⁸³ Similarly, gel-gel transitions are also possible with gel systems becoming more homogeneous and leading to more robust materials.¹⁷

1.5.9. The importance of self-assembly pathways

It is increasingly recognised that a single molecular structure may give rise to various superstructures making non-equilibrium kinetically controlled molecular assembly a topic of significant current interest.^{84, 85} In kinetically governed self-assembly processes, the outcome of self-assembly is dictated by the pathway rather than the free energy of the final assembled state.⁸⁶ The final structure expresses the preferred self-assembled state that reflects its preceding environmental conditions. Since nucleation and growth mechanisms affect the microstructure of the gel matrix, Raeburn *et al.* (2013) have showed that kinetics and pathways of self-assembly dictate rheological properties of a variety of supramolecular gels.²⁸ Gaining the control of the microstructure can be achieved fundamentally by changing the method of assembly (pH, temperature, heating/cooling rate) and therefore, tuning the gel material for the desired applications.²⁸ Hence, the pathway dependence of the outcome of gelation should not be underrated when developing gel materials.

1.5.10. The role of solvent

The importance of solvent properties is often disregarded when developing gelator molecules. Roger's group predicted the gelation behaviour of 12-hydroxystearic acid in a variety of solvents and proved how the prediction of gelation behaviour can only be successful if the chemical structure of the solvent and the solvent-gelator interactions are taken into account.⁸⁷ Solvent properties play a central role in determining free energy and gelation efficiency, and in mediating aggregation and self-assembly of molecular gelators.^{52, 72} Hence, solvent molecules affect nucleation and growth of fibres.⁷² Moreover, solvents' properties, as pH of the solution (which affects the competing solvation between donor and acceptor sites of hydrogen bonds), salt effects, type of salt ion and ionic strength (impacting on the strength of electrostatic interactions) have a huge influence on the solvation effect.^{48, 52, 72}

To illustrate the importance of solvent in dictating gelation outcome, numerous attempts have been made trying to correlate the solubility parameters of solvents with the gelation ability of molecular gelators.^{72, 88-90} Amongst the most promising, and hence most frequently used, are the Hansen solubility parameters.^{46, 72} These are a multi-parameter

solubility term that accounts for dispersion forces (δ_d), dipolar intermolecular forces (δ_p) and hydrogen bonds (δ_h) between molecules, and an associated Hansen distance (Figure 1.12).^{46, 48} These reflect the solvent's ability of solvating and interacting with solutes and are means to predict whether a certain solvent has the ability to dissolve a certain solute.⁴⁸

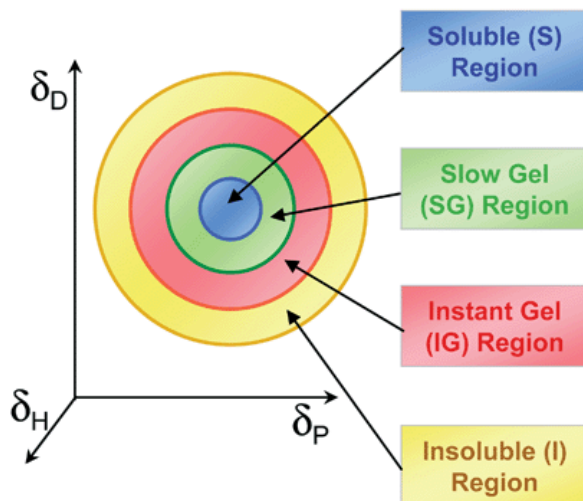


Figure 1.12. Schematic representation of Hansen solubility parameters (dispersion forces – δ_d , dipolar intermolecular forces – δ_p and hydrogen bonds – δ_h) in the 3D Hansen space and their correlation with gelation outcome.⁹¹ Dien *et al.* (2014) noticed a correlation between Hansen solubility parameters and the ability of a sorbitol derived organogelator to gelate in various organic solvents. The results followed a pattern of concentric spheres with the central solubility sphere being surrounded by spherical regions corresponding to slow gelation, instant gelation and insolubility cases. This pattern highlights that gelation requires a balance between solubility and insolubility.

Another predictive approach is the determination of the components of the molar Gibbs free energy, enthalpy and entropy, for the dissolution of molecular gelators in certain solvents, which can also be used to define the influence of the solvent on a chemical equilibrium.^{46, 72}

1.5.11. Multi-component gel systems

Multi-component gel systems are composed of two or more molecules.^{51, 92} The introduction of co-gelators or non-gelating additive molecules has been reported previously to create an additional level of control and therefore allow tailoring the

physical properties of gels through modifications to their supramolecular structure (Figure 1.13a).^{51, 92} They can form gels only when combined, gel independently (Figure 1.13b) or have their properties modified in the presence of non-gelling additives (Figure 1.13c).⁵¹

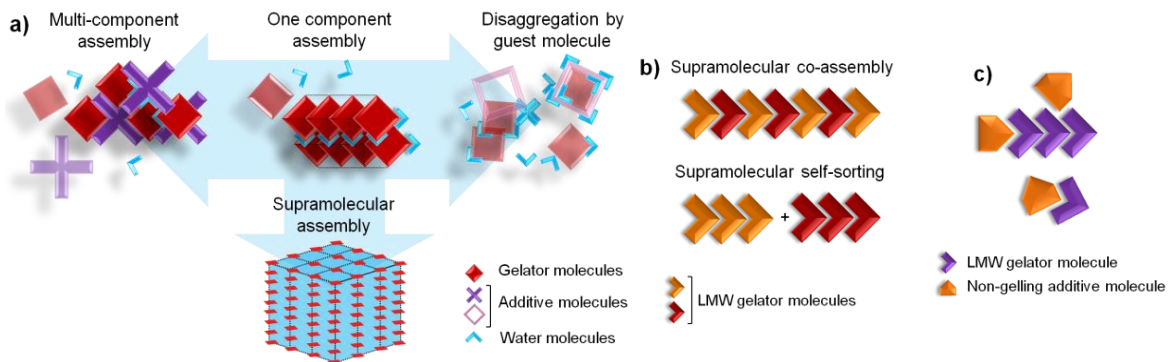


Figure 1.13. a) Low molecular weight gelators form complex supramolecular structures through non-covalent interactions. The introduction of additive molecules can either modify the physical properties of the hydrogel (left) or prevent its formation (right). b) Supramolecular co-assembly and self-sorting processes can occur when both molecules are low molecular weight gelators. c) When the additive is a non-gelling molecule, the physical properties of the resulting gel material might be modulated. Adapted from reference ⁵¹.

When both molecules form gel networks on their own (Figure 1.13b), the resulting mixed material is named multiple gelator system. It may be formed by interpenetrated structures of the pure gelators, termed self-sorting, where the different gelator molecules do not exhibit any interaction with each other and self-assemble separately.^{17, 51, 93} Moffat and Smith (2009) reported a two-component system formed of dramatically different morphologies of pure gelators, and showed that one of the fibres could be selectively polymerised with the other fibre being subsequently washed away, giving rise to a porous nanostructure.⁹³ At the other end of the scale, gelators give rise to new intimately blended mixed architectures, a process designed as co-assembly, where gelator molecules are strongly coupled.^{17, 51} The resulting mixed fibres form new tridimensional structures or one of the structures can act as the structural template for the mixed fibre.⁹⁴

When weak interactions occur between gelator molecules, a range of interesting possible behaviours arise.¹⁷ Furthermore, self-sorted and co-assembled structures might be present on varying length scales, and the presence of each component can influence the outcome

of the assembly of the other one. Since solubility constraints and kinetic factors dictate the rate of formation of each process, there might exist temporal, as well as spatial separation of the different assemblies.¹⁷ Self-sorted and co-assembled orthogonal materials may be physically entangled only at longer length scales.¹⁷ Buerkle and Rowan (2012) hypothesised that gelators with different molecular structure, size, chirality and/or self-assembly properties would show a tendency for self-sorting, whereas similar molecules should present a thermodynamic preference to form mixed assemblies.⁵¹ They also accepted the co-existence of self-sorted and co-assembled structures in a delicate balance.⁵¹

Self-assembly in the presence of non-gelling additives can equally impact gel properties (Figure 1.13c).⁵¹ Such molecules can be added with the purpose of fine tuning of the thermo and mechanical properties of the resulting system, modifying the morphology of supramolecular assemblies, introducing functionalisation, stabilising the gel matrix and/or preventing gel-crystal transitions.⁵¹ Occasionally, the addition of these molecules can interfere with self-assembly processes and fully prevent gelation.⁵¹ It was found that some drugs (diclofenac and methotrexate) hinder or retard gel formation of a gemini imidazolium-based amphiphile, in contrast with ibuprofenate and indomethacin.⁹⁵

For these reasons, multi-component materials exhibit more sophisticated functionality and morphology. Generally, the introduction of molecules into single gelator materials provides greater level of control of the outcome, whether these have themselves gelling properties or not. Therefore, understanding at the molecular level the structure of multi-component hydrogels provides opportunities for the design of customised soft materials.

Despite the theoretical understanding of multi-component gel materials, Draper and Adams (2016) defend that, at the moment, the scientific community is still not able to “directly image multi-component self-sorted networks on a longer scale, and show clearly whether the self-sorting is just a local phenomenon or rather that the assembly is truly made of two distinct fibrous networks. The properties of the resulting gel will also greatly depend on how the two networks co-exist; are they present as a genuinely interpenetrated, distinct two-network system, or, for example, does one network template the other? Do the fibres formed from one gelator prefer to entangle with themselves, or is there no discrimination at that step? These are questions that have until now been beyond our capability to answer.”.⁹⁶

Kumar and Steed stated in 2014 that “thermodynamic self-assembly has been used to construct complex self-assembled architectures, given access to nanoscale molecular containers and, in some cases, functional molecular devices such as shuttles, rotors and switches. Crucially, however, systems produced by equilibrium self-assembly are ‘dead ends’ as far as exhibiting complex, emergent or adaptive behaviour. Nature relies on equilibrium self-assembly. However, Nature’s systems are much better characterised as being self-organised, exhibiting dynamic and adaptive properties that are far from equilibrium”.¹⁷ Here, Kumar and Steed described the dynamic behaviour of supramolecular gels and defended their development.

1.6. Characterisation techniques

Supramolecular self-assembled materials are hierarchical structures that combine domains with drastically different degrees of ordering and molecular mobility, making their full characterisation a significant methodological and experimental challenge.^{12, 68, 96} Whereas some techniques can probe local assembly, giving an insight into the packing of the individual building blocks, it remains a challenge to determine longer length scales of organisation.⁹⁶ Hence, the combination of a wide range of methods is needed, as microscopy, rheology, diffraction and nuclear magnetic resonance (NMR) (Figure 1.14).^{68, 97} These are combined to provide a more complete understanding of the physical properties of these heterogeneous materials, including their thermal behaviour, mechanical stability, packing motifs, intermolecular interactions and molecular environments.⁹⁷

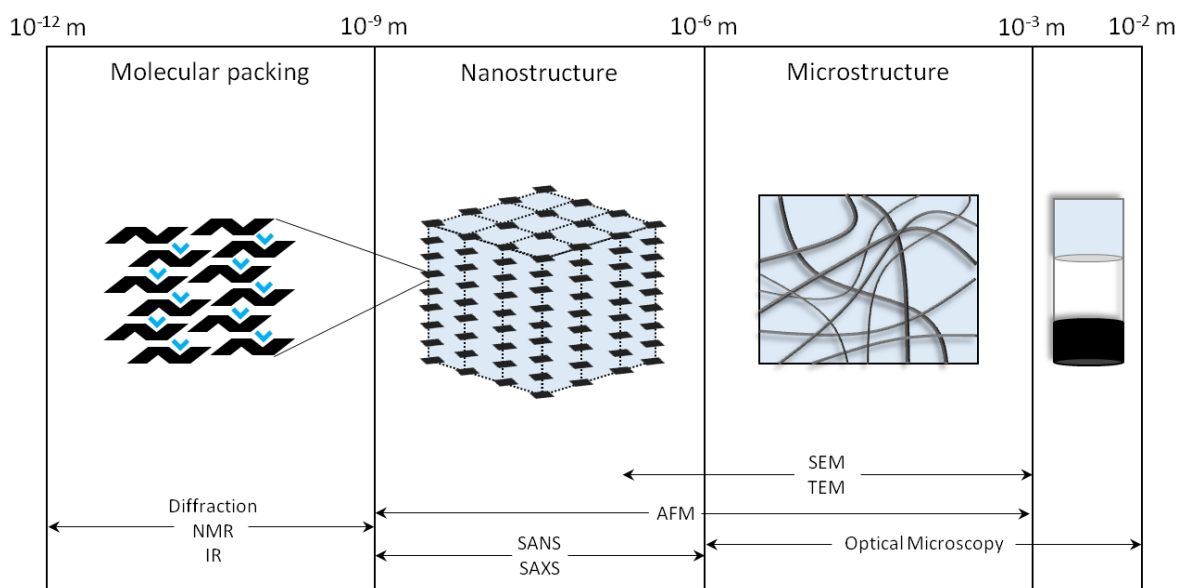


Figure 1.14. Characterisation techniques able to investigate the hierarchical organisation of supramolecular gels, highlighting the presence of several length scales of organisation.

1.6.1. Wet vs. dry gel samples

For supramolecular gels, preference is usually given to the techniques that do not require processing the sample over techniques that require solvent removal, freezing or staining.⁶⁸ Drying/staining artefacts may be incorporated and profoundly modify the physical state of the material, which is an object of study.⁹⁶⁻⁹⁸ During drying processes, gelator molecules

and fibres have time to diffuse and rearrange, resulting in fibre bundling and changes in morphology.⁴⁶ Moreover, removing the solvent changes local concentrations and therefore modifies solubility equilibrium. Methods that rapidly freeze the sample – as cooling under cryogenic conditions or with supercritical carbon dioxide – avoid the incorporation of morphological changes at the intermolecular and interfibrillar length scales and retain the original SAFiN structure with relative good confidence.⁴⁶

Furthermore, some cases have been reported in which the removal of solvent promotes crystallisation.⁴⁶ Dastidar and co-workers showed that the molecular packing of the gel fibres based on imidazole derivatives was affected by drying and promoted a transition to a different polymorph.⁹⁸ Consequently, some authors defend that observations acquired on dried samples are not reliable as they do not provide information regarding the real (native) morphology of the aggregating structures.⁹⁷ However, valuable information can still be obtained if experiments conducted in the dried state are validated by complimentary techniques performed in the fully solvated sample.⁴⁶

1.6.2. Macroscopic determination

The initial characterisation of a gel is frequently performed by visually assessing whether the material is able to withstand its own weight when inverting a vial, named vial inversion test.^{52, 68} This methodology can be used to determine the concentration that prompts spontaneous fibril formation, termed critical gelation concentration (CGC), and the temperature above which a thermoreversible gel loses its self-supporting ability (or structural integrity), designed as the gel-to-solution transition temperature (T_{gel}).⁹⁷ T_{gel} can also be determined using the “dropping ball” experiment (the temperature at which a small metal ball breaks through the gel), differential scanning calorimetry (the heat of gel melting or formation), circular dichroism and rheology.⁶⁸ Differential scanning calorimetry provides information on the thermodynamics of the system, mainly clarifying the thermal energy associated with certain phase transitions.⁶⁸ Besides this, thermogravimetric analysis can be applied for quantification of the mass lost by solvent evaporation or degradation.

Different techniques will detect different transitions, hence reflecting a broad scope of processes that occur at different temperatures. The combination of results from these

different methodologies provides useful information.⁶⁸ Despite the straightforward interpretation of such measurements, these can give only an initial indication of fibre strength and stability of intermolecular interactions, as their determination is highly dependent on the measurement protocol (*i.e.*, sample volume, vial diameter, heating rate and history of the gel).^{46, 97}

1.6.3.Rheology

A more quantitative determination of gel strength is the determination of its dynamic mechanical properties using rheology studies. According to Piepenbrock *et al.* (2009), viscoelasticity might be the most important defining feature of a supramolecular gel, as rheology is the only reliable method of determining whether a material is a gel.^{5, 99} More importantly, rheological properties are crucial in determining whether a biomaterial is potentially suitable for biomedical uses.⁵

This methodology determines the deformation and flow of the material in response to an applied force, determining the viscoelasticity of the system.⁶⁸ The mechanisms by which a gel rearranges to accommodate external stress are influenced by the microstructure of the gel which, in turn, is reflected by a macroscopic rheological response.⁴⁹ To fully correlate viscoelastic parameters with internal structure it is necessary to probe the different time scales of mechanical deformation present.^{11, 49} For many soft materials, the typical time it takes the material to adjust to an equilibrium stress after an applied deformation lies between milliseconds and minutes.¹¹ Therefore, oscillatory measurements are performed with frequency and amplitude sweeps. The most common setups are parallel plates and cone and plate geometries (Figure 1.15a,b).

Real soft materials as gels possess the elastic properties of ideal solids and the viscosity properties of Newtonian liquids (Figure 1.15c).^{11, 12} Due to this intermediate mechanical behaviour,^{11, 49} their phase angle (δ) values range between 0° and 10° .^{43, 49} Kramer and co-workers' rheological description of gels claims that the loss modulus (G'') should be considerably smaller than the storage modulus (G') in the plateau region.¹⁰⁰ For robust gels, an order of magnitude difference between G' and G'' values is expected, $\frac{G''}{G'} \sim 0.1$.^{11, 28, 49}

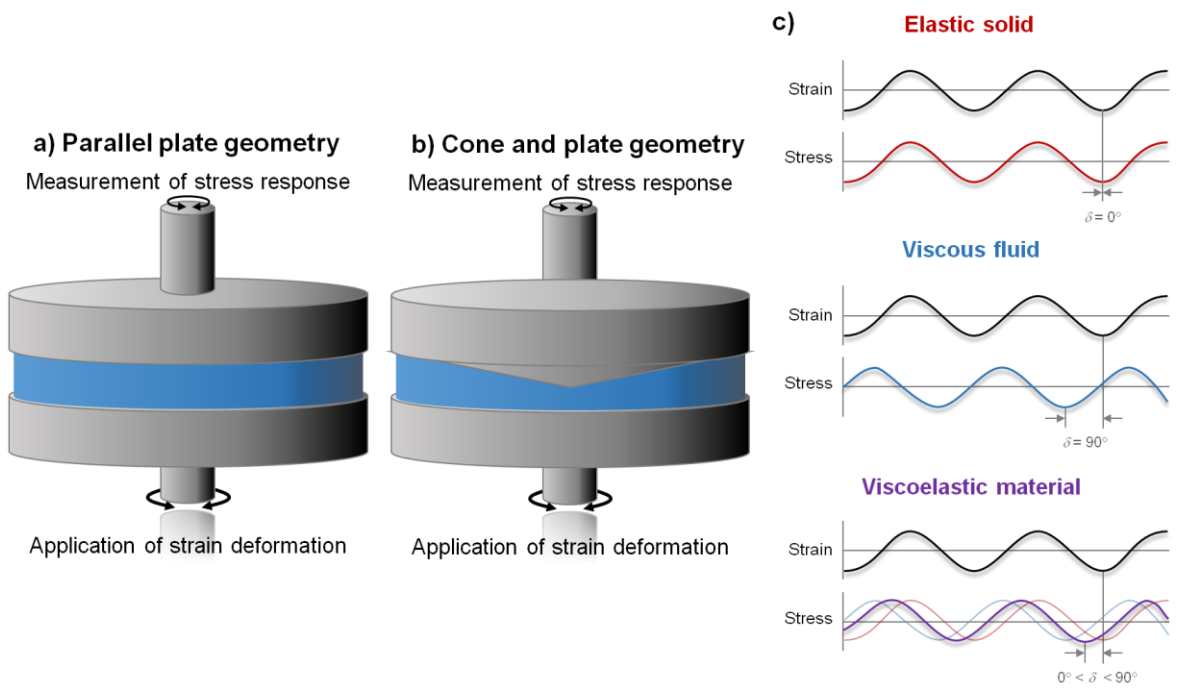


Figure 1.15. Schematic representation of **a)** parallel plate and **b)** cone and plate geometry setups. The sample is placed between both surfaces and while the top plate or cone rotates the bottom plate remains stationary. **c)** Schematic stress response to oscillatory strain deformation for an elastic solid, a viscous fluid and a viscoelastic material, where δ is the phase angle. Adapted from reference ¹⁰¹.

1.6.3.1. Relationship between viscoelasticity and mesoscopic organisation

Knowledge of the relationship between viscoelastic properties and nanostructure allows one to finely engineer gel stiffness according to intended applications.^{12, 28} Raeburn *et al.* (2013) reviewed the relationship between nano and microscale organisation of a supramolecular gel network and the resulting mechanical properties.²⁸ Their main findings showed that rheological properties were mainly determined by fibre thickness, degree and distance of fibre branching (correlation length, ξ) and number and type of non-covalent cross-links between fibres (Figure 1.16a,b).^{28, 97, 102}

Cross-links at the junction zones can arise either from entanglement or branching of fibres.²⁸ Lan *et al.* (2015) defended that junction zones and branching of fibres serve as the “glue” that combine fibres into tridimensional networks and are therefore responsible for the rigidity of the microstructure of gel networks.⁵² Junction zones break and reform before the bulk of the fibres when a mechanical strain is applied, hence Weiss (2014) attributed to them great importance when designing gels that are desired to melt at high temperatures, are thixotropic or rheologically strong.⁴⁶ Even though junction points

represent only a small fraction of the gel network, the importance of studying them lies in the fact that these are considered more disordered and less elastic than the rest of the fibre.⁴⁶ The mode of molecular packing at the junction zones remains a piece of missing information, due to the lack of useful methodologies that directly study these intersection points.⁴⁶ However, elasticity is dominantly affected by the number of permanent junctions as branching points, because transient fibre interpenetration has a much less marked role.²⁸ Overall, these features dictate gel dynamics, which is influenced by the strength and lifetime of bonds between gelator molecules and is therefore responsible for accommodating external stress.^{97, 103}

The distribution of the gel fibres at larger length scales, designated as gel microstructure, was also shown to be determinant.^{12, 28} Moreover, since self-assembly processes dictate primary nucleation and hierarchical growth of fibres, it was consistently reported that supramolecular organisation (and, consequently, mechanical properties) is conditioned by the process (and primarily kinetics) of self-assembly.^{12, 28} Since nucleation centres occur simultaneously, the majority of gel materials are formed by individualised multi-domains. The level of interpenetration between domains is known to affect gel strength.^{12, 73}

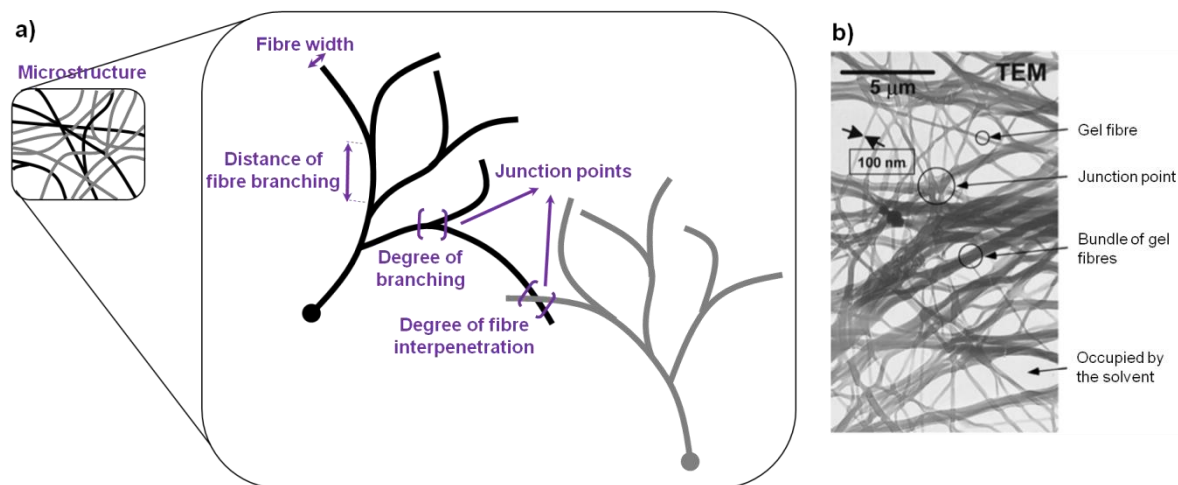


Figure 1.16. **a)** Factors that determine gel strength, adapted from reference ⁷³. Raeburn *et al.* (2013) found that rheological properties were mainly determined by fibre width, degree and distance of fibre branching and degree of fibre interpenetration. **b)** Transmission electron microscopy image of a freeze-dried sample prepared from a α -manno/p-xylene gel, highlighting the same features in a real fibre.⁵⁰

Li *et al.* (2005) found a strong correlation between rheological properties and correlation length (ξ) for a model small molecule organic gelator, *N*-lauroyl-*L*-glutamic acid di-*n*-butylamide, in isostearyl alcohol (Figure 1.17a).^{73, 102} A higher G' value resulted from increased density of branching points or smaller ξ .⁷³ Later, in 2009, Shi *et al.* showed that G' increased monotonically with the junction density (number of junctions per network area) (Figure 1.17b).¹⁰² The importance of these factors could be visualised in Figure 1.18, where they showed the processes of stress distribution in the gel networks with variable fibre lengths (and therefore, different ξ).

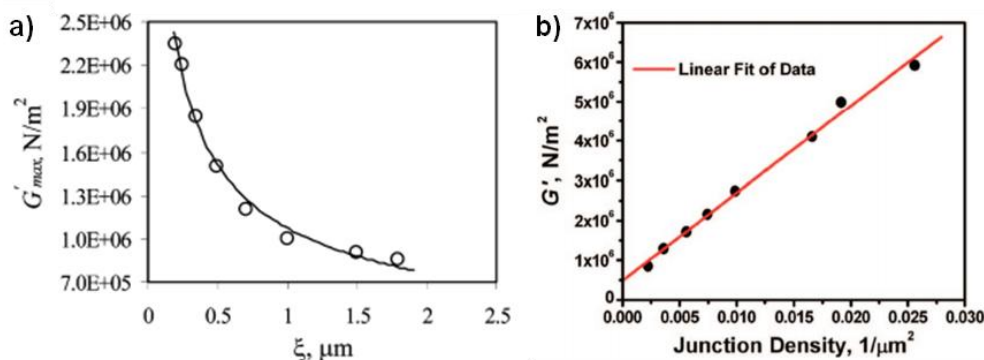


Figure 1.17. **a)** Maximum of storage modulus (G'_{max}) as a function of correlation length (ξ) for *N*-lauroyl-*L*-glutamic acid di-*n*-butylamide gels in isostearyl alcohol.⁷³ **b)** Simulation of storage modulus (G') as a function of junction density for *N*-lauroyl-*L*-glutamic acid di-*n*-butylamide gels in isostearyl alcohol.¹⁰²

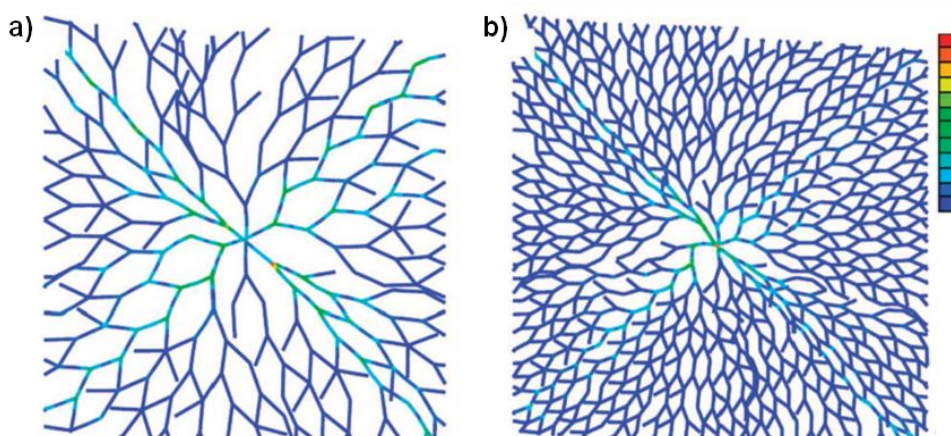


Figure 1.18. Stress distribution in networks with **a)** long fibre length (long ξ) and **b)** short fibre length (short ξ). From red to blue, the stress distribution varies from maximum to minimum, respectively. When the fibre length is long (**a**) the stress is distributed over a large area, while, whereas when the fibre length is short (**b**) the stress distribution occurs mainly along several radii.¹⁰²

1.6.4. Morphology of self-assembled fibrillar networks

Gel morphology encompasses fibre shape, surface, width, length and entanglement, and can be characterised by a variety of microscopic techniques.⁹⁷ Polarised light microscopy images have the unparallel advantage of being recorded on solvated samples, avoiding the introduction of drying or staining artefacts. In these studies, several fundamental processes can be monitored, such as formation of macroscopic centres of fibre formation, fibre growth and branching and birefringence¹⁰⁴ (intimately linked with molecularly ordered materials). When these instruments are coupled to a temperature unit, hot stage microscopy can be performed and allows to follow dissolution/melting processes and to determine T_{gel} . Their resolution is however limited by the limit of the wavelength of visible light, having a resolution at the micrometre level.⁶⁸

Scanning electron microscopy (SEM) and transmission electron microscopy (TEM) have nanometre and sub-nanometre resolutions, respectively, but require drying and/or staining of the gel samples.⁹⁷ Drying might allow nanoscale reorganisation, whereas coating molecules have the potential of interacting with the gel molecules, potentially leading to distortion of the original assemblies.^{68, 97} Cryogenic SEM (cryo-SEM) and cryo-TEM enable the analysis of soft materials in a pseudo-native state, since the samples are quickly frozen to prevent molecular rearrangement.⁹⁷ Cryo-tomography methods are also being developed to investigate the structure of cells with a depth resolution lower than 10 nm and may be soon possible for the study of molecular gel samples.⁴⁶ Nevertheless, in order to allow visualisation of the gel fibres without sample processing, environmental SEM was developed, but the cost of the instruments still prevents its widespread utilisation.⁹⁷

Atomic force microscopy (AFM) produces high resolution images of structures that can range from nano- to submillimetre length scales.⁹⁷ This technique does not require sample coating and can be performed with solvated samples, although analysis is facilitated upon drying.⁶⁸ Nonetheless, this is a contact microscopy technique and the soft surface of these materials may be modified (apparent flattening, change of shape, distribution or connectivities between fibres) when interacting with the cantilever during AFM measurements.^{46, 97} An alternative has been performed in materials immersed in a liquid

by Whitten and co-workers, in which they successfully monitored *in situ* aggregation and fibre formation of a steroid gelator in octanol.¹⁰⁵

Therefore, the selection of the microscopic technique strongly depends on the physical properties of the gel sample and the type of information required. However, complete understanding of gel morphology usually requires the combination of the available microscopic techniques.⁹⁷ Development of future instrumental and sample preparation techniques should make imaging of gel networks using cryo-techniques more routine.⁴⁶

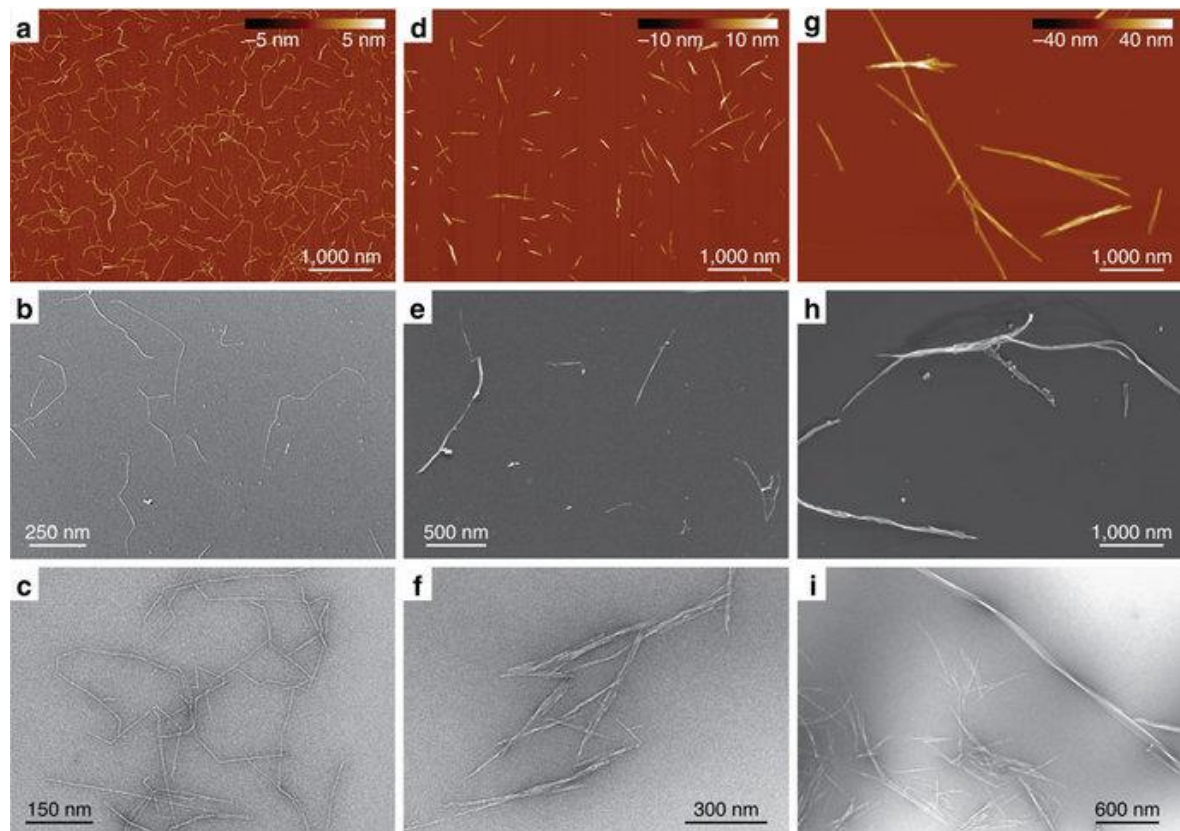


Figure 1.19. Overview microscopy images of nanocellulose samples acquired using **a,d,g)** atomic force microscopy, **b,e,h)** cryo scanning electron microscopy and **c,f,i)** transmission electron microscopy.¹⁰⁶

1.6.5. Circular dichroism spectroscopy

Circular dichroism (CD) spectroscopy is based in the differential absorption of left and right circularly polarised light by chiral structures, giving rise to a spectrum. It is a very sensitive and quick instrumental method, being more powerful than other absorption spectroscopies (as UV, VIS and IR).^{97, 107} CD can provide an insight into the nanoscale assembly of supramolecular chiral structures. This information is usually “encoded”

within the chirality of the gelator molecule and then conditions the orientation of the supramolecular assemblies.^{97, 107} This is expressed at larger scales in the morphology of the self-assembled fibres. Each supramolecular assembly has a characteristic wavelength, making it is possible to conclude on the conformation of macromolecules. The wavelength range typically examined for supramolecular gels is between 200 and 600 nm. This technique also allows monitoring kinetics and thermodynamics of self-assembly, conformation and structural changes and enables concluding on the interactions responsible for molecular stacking. As molecular chirality favours unidirectional assembly, many gelator molecules contain chiral centres.^{97, 107}

1.6.6. Powder X-Ray diffraction

Powder X-ray diffraction (PXRD) enables the elucidation of crystal structures forming gel networks.^{22, 68} This knowledge can contribute for identifying the main supramolecular interactions (synthons) responsible for SAFiN formation, enabling the rational design of gelator molecules.²²

This technique gives information on the long range ordering of materials.⁶⁸ Crystals with precise periodicities over long distances give rise to sharp and clear diffraction peaks in PXRD patterns. Crystals with defects (such as impurities, dislocations, planar faults, internal strains or small precipitates) also have distinct diffraction patterns, but display broadened, distorted and weakened diffraction peaks. Contrarily, the absence of an ordered arrangement in amorphous materials results in considerably broad peaks. Some supramolecular self-assembled networks are amorphous, and their lack of a well-defined tridimensional organisation makes structure determination very challenging.^{12, 108, 109}

Independently of how ordered the fibres are, PXRD is an effective method of finding out the structural packing motifs of the gelator molecules in the solid state.⁹⁷ But growing single-crystals of a gelator molecule is extremely difficult. Recording good quality patterns of gel fibres in the native form suffers from the scattering contribution of the solvent molecules and from the inherent disorder of the less crystalline nature of the gel fibres.¹¹⁰ Hence, Weiss and co-workers developed a method of obtaining PXRD patterns in the wet state of gels, overcoming the issues associated with drying and the scattering contribution of the solvent molecules.¹¹⁰ To better discern the PXRD peaks that arise from

the molecular packing of gelators, they subtracted the amorphous PXRD background from the solvent with neat liquid to the pattern acquired on a wet gel sample, $\text{PXRD}_{\text{wet gel}} - \text{PXRD}_{\text{solvent}} = \text{PXRD}_{\text{fibres}}$ (Figure 1.20).¹¹⁰ The remaining signals were used to obtain information about the molecular packing of fibres and indexed to produce unit cell parameters.⁴⁶

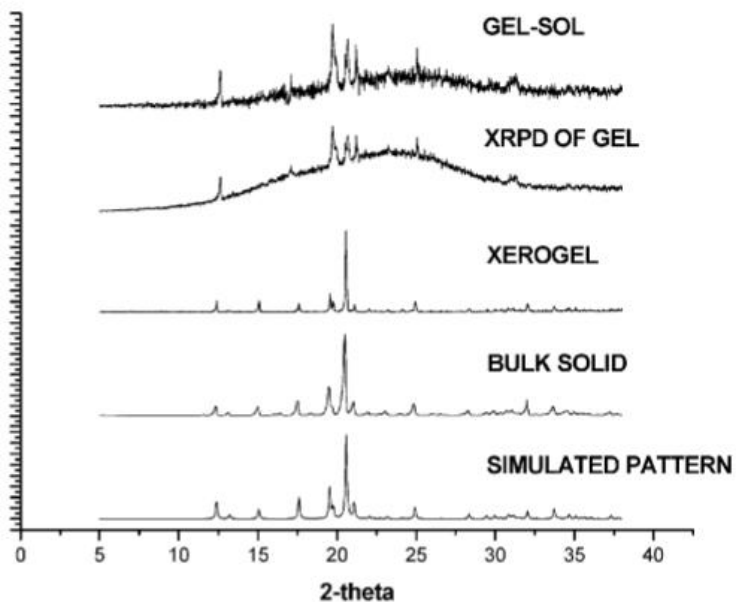


Figure 1.20. Powder X-ray diffraction patterns of “gel – sol” (which corresponds to the subtraction of the diffraction pattern of the neat solvent to the diffraction pattern of the wet gel, as described by Weiss¹¹⁰), wet gel, xerogel, bulk reference solid and simulated pattern from single-crystal data of an imidazole derivative, highlighting the difference between the supramolecular organisation of the gel and the neat crystals.⁹⁸

Adams and co-workers defend that “an important question is the relationship between the tridimensional packing of the gelator molecules in a crystal and the (possibly) less ordered aggregates leading to gels”.⁴⁹ Similarities between the packing arrangement of gels and crystals have been reported and are described below, suggesting a close relationship between both states.^{12, 22, 49, 108} Ostuni *et al.* (1996) were able to indirectly determine the molecular packing within the gel fibres, because of the good agreement found between the PXRD pattern of the fibres and the powder pattern simulated from the single-crystal data.^{22, 110} Moreover, it was reported that a sugar-biphenyl metastable gel in a water/dioxane mixture phase transitioned into a crystalline state with similarities to the single-crystal.¹¹¹ In addition, Trivedi *et al.* (2005) found identical PXRD patterns for the

xerogel, the bulk solid as well as that simulated from the neat crystals of secondary ammonium salts (Figure 1.21).¹¹² The correlation between the crystal structure of molecules and their ability to gelate is especially important for crystal engineering.²²

Dastidar disagreed with Adams and defended that “the crystal structures of the neat gelator and the gel fibres in the native (gel) state do not need necessarily to be identical and therefore, such a correlation between the neat crystal structure and gelation ability may not be that relevant.”²² There are some examples in literature where the structure of the gel formed does not correspond to any of the known crystals.^{22, 83} Dastidar and co-workers obtained a gel from imidazole derivatives in nitrobenzene, with the crystal packing of the gel fibres in its native environment being different from that present in the neat crystal and the bulk solid (Figure 1.20).⁹⁸

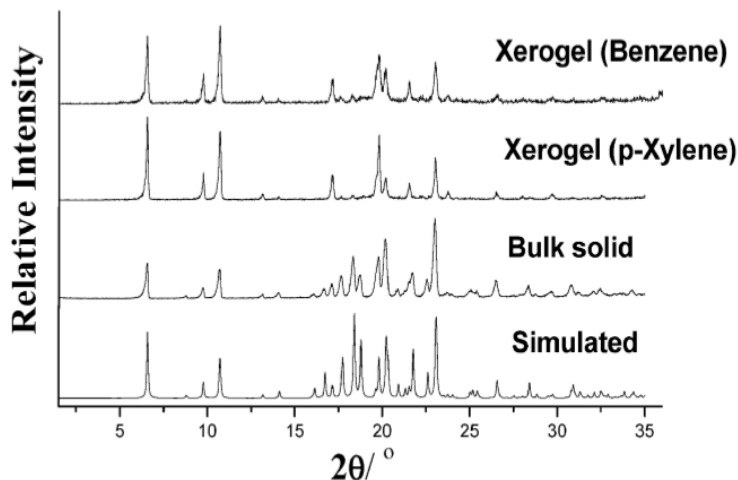


Figure 1.21. Powder X-ray diffraction patterns of the xerogel, bulk reference solid and simulated from single-crystal data of a secondary ammonium salt, highlighting the similarity between the supramolecular organisation of the gel and crystal structure.¹¹²

Sub-nanometer resolution might be achieved in the near future for structural characterisation of molecular gels, as it has been demonstrated recently that it is possible to obtain synchrotron-derived data on multiple, unoriented, sub-micrometer-sized crystals.⁴⁶ Also, cryocrystallisation techniques can be conducted using sub-micrometer-sized crystals, overcoming current issues with the small sizes of the gel crystals. Moreover, pulsed X-ray free electron lasers are currently being used to attain near atomic resolution of structures in micrometre-sized crystals. Although these approaches have

focused on molecules with biological relevance, they should be soon applicable to investigate fibres of molecular gel networks. This is a step closer to getting atomic-level resolution and detailed structural packing of fibres.⁴⁶

1.6.7. Computational techniques

Computational approaches are currently used to simulate molecular and atomic behaviour based on fundamental descriptions of orbitals (*ab initio* quantum mechanics), experimental data (*a priori* molecular mechanics) or these use a combination of both (semi-empirical methods).⁹⁷ Computational approaches play an important role in the investigation of interactions between the gelators, which considerably helps understanding gelation mechanisms.⁹⁷ Moreover, possible modes of aggregation for gelators can be identified by using high level energy minimisation and molecular dynamics calculations.⁹⁷

Determining gelation of small molecules is still an empirical science, so molecular modelling hopes to overcome this obstacle.⁵² The main goal of crystal engineering is to understand intermolecular interactions in the context of crystal packing and the application of such understanding in the design of new molecular solids with desired physical and chemical properties.²² It is important to identify supramolecular spatial arrangements of intermolecular interactions that are frequent enough to ensure generality and predictability of the resulting solid.²²

1.6.7.1. Crystal structure prediction

Crystal structure prediction (CSP) methods calculate the preferred solid state assembly of organic molecules using a global search of the lattice energy surface.^{49, 108} This global optimisation approach explores the molecular packing possibilities and predicts low energy crystal packing arrangements by sampling all possible crystal packing motifs with different molecular conformations, unit cells and space group symmetries.⁴⁹ It seeks to locate and assess the relative stabilities of all possible ways of packing molecules into ordered crystal structures, taking no account of the required kinetic pathways to form these structures.¹⁰⁸ In the end, it generates an energy ranked list of the most favourable

crystal packing possibilities of a molecule, designed as the crystal energy landscape.^{49, 108} This is a powerful approach for exploring the solid state structural landscape of molecules and can give an insight into possible polymorphism, as well as hydrate formation and gelation.

These calculations have recognised accuracy in building the structural landscape for small, rigid molecules, but some groups have extended recently the applicability of these methods to more complex, flexible molecules.⁴⁹ CSP methods are currently very efficient in predicting structures of molecular solids.¹¹³ Even though CSP calculations have been applied to challenging molecules, due to the size and possible conformational flexibility of complex molecules, the extent to which their crystal packing possibilities can be sampled is limited.¹⁰⁸ Moreover, CSP generates perfect crystalline arrangements of the molecules, which might not correspond to the true packing motif that is present in the gel fibres.¹⁰⁸

Since computational approaches yield hypotheses that must be proved experimentally, CSP calculations are usually followed by simulating a PXRD pattern and comparing it with the observed pattern of the xerogel.^{46, 49} Additional information on the molecular packing of gelator molecules at the atomic resolution level can then be obtained if the theoretical PXRD pattern of a single crystal of the gelator matches the diffraction pattern of the gel.⁴⁶ Currently, solving the crystal structure of gel fibres *ab initio* from its polycrystalline PXRD data is not routine yet and requires use of synchrotron beam line.²²

To fully characterise gelation it is important to study how molecules associate at the different stages of their self-assembly processes.⁴⁶ As CPS solely studies the final assemblies, density functional theory, molecular dynamics and other types of calculations are being used to discern the details of association between molecular gelators at earlier stages of their aggregation.⁴⁶

1.6.7.2. Molecular dynamics

Considering the existing conformational changes during time-dependent self-assembly, molecular dynamics (MD) simulations are more favourable than simple energy minimisations to study self-assembly of gelators.¹¹⁴ Besides providing atomistic information on kinetics, thermodynamics and time evolution of molecular conformations,

MD can also remove unfavourable interactions that remain after energy minimisations. Therefore, MD overcome the minimisation's inadequacy in predicting the entropically favoured conformations and therefore has been widely used in self-assembly studies. Mu *et al.* (2013) applied MD calculations to study the self-assembly of a Fmoc-dipeptide and they showed that Fmoc-Ala-Ala molecules assemble into well-defined fibril structures independently of the starting conditions. These computational data were validated by PXRD experimental findings.¹¹⁴

1.6.8.NMR spectroscopy

Nuclear magnetic resonance (NMR) provides structural and dynamic information about molecular and supramolecular structures, based on short range interactions between nuclear spins.^{50, 115} Detailed description of the fundamentals of NMR spectroscopy can be found in Chapter 2 (section 2.3, page 89). This is a minimally invasive technique, yet very powerful, that allows the study of samples in their native state with negligible effects on the original supramolecular organisation.⁵⁰

1.6.8.1. Timeline of NMR techniques in the study of soft materials

There has been significant interest in the characterisation of gels using NMR spectroscopy in the last decades, so only the pioneering and most important applications are described here (Figure 1.22).⁴⁶ These discoveries came hand in hand with the interest and subsequent investment in the field of gels, which started in the 60s but only grew exponentially after the year of 2000.³ The field saw its evolution limited by technological and instrumental advances of NMR spectroscopy.

1971	Highly resolved ^{13}C solid-state NMR spectra of swollen polymeric gels by Schaefer
1972	Solid-state ^1H NMR relaxation studies conducted at variable temperature and concentration of agarose gels by Child and Pryce
1974	Solid-state measurements of self-diffusion coefficients at variable temperature and concentration of agarose gels by Derbyshire and Duff
1978	Calculation of correlation times from solid-state ^{13}C NMR T_1 , T_2 and nOe measurements of cross-linked polystyrene gels by Yokota <i>et al.</i>
1985	Solid-state ^2H NMR experiments of wet poly(<i>D,L</i> -lactide-co-glycolide) gel by Schmitt <i>et al.</i> Highly resolved ^1H - ^{13}C CP/MAS spectra obtained when spinning swollen polystyrene gel by Ford <i>et al.</i>
1995	Combination of ^1H - ^{13}C CP/MAS and PST/MAS to identify dynamics on poly(vinyl alcohol) gels by Kobayashi <i>et al.</i>
2000	Well-resolved ^1H - ^{13}C CP/MAS solid-state NMR spectra on wet supramolecular gels of 1,2-bis-urea benzene derivatives by Schoonbeek <i>et al.</i>
2005	2D ^1H - ^1H NOESY spectra of supramolecular gels of geminal bis-urea by Behanna <i>et al.</i>
2010	STD NMR experiments of supramolecular hydrogels of glutathione by Mahajan <i>et al.</i>
2017	^1H PFG HR-MAS NMR experiments of supramolecular gels by Iqbal <i>et al.</i>

Figure 1.22. Pioneering studies on the characterisation of gels using NMR spectroscopy conducted by Schaefer,¹¹⁶ Child and Pryce,¹¹⁷ Derbyshire and Duff,¹¹⁸ Yokota *et al.*,¹¹⁹ Schmitt *et al.*,¹²⁰ For *et al.*,¹²¹ Kobayashi *et al.*,¹²² Schoonbeek *et al.*,¹²³ Behanna *et al.*,¹²⁴ Mahajan *et al.*,¹²⁵ and Iqbal *et al.*.¹¹⁵

NMR spectroscopy was firstly used in the study of gels after being well established in the characterisation of biological systems, due to their similar viscoelasticity and high water content.⁴⁶ At an early stage, ^1H NMR experiments were not useful for the characterisation of polymeric networks, since their rigid fibres gave rise to broad signals.⁴⁶ In 1971, Schaefer swelled the network of polymeric gels with solvent and ^{13}C peaks became sufficiently resolved to obtain structural information from high-resolution pulsed ^{13}C

NMR spectra.¹¹⁶ After Schaefer established ¹³C NMR as an alternative to ¹H NMR experiments, these studies dominated the field of investigation of polymeric gels.¹²⁶

In 1972, Child and Pryce relied on ¹H NMR spectroscopy, monitoring molecular motions throughout the sol-gel transitions by measuring ¹H NMR relaxation times of water and polymer chains of agarose hydrogels.¹¹⁷ This study introduced the idea of understanding gelation mechanisms (which are very dynamic and environment-dependent) by varying experimental conditions. This prompted numerous measurements of ¹H NMR relaxation times and self-diffusion coefficients at variable temperature, concentration, field strength and/or hydration level of agarose gels, used as model materials to investigate the role of water in soft materials, namely in biological systems.^{118, 127} Consequently, these authors identified the presence of exchanging water molecules between bulk water and bound to macromolecules and started trying to quantify these fractions.^{118, 127}

With this goal in mind, ²H NMR solid-state experiments became more popular for identification and quantification of water in polymeric networks.¹²⁰ ²H NMR spectroscopy allows for distinguishing between different types of molecular motions by observing the variation in the typical pattern that arises from quadrupolar interactions.⁵⁰ Despite being complex, quadrupolar interactions convey valuable dynamics information.⁵⁰ When D₂O molecules are free, the quadrupolar interactions are averaged to zero as a result of rapid molecular motions and narrow singlets are observed, whereas anisotropic water molecules interacting with a solid have their molecular rotation hindered, which results in a doublet.^{50, 120} Since decreasing the mobility of a sample results in the typical Pake Pattern, different types of molecular motions can be distinguished by observing the variation of the typical pattern as a function of temperature.⁵⁰ Using D₂O as a probe for investigating water environments was imported by Schmitt *et al.* (1994) from McCall's studies in solids.¹²⁸ They successfully quantified the two types of water present: bulk water with free rotation (narrow signal) and bound water with hindered rotation (broad signal) (Figure 1.23a).¹²⁰

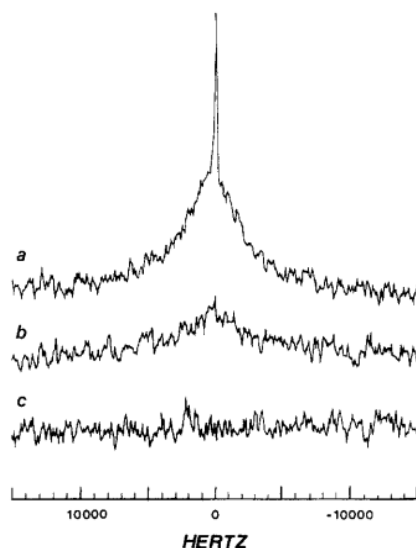


Figure 1.23. Solid-state ^2H NMR spectra acquired on poly (DL-lactide-co-glycolide) 50:50 containing **a**) 1.17 % of $^2\text{H}_2\text{O}$, **b**) dried under vacuum and **c**) dried further under high vacuum, using a 300 MHz solid-state spectrometer.¹²⁹

The different segmental motions in cross-linked polymeric hydrogels were fully characterised by Yokota *et al.* (1978), in order to understand the various factors that determine chain mobility in gels.¹¹⁹ With this in mind, they calculated rotational correlation times from the measurement of ^{13}C T_1 , T_2 and nuclear Overhauser effect (nOe) at variable hydration, temperature and cross-linking degree, according to the equations developed by Doddrell *et al.* (1972).^{119, 130} This is the first example in the literature of the application of nOe in the study of gels.

With the purpose of improving resolution in the solid-state, Ford *et al.* later attempted to obtain ^1H - ^{13}C CP/MAS NMR spectra from CDCl_3 -swollen polystyrene gels spinning at 2 kHz using conventional Kel-F rotors, but they encountered several practical challenges, such as leaking of the solvent.¹²¹ After several unsuccessful attempts with sealed glass tubular inserts, they decided to fuse the Kel-F cap to the insert to prevent leakage.¹²¹ In 1985, they successfully demonstrated it was possible to acquire high-resolution ^1H - ^{13}C CP/MAS solid-state NMR spectra when spinning swollen polystyrene gel at an MAS rate of 4 kHz (Figure 1.24).¹²¹

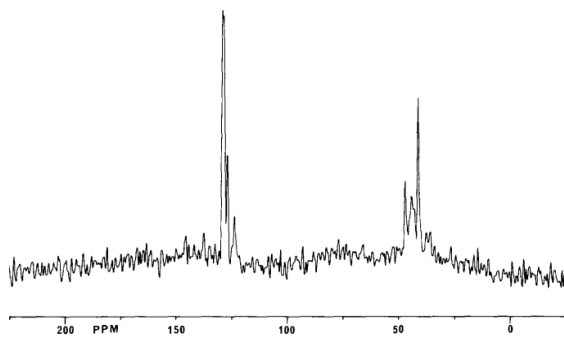


Figure 1.24. First highly-resolved ^1H - ^{13}C CP/MAS NMR spectrum acquired on CDCl_3 -swollen polystyrene gels using an MAS rate of 4 kHz and a 25 MHz solid-state spectrometer (^{13}C line widths < 15 Hz).¹²¹

This was followed by Ginter *et al.* (1989) work, who improved the previously reported approach using conventional MAS rotors sealed by endcaps containing O-rings instead, to overcome the difficulties in obtaining axisymmetry distribution and avoid using non-reusable sealed inserts.¹³¹ They obtained highly resolved ^{13}C and ^{29}Si peaks for poly(ethylene oxide) gels in water, comparable to a liquids probe.¹³¹ They were the first authors to report the presence of two sets of superimposed peaks, with sharper resonances overlapped with a broader one, attributed to the presence of two distinct components in the gel, mobile and immobile.¹³¹ Similarly, Kobayashi *et al.* (1995) focused on the study of mobile and immobile structures. They investigated the amount of hydrogen bonds between interchains of poly(vinyl alcohol) gels to determine dynamics of polymer chains using the complementarity of ^{13}C CP/MAS and ^{13}C pulse saturation transfer (PST) MAS at variable concentration. In PST/MAS, nOe enhances ^{13}C magnetisation for the mobile components, whereas in CP/MAS strong heteronuclear dipolar couplings are responsible for enhancing ^{13}C peaks from rigid structures. They established the potential of ^{13}C CP/MAS experiments in the detection of immobile and less rigid components in soft materials.¹²²

Studies conducted on polymeric gels formed the basis for the investigation of many molecular gels.¹³² Solid-state NMR studies of molecular gels is not a straightforward task.¹³² Recording CP/MAS NMR spectra of supramolecular self-assembled materials is difficult due to centrifugal disintegration of the sample, low crystallinity and very low gelator concentration.¹³² In 2000, Schoonbeek *et al.* showed that supramolecular gels can be studied in their native state. They successfully acquired well-resolved ^1H - ^{13}C CP/MAS NMR spectra on gels composed of 1,2-bis-urea benzene derivatives in toluene, avoiding

introducing drying artefacts, hence establishing the potential of this technique in the field.^{123, 133} Even though the spectra acquired in the native state had poor signal-to-noise ratio, they found a very good agreement between the solid and the gel spectra.¹²³ Since CP/MAS relies on strong dipolar couplings, typical of rigid components, these experiments probe exclusively the gel fibres.⁵⁰ Kolehmainen's group followed by combining solid state ^1H - ^{13}C CP/MAS NMR, PXRD and thermo analytical techniques, and they managed to find out the packing pattern of molecules within the gel fibres of esters of cholic acids.¹²⁹ Consequently, this unlocked several advanced and multidimensional solid-state experiments that can now be conducted in the gel state of molecular gels.

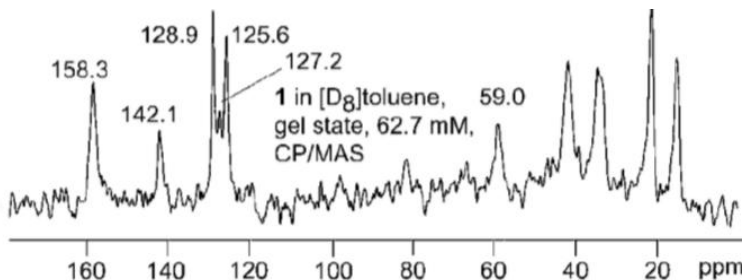


Figure 1.25. First ^1H - ^{13}C CP/MAS NMR spectrum acquired on a wet supramolecular gel of a 1,2-bis-urea derivative toluene-d₈, using an MAS rate of 1.8 kHz and a 400 MHz solid-state spectrometer.¹²³

The potential of nOe-based experiments in the characterisation of molecular gels was recognised by Stupp's group.¹²⁴ They performed 2D NOESY experiments in gels of amphiphilic peptides and the presence of negative nOe enhancements at very low mixing times proved the presence of aggregates and showed close contacts between protons of different amino acids, supporting the conclusion that these molecules co-assembled within the same nanofibre.¹²⁴ Consequently, this enabled more advanced NMR studies on supramolecular gels to be performed, such as 2D ^1H - ^{19}F HOESY.¹³⁴ Afterwards, Mahajan *et al.* (2005) imported into the gel field a ligand-based experiment conducted during protein studies, namely saturation transfer difference (STD) NMR spectroscopy.¹²⁵ They proved the applicability of the technique to molecular gels by determining site-specific interactions between water and the rigid network of supramolecular hydrogels of glutathione.¹²⁵

Some of the studies described before contributed to recognition of MAS in increasing resolution in materials that are not strictly solids by averaging differences in magnetic susceptibility and residual dipolar couplings.¹³⁵ Consequently, a hybrid probe started being developed especially for soft materials in the mid-90s.¹³⁵ It was named high-resolution magic-angle spinning (HR-MAS) NMR spectroscopy. As this powerful methodology was developed, its potential to gain insight into gelation of supramolecular gels was identified in 2008.¹³⁶ Brand *et al.* found a clear relationship between the variation of the diffusion coefficients acquired at variable temperature and the sol-gel transition.¹³⁶ However, they struggled to accurately determine the relaxation times for the different species, mainly due line broadening upon gelation.¹³⁶ Two years later, Iqbal *et al.* (2010) successfully studied the role of the solvent's polarity in the process of supramolecular assembly to unravel the network's mobility.¹¹⁵ In order to overcome the problems initially encountered by Brand *et al.*, their approach involved the use of pulsed-field gradient (PFG) experiments.¹¹⁵ The application of a diffusion filter in the pulse sequence enabled the elimination of undeniable signals from free gelator molecules.¹¹⁵ The comparison between the spectra obtained with and without the diffusion filter therefore allowed the identification of flexible and semi-solid structures.¹¹⁵ The intensity of the signals decreased considerably after the application of the diffusion filter (Figure 1.26a) indicating that the signals observed before (Figure 1.26b) corresponded mainly to free non-aggregated gelator molecules.¹¹⁵ The reduction of peak intensities was more evident for the aromatic protons, suggesting that aliphatic groups were grafted onto the fibres.¹¹⁵

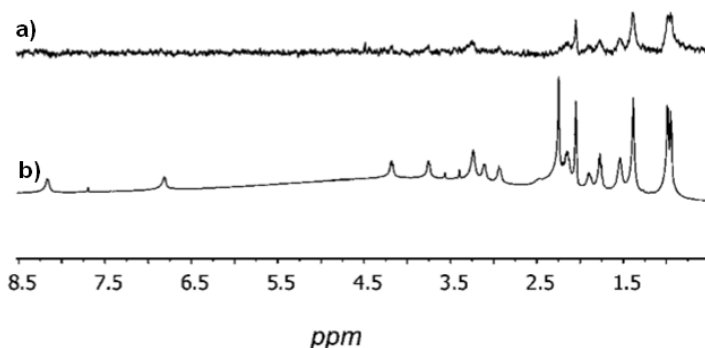


Figure 1.26. ^1H HR-MAS NMR spectra acquired on supramolecular gels **a)** with a 50 % diffusion filter and **b)** without a diffusion filter, using an MAS rate of 4 kHz and a 500 MHz spectrometer.¹¹⁵

This timeline highlighted the metamorphic nature of NMR spectroscopy. The progress in NMR methods and techniques (high field, fast magic-angle spinning (MAS), pulse sequences for high-resolution, sensitivity enhancement techniques for faster acquisition) has given access to the resolution and visibility of structural features, even for complex (soft) materials.¹³⁷ Currently, NMR characterisation of supramolecular gels is very well-established, with the hierarchical levels of self-assembly and the different length scales of organisation being fully described utilising solution, solid-state and HR-MAS NMR spectroscopy. It is the combination of an extended library of NMR experiments that reveals the hidden structure, dynamics, exchange and interactions between gelator, additives and solvent molecules in supramolecular gels.

1.6.8.2. Solid-state NMR Spectroscopy

Solid-state NMR has the ability of probing mobility of molecular regions of gels, since ¹³C experiments are modulated by molecular motions. It is commonplace to combine findings from ¹H-¹³C CP/MAS and single-pulse ¹³C excitation MAS NMR to investigate motionally heterogeneous materials.

¹H-¹³C CP/MAS signals arise from carbons strongly dipolar coupled to protons, typical of rigid structures. Intermediate molecular motions, as those encountered in gels, can affect the cross-polarisation transfer efficiency *via* the motional modulation of ¹H-¹³C dipolar interactions (*ca.* 20–30 kHz), leading to reduction of signal intensity. This loss of signal can provide important information about changes in the local dynamics of the materials, traditionally studied through CP kinetics build-up curves.

Contrarily, single-pulse ¹³C MAS NMR involves direct excitation of ¹³C spins combined with high-power decoupling of protons. Molecular motions ¹H-¹³C dipolar interactions through partial uncoupling of protons from the field. Hence, motions on a similar time scale to the ¹H *r.f.* decoupling field (50–100 kHz) can reduce the efficiency of heteronuclear dipolar decoupling. This is manifested as line broadening of carbon signals and reduced spectral resolution of both ¹H-¹³C CP/MAS and ¹³C MAS NMR spectra.

Regarding fast motions ($\tau_c < 0.01 \mu\text{s}$), these can lead to the complete loss of ¹H-¹³C CP/MAS NMR signals, as they interfere with the cross-polarisation transfer step, and lead to the observation of sharp ¹³C resonances in ¹³C MAS NMR spectra. Since CP becomes

inefficient in the case of the weak dipolar couplings from mobile components, Ramamoorthy and co-workers recently developed an approach to overcome this limitation, combining CP with heteronuclear Overhauser effect (CP-NOE).¹³⁸ They demonstrated enhancement in the signal-to-noise ratio of mobile components, without affecting the signals from rigid structures. This experiment is of high importance for multiphasic and heterogeneous systems, as supramolecular gels.¹³⁸

1.6.8.3. Effect of sample spinning

The use of high spinning speeds during MAS measurements has the potential to cause undesirable effects.¹³⁹ The friction between a spinning rotor and the bearing gas produces localised heating effects on the sample, with the rise in temperature being proportional to the MAS rate.^{135, 139-141} Therefore, the temperature dependence of self-diffusion coefficients¹⁴⁰ and of longitudinal relaxation times¹⁴² becomes a complication. Frictional heating also affects molecular motions, consequently weakening ¹H-¹H dipolar couplings, which is reflected by sharper peaks.¹⁴² These effects should to be compensated for by thorough temperature regulation.¹³⁵

Samples also experience high centrifugal forces (inner pressure), which can cause sample turbulence and structural and motional changes¹⁴² due to vortex effects in higher volume rotors, therefore being preferential the use of smaller volume rotors for semi-solid samples.^{141, 143} Rotor geometry also determines the grade of such effects, hence spherical rotors are preferred.¹⁴⁰ Moreover, variation of chemical shielding is produced by sample spinning due to induced atomic displacements and consequential change in electron density distribution.^{140, 141}

Depending on the nature and physical properties of the sample, namely its intrinsic mobility, molecular dynamics and proton density, these effects can be more or less marked.^{142, 144} For example, the magnitude of their effects are enhanced in soft materials, whereas granular materials can have the stress fields distributed uniformly through the sample.¹⁴¹ Since the samples studied throughout this project were mainly soft materials, these artefacts are important to account for. Viel *et al.* (2008) studied thoroughly the effect of MAS on diffusion measurements of liquids, which are considered model systems to understand the impact of centrifugal forces on soft materials.¹⁴⁰ They showed how rotor

volume and spinning rate affected the self-diffusion coefficient, with more accurate and reliable results being achieved with small active volume rotors (12 μL) and MAS rates in the range of 3 and 4 kHz.¹⁴⁰

1.6.8.4. High-resolution magic-angle spinning

The popularity of HR-MAS rapidly rose for biological and biomedical applications, due to the heterogeneous nature of cells and soft tissues, being currently highly recognised in metabonomic studies and identification of abnormal tissues (*i.e.* cancerous tissues).¹³⁵ The potential of HR-MAS NMR spectroscopy in material science, especially for the analysis of soft materials, was recognised by Shapiro and Keifer.^{145, 146} Its application was focused initially on the analysis of solvent swollen solid-phase synthesis or combinatorial solid-phases, by increasing mobility of the attached ligands.¹³⁵

However, it were Iqbal *et al.* (2010) who successfully showed the ability of HR-MAS in differentiating molecular mobility regimes in supramolecular gels.¹¹⁵ Despite being mainly used to determine apparent self-diffusion coefficients, PFG HR-MAS experiments can also take advantage of selective filtering to remove unwanted signals (as for solvent suppression) or to separate motional regimes due to their different translational diffusion.^{115, 135} Iqbal *et al.* applied this filter to ^1H HR-MAS experiments to eliminate signals from isotropic free gelator molecules overlapped with broad lines from the gel network (Figure 1.26).^{115, 118} This is called diffusion-filtered HR-MAS NMR and enables direct observation of the slower diffusing components grafted onto the network.^{115, 140} Hence, PFG HR-MAS can be used to probe semi-solid components at the interfaces between the hydrogel fibres and the pools of water.

1.6.8.5. Effect of MAS on diffusion measurements

HR-MAS D values differ from those calculated from solution-state experiments, since diffusion of molecules is affected by sample rotation and frictional heating.¹⁴⁰ Viel *et al.* (2008) thoroughly studied the effect of MAS on diffusion measurements of liquids, which are considered model materials to understand the impact of centrifugal forces on gels.¹⁴⁰ They showed how rotor volume and spinning rate affected the self-diffusion coefficients,

having more accurate and reliable results with small active volume rotors (12 μL) and MAS rates in the range of 3 and 4 kHz. They also concluded that these effects were dependent on the viscosity and physicochemical properties of the sample, without a linear correlation.¹⁴⁰ Hence to achieve quantitative measurements, calibration of the MAS rate should be performed with a substance of known diffusivity using pulse sequences with rotor synchronisation.¹⁴⁰

1.6.8.6. Solution-state NMR spectroscopy

1.6.8.7. NMR “visible” *vs.* “silent” molecules

NMR is sensitive to local molecular environments and conformational variations, frequently translated by changes in chemical shifts. Hence, ^1H NMR spectral variations, *i.e.* differences in peak intensities, line broadening (quantified through the measurement of full peak width at half maximum) and chemical shifts, can serve as an indication of the degree of incorporation of free molecules into the rigid components of gels.¹⁴⁷ Supramolecular gelation starts with aggregation of fast isotropic molecules into larger and less mobile structures, resulting in gradual formation of rigid components which are “silent” in ^1H solution-state NMR spectra, due to their short transverse relaxation times, strong dipolar couplings and chemical shift anisotropy.^{147, 148} As gelation occurs, very sharp and intense peaks (from the averaging of homonuclear dipolar interactions in isotropic environments) gradually become broader and less intense.¹⁴⁷ Since gelator molecules can keep enough thermal motion in the gel to provide a ^1H NMR signal, spectra of molecular gels have characteristic features, as decreased peak intensity, broadened peaks and chemical shift variation in comparison with the corresponding solutions.^{50, 147}

^1H NMR is a quantitative analytical method and hence it allows determining the ratio between molecules dissolved in solution and molecules forming the rigid gel network, by measuring peak intensity and consequently determining the concentration of NMR “silent” *vs.* “visible” gelator molecules in solution-state NMR spectra. Peak intensities from ^1H NMR spectra can be correlated with the concentration of diluted species when long enough recycle delays are applied. This can be used to derive the ratio between gelator molecules in the isotropic phase and solution-state NMR “silent” molecules forming the rigid fibres of supramolecular hydrogels.¹⁴⁸ The information obtained can

only give a rough idea of the ratio between isotropic and rigid molecules, as exchange occurs between both states.^{147, 149} This dynamic behaviour has been described by Escuder *et al.* (2006) for valine-based organogels (Figure 1.27).¹⁴⁷ The authors discussed various equilibria between free gelator molecules and oligomeric aggregates in solution, in the light of the time scales of different NMR experiments.¹⁴⁷ Peak intensity is therefore highly dependent on the rate of exchange being faster or slower than the NMR frequency time scale.⁵⁰ The phenomenon of solution-state NMR spectra containing information from the hydrogel fibres due to fast molecular exchange between solution and gel states has been described previously.^{148, 149} The dynamic character of supramolecular hydrogels is an advantageous feature, as molecules bound onto the surface of the fibres carry information from the network when returning to solution.

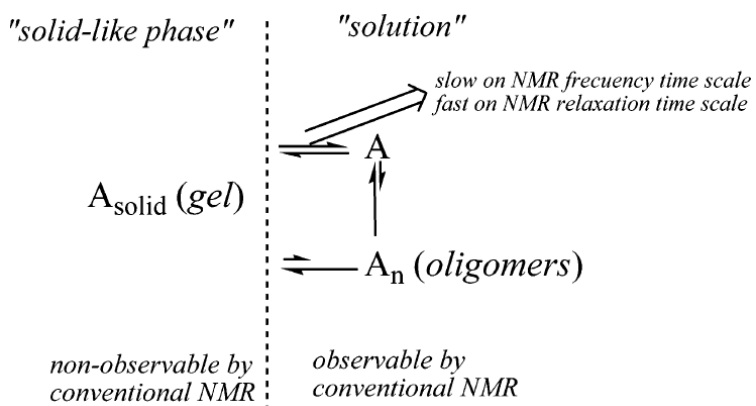


Figure 1.27. Distinction between observable and non-observable species on the different solution-state NMR time scales.¹⁴⁷

Conventionally, NMR studies of gels focus on the study of chemical shifts, intensity of signals and relaxation times at variable composition, concentration or temperature.⁵⁰ These titration experiments provide information regarding the involvement of functional groups in intermolecular interactions through the degree of variation of their chemical shift throughout aggregation processes.⁵⁰

1.6.8.8. Determination of thermodynamic parameters

Van't Hoff treatment of solubility data, determined from ^1H NMR peak intensities acquired at variable temperature, allows the derivation of thermodynamic parameters, such as enthalpy of dissolution, a value which reflects the enthalpic cost of disrupting the favourable gelator-gelator interactions and the enthalpic gain from newly formed solvent-gelator interactions.^{45, 46, 150} For an ideal solution, the solubility (sol) at a given temperature can be expressed by the van't Hoff equation:

$$\ln(\text{sol}) = \left(-\frac{\Delta H_{\text{diss}}}{RT}\right) + \left(-\frac{\Delta S_{\text{diss}}}{R}\right) \quad \text{Equation 1.1}$$

where ΔH_{diss} is the molar enthalpy and ΔS_{diss} is the molar entropy for the dissolution process (*i.e.*, gel-to-solution transformation), T is the equilibrium temperature and R is the ideal gas constant. The resulting van't Hoff plot of $\ln(\text{sol})$ *vs.* $\frac{1}{T}$ can be used to calculate H_{diss} and ΔS_{diss} , therefore the solubility at different temperatures can be determined.¹⁵⁰ The analysis of these parameters allows determining and comparing whether self-assembly of a certain gelator molecule in a certain solvent is an energetically favourable process. As a fraction of the solute is NMR "silent", the concentration calculated from NMR parameters corresponds to the maximum solubility of the gelator with temperature.¹⁵¹ This analysis should be conducted at concentrations higher than CGC and temperatures lower than T_{gel} in order to circumvent initial stages of aggregation.⁵⁰ A limitation of this approach is assuming that an ideal solution is obtained, which is not totally accurate, as increasing temperature leads to a sol with dispersed aggregates. Moreover, peak intensity of these dynamic materials is highly dependent of the rate of gel/solution exchange. As a result, significant differences have been noted between NMR and calorimetry determined thermodynamic parameters.^{50, 150}

1.6.8.9. NOESY

NOESY solution-state NMR experiments are able to provide reliable information on spatial connectivities between molecular regions of supramolecular gels, mainly regarding the gel structure.¹²³ This technique relies on the nuclear Overhauser effect (nOe), which is a through-space manifestation of the dipolar coupling between protons in close proximity ($< 5 \text{ \AA}$).¹⁵² Quantitative measurements have been optimised for organic

molecules tumbling isotropically in non-viscous solvents, *i.e.* in the fast tumbling regime.¹⁵³ Hence, the nuclear Overhauser effect can be used to measure interproton distances, but its accuracy suffers from the contribution of spin diffusion in macromolecules.¹⁵³ In the case of supramolecular gels, strong ¹H-¹H dipolar couplings lead to spin diffusion, making these slow tumbling, small molecules acquire the kinetic features of medium-to-large molecules (therefore appear as negative cross-peaks in NOESY spectra), which transfer magnetisation efficiently through dipolar interactions.¹⁴⁸ To overcome these limitations, the initial rate approximation approach is applied to derive quantitative information from kinetic nOe measurements (this topic is discussed in Chapter 2, section 2.3.16.3, page 116). It is important to note that, even in the case of large molecules, the present tendency is to use NOESY data more quantitatively.¹⁴⁸

1.6.8.10. Saturation transfer difference NMR spectroscopy

In 1999, Mayer and Meyer described a technique capable of not only identifying ligands bound to a protein, but also to construct the ligand's binding epitope, a method they termed STD NMR.¹⁵⁴ In 2005, Mahajan *et al.* reported the use of STD NMR in the study of supramolecular gels with the purpose of identifying molecular moieties affected by gelation processes in hydrogels of glutathione upon saturation of the water peak.¹²⁵ Currently, the potential of STD NMR in the studies of supramolecular gels has been recognised.^{125, 149, 155, 156}

For amino acid-based hydrogels, the network is considered as the supramolecular entity that can be saturated selectively. Such saturation might then be transferred *via* nOe throughout the network and finally intermolecularly passed over to the bound gelator molecules. Dissociation of the weakly bound molecules from the network into the pools of water results in accumulation of saturation in the isotropic solution phase for molecules that exchange faster than their relaxation rates (Figure 1.28). This accumulation occurs due to the much longer longitudinal relaxation times for unbound fast tumbling molecules than for bound slow tumbling molecules.¹⁵⁷ In this way, the STD difference spectrum will only exhibit signals of protons of gelator molecules that, being in solution, have been in contact with (and hence received saturation from) the fibrous network.¹⁴⁹

This relationship can be reflected when considering an analogous dependence of the fractional STD response with concentration as in the case of protein-ligand (PL) studies:

$$\eta_{\text{STD}} = \frac{I_{\text{STD}}}{I_0} = \alpha_{\text{STD}} \frac{[\text{PL}]}{[\text{L}]_{\text{T}}} = \alpha_{\text{STD}} \frac{[\text{Net-G}]}{[\text{G}]_{\text{T}}}, \quad \text{Equation 1.2}$$

where η_{STD} is the fractional STD response, I_{STD} is the signal intensity from the difference spectrum and I_0 is the signal intensity from the off-resonance spectrum. It was considered that the concentration of the network-bound gelator, $[\text{Net-G}]$, and the total gelator concentration, $[\text{G}]_{\text{T}}$, were equivalent to the concentration of protein receptor-ligand complex, $[\text{PL}]$, and the total ligand concentration, $[\text{L}]_{\text{T}}$, respectively.¹⁵⁸

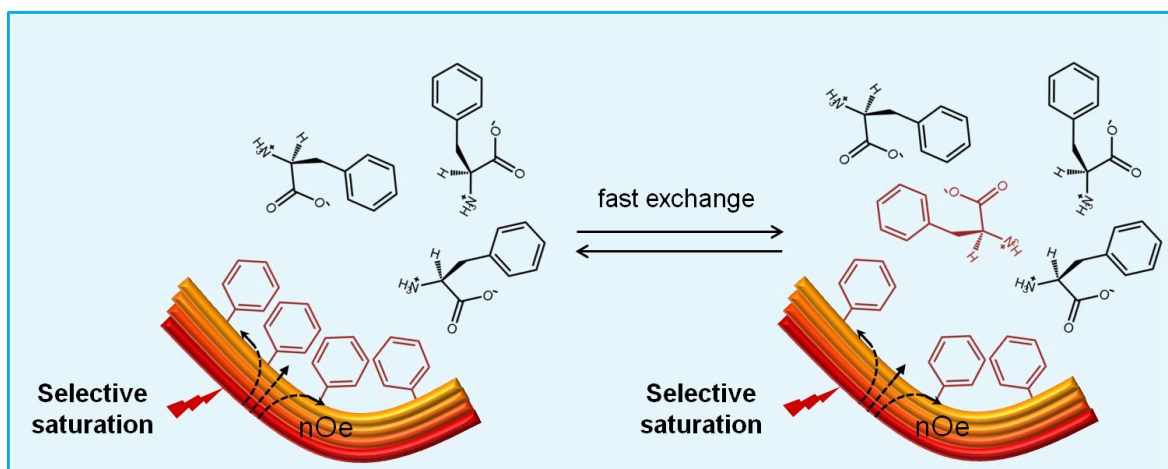


Figure 1.28. Proposed mechanism for transfer of saturation in STD NMR experiments performed with supramolecular hydrogels. Gelator molecules forming the network (bound state, left) are in fast exchange with those in the bulk solution phase (free state, right), allowing accumulation and detection of saturation in solution.

1.6.8.11. Summary

Only the combination of solution, solid-state and HR-MAS NMR experiments is capable of providing the in-depth understanding of such complex, multiphasic soft materials (Figure 1.29). CP/MAS solid-state NMR experiments can be used to detect the solid-like fibrous components, whereas PFG HR-MAS NMR experiments may be performed in order to investigate molecules at the fibre-solution interfaces with intermediate frequencies of motion. Furthermore, characterisation of spectral variations from solution-state NMR experiments and longitudinal relaxation measurements throughout the gel-to-

solution transitions can be carried out to describe structure and dynamics of species in solution. Finally, STD NMR experiments assess exchange phenomena at the gel/solution interfaces, with particular potential for the identification of the role of each molecule in the processes of self-assembly of multi-component materials.

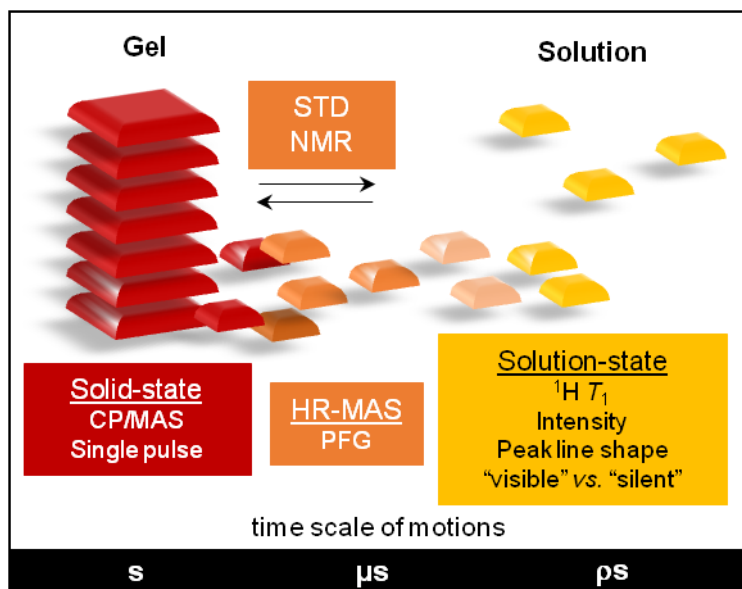


Figure 1.29. Schematic representation of the application of NMR methods to probe different time scales of motions and self-organisation in supramolecular materials at variable length scales.

1.6.9.NMR crystallography

Since the year of 2000 there has been rapid progress within the field of NMR crystallography.¹³² This methodology encompasses the combination of diffractometry, NMR spectroscopy and first-principles calculations (Figure 1.30). It achieves a more efficient structure search and provides a more accurate structural model than using these techniques independently.¹³⁷ Structure determination encompasses the sequential steps of determining unit cell parameters of one (or a set of) space group in agreement with the observed reflections, building an approximate model from these data and, finally, refining the developed model.¹¹³ Accurate knowledge of the structure of crystalline materials is essential for better understanding and monitoring of their properties.¹¹³

The nature of molecular and supramolecular interactions in the solid state is often investigated using isolated diffraction techniques, as single-crystal and powder X-ray powder diffraction, small-angle X-ray scattering or small angle neutron scattering

analysis.¹³² Since for single-crystal XRD measurements it is required to have large, stable and good quality crystals, when this not possible, structure determination is conducted on polycrystalline powders, named powder XRD.¹³⁷ Unfortunately, the presence of an ensemble of small crystals with their own orientation is a major disadvantage for the determination of crystal structures from the resulting data set.¹³⁷ Regarding supramolecular gels, their inherent disorder fails to form suitable crystals and gives rise to broader diffraction peaks, which makes structure determination considerably more challenging.¹³²

Solid-state NMR spectroscopy overcomes these requirements of strict periodicity and crystal size and provides a unique opportunity to study crystals that are not necessarily periodic, that might have local disorder or mobility. Examples include less crystalline materials, amorphous powders and gels, making it an emerging and highly complementary technique to diffraction studies.^{113, 132, 137} Currently, solid-state NMR is used to refine diffraction results, occasionally enabling the solving of crystal structures with minimal diffraction data.¹⁵⁹ As NMR spectroscopy is sensitive to the local environment of atoms, the same atom in different molecules of an asymmetric unit will display different chemical shift values. Hence these values can immediately show the number and multiplicity of crystallographically non-equivalent positions in the asymmetric unit.^{113, 137, 160} NMR also provides information on intermolecular distances, through-space proximities or through-bond connectivities.¹¹³ The possibility of correlating chemical shifts and tensor components with the crystallographic location of atoms in the unit cell transformed NMR into an essential technique in accurate structure determination.^{113, 159}

Molecular modelling created a bridge between diffraction techniques and NMR. Rietveld refinement consists on performing small variations of the atomic coordinates in order to provide the best match to powder diffraction patterns.¹³⁷ The strength of NMR crystallography comes from allying the previous techniques to first-principles calculations, which altogether provide accurate calculation of NMR parameters and enable linking structural data to solid-state NMR observables.^{137, 161} In order to calculate NMR parameters of a solid a 3D model of a structure is necessary, from which the fundamental NMR interaction tensors can be derived. These models can be generated

from diffraction data. This is particularly important for materials that are disordered, lack periodicity or present dynamic behaviour.¹⁶⁰

Single molecule density functional theory (DFT) calculations are performed to investigate the electrostatic potential around molecules which can be mapped on the Hirshfeld surface.^{82, 108} Henceforth, the molecular geometry of each molecule can be optimised with DFT.¹⁰⁸ CASTEP¹⁶² is a quantum mechanical software program based on DFT with a plane wave basis set able to calculate NMR parameters from crystal structures, hence generating ¹³C chemical shift values.^{108, 160} These are mostly used as a validation step from diffraction data or from CSP methods.¹¹³ The isotropic NMR shieldings computed with CASTEP are converted to chemical shifts using the following equation, $\sigma_{calc} = \sigma_{iso} - \sigma_{ref}$, where σ_{iso} is the isotropic chemical shielding generated from first-principles calculations and σ_{ref} is chosen as the zero intercepts of the fits of the calculated shieldings *vs.* experimental chemical shifts plot.⁸² The software uses the information from these chemical shielding tensors to test simulated trial structures from DFT calculations for compatibility. If a good agreement is found between the calculated and experimental data, this is a great contribution for confidently determining crystal structure. Even though first-principles computations are most accurate when calculating precise structures, this approach has proven successful in surfactant-templated silicate frameworks without 3D periodicity.¹⁶¹ DFT calculation of NMR parameters of molecular solids is becoming a well-established technique.¹³⁷

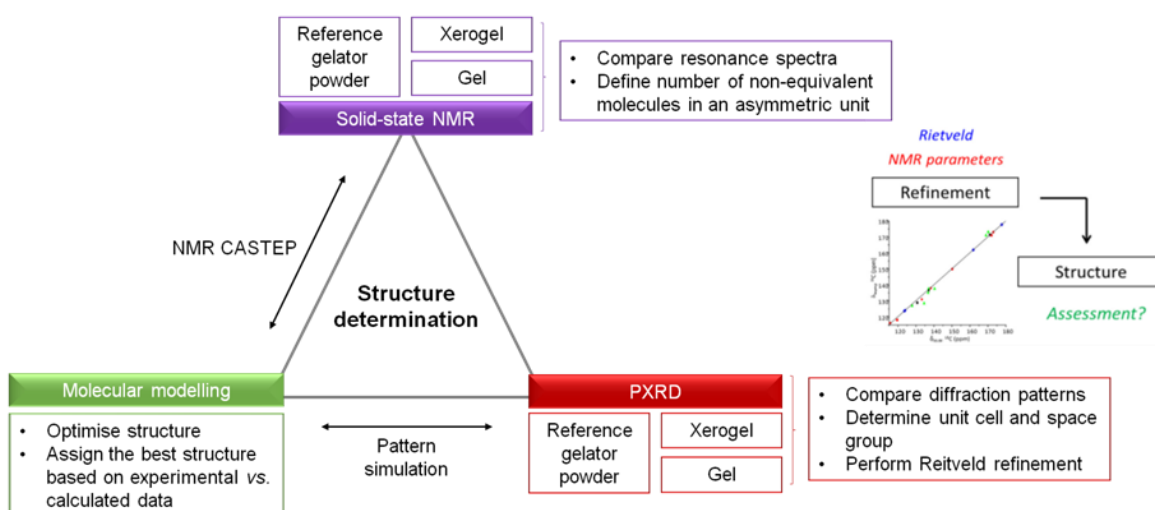


Figure 1.30. Complimentary techniques used in NMR crystallography studies of supramolecular gels, adapted from references ^{132, 137}. Rietveld refinement consists of performing small variations of the atomic coordinates in order to provide the best match to powder diffraction patterns.¹³⁷

1.7. Aims of the project and associated challenges

Currently, it is still difficult to predict whether a molecule will give rise to a gel, crystallise or precipitate. The field of supramolecular gelation is still an empirical science because of the challenges associated with their full characterisation, which pose a significant methodological and experimental challenge. Furthermore, this is an inter-disciplinary field that requires expertise in supramolecular chemistry, crystallisation theory, advanced characterisation methodologies, rheology and crystallography. The current work addresses an important knowledge gap in the field, as it attempts to optimise the existing analytical tools and utilise them for less conventional applications, with the purpose of understanding structure and dynamics of soft fibrillar materials at different length scales and mobility regimes.

The serendipitous nature of the discovery of new gelator molecules can also be explained by the fact that other factors besides molecular structure condition the outcome of gelation (similarly to crystallisation), as self-assembly pathways and solvent properties. To gain control of the properties of the gel materials and to tune them for specific applications, fundamental understanding of the mechanism of formation of tridimensional molecular networks is essential. Due to their biomedical relevance as matrices for cellular growth, tissue engineering and targeted drug delivery, I proposed myself to study the consequences of incorporating modifications to the molecular structure or introducing a variety of structurally diverse additives on the self-assembly mechanisms and bulk properties of the resulting gels. The presence of several molecules (gelator, solvent and additives) co-existing in multi-component gels entails complex and dynamic interaction patterns.

In addition, supramolecular gels are not conventional solids or liquids. From a characterisation point of view, these materials are challenging to analyse due to their heterogeneous nature, in which very rigid solid components are in equilibrium with a dynamic and highly mobile solution phase. Henceforth, gaining complete understanding of morphology, dynamics and supramolecular organisation of these systems requires the use of several complementary analytical techniques able to probe the existing time scales of molecular motions. While bulk properties can be assessed using rheology and differential scanning calorimetry, morphologic features may be examined using

microscopy, and supramolecular packing motifs of the fibres can be investigated using X-ray diffraction and computational techniques.

In the present project, more emphasis is given to NMR spectroscopy, due to its proven ability to detect a wide range of mobility regimes. The heterogeneous character of these materials requires the application of solid, solution-state and HR-MAS NMR techniques. The existence of solid structures in the gel matrices (which are anisotropic and strongly dipolar coupled) entails the use of magic-angle spinning. Centrifugal forces can introduce changes to these soft materials; the degree of modification being dependent on the strength of the intermolecular interactions and the viscoelastic properties of the gel. In order to avoid the introduction of spinning artefacts, solid-state NMR experiments can be performed on dry gel samples, which enable faster acquisition and detection of well-resolved spectra. However, any conclusions drawn have to be validated by measurements conducted on wet gel samples, as drying might lead to collapse and reorganisation of the network, variation of the dissolved/non-dissolved equilibrium and modification of molecular mobility. Moreover, careful interpretation of the NMR data is required due to the dynamic character of supramolecular gels, characterised by the exchange processes occurring at the fibre/solution interfaces. Depending on the gel properties and on the time scale of the experiment, this exchange might lead to the observation of an averaged value that reflects a variety of motionally-averaged molecular environments. In summary, interpretation of the NMR data acquired on molecular gels is expected to be challenging, but the presence of a wide range of motionally diverse environments opens opportunities to conduct more advanced NMR experiments.

In conclusion, the main purpose of this work is to gain molecular level understanding of model single and multi-component supramolecular materials, in parallel with the development, validation and optimisation of NMR-based protocols for the complete characterisation of supramolecular soft materials. The applicability and limitations of each technique in the study of this particular type of dynamic multiphasic soft solids will be assessed. Common gelation factors relevant to several gel systems are expected to be identified and to contribute to the elucidation of some of the fundamental intermolecular interactions associated with the formation of supramolecular fibrillar gels. These findings might help determine which factors favour gelation over crystallisation, which is particularly important when predicting the outcomes of self-organisation processes.

Chapter 2

2. Characterisation techniques

This chapter summarises the theory behind the various analytical techniques used to characterise supramolecular gels, solids and solutions. The experimental conditions used for each technique are discussed in Chapter 3 (page 120).

2.1. Rheology

Rheology is the study of the response of materials when shear stress deformation is applied.^{11, 163} Upon the application of mechanical stress, the material can flow or resist, depending on its inelastic or elastic nature, respectively. According to Newton's law, the relationship between stress (σ), strain (γ) and viscosity (η) is given by

$$\eta = \frac{\sigma}{\gamma} \quad \text{Equation 2.1}$$

where stress is the force (F) applied *per* unit of surface area (A), $\sigma = F/A$, and strain is a unitless parameter quantifying the extent of deformation after the application of stress.¹¹

Since viscoelastic materials show time dependence, dynamic (sinusoidal) deformation is used to study their viscoelastic behaviour by the application of an oscillatory strain with a frequency ω .¹⁶³ The dependence of stress and strain in these oscillatory experiments can be expressed as

$$\text{Strain, } \gamma = \gamma_0 \sin(\omega t) \quad \text{Equation 2.2}$$

$$\text{Stress, } \sigma = \sigma_0 \sin(\omega t + \delta) \quad \text{Equation 2.3}$$

where t is time.¹⁶³ The angle formed between the phases of stress and strain is referred to as the phase angle, δ (Figure 2.1), and reflects the viscoelasticity of the material.^{11, 43} Purely elastic materials, as ideal Hookean solids, have stress and strain in phase, therefore creating a phase angle of 0° .^{11, 43} Contrarily, ideal Newtonian liquids exhibit values of 90° .^{11, 43} The relationship between stress and strain is dependent on the complex modulus (G^*), a quantitative measure of the material's stiffness or resistance to deformation,

$$\sigma = G^* \gamma$$

Equation 2.4

The complex modulus is composed of the storage (G') and loss (G'') moduli,

$$G^* = G' + iG''$$

Equation 2.5

where i is the imaginary number $\sqrt{-1}$.¹⁶³ The storage modulus reflects the elasticity of the material, while the loss modulus reflects the amount of energy lost from the system by non-elastic behaviour.^{43, 163} These moduli components can be conveyed in terms of the phase angle as

$$G' = G^* \cos \delta$$

Equation 2.6

$$G'' = G^* \sin \delta$$

Equation 2.7

therefore the tangent of the phase angle can give the ratio of loss to storage moduli

$$\tan \delta = \frac{G''}{G'}$$

Equation 2.8

For robust gels, an order of magnitude difference between G' and G'' values is expected,

$$\frac{G''}{G'} \sim 0.1.$$
^{11, 28, 49}

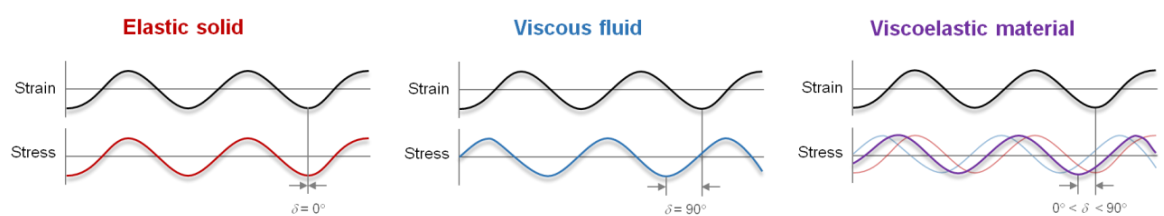


Figure 2.1. Schematic stress response to oscillatory strain deformation for an elastic solid, a viscous fluid and a viscoelastic material, where δ is the phase angle. Adapted from reference ¹⁰¹.

2.2. Elastic scattering techniques

Scattering techniques allow indirect measurement of the tridimensional organisation of materials as a result of the scattering of an incident wave by the electrons of a crystal. Depending on the wavelength and the angle of incidence, information on local or long range ordering can be achieved.^{164, 165} Atomic periodicities with long repeat distances cause diffraction at small angles, while short repeat distances from small interplanar spacings cause diffraction at high angles (X-ray crystallography).^{164, 165}

2.2.1. Wide-angle scattering and X-ray crystallography

X-ray crystallography measures the scattering of an incident wave to wider angles (usually 2θ values higher than 5°), which implies they are caused by sub-nanometer-sized structures. From the angles and intensities of these diffracted beams, a picture of the density of electrons within the crystal can be determined, which in turn can help the precise definition of unit cell parameters to solve crystal structures (single-crystal X-ray diffraction) or to identify different crystalline or amorphous materials (powder X-ray diffraction).⁹⁷

X-rays have wavelengths in the range of 0.01 to 10 nm, therefore they induce movement of electrons in the electronic clouds due to their nanometre scale size. Electrons diffract and re-irradiate X-ray waves that have the same frequency, giving rise to scattering of the original wave (Figure 2.2).^{97, 164, 165} Constructive or destructive interference can occur along different directions as waves are scattered by atoms of different types and positions. There is a profound geometrical relationship between the directions of waves that interfere constructively, which comprise the diffraction pattern, and the crystal structure of the material. A crystal can be thought of as an infinite 3D lattice of atoms (points) repeating periodically in all three dimensions. Atoms aligned in a particular pattern can be seen as forming small boxes, designed as unit cells, of which the lattice is comprised.⁹⁷

^{164, 165}

A crystalline solid can be defined by its symmetrically arranged plane surfaces, intersecting at characteristic angles. Crystalline materials have a 3D disposition of atoms that gives rise to constructive interference through satisfaction of the Bragg's model of diffraction. Bragg's Law treats crystals as built from planes of atoms acting as semi-transparent mirrors (Figure 2.2),

$$2d \sin \theta = n\lambda \quad \text{Equation 2.9}$$

where n is the order of the beam, λ is the wavelength of the X-ray beam, d is the distance between adjacent planes and θ is the angle of incidence of the X-ray beam. d -spacings are calculated using known values of λ and θ .^{97, 164, 165} The resulting diffraction pattern of X-rays typically contains many distinct peaks, each corresponding to a different interplanar spacing, d . This unique pattern is a "fingerprint" for that solid.⁹⁷

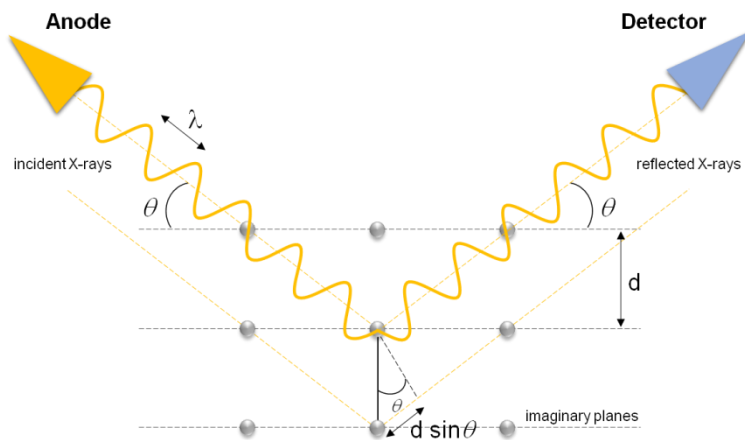


Figure 2.2. Geometry for interference of a scattered wave, needed to derive Bragg's Law. The dashed lines are parallel to the crests of the incident and diffracted wavefronts. The angle of incidence of the two parallel rays is θ . The interplanar spacing, d , sets the difference in path length for the ray scattered from the top plane and the ray scattered from the bottom plane. This difference in path lengths is $2d \sin \theta$. Constructive wave interference (and hence strong diffraction) occurs when the difference in path length for the top and bottom rays is equal to one wavelength (λ), $2d \sin \theta = n\lambda$ (Bragg's law). Adapted from reference ¹⁶⁶.

2.3. Nuclear magnetic resonance spectroscopy

Nuclear magnetic resonance (NMR) spectroscopy relies on the interaction of nuclei with angular momentum, referred to as nuclear spins, with oscillating radiofrequency electromagnetic fields. The results can provide detailed information regarding structure and dynamics of a variety of materials. The complexity of NMR spectroscopy requires bringing together quantum mechanics, product operator formalism and the vector model to understand NMR experiments. Despite this, a semi-classical approach will be used to explain NMR concepts.

2.3.1. Basic NMR principles

The nuclear magnetic moment is the magnetic moment of nuclei that possess the intrinsic property of angular momentum, often referred to as nuclear spin. The magnetic moment ($\vec{\mu}$) of a nucleus is given by

$$\vec{\mu} = \gamma \hbar \vec{I} \quad \text{Equation 2.10}$$

where γ is the gyromagnetic ratio of the nucleus, \hbar is the Planck's constant divided by 2π and \vec{I} is the spin angular momentum.¹⁶⁷⁻¹⁷⁰ To be magnetically active, the quantum number

(I) of the spin angular momentum must be $I \neq 0$ ($I = \frac{1}{2}, 1, \frac{3}{2}, 2$, etc.). Both angular momentum and magnetic moment are vector quantities, as they have magnitude and direction.¹⁶⁷⁻¹⁷⁰

Table 2.1. Properties of nuclei spin $I = \frac{1}{2}$ used throughout the project.¹⁷¹

Spin	$\gamma / 10^7 \text{ rad s}^{-1} \text{ T}^{-1}$	Isotopic abundance / %
¹ H	26.75	99.99
¹⁹ F	25.18	100
¹³ C	6.73	1.11
¹⁵ N	-2.71	0.37

2.3.2. Hamiltonian operators

The Hamiltonian operators (\hat{H}) represent the energy present in the system and generally provide a quantum mechanical description of the possible interactions between nuclear spins and magnetic field.^{168, 170} These quantum mechanical terms are described by two components: the spin angular momentum operator component (\vec{I}) and the geometric component (A),

$$\hat{H} = \vec{B} A \vec{I} \quad \text{Equation 2.11}$$

where A is the orientation dependence of the NMR interaction, \vec{I} is the spin term and \vec{B} is the magnetic field. The spin angular momentum operator represents the x , y , and z components of the magnetization along the axis, I_x, I_y, I_z . The secular approximation is often made with the purpose of simplifying the Hamiltonians, and retains only the component parallel to the z -axis.¹⁶⁸ The geometric component contains the spatial variation of the interactions regarding the external field.^{168, 170}

The quantum mechanical description of the energy of all nuclear spin interactions which may contribute to the observed line widths in the NMR spectrum are implemented in the spin Hamiltonian equation,

$$\hat{H}_{\text{TOTAL}} = \hat{H}_Z + \hat{H}_{\text{CS}} + \hat{H}_J + \hat{H}_D + \hat{H}_Q \quad \text{Equation 2.12}$$

where \hat{H}_Z is the Zeeman interaction Hamiltonian, \hat{H}_{CS} is the chemical shielding Hamiltonian, \hat{H}_J is the scalar coupling Hamiltonian, \hat{H}_D is the dipolar coupling Hamiltonian and \hat{H}_Q is the quadrupolar coupling Hamiltonian (observed only if $I > \frac{1}{2}$).¹⁶⁸

Table 2.2. Strength of interactions affecting line widths in NMR spectra and their impact in spectra of liquids and solids.¹⁷²

Interaction	Symbol	Size / Hz	Properties in liquids	Properties in solids
Zeeman	\hat{H}_z	$10^7 - 10^9$	Present	Present
Chemical shielding	\hat{H}_{CS}	$10^2 - 10^5$	Isotropic	Anisotropic
Scalar coupling	\hat{H}_J	$10^0 - 10^3$	Isotropic	Anisotropic
Dipolar coupling	\hat{H}_D	$10^3 - 10^5$	Absent	Anisotropic
Quadrupolar coupling	\hat{H}_Q	$10^3 - 10^7$	Absent	Anisotropic

2.3.3. Zeeman interaction Hamiltonian

The Zeeman interaction Hamiltonian (\hat{H}_z) describes the energy of each spin according to its orientation regarding an external magnetic field (B_0), arbitrarily chosen to be oriented along the z -axis,

$$\hat{H}_z = -\mu_z B_0 = -\hbar\gamma B_0 m_I \quad \text{Equation 2.13}$$

where m_I is the spin's magnetic quantum number, taking $2I + 1$ values in integer steps between $+I$ and $-I$ with a selection rule of $\Delta m_I \pm 1$, according to quantum mechanics.^{168, 170} Without the presence of an external magnetic field, magnetic moments are randomly orientated, with all orientations ($2I + 1$) having the same energy. Under the presence of an external magnetic field, the energy levels of the nucleus are then split into $2I + 1$ non-degenerated levels, which are separated by an energy difference (ΔE) proportional to the applied field and the gyromagnetic ratio.^{168, 170}

My work will only focus on the study of spin-half nuclei, whose interaction with the magnetic field gives rise to two energy levels. Spins with half-integer quantum number, $I = \frac{1}{2}$, have two possible orientations, either parallel ($m_I = +\frac{1}{2}$ or α -state) or antiparallel ($m_I = -\frac{1}{2}$ or β -state) with regards to the external magnetic field. Spins in the α -state are oriented along B_0 , hence these are in a lower energetic level than spins in the β -state (Figure 2.3).^{168, 170} The separation into the possible energy levels is called Zeeman splitting. The difference between these two levels (ΔE) is very small but measurable, justifying the terminology of spectroscopy,

$$\Delta E_{\alpha, \beta} = \hbar\omega_0 \quad \text{Equation 2.14}$$

where ω_0 is the spin's rate of nuclear precession around the external magnetic field, termed Larmor precession.^{168, 170, 171}

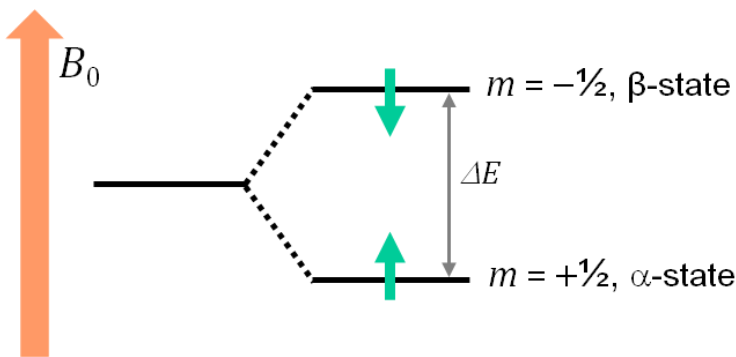


Figure 2.3. Relative nuclear energy levels of α and β -states of a spin $1/2$ caused by an external magnetic field (B_0), designated as Zeeman splitting. Adapted from reference ¹⁷¹.

2.3.4. Bulk magnetisation vector

Quantum mechanics tells us that the magnetic moment can be aligned in any direction. If all the magnetic moments present pointed towards random directions, then the small magnetic fields individually generated would cancel each other out and there would exist no net magnetisation.^{168, 170, 175} However, nuclear spins placed in an external magnetic field, at a certain temperature, achieve thermal equilibrium according to the Boltzmann distribution,

$$\frac{n_{+1/2}}{n_{-1/2}} = e^{\frac{\Delta E}{kT}} \quad \text{Equation 2.15}$$

where k is the Boltzmann constant, T is the absolute temperature and n is the population of spins in different states.^{168, 170, 175} At equilibrium, the magnetic moments are not aligned randomly as there is an extremely small excess of spins in the α -state in comparison with the β -state. This small difference gives rise to the net magnetisation aligned along z -axis which is called bulk magnetisation (M_0). This magnetisation can be represented by a vector, called the magnetisation vector, pointing along the direction of the applied field (z), as shown in Figure 2.4.¹⁷¹ The axis system frequently used is a right-handed set.^{168, 170, 175}

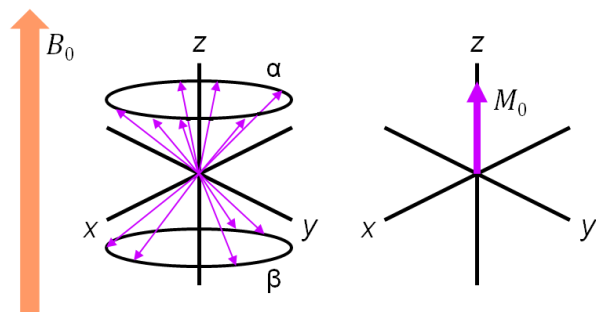


Figure 2.4. The external static magnetic field causes nuclear spins to precess around the z -axis, represented as a vector moving on the surface of a cone (left). Vector model of bulk magnetisation for spin $\frac{1}{2}$ nuclei, where the excess in populations of spins in the α -state states give rise to bulk magnetisation (M_0) aligned along the external magnetic field (B_0). Adapted from reference ¹⁷¹.

2.3.5. Larmor precession

The effect of a static field on the magnetic moment of a nuclear spin can be described in terms of classical mechanics.¹⁶⁸⁻¹⁷⁰ Any spin placed in an external magnetic field experiences a torque, which acts on the magnetic moment and promotes circular movement about the direction of the magnetic field (Figure 2.4).¹⁶⁸⁻¹⁷⁰ The resulting magnetisation vector is said to precess about B_0 , hence this particular motion is known as Larmor precession, which is characterised by the Larmor frequency (ω_0),

$$\omega_0 = \left| \frac{\gamma}{2\pi} \right| B_0. \quad \text{Equation 2.16}$$

This motion is specific to each type of nucleus and its direction is determined by the sign of γ .¹⁶⁸⁻¹⁷⁰ It is named after Sir Joseph Larmor, a brilliant theoretical physicist and mathematician who discovered and proved the existence of nuclear precession. Throughout his work, he made major contributions to the understanding of matter, electricity and thermodynamics.¹⁷³

2.3.6. Pulsed NMR

In any NMR experiment, there is detection of the precession of the magnetisation vector by a small coil of wire around the sample, with the axis of the coil aligned in the xy -plane. The coil detects the decay of the x -component of the magnetisation, called free induction signal.¹⁶⁸⁻¹⁷⁰

Electromagnetic radiation (*r.f.* pulses) oscillating at the Larmor frequency is applied in NMR spectroscopy to measure a variety of nuclear properties. This oscillating current creates an oscillating magnetic field along the direction of the applied field, called the *r.f.* field (B_1).¹⁶⁸⁻¹⁷⁰ The *r.f.* field imposes a torque on the bulk magnetisation vector in a direction that is perpendicular to the direction of the B_1 field, which rotates the vector away from its equilibrium position (along the z -axis) towards the xy -plane.¹⁶⁸⁻¹⁷⁰ The precession frequency (ω_1) about the B_1 field is

$$\omega_1 = -\gamma B_1. \quad \text{Equation 2.17}$$

If the *r.f.* field is applied for a time t_p , the flip or nutation angle of the pulse (θ) through which the magnetisation is rotated is given by

$$\theta = \omega_1 t_p. \quad \text{Equation 2.18}$$

2.3.7. Laboratory and rotating frames of reference

To aid visualisation of the effects of *r.f.* pulses on the bulk magnetisation vector, the concept of rotating frame of reference was introduced.¹⁶⁸⁻¹⁷⁰ Whereas in the laboratory frame the x , y and z coordinates are static, the rotating frame of reference uses x' , y' and z' coordinates with an angular velocity of the *r.f.* frequency (ω_1).¹⁷¹ Therefore, the time dependency of the *r.f.* field is removed and both M_0 and B_1 appear to be stationary and perpendicular to each other.¹⁶⁸⁻¹⁷⁰

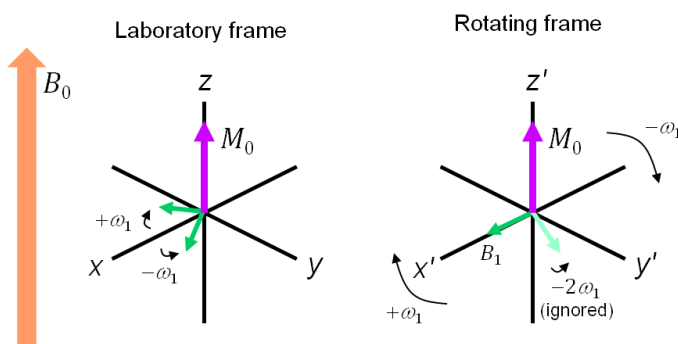


Figure 2.5. Representation of laboratory and rotating frames of references.¹⁷¹

2.3.8. Transition probability equations

At this point, transition probability equations should be described to understand the dependence of the spectral density function on the frequency of molecular motions (section 2.3.9, page 97), and be able to interpret and manipulate the nuclear Overhauser effect (nOe) (section 2.3.16.1, page 113).^{152, 168, 171} For a dipolar coupled, two-spin system, I and S , there are 4 energy levels present under the effect of an external magnetic field: α/α_S , α/β_S , β/α_S and β/β_S (Figure 2.6). The existent dipolar interaction can induce transitions between these levels promoted by longitudinal relaxation.^{152, 168, 171} The associated rate constants for each process are

Single-quantum (SQ) transitions for each spin: W_{1I} and W_{1S} , that correspond to α and β interconversions ($\alpha\alpha \leftrightarrow \beta\alpha$, $\alpha\alpha \leftrightarrow \alpha\beta$, $\alpha\beta \leftrightarrow \beta\beta$ and $\beta\alpha \leftrightarrow \beta\beta$)

Zero-quantum (ZQ) transition: W_{0IS} , that corresponds to spins being flipped in opposite directions, termed “flip-flop” transition ($\alpha\beta \leftrightarrow \beta\alpha$)

Double-quantum (DQ) transition: W_{2IS} , that corresponds to both spins being flipped in the same direction, termed flip-flip transition ($\alpha\alpha \leftrightarrow \beta\beta$).^{152, 168, 171}

The corresponding transition probabilities are

$$W_{1S} = \frac{3}{20} d^2 j(\omega_{0S}) \quad \text{Equation 2.19}$$

$$W_{1I} = \frac{3}{20} d^2 j(\omega_{0I}) \quad \text{Equation 2.20}$$

$$W_{0IS} = \frac{1}{10} d^2 j(\omega_{0I} - \omega_{0S}) = \frac{1}{10} d^2 j(0) \quad \text{Equation 2.21}$$

$$W_{2IS} = \frac{3}{5} d^2 j(\omega_{0I} + \omega_{0S}) = \frac{3}{5} d^2 j(2\omega_0), \quad \text{Equation 2.22}$$

$$\text{where } d \text{ is the dipolar constant, } d = \frac{\mu_0 \hbar \gamma_I \gamma_S}{4\pi r_{IS}^{-3}}, \quad \text{Equation 2.23}$$

$j(\omega)$ is the reduced spectral density at the frequency of the transition, μ_0 is the permeability of vacuum, \hbar is the Planck constant, γ_I and γ_S are the gyromagnetic ratios of the two spins and r_{IS} is the internuclear distance. When the spins of interest are of the same type (^1H s) with similar Larmor frequencies, the assumption that $\omega_{0I} = \omega_{0S}$ can be made. Since double and zero-quantum transitions are not allowed by the conventional selection rules, these are not observable.^{152, 168, 171}

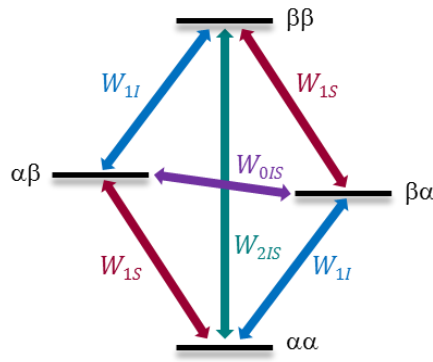


Figure 2.6. Energy levels for a two-spin system in equilibrium. Adapted from reference ¹⁶⁸.

The differential equations expressing the deviation of the population of each level from equilibrium, in terms of z -magnetisation, are

$$\frac{dI}{dt} = -(I_z - I_z^0)(W_{0IS} + 2W_{1I} + W_{2IS}) - (S_z - S_z^0)(W_{2IS} - W_{0IS}) \quad \text{Equation 2.24}$$

$$\frac{dS}{dt} = -(S_z - S_z^0)(W_{0IS} + 2W_{1I} + W_{2IS}) - (I_z - I_z^0)(W_{2IS} - W_{0IS}) \quad \text{Equation 2.25}$$

$$\frac{d2I_zS_z}{dt} = -2I_zS_z(2W_{1I} + 2W_{1S}) \quad \text{Equation 2.26}$$

where I_z^0 and S_z^0 are the equilibrium magnitudes of I_z and S_z operators, respectively.¹⁶⁸ These equations can be simplified by expressing the rate constants as

$$\rho_I = W_{0IS} + 2W_{1I} + W_{2IS} \quad \text{Equation 2.27}$$

$$\rho_S = W_{0IS} + 2W_{1S} + W_{2IS} \quad \text{Equation 2.28}$$

$$\sigma_{IS} = W_{2IS} - W_{0IS} \quad \text{Equation 2.29}$$

$$\rho_{IS} = 2W_{1I} + 2W_{1S} \quad \text{Equation 2.30}$$

where ρ_I , ρ_S and ρ_{IS} are the auto-relaxation rate constants and σ_{IS} is the rate at which magnetisation is transferred from spin I to spin S by relaxation processes, termed cross-relaxation rate constant. This is a unique feature of dipolar relaxation processes and it is the mechanism responsible for the observation of nuclear Overhauser effect enhancements.¹⁶⁸ The differential equations shown above can be simplified to give the Solomon equations

$$\frac{dI_z}{dt} = -\rho_{IS}(I_z - I_z^0) - \sigma_{IS}(S_z - S_z^0) \quad \text{Equation 2.31}$$

$$\frac{dS_z}{dt} = -\rho_{IS}(S_z - S_z^0) - \sigma_{IS}(I_z - I_z^0) \quad .^{168} \quad \text{Equation 2.32}$$

2.3.9. Spectral density function

Random fluctuations generate a distribution of frequencies that can be expressed by a correlation function.^{168, 170} For an isotropic rotational diffusion of a hard sphere, its correlation function is

$$G(\tau) = \overline{B_{local}^2} e^{\frac{-|\tau|}{\tau_c}} \quad \text{Equation 2.33}$$

where B_{local} is the local field, τ is the modulus of the time and τ_c is the average time a molecule takes to rotate through one radian, defined as correlation time.^{168, 170} τ_c is a key NMR parameter because it enables molecular tumbling motions to be determined, as it is affected by molecular size, solvent viscosity and temperature.^{168, 170} Generally, τ_c is in the order of picoseconds for small molecules in non-viscous solvents at room temperature (in the fast motion or extreme narrowing limit), and in the order of nanoseconds for macromolecules in aqueous solutions (in the slow motion or spin diffusion limit).^{168, 170}

The exponential part of the correlation function is independent of the source of the local fields; it is therefore possible to simplify the equation by defining a reduced correlation function, $g(\tau)$, which is independent of the size of the local fields

$$g(\tau) = e^{\frac{-|\tau|}{\tau_c}}. \quad \text{Equation 2.34}$$

The Fourier transform of the correlation function is called spectral density function, $J(\omega)$, and translates the distribution of molecular motions at the correct angular frequency (ω) that cause energy level transitions

$$J(\omega) = \overline{B_{local}^2} \frac{\frac{2\tau_c}{1+\omega^2\tau_c^2}}{.} \quad \text{Equation 2.35}$$

The reduced spectra density, $j(\omega)$, does not depend on the size of local fields and it is expressed as

$$j(\omega) = \frac{2\tau_c}{1+\omega^2\tau_c^2}. \quad \text{Equation 2.36}$$

Figure 2.7 shows that the dependence of the spectral density for a hard sphere with frequency follows a Lorentzian function, and highlights its dependence on the correlation time.^{168, 170} Fast tumbling molecules (small molecules, non-viscous solvents or high temperatures) have the ability to probe a wide range of motional frequencies and therefore show a wide spectral density distribution (represented by the grey line in Figure

2.7).^{168, 170} The spectral density function is almost independent of ω , and the numerical factors in transition probabilities equations govern the relative magnitude of the transition probabilities. In conclusion, for short rotational correlation times, the transition probabilities have the following relationship $W_{2IS} > W_{1I} > W_{0IS}$. In contrast with the above, slowly tumbling molecules (large molecules, viscous solvents or low temperatures) can only experience slower frequencies of movement, having a narrower but more intense distribution of frequencies (represented by the black line in Figure 2.7).¹⁶⁸ Hence, the spectral density function is sharply peaked around $\omega = 0$ and $j(0)$ governs the magnitude of the transition probabilities.¹⁷⁰ In conclusion, for long rotational correlation times, the transition probabilities have the following relationship $W_{0IS} > W_{1I} > W_{2IS}$.^{168, 170}

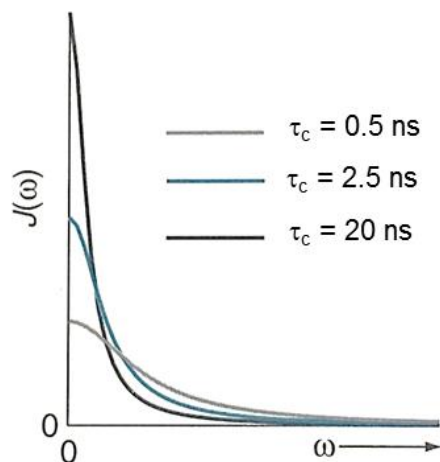


Figure 2.7. Spectral density function ($J(\omega)$) as a function of frequency of molecular motions for different correlation times (τ_c). The area under the curve is independent of τ_c . Adapted from reference ¹⁶⁸.

2.3.10. Nuclear relaxation

After the application of a *r.f.* pulse, perturbation of the distribution of the spin energy levels predicted by the Boltzmann distribution occurs. Nuclear spin relaxation is the process by which the spins return to thermal equilibrium.¹⁶⁸⁻¹⁷⁰ Relaxation is not a spontaneous process, since it is mediated by fluctuating magnetic interactions (dipolar interactions, chemical shift anisotropy, spin rotation and quadrupolar interactions). The fluctuations are modulated by random molecular motions, which cause spins to experience time-dependent local magnetic fields.¹⁶⁸⁻¹⁷⁰ The most relevant mechanism of nuclear spin relaxation arises from the modulation of dipolar couplings by molecular

motions. But relaxation *via* chemical shift anisotropy is particularly important in spin $1/2$ nuclei that exhibit a large chemical shift range, as with ^{19}F . Since it shows great field-dependence, it will be larger at higher B_0 .¹⁶⁸⁻¹⁷⁰ Nuclear spin relaxation may be a few seconds or minutes, which provides sufficient time to manipulate the spin systems in NMR experiments.¹⁶⁸⁻¹⁷⁰

Relaxation can occur either through spin-spin interactions or transverse relaxation (T_2), or through energy transfer to the surroundings, known as spin-lattice relaxation or longitudinal relaxation (T_1).¹⁶⁸⁻¹⁷⁰ Another important manifestation of relaxation is the nuclear Overhauser effect, described below in section 2.3.16.1, page 113.

2.3.10.1. Longitudinal relaxation time

Longitudinal or spin-lattice relaxation time (T_1) represents the exponential gain of z -magnetisation (Figure 2.8). It involves bringing the spins into thermal contact with their surroundings (lattice), in which energy is dissipated in the form of heat. As the interacting nuclei are not identical, a change in the net energy of the system occurs. The energy variation is very small and the change in temperature of the sample is undetectable. This process occurs until equilibrium is established with a rate dependent on T_1 .¹⁶⁸⁻¹⁷¹ Recovery of the z -magnetisation back to thermal equilibrium follows the exponential decay described by the Bloch equation

$$\frac{dM_z(\tau)}{d\tau} = \frac{M_0 - M_z(\tau)}{T_1} \quad \text{Equation 2.37}$$

where M_z is the z -component of magnetisation, M_0 is the equilibrium magnetisation and τ is the time delay. According to Bloch's theory, longitudinal relaxation follows first order kinetics with a rate constant R_1 .¹⁶⁸⁻¹⁷⁰

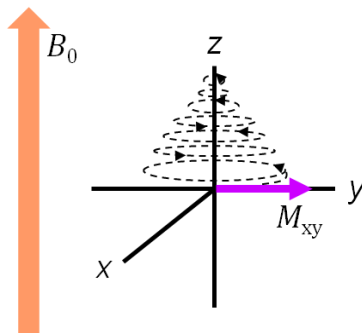


Figure 2.8. Process of loss of z -magnetisation *via* T_1 relaxation. Adapted from reference¹⁷¹.

Energy is transferred to nuclear spins from the chaotic tumbling of molecules. Longitudinal relaxation only occurs when these molecular motions create a time-dependent magnetic field fluctuating at the Larmor frequency. Since T_1 depends on the probability of components oscillating at the appropriate frequency, the relaxation rate is proportional to the spectral density (Figure 2.10). The maximum relaxation rate occurs when $\omega_0\tau_c = 1$, which corresponds to $J(\omega_0) = \frac{1}{\omega_0}$.¹⁷¹

2.3.10.2. Transverse relaxation time

Transverse or spin-spin relaxation time (T_2) represents the exponential loss of coherence in the transverse xy -plane (Figure 2.9). It involves mutual exchange between the spin energy levels (α and β), without change in the net energy of the system. Inhomogeneities in the magnetic field result in differences of precession frequencies of nuclear spins, leading to loss of phase coherence. This process occurs until equilibrium is established with a rate dependent on T_2 .¹⁶⁸⁻¹⁷¹ Magnetic field differences arise from B_0 inhomogeneities throughout the sample and from local magnetic fields created by intermolecular interactions. The relaxation time constant for these two sources combined is designated T_2^* ,

$$\frac{1}{T_2^*} = \frac{1}{T_2} + \frac{1}{T_{2(\Delta B_0)}} \quad \text{Equation 2.38}$$

where T_2 refers to the contribution from local relaxation processes and $T_{2(\Delta B_0)}$ to that from field inhomogeneity.¹⁶⁸⁻¹⁷⁰

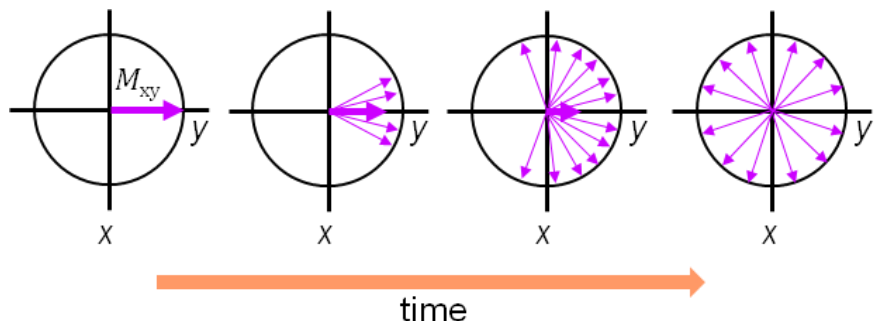


Figure 2.9. Process of loss of coherence in the transverse xy -plane via T_2 relaxation, leading to zero net magnetisation. Adapted from reference¹⁷¹.

2.3.10.3. Comparison between T_1 and T_2 relaxation processes

The dependence of longitudinal and transverse relaxation on molecular tumbling is shown in Figure 2.10. The relaxation mechanisms that promote longitudinal relaxation also cause transverse relaxation.¹⁶⁸⁻¹⁷¹ T_2 increases as the rotational correlation time decreases and their relationship can be expressed by the random fields relaxation mechanism,

$$\frac{1}{T_2} = \frac{1}{2}\gamma^2\langle B^2 \rangle J(\omega_0) + \frac{1}{2}\gamma^2\langle B^2 \rangle J(0) \quad \text{Equation 2.39}$$

where $\frac{1}{2}\gamma^2\langle B^2 \rangle J(\omega_0)$ corresponds to $\frac{1}{2}T_1^{-1}$ and represents the contribution from longitudinal relaxation. In the fast motion or extreme narrowing limit ($\omega_0\tau_c \ll 1$), both relaxation times are identical, as $(\omega_0) = J(0)$, and so $T_1 = T_2$.¹⁷¹ In the slow motion or spin diffusion limit ($\omega_0\tau_c \gg 1$), the contribution of longitudinal relaxation to T_2 is negligible and transverse relaxation becomes proportional to the correlation time, $J(0) = 2\tau_c$. This “limit” depends on the Larmor frequency, which in turn is dependent on the nucleus properties and the magnetic field.¹⁶⁸⁻¹⁷¹

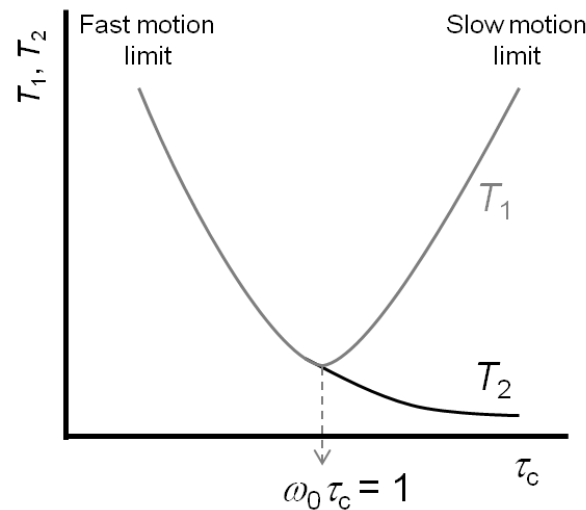


Figure 2.10. Motional dependence of longitudinal (T_1) and transverse (T_2) relaxation times. The T_1 minimum occurs when $\omega_0\tau_c = 1$. Adapted from reference ¹⁷¹.

2.3.11. Dipolar coupling

The dipolar coupling is a through space manifestation of the interaction between nuclear magnetic moments of two spins within reasonable proximity of each other (< 10 Å). It can either occur between two like spins (homonuclear, *II*) or two spins of different nuclei (heteronuclear, *IS*).^{171, 174}

2.3.11.1. Homonuclear dipolar coupling

The homonuclear dipolar coupling is an interaction between the magnetic moments of like spins, described by the homonuclear dipolar coupling Hamiltonian for a two spin system,

$$\hat{H}_{II} = -\left(\frac{\mu_0}{4\pi}\right) \frac{\hbar\gamma_{I_1}\gamma_{I_2}}{r_{I_1I_2}^3} \frac{1}{2} (3\cos^2\theta_{I_1I_2} - 1) [2I_{1z}I_{2z} - \frac{1}{2}(I_1^+I_2^- + I_1^-I_2^+)] \quad \text{Equation 2.40}$$

where the dipolar constant (*d*) corresponds to

$$d = \left(\frac{\mu_0}{4\pi}\right) \frac{\hbar\gamma_{I_1}\gamma_{I_2}}{r_{I_1I_2}^3}, \quad \text{Equation 2.41}$$

$r_{I_1I_2}$ is the internuclear distance between two like spins, μ_0 is the permeability of free space ($\mu_0 = 4\pi \times 10^7 \text{ NA}^{-2}$) and θ is the angle that describes the orientation of the internuclear vector with respect to the external magnetic field.^{171, 174} The terms $I_1^+I_2^-$ and $I_1^-I_2^+$ express the energy conserving “flip-flop” transition of two like spins with similar resonance frequencies, colloquially termed as spin diffusion. The raising operator $I^+ = I_x + iI_y$ expresses an increase in the angular momentum of a spin, representing the flip of a spin from “down” to “up” orientation.^{171, 174} The lowering operator $I^- = I_x - iI_y$ expresses a decrease in the angular momentum of a spin, representing the flip of a spin from “up” to “down” orientation.^{171, 174} By rearranging the term

$$I_1I_2 = I_{1x}I_{2x} + I_{1y}I_{2y} + I_{1z}I_{2z} \quad \text{Equation 2.42}$$

the homonuclear dipolar coupling Hamiltonian can be simplified to

$$\hat{H}_{II} = -\left(\frac{\mu_0}{4\pi}\right) \frac{\hbar\gamma_{I_1}\gamma_{I_2}}{r_{I_1I_2}^3} \frac{1}{2} (3\cos^2\theta_{I_1I_2} - 1) [3I_{1z}I_{2z} - (I_1I_2)]. \quad \text{Equation 2.43}$$

From the dipolar constant component (*d*), it is clear that dipolar interactions are directly proportional to the gyromagnetic ratio of interacting spins. Nuclei with larger magnetic

moments produce stronger local magnetic fields and hence increase the dipolar coupling interaction. For abundant nuclei, with high gyromagnetic ratio, dipolar interactions are extremely strong (^1H - ^1H in the range of 100 kHz), while for pairs of nuclei with low gyromagnetic ratio and low natural abundance these are almost negligible (^{13}C - ^{13}C do not exceed 5 kHz). Since d is inversely proportional to the cube of the internuclear distance, the interaction falls off rapidly as the nuclei are moved farther apart.^{171, 174}

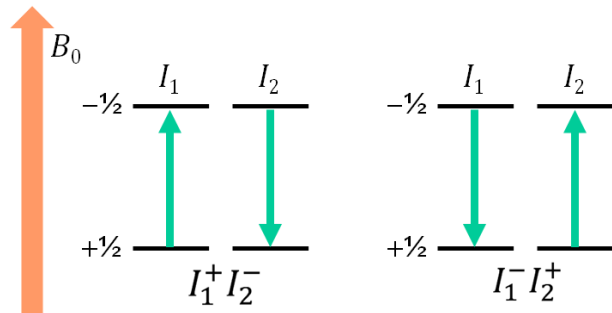


Figure 2.11. Energy conserving “flip-flop” interaction between two like spins occurs since $\omega_{I_1} = \omega_{I_2}$.¹⁷¹

2.3.11.2. Heteronuclear dipolar coupling

The heteronuclear dipolar coupling is an interaction between the magnetic moments of unlike spins. By convention, nuclear spins are labelled as I for abundant spins (^1H , ^{19}F) and S for rare spins (^{13}C , ^{15}N).^{171, 174} The heteronuclear dipolar coupling Hamiltonian ($\hat{H}_{I,S}$) for a two spin system is described by

$$\hat{H}_{I,S} = -\left(\frac{\mu_0}{4\pi}\right) \frac{\hbar\gamma_I\gamma_S}{r_{IS}^3} (3\cos^2\theta_{IS} - 1) I_z S_z \quad \text{Equation 2.44}$$

where r_{IS} is the internuclear distance between two unlike spins.^{171, 174} The spin component ($I_z S_z$) is significantly simplified, because the energy conserving “flip-flop” transition is not possible between two spins with different resonance frequencies (Figure 2.12). Similarly to homonuclear dipolar couplings, the strength of heteronuclear dipolar interactions depends on the gyromagnetic ratio of interacting spins, the distance between both nuclei and their orientation with respect to the external magnetic field.^{171, 174}

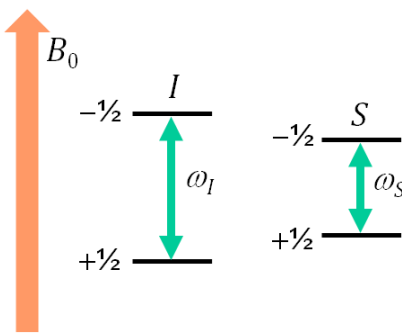


Figure 2.12. Energy conserving “flip-flop” transitions cannot occur between two unlike spins since $\omega_I \gg \omega_S$.¹⁷¹

2.3.12. Chemical shielding

Electrons circulating in their orbitals have profound effects on neighbouring nuclear spins. Electrons have magnetic moments and create circulating currents, acting themselves as magnets. The resulting local magnetic fields (B') modulate the effective magnetic field (B) felt by the nucleus.^{168, 171, 174} The effective magnetic field is slightly smaller than the applied external magnetic field, due to the “shielding” effect of electrons,

$$B = B_0 - B' = B_0(1 - \sigma) \quad \text{Equation 2.45}$$

where σ is the shielding constant. This is termed shielding interaction and it is described by the chemical shielding Hamiltonian (\hat{H}_{CS}),

$$\hat{H}_{CS} = -\gamma \hat{I}_z(1 - \sigma)B_0. \quad \text{Equation 2.46}$$

Since the local magnetic fields produced by moving electrons are considerably smaller than B_0 , the chemical shift (δ) values are given as part per million (ppm) of the external field.¹⁷⁴ The chemical shift is determined as the difference between the frequencies of the analysed nucleus (ν) with respect to a reference compound (ν_{ref}) of known frequency (equal to 0 ppm, by convention),

$$\delta_{\text{ppm}} = 10^6 \left(\frac{\nu - \nu_{ref}}{\nu_{ref}} \right). \quad \text{Equation 2.47}$$

Different standard reference compounds are used for different nuclei, e.g. tetramethylsilane is a standard for ^1H and ^{13}C , CFCl_3 for ^{19}F and liquid NH_3 for ^{15}N chemical shift referencing.¹⁷⁴

Different atoms experience different electron cloud densities. The electron density around atoms in molecules is rather complex and depends on several factors including formation

of hydrogen bonds, presence of electronegative nuclei in close proximity, unpaired electrons or through space interactions within molecular clusters.^{168, 171, 174}

2.3.13. Chemical shift anisotropy

The distribution of electrons in the electronic clouds surrounding a nuclear spin is not spherically symmetric; it is instead usually elongated as an ellipsoid along bonds or non-bonding *p*-orbitals (Figure 2.13).^{168, 171, 174} The degree to which the electron density affects the resonance frequency depends on the orientation of this ellipsoid with respect to the external field (anisotropy). This orientation dependence leads to the presence of an anisotropic term in the corresponding Hamiltonian.^{171, 174} As the chemical shielding interaction felt by the nucleus is slightly different in all three dimensions, a distribution of chemical shift values is observed. For a shielding tensor with axial symmetry, $\delta_{11} = \delta_{22}$, the chemical shift anisotropy (CSA) Hamiltonian (\hat{H}_{CS}).^{168, 171, 174}

$$\hat{H}_{\text{CS}} = \gamma B_0 I_z [\delta_{\text{iso}} + \frac{1}{2} \delta_{\text{CSA}} (3\cos^2 \theta - 1)] \quad \text{Equation 2.48}$$

where δ_{iso} is the isotropic chemical shielding factor,

$$\delta_{\text{iso}} = \frac{1}{3} (\delta_{11} + \delta_{22} + \delta_{33}) \quad \text{Equation 2.49}$$

and δ_{CSA} dictates the magnitude of the CSA,

$$\delta_{\text{CSA}} = \delta_{\text{iso}} - \delta_{33}. \quad \text{Equation 2.50}$$

When the narrowest part of the ellipsoid is oriented along B_0 (Figure 2.13a), it gives rise to the most deshielding effect, represented by the principal component of the chemical shift value δ_{11} , whereas the orientation of the widest part of the ellipsoid along B_0 (Figure 2.13c) has the most shielding effect and is represented by the principal component of the chemical shift value δ_{33} .¹⁷⁴ Perpendicular orientation of the ellipsoid (Figure 2.13b) is represented by the principal component of the chemical shift value δ_{22} .¹⁷⁴

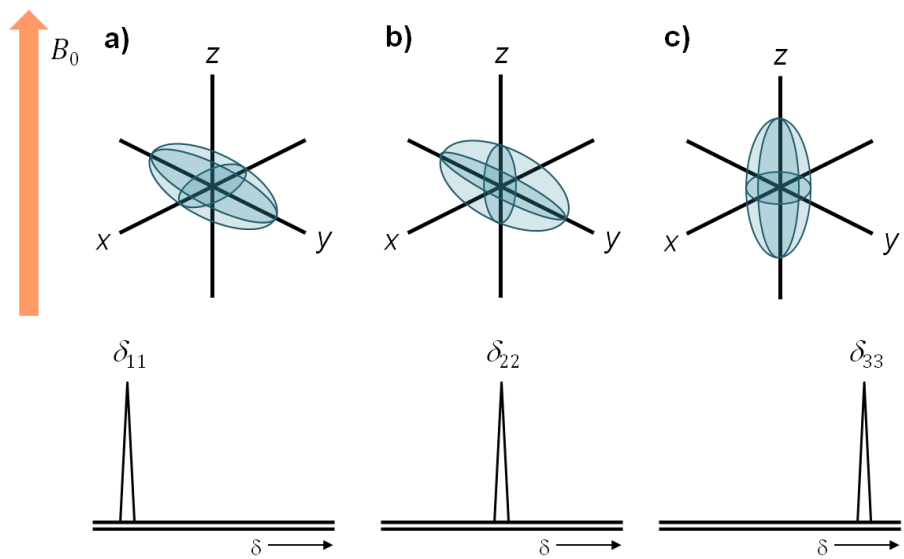


Figure 2.13. Representation of preferential orientation of the ellipsoidal electron cloud of a carbonyl carbon with respect with the external magnetic field, with the corresponding values of chemical shift tensors, **a)** δ_{11} , **b)** δ_{22} and **c)** δ_{33} . Adapted from reference ¹⁷⁴.

2.3.14. Solid-state NMR spectroscopy

In solids, the low molecular mobility leads to dramatic line broadening due to the presence of orientation-dependent nuclear spin interactions: heteronuclear and homonuclear dipolar couplings and chemical shift anisotropy.^{144, 174, 175} Some approaches of coherently manipulating and averaging out such sources of broadening are discussed below.^{144, 174, 175}

2.3.14.1. Magic-angle spinning

Since the geometric component of the Hamiltonians for dipolar and CSA interactions has an angular dependence, $3\cos^2\theta - 1$, this term cancels to zero when the sample is spun at an axis oriented at the angle $\theta = 54.74^\circ$ with respect to the external magnetic field.^{144, 174, 175} This technique is known as magic angle spinning (MAS), and is based on the events that naturally occur in solution-state NMR, in which the rapidly tumbling molecules produce narrow isotropic chemical shifts because molecules sample all possible orientations of the ellipsoid. This approach was proposed by Andrew *et al.* (1958) for a single crystal of sodium chloride and revolutionised the field of solid-state NMR.¹⁷⁶

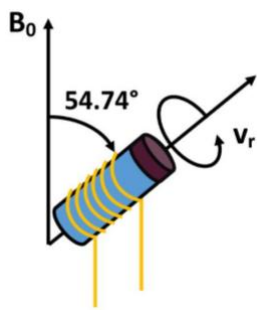


Figure 2.14. Representation of a rotor spun at the magic-angle spinning ($\theta = 54.74^\circ$).¹⁷⁷

To effectively eliminate the geometric term of these magnetic interactions, MAS rates need to be at least three times higher than the strength of the interactions. When the MAS rate is weaker than the strength of the CSA contribution, there is incomplete averaging of the revolving CSA ellipsoid.^{144, 174, 175} Consequently, this gives rise to numerous peaks that arise separated by frequency distances of integer multiples of the spinning speed. These peaks are named spinning sidebands.^{144, 174, 175} As the spinning speed is increased, the envelope of the spinning sidebands begins to resemble a static NMR spectrum. The application of an MAS rate of 10-15 kHz can successfully eliminate ^1H - ^{13}C heteronuclear dipolar couplings. However, much stronger homonuclear dipolar interactions (in the range of 80 kHz) are frequently observed between nuclear spins of high abundance and high gyromagnetic ratio (^1H and ^{19}F).^{144, 174, 175}

2.3.14.2. Heteronuclear dipolar decoupling

Even though the application of MAS is an effective approach to eliminate CSA, it shows limitations when applied to systems with strong homo- and heteronuclear dipolar couplings. In the case of the detection of ^{13}Cs , the dominant interaction is the strong heteronuclear coupling with ^1H s, with strengths that are typically between 20 and 30 kHz (at a distance of about 1 Å). To further improve the resolution of solid-state NMR spectra of such materials, MAS can be combined with decoupling techniques using complex *r.f.* pulses.^{144, 174, 175}

Close inspection of the heteronuclear dipolar coupling Hamiltonian (Equation 2.30) shows there are two mechanisms of decreasing this broadening interaction: application of MAS to average the geometrical component and elimination of the spin component ($I_z S_z$) by

removing the effect of ^1H on ^{13}C nuclei. This can be achieved by constantly alternating the orientation of ^1H spins between high and low energy states (either spin-up or spin-down). The sign of the energy determined by I_zS_z oscillates between positive and negative, producing a time averaged value of zero.^{144, 174, 175} Continuous wave (CW) decoupling is the continuous application of high *r.f.* field on the abundant spin I during acquisition of the dilute spin S . As the continuous application of decoupling *r.f.* pulses during long acquisition periods may lead to sample and probe overheating, CW decoupling methods became less popular. The most frequently used pulse sequence in heteronuclear dipolar decoupling is the two pulse phase modulation (TPPM)¹⁷⁸ which consist of two high power pulses $P = 165^\circ + \varphi$ and $P^- = 165^\circ - \varphi$ with a phase shift (φ) of 10 to 70°. This pulse sequence was further employed to build supercycles of high decoupling efficiency known as SPINAL-X¹⁷⁹ (where X is number of P or P^- pulses in the supercycle, *i.e.* 16, 32, 64 or 128).^{144, 174, 175}

2.3.14.3. Cross-polarisation magic-angle spinning

Since the majority of nuclei of interest in solid-state NMR have low gyromagnetic ratios coupled to low isotopic abundance (^{13}C and ^{15}N), some techniques have been developed to enhance signal intensity. The current success associated with the use of solid-state NMR for structural studies arises from the development of combined MAS with cross-polarisation (CP) and high-power heteronuclear decoupling in 1976 by Schaefer and Stejskal.¹³² This is a double-resonance technique that relies on the high polarisation and short relaxation times of ^1H spins to transfer magnetisation to dilute spins, termed cross-polarisation. Such low abundance nuclear spins have very long relaxation times, because homonuclear dipolar couplings, which are highly efficient in promoting relaxation, are very weak in dilute spins. However, in CP/MAS experiments, there is no need to use long recycle delays.^{144, 174, 175}

The driving force of this transfer of magnetisation is similar to heat flow between bodies with different temperatures. Magnetisation tends to flow from highly polarised nuclei (hot) to nearby nuclei with lower polarisation (cold). As it was seen above, thermal equilibrium occurs spontaneously in homonuclear pairs of dipolar coupled spins *via* “flip-flop” transitions (Figure 2.11), with conservation of energy.^{144, 174, 175} Contrarily, in

heteronuclear pairs of dipolar coupled spins, these transitions are not favourable and therefore have to be promoted by the application of *r.f.* fields. An energy conserving dipolar contact between two different spin systems *I* and *S* is created by simultaneously applying two continuous *r.f.* fields at the resonance frequency of each spin. To transfer magnetisation from abundant to dilute spins, the amplitude of the contact pulse (more details on the pulse sequence can be found in Chapter 3, Figure 3.4, page 125) has to be carefully set in order to match the Hartmann-Hahn condition,

$$\omega_{1I} = \omega_{1S} \Leftrightarrow \gamma_I B_{1I} = \gamma_S B_{1S} \quad \text{Equation 2.51}$$

where ω_{1I} and ω_{1S} are the precession frequencies imposed by the *r.f.* fields. Since the rotation of the magnetisation about the axis of the applied field depends on the amplitude and duration of the *r.f.* field (Equation 2.18), both spins can be rotated independently around a particular axis.^{144, 174, 175} The Hartmann-Hahn match is met when both spins precess at the same rate in the rotating frame, *i.e.* when the energy gaps of both spin states of spin *I* and *S* is equal (irrespective of their Zeeman energies in the laboratory frame) (Figure 2.15). Hence, energy can be transferred between *I* and *S* spins in an energy conserving mechanism. One way of visualising the effect of the simultaneous application of continuous *r.f.* fields is by using the doubly rotating frame model, which considers that the spacing between the energy levels is equal for the *I* and *S* spins (Figure 2.15), as the differences in energy are compensated by the *r.f.* fields.^{144, 174, 175}

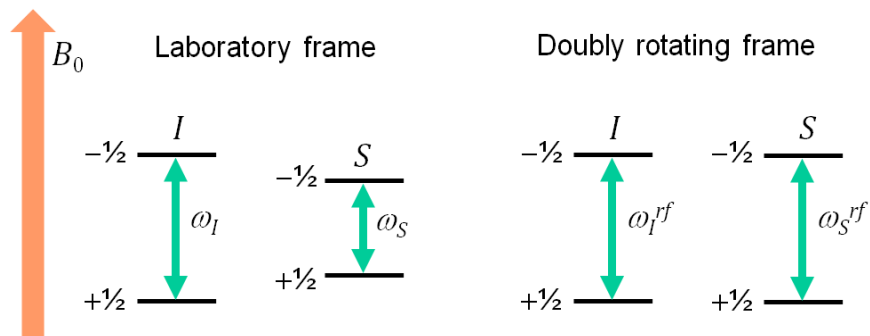


Figure 2.15. Energy differences between the transitions of the *I* and the *S* spins can be made equal in a doubly rotating frame when the nutation frequencies on both spins are equal ($\omega_I = \omega_S$).¹⁷⁴

The enhancement of magnetisation for the S spin is dependent on the strength of the dipolar coupling.¹⁷⁴ Efficient transfer of magnetisation occurs only under the condition of strong heteronuclear dipolar couplings. Intermediate motions can affect cross-polarisation transfer efficiency *via* the motional modulation of dipolar interactions, leading to a reduction in signal intensity.

The combination of high-power heteronuclear decoupling, cross-polarisation and high-speed MAS is nowadays routinely applied as it can rapidly produce well-resolved solid-state spectra of rare nuclei (^{13}C and ^{15}N).^{144, 174, 175}

2.3.15. High-resolution magic-angle spinning

High-resolution magic-angle spinning (HR-MAS) experiments give rise to spectra with sharp peaks that would be observed in solution state NMR by averaging out dipolar broadening, chemical shift anisotropy and magnetic susceptibilities of semi-solid materials using moderate MAS rates (*ca.* 4 kHz).¹³⁵ In semi-solid materials, the residual motional averaging and differences in magnetic susceptibility partially remove broadening interactions. According to Alam and Jenkins, these “dynamically averaged or susceptibility broadened systems are the niche of HR-MAS NMR”.¹³⁵

HR-MAS can provide resolution and dynamic information where standard solution or solid-state NMR techniques are unsuccessful. It is a hybrid technique that allows pulse sequences from both solution and solid-state NMR to be used, due to the dramatic increase in resolution, but also residual anisotropic interactions. Some liquid-state experiments applied previously to semi-solid materials include solvent suppression, gradient-assisted sequences and multidimensional experiments, as INEPT, NOESY, COSY, TOCSY, HETCOR, HMQC and HMBC.^{135, 140, 180, 181} Regarding successfully conducted solid-state NMR techniques in semi-solid materials, these encompass the measurement of residual homonuclear dipolar interactions, as DQ-COSY and the insertion of a radio frequency dipolar recoupling sequence into the standard NOESY experiment.^{135, 140, 180, 181}

2.3.15.1. Pulsed-field gradient experiments

Pulsed-field gradient (PFG) HR-MAS enables the separation of molecules according to their diffusion regimes, which is essential to understand dynamics of heterogeneous systems. The conduction of PFG HR-MAS experiments was only possible after Maas *et al.* (1996) successfully developed a gradient coil at the magic-angle ($\theta = 54.74^\circ$) in an HR-MAS probe.¹⁸² The main goal of aligning the gradient coil along the spinner axis was to avoid rotational averaging of the magnetic field gradient. Consequently, sensitivity and resolution in multidimensional experiments was increased as unwanted artefacts from indirect dimension (t_1 noise) were also suppressed, incorporating the possibility of easily selecting coherence pathways.¹⁸² This approach became known as magic-angle gradient (Figure 2.16). This is the main difference between a standard MAS and an HR-MAS stator. Consequently, this enabled PFG experiments to be conducted efficiently on semi-solid samples.^{50, 135, 140, 182}

The PFG stimulated echo pulse sequence with dipolar gradients and spoil gradient is beneficial for samples which exhibit differences in magnetic susceptibility across the sample – as semi-solid heterogeneous samples. PFG studies have their potential recognised in the study of diffusion in zeolites, nanoparticles, liquid crystals, polymer solutions and melts, as well as of species adsorbed onto polymers, including gases, water, organic solvents and electrolytes.^{50, 135, 140, 182}

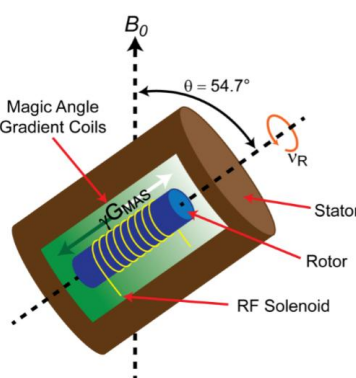


Figure 2.16. HR-MAS stator with a magic-angle gradient (GMAS) along the rotor spinning axis.¹³⁵

Diffusion experiments (PFG and DOSY) are key experiments in the investigation of heterogeneous materials, as the determination of tortuosity and diffusivity in porous materials,^{183, 184} thermodynamic binding constants,¹⁸⁵ rates of exchange processes¹⁸⁶ and dynamics of polymer chains.¹⁸⁷ This technique enables inferences to be made on the translational displacement of molecules, by applying a gradient which “tags” a nuclear spin with a phase that is related to its spatial position. If the position of the spin does not change during the diffusion period, the dephasing shown in Figure 2.17a is refocused and the original signal intensity is recovered. Contrarily, if the spin diffuses, the dephasing for that spin is not refocused and the signal intensity decreases.¹³⁵ This is obtained by the application of two symmetrical gradients, as illustrated in the pulse sequence in Figure 3.7 from the experimental section (Chapter 3, page 128).¹³⁵

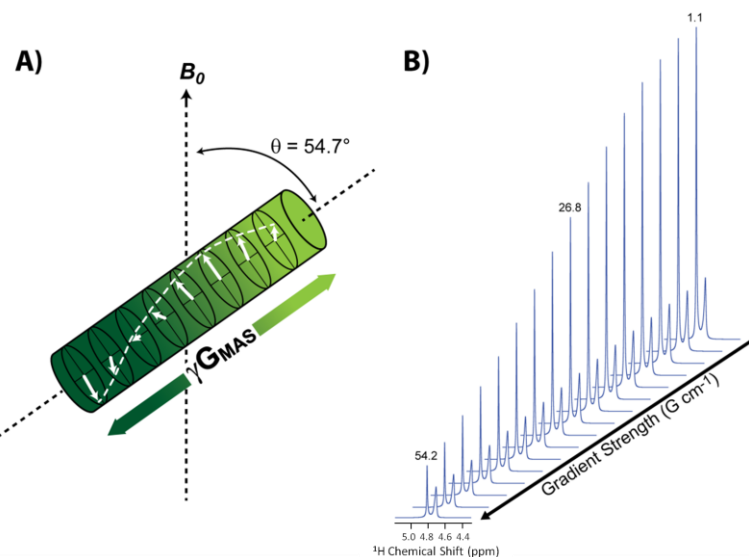


Figure 2.17. a) Representation of the gradient produced along the magic-angle of the rotor. b) Typical decay of ^1H -peak intensity with increasing gradient strength in a PFG HR-MAS experiment.¹³⁵

In HR-MAS experiments, the resulting values do not correspond to true diffusion coefficients, as molecules experience centrifugal forces under MAS, so these are named apparent self-diffusion coefficients. The full scope of the effects of spinning soft materials is discussed in Chapter 1, section 1.6.8.3, page 74. Moreover, some reports discuss that the measurement of translational diffusion within confined geometries, in the presence of barriers, exchange between compartments, binding and anisotropy limits molecular diffusion and deviates the decay curves from a single exponential function.^{183, 188}

Heterogeneities in magnetic susceptibility lead to non-uniform sample magnetisation and the background gradients cause a decrease in the observed transverse relaxation processes and interfere with diffusion measurements.¹⁸⁶ Currently, the goal of the field is to improve these techniques in order to obtain accurate and quantitative measurement of diffusion coefficients of semi-solid samples by HR-MAS.

2.3.16. Solution-state NMR spectroscopy

Liquids show completely different behaviour relative to solids in terms of their nuclear spin interactions. In the solution state, the complex interactions that lead to considerable line broadening in solids are motionally averaged out, due to the random and fast molecular motions that occur in solution (in the range of $10^{12} - 10^{15}$ Hz).^{171, 189} Therefore, ^1H NMR spectra of liquids are quite simplified, with the detection of very sharp ^1H peaks (line widths *ca.* 1 Hz) at the isotropic chemical shift. The resulting highly resolved spectra enable detailed site-specific information on molecular structure, dynamics and function to be obtained.^{171, 189}

2.3.16.1. The nuclear Overhauser effect

The nuclear Overhauser effect is the basis for many structural characterisation studies, as it is a through-space manifestation of relaxation of nuclei in close proximity (< 5 Å), *i.e.* it is one of the processes by which spins return to equilibrium after a perturbation.^{152, 168-170, 190}

When S spin magnetisation deviates from equilibrium by application of a continuous selective *r.f.* pulse, the allowed relaxation pathways are W_{0IS} and W_{2IS} , as single-quantum transitions of spin S are saturated (Figure 2.18). As these are not single-quantum transitions they cannot be detected, but their effects are observable in a ^1H NOESY difference spectrum. There will be a change in the I spin magnetisation that will manifest itself as modification of peak intensity of I , termed nOe enhancement (Figure 2.19).^{152, 168-170,}

¹⁹⁰

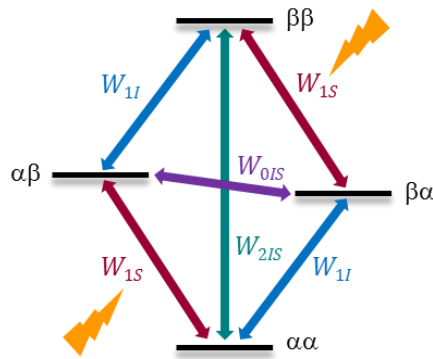


Figure 2.18. Energy levels for a two-spin system upon saturation of spin S . Adapted from reference ¹⁶⁸.

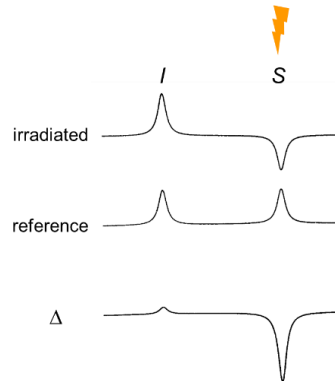


Figure 2.19. Example of 1D NOESY difference spectrum. When spin S is irradiated (as indicated by the negative peak intensity), peak intensity of spin I is increased due to cross-relaxation from spin S , which is more evident in the difference (Δ) spectrum. It has been assumed that the cross-relaxation rate is positive, so the nOe enhancement is positive. Adapted from reference ¹⁶⁸.

2.3.16.2. Cross-relaxation rate

The sign and magnitude of the nOe enhancement (η) are proportional to the cross-relaxation rate (σ_{IS}),

$$\eta = 2\sigma_{IS}\tau_c \quad \text{Equation 2.52}$$

and the magnitude of the nOe can be calculated according to the following formula

$$\varepsilon_{noe} = 1 + \frac{\gamma_I}{\gamma_S} \frac{(W_{2IS} - W_{0IS})}{(W_{0IS} + 2W_{1S} + W_{2IS})}, \quad \text{Equation 2.53}$$

In turn, the sign of the cross-relaxation rate is dependent on the equilibrium between the sizes of the Larmor frequencies and the correlation time,

$$\sigma_{IS} = W_{2IS} - W_{0IS} = \frac{3}{5}d^2j(2\omega_0) - \frac{1}{10}d^2j(0). \quad \text{Equation 2.54}$$

What dictates the sign of the NOESY peak is which process, W_{0IS} or W_{2IS} , is more favourable.^{152, 168-170, 190}

In the fast motion or extreme narrowing limit (defined as $\omega_0\tau_c \ll 1$), where motions are very fast and correlation times very short,

$$j(\omega_0) = 2\tau_c = j(0), \quad \text{Equation 2.55}$$

$$\text{therefore } \sigma_{IS} = \frac{1}{2}d^2\tau_c. \quad \text{Equation 2.56}$$

Under this condition, the sign of σ_{IS} is positive since $W_{2IS} > W_{0IS}$, resulting in a positive nOe enhancement.^{152, 168-170, 190}

In the slow motion or spin diffusion limit (defined as $\omega_0\tau_c \gg 1$), where motions are very slow and the correlation time very long,

$$j(\omega_0) = \frac{2}{\omega_0^2\tau_c} = \frac{j(0)}{\omega_0^2\tau_c^2}, \quad \text{Equation 2.57}$$

$$\text{therefore } \sigma_{IS} = -\frac{1}{10}d^2\tau_c. \quad \text{Equation 2.58}$$

Under this condition, the sign of σ_{IS} is negative since $W_{2IS} < W_{0IS}$, resulting in a negative nOe enhancement.^{152, 168-170, 190}

For medium-sized molecules $W_{2IS} = W_{0IS}$, hence σ_{IS} vanishes at the critical correlation time and no nOe enhancement is recorded. This is termed the cross-over point (Figure 2.20) and it can be overcome by performing rotating frame nOe experiments (ROESY), modifying the external magnetic field or changing the molecular environment (temperature and/or solvent viscosity).^{152, 168-170, 190}

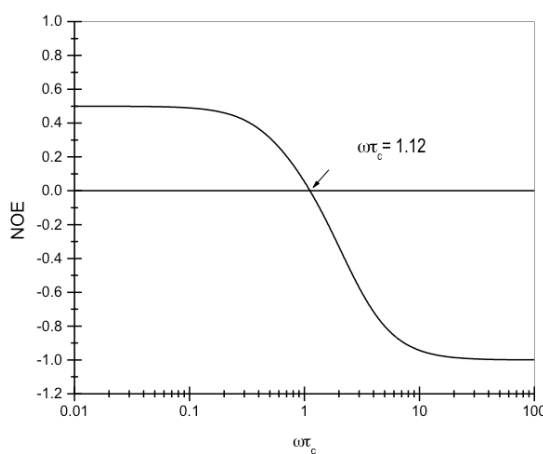


Figure 2.20. Dependence of nOe peak intensity and signal with correlation time (τ_c). The cross-over point is characteristic of medium-sized molecules and corresponds to the absence of nOe enhancement (occurs when $\omega_0\tau_c = 1.12$). Adapted from reference¹⁶⁸

2.3.16.3. NOESY experiments

Transient nOe experiments (as 2D NOESY experiments) allow the cross-relaxation rate, σ_{IS} , to be measured. The cross-relaxation rate constant is proportional to the inverse sixth power of the distance between the two dipolar interacting spins. This strong dependence of σ_{IS} on the distance between spins makes the observation of nOe diagnostic of dipolar relaxation and proximity of pairs of spins.¹⁶⁸ The cross-relaxation rate for a homonuclear two-spin system (assuming $\gamma_I = \gamma_S = \gamma$) is given by

$$\sigma_{IS} = \frac{\hbar^2 \mu_0^2 \gamma^4 \tau_c}{10\pi^2 r_{IS}^6} \left\{ -1 + \frac{6}{1+4\omega_0^2 \tau_c^2} \right\} \quad \text{Equation 2.59}$$

$$\text{hence, } \sigma_{IS} \propto \gamma^4 \left\{ \frac{6}{1+4\omega_0^2 \tau_c^2} - 1 \right\} \frac{\tau_c}{r_{IS}^6} \quad \text{Equation 2.60}$$

where \hbar is the Planck constant, μ_0 is the permeability of vacuum, γ is the gyromagnetic ratio and r_{IS} is the internuclear distance.¹⁶⁸

Optimisation of the mixing time used in a NOESY experiment should take into account the following processes. As a consequence of spin diffusion, cross-peaks between pairs of protons that are far apart will gain intensity from magnetisation that has been transferred *via* intervening spins, termed relayed nOe enhancements.¹⁶⁸ Similarly, cross-peaks between pairs of protons that are close together will be decreased by the loss of magnetisation to nearby protons. Spin-diffusion effects may be minimised by using short mixing times. Moreover, since dipolar relaxation is more efficient in systems with long rotational correlation times, shorter mixing times are required to limit spin-diffusion from contributing substantially to cross-peak intensity in large molecules.¹⁶⁸

To overcome the uncertainty of these measurements when calculating internuclear distance, the initial rate approximation was developed, which establishes that in the initial rate regime, the cross-peak intensity is proportional to the cross-relaxation rate constant (Figure 2.21),^{152, 168}

$$\left(\frac{dI_z}{dt} \right)_{init} = -\rho_{IS}(I_z(0) - I_z^0) - \sigma_{IS}(S_z(0) - S_z^0) = 2\sigma_{IS}S_z^0. \quad \text{Equation 2.61}$$

The cross-relaxation rate can therefore be determined from the initial slope of the build-up curve (I_{IS} as function of τ_m), where the nOe enhancement (I_{IS}) is defined as the ratio between the intensity of the cross-peak at a certain mixing time and the intensity of the diagonal peak at zero mixing time

$$I_{IS} = \frac{I_z}{I_{eq}}.$$
¹⁴⁸

Equation 2.62

In turn, the cross-relaxation rate will be proportional to the inverse sixth power of the internuclear distance (Equation 2.61).¹⁴⁸

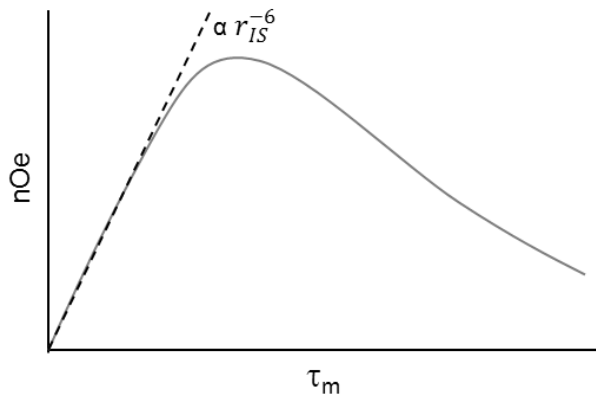


Figure 2.21. Evolution of nOe enhancement with mixing time (τ_m). The nOe grows linearly initially, reaches a maximum and then decreases back to equilibrium as the equilibrium population differences are restored through relaxation. Adapted from reference ¹⁷¹.

2.3.16.4. Saturation transfer difference NMR

Saturation transfer difference (STD) NMR spectroscopy is a ligand-based technique applied frequently to identify the functional groups of a small molecule (usually, a ligand) responsible for binding to its receptor (a protein, typically), enabling the group epitope mapping to be built.^{154, 191-196}

This method relies on the transfer of saturation through cross-relaxation from a saturated macromolecule to a small bound molecule.^{154, 191-196} The macromolecule is selectively saturated by a low power *r.f.* pulse during a certain period (saturation time). Due to its large dimensions, cross-relaxation is the preferential longitudinal relaxation process. This is followed by propagation of saturation *via* the vast network of ¹H-¹H cross-relaxation routes and strong network of ¹H-¹H homonuclear dipolar couplings, named spin diffusion. Such saturation is then transferred *via* strong, negative nOe throughout the macromolecule and finally intermolecularly passed over to the protons of the bound molecule that are in close contact. Dissociation of the weakly bound molecule results in accumulation of saturation in solution for molecules that exchange faster than their

relaxation rates. This accumulation occurs due to the less efficient relaxation pathways of free small molecules in comparison with bound slow tumbling molecules. The saturated protons will appear in the STD difference spectrum and, depending on their relative intensities, a map of binding preferences can be built.^{154, 191-196}

Saturation transfer takes place to molecules bound to the macromolecule with a rate that depends on the macromolecular mobility, complex lifetime and geometry. STD NMR experiments are successful under the conditions of low affinity interactions (dissociation constant, K_D , in the range of 10^{-3} and 10^{-8} M).^{154, 191-196} The rate of exchange between free and bound states is fast enough to allow build-up of a population of saturated small molecule in solution. For high-affinity binding (K_{off} rates in the range of 0.1 to 0.01 s^{-1}), the bound molecule starts losing magnetisation due to efficient transverse relaxation (typical of macromolecules), preventing saturation from being accumulated in solution. On the other hand, when binding is very weak, the probability of the small molecule interacting with the receptor site becomes very low resulting in weak STD signals.^{154, 191-196}

Important factors that affect peak intensity in the difference spectrum are the kinetics of magnetisation relaxing back to equilibrium and rebinding phenomena. When the longitudinal relaxation times of individual protons are significantly different, the resulting STD does not produce an accurate epitope map. This effect is most considerable at longer saturation times, and this is why only the initial build-up rates are taken into account in comparative studies. Regarding rebinding effects, if a certain ligand molecule re-enters the binding site after a preceding binding event (and this rebinding is fast enough related to the relaxation properties), then the ligand spin populations will be partially perturbed due to the previous transfer step.^{154, 191-196} Its capacity to receive more saturation from the receptor will be different than that from a fresh ligand molecule.¹⁹¹⁻¹⁹⁶

2.3.16.5. The STD experiment

The STD NMR experiment is a double resonance nOe pulse sequence, as it involves subtracting a spectrum in which the macromolecule is selectively saturated from one recorded under conditions of thermal equilibrium (Figure 2.22). The on-resonance experiment (STD_{on}) consists of irradiating a region of the spectrum that contains only resonances of the macromolecule, such as 1 to -1 ppm . In the off-resonance experiment

(STD_{off}), a reference spectrum is recorded under the same conditions of STD_{on} , but the frequency is set far away from any resonances present in the system (usually set at 40 ppm). Therefore, the STD difference spectrum ($\text{STD}_{\text{diff}} = \text{STD}_{\text{off}} - \text{STD}_{\text{on}}$) only yields those resonances that received saturation in the on-resonance experiment,¹⁹³

$$I_{\text{STD}} = I_0 - I_{\text{SAT}} \quad \text{Equation 2.63}$$

where I_{STD} is the peak intensity from the difference spectrum, I_0 is the peak intensity from the off-resonance spectrum and I_{SAT} is the peak intensity from on-resonance spectrum.¹⁹³

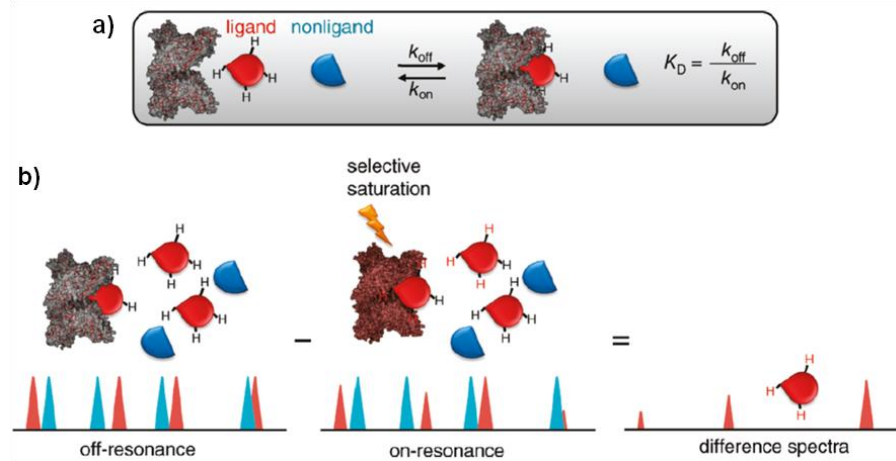


Figure 2.22. Schematic representation of an STD NMR experiment. **a)** Protein-ligand complex. **b)** Off-resonance (STD_{off}) and on-resonance (STD_{on}) spectra, and the STD difference spectrum resulting from the subtraction of STD_{on} to STD_{off} .¹⁹³

Chapter 3

3. Experimental section

3.1. Materials

Reagent grade (> 98 %) 4-amino-*L*-phenylalanine, [¹⁵N]-*L*-glycine, *L*-leucine, *L*-phenylalanine, [¹³C₉,¹⁵N]-*L*-phenylalanine, *L*-serine, *L*-tryptophan, *L*-tyrosine, hexamethylbenzene (HMB), poly(vinylidene fluoride) (PVDF) and polytetrafluoroethylene were purchased from Sigma-Aldrich. 4-bromo-*L*-phenylalanine, 3,4-dichloro-*D*-phenylalanine, 4-fluoro-*L*-phenylalanine, 3,4-difluoro-*L*-phenylalanine, pentafluoro-*L*-phenylalanine, 4-iodo-*L*-phenylalanine were purchased from Fluorochem. 4-chloro-*D*-phenylalanine was purchased from Acros Organics. Deuterium oxide, deuterated dimethyl sulfoxide, 4,4-dimethyl-4-silapentane-1-sulfonic acid (DSS) and tetramethylsilane (TMS) were purchased from Goss Scientific. Pure water was obtained with a Thermo Scientific Barnstead NANOpure purification system coupled to a Barnstead hollow fibre filter.

3.2. Preparation of gels

Gels were prepared by dispersing gelator molecules in 1 mL of D₂O, H₂O or DMSO in a glass vial (2 mm diameter), promoting dissolution with a vortex mixer for 30 s. Samples were then heated up to 363 K with a hot plate (JK IKA Labortechnik) coupled to an electric thermometer (JK IKA Werke). After obtaining a clear solution, the samples were immediately quenched in an ice bath. The gel samples were left resting overnight at room temperature and analysed 24 hours after preparation. When required, gels were then dried under vacuum.

3.3. Vial inversion test

The vial inversion test is a straightforward method of confirming gelation by inverting the vial containing the gel and investigating whether the sample displays gravitational flow.

3.4. Gel-to-solution transition temperature

The vial inversion test was the chosen method for determination of the gel-to-solution transition temperature (T_{gel}), above which significant dissolution of the gel network starts occurring. The sample volume, vial dimensions and heating rate (1 K min^{-1}) were kept constant to enable comparison between samples.

3.5. Differential scanning calorimetry

Differential scanning calorimetry measurements were performed using a Q2000 MT DSC TA Instrument, with standard TA 100 μL aluminium pans. The sample weight was *ca.* 20 mg. A heating rate of 5 K min^{-1} was applied under a N_2 purge of 50 mL min^{-1} .

3.6. Polarised light microscopy coupled to a hot stage unit

Polarised light images were acquired using a microscope Leica DMLS2 with $\times 40$ magnification coupled to a temperature unit Mettler Toledo and a FP90 central processor. The images were obtained using a JVC colour video camera. 20 μL of hot solutions were pipetted onto a glass slide and allowed to gelate *in situ*.

3.7. Scanning electron microscopy

Scanning electron microscopy (SEM) experiments were carried out using a Jeol JSM-5900 LV Oxford instrument with an accelerating voltage of 2.1 kV. Gels were mounted on aluminium stubs with double sided carbon adhesive and allowed to dry before analysis. Dry gel samples were then gold-coated using a Quorum Technologies Polaron SC7640 gold sputter coater.

Environmental SEM experiments performed on urea-based supramolecular gels (Chapter 9) were analysed using a Philips XL-30 instrument with an accelerating voltage of 10.0 kV. Xerogels were mounted on a multiple pin sample holder. No sample coating was necessary.

3.8. Atomic force microscopy

Atomic force microscopy experiments were conducted using a JPK NanoWizard instrument with a silicon cantilever at a nominal spring constant of 40 N m^{-1} , operated with intermittent contact for imaging. Hot solutions (*ca.* 10 μL) were pipetted onto a sample holder and allowed to dry before analysis. The force–distance data were recorded in contact mode. Force spectra were collected in arrays of 100×100 data points over areas of $10 \times 10\text{ }\mu\text{m}$. Force spectra were exported and analysed using JPK's data processing software.

3.9. Rheology

The majority of rheology measurements were performed using a Bohlin Gemini HR nano Rotonetic drive 2 equipped with a Julabo F12 water cooler and circulator controlling the temperature of the bottom Peltier plate. Parallel plate, or cone and plate geometry systems (truncated 4/40 cone, 4° cone angle and 40 mm diameter) were used (Figure 3.1). Hot solutions (*ca.* 1.5 mL) were pipetted into a 300 or 500 μm gap, with the temperature of the plate maintained at 323 K for sample preparation. The temperature was then lowered to 293 K, covered with a solvent trap to prevent solvent evaporation and the gels were left stabilising for 1 h. Phase angle, storage and loss moduli were monitored and recorded as a function of frequency and stress. All samples were subjected to frequency sweeps in the range of 0.1 to 100 Hz and applied stress of 500 or 700 Pa, as well as stress amplitude sweeps in the range of 500 to 10000 Pa or 0.1 to 7000 Pa. Experimental conditions were optimised for each sample and are specified in the corresponding figure caption.

Rheology experiments performed on urea-based supramolecular gels (Chapter 9) were conducted using an AR2000EX instrument with 40 mm crosshatched stainless steel plates forming a gap of 1000 μm and recorded at room temperature. A constant oscillatory shear

stress of 0.4 Pa was applied to monitor the dependence of viscoelastic parameters on angular frequency ranging between 1 and 100 Hz.

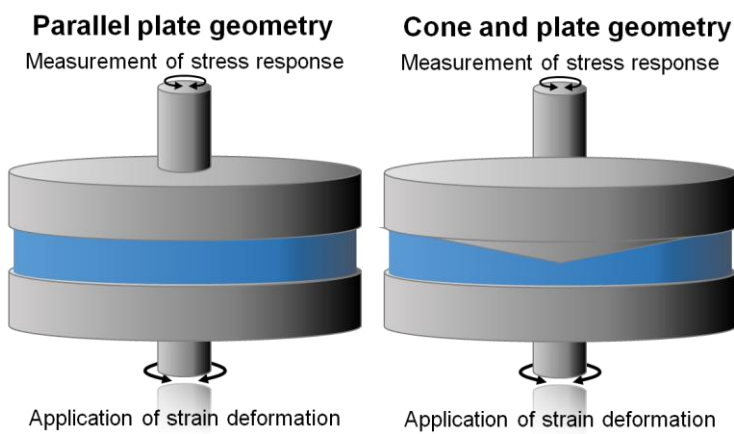


Figure 3.1. Schematic representation of parallel plate and cone and plate geometry setups, with the gel being placed between both surfaces, adapted from reference ¹⁰¹.

3.10. Powder X-Ray diffraction

Powder X-ray diffraction patterns were obtained using a Thermo Scientific ARL XTRA powder diffractometer under Cu K α radiation ($\lambda = 1.54$ nm). Samples were analysed in the 2θ range of 3 to 36°, with a step size of 0.01° 2θ and a scan time of 6 s. Gels (*ca.* 1 mL) and dry samples were placed onto stainless steel sample holders and analysed immediately to prevent dehydration.

3.11. NMR Spectroscopy

3.11.1. Solid-state NMR spectroscopy

Low field solid-state NMR spectra were acquired at 9.4 T using a Bruker Avance III wide bore solid-state spectrometer equipped with a 4 mm $^1\text{H}/\text{X}/\text{Y}$ triple resonance probe head operating at 400.23 (^1H), 376.30 (^{19}F), 100.64 (^{13}C) and 40.56 MHz (^{15}N). Gels were prepared by pipetting *ca.* 40 μL of hot solutions into Kel-F plastic inserts and allowed to gelate inside the insert. A stopper was added to prevent spillage promoted by centrifugal forces. Dry gel samples were directly packed inside 4 mm diameter zirconia rotors.

High field solid-state NMR spectra were acquired at 20 T using a Bruker Avance III wide-bore solid-state spectrometer equipped with a 2.5 mm $^1\text{H}/\text{X}$ (^{19}F) triple resonance probe head and a 3.2 mm $^1\text{H}/\text{X}/\text{Y}$ triple resonance probe head operating at 850.22 (^1H), 799.91 (^{19}F), 231.81 (^{13}C) and 86.15 MHz (^{15}N). Gels were prepared by syringing *ca.* 12 μL of hot solutions directly into 2.5 mm diameter zirconia rotors and allowed to gelate inside the rotor. Dry gel samples were directly packed inside 2.5 mm or 3.2 mm diameter zirconia rotors.

Very fast solid-state NMR spectra were acquired at 20 T using a Bruker Avance III wide-bore solid-state spectrometer equipped with a 1.0 mm $^1\text{H}/\text{X}$ double resonance Jeol probe head operating at 850.22 (^1H) and 231.81 MHz (^{13}C). Dry gel samples were directly packed inside 1.0 or 1.3 mm diameter zirconia rotors.

Pulse delays and MAS rates were optimised for each experiment and are specified in the corresponding figure caption. All experiments were conducted at 298 K, unless otherwise specified. The chemical shifts of ^1H and ^{13}C were referenced with respect to external TMS, ^{19}F was referenced to external trichlorofluoromethane (CFCl_3) and ^{15}N was referenced to external liquid NH_3 at room temperature.

3.11.1.1. One-dimensional magic-angle spinning

^1H and ^{19}F single pulse MAS experiments were acquired using the single pulse sequence shown in Figure 3.2.

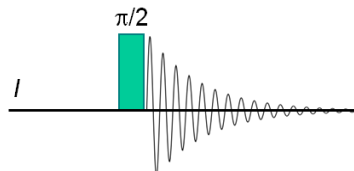


Figure 3.2. Representation of a single pulse experiment. The $\pi/2$ pulse converts equilibrium magnetisation of the I nuclei into transverse magnetisation. During the acquisition time, chemical shifts and spin-spin couplings develop in the x,y -plane.¹⁷²

3.11.1.2. Single pulse ^{13}C with high-power ^1H decoupling

^{13}C -MAS experiments were acquired using a single pulse sequence with SPINAL-64¹⁹⁷ for heteronuclear decoupling during acquisition (Figure 3.3), using a ^1H *r.f.* decoupling field of 78 kHz.

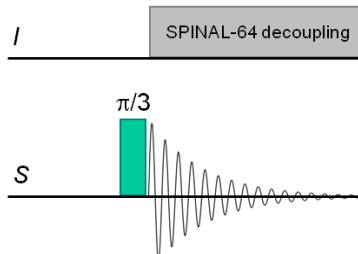


Figure 3.3. Representation of a single pulse experiment pulse sequence using high-power decoupling of the I spins during acquisition of the S spins.

3.11.1.3. ^1H - ^{13}C , ^1H - ^{15}N , ^{19}F - ^{13}C and ^1H - ^{19}F CP/MAS

Cross-polarisation magic-angle spinning (CP/MAS) NMR experiments were acquired using a ramped-amplitude cross-polarisation pulse sequence with SPINAL-64¹⁹⁷ for heteronuclear decoupling during acquisition (Figure 3.4), using a ^1H *r.f.* decoupling field of 78 kHz (for ^{13}C experiments) and 83 kHz (for ^{19}F and ^{15}N experiments). The Hartmann-Hahn matching conditions were set using HMB for ^1H - ^{13}C experiments, $[^{15}\text{N}]$ -glycine for ^1H - ^{15}N experiments and PVDF for ^1H - ^{19}F and ^{19}F - ^{13}C experiments.

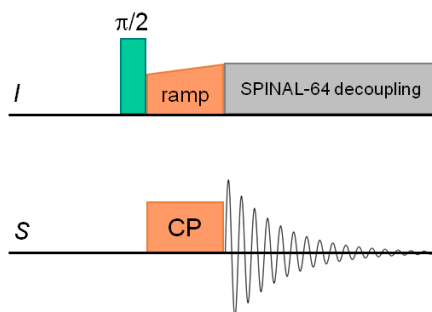


Figure 3.4. Representation of an I - S CP/MAS NMR pulse sequence. The first $\pi/2$ pulse brings equilibrium magnetisation of the I nuclei along the x,y -plane. This magnetisation is locked by a ramped spin lock pulse on I , in which the spin lock power is changed from 70 to 100 % during the spin lock time. Under MAS, the Hartmann-Hahn condition splits into a set of matching sidebands. With a ramped contact pulse, the Hartmann-Hahn is swept over these possible match conditions and becomes insensitive to minor miss-

settings, instrumental instabilities or different MAS rates. Simultaneously, a spin lock pulse on S assures the same precession frequency for the S spins, to satisfy the Hartmann-Hahn condition (described in Chapter 2, section 2.3.14.3, page 108). During this CP period, I and S spins can exchange energy in their respective rotating frames, which transfers polarisation to the S spins from the large energy bath of the abundant I . High-power decoupling of the I spins is applied during acquisition of the S spins. The repetition time of the pulse sequence is governed by I relaxation.^{172, 174}

Solid-state NMR experiments performed on urea-based supramolecular gels (Chapter 9) were conducted using a 400 MHz solid-state NMR spectrometer. All experiments were performed using an MAS rate of 10 kHz and a contact time of 2 ms. ^1H - ^{15}N CP/MAS spectra of reference solid powders were acquired using 2048 scans and a recycle delay of 15 s. A ^1H pulse length of 3.2 μs and ^{15}N pulse length of 3.0 μs were used. ^1H - ^{13}C CP/MAS NMR experiments of powder references were acquired using 256 scans and a recycle delay of 20 s. The spectra of gel samples were acquired using 2048 scans and a recycle delay of 10 s. The spectra of frozen gel samples were acquired using 1024 scans and a recycle delay of 20 s. A ^1H pulse length of 4.0 μs and ^{13}C pulse length of 3.0 μs were used.

3.11.1.4. ^1H - ^{19}F - ^{13}C Double CP/MAS

Double CP/MAS NMR experiments were acquired using a ramped-amplitude cross-polarisation pulse sequence (doublecp) with SPINAL-64¹⁹⁷ for heteronuclear decoupling during acquisition (Figure 3.5), using a ^1H *r.f.* decoupling field of 78 kHz. The Hartmann-Hahn matching conditions were set using PVDF.

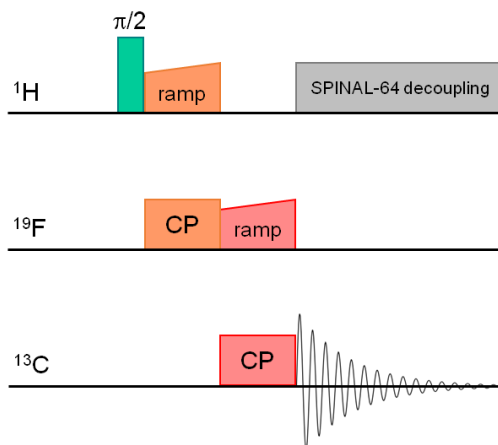


Figure 3.5. Representation of an ^1H - ^{19}F - ^{13}C double CP/MAS NMR pulse sequence. The experiment uses two consecutive cross-polarisation steps that involve the sequential transfer of polarisation among three spins.^{168, 198}

3.11.1.5. 1D ^{19}F - ^1H HOESY

1D ^{19}F - ^1H Heteronuclear Overhauser effect (HOESY) NMR experiments were recorded using a rotor synchronised 2D exchange NMR pulse sequence in rotating solids (cpnoesy) (Figure 3.6).

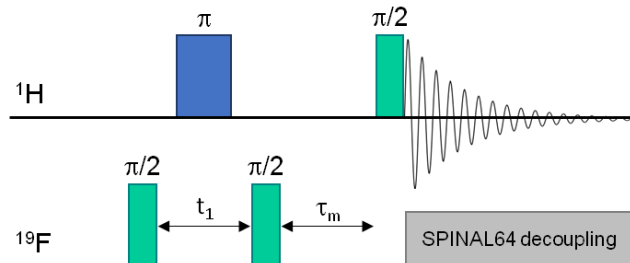


Figure 3.6. Representation of a 1D ^{19}F - ^1H HOESY NMR pulse sequence. The first $\pi/2$ pulse creates ^{19}F magnetisation on the x,y -plane. In the evolution period, a π pulse is located in the middle of t_1 , during which ^{19}F chemical shifts evolve and the π pulse on ^1H eliminates $J(\text{F},\text{H})$ couplings. This creates negative z -magnetisation for ^1H s. Afterwards, the second $\pi/2$ pulse changes ^{19}F transverse magnetisation into the negative z -direction. At the beginning of the mixing time, τ_m , both spins are in the $-z$ -directions so the ^{19}F signal is modulated with this chemical shift information. During the mixing time, the spins undergo cross-relaxation. The final $\pi/2$ pulse realigns the vectors into the x,y -plane and creates ^1H transverse magnetisation. Heteronuclear decoupling of the ^{19}F spins is applied during acquisition of the ^1H spins.^{172, 199}

3.11.2. HR-MAS NMR spectroscopy

High-resolution magic-angle spinning (HR-MAS) NMR spectra were acquired at 18.8 T using a Bruker Avance III spectrometer equipped with a 4 mm $^1\text{H}/\text{X}$ double resonance probe head and a z -gradient coil reaching a maximum field gradient intensity of 49.5 G cm^{-1} , operating at 800.23 (^1H) and 201.24 MHz (^{13}C). Gels were prepared by pipetting *ca.* 40 μL of hot solutions into Kel-F plastic inserts and allowed to gelate inside the insert. A stopper was added to prevent spillage promoted by centrifugal forces. All experiments were conducted with a recycle delay of 2 s and a $\pi/2$ pulse length of 4.4 μs (^1H) at 298 K. Pulse delays and MAS rates were optimised for each experiment and are specified in the corresponding figure caption.

3.11.2.1. One-dimensional experiments

^1H single pulse experiments were acquired using the single pulse sequence shown in Figure 3.2.

3.11.2.2. ^1H PFG HR-MAS

Pulsed-field gradient (PFG) HR-MAS NMR experiments were carried out using a stimulated echo and longitudinal eddy current delay diffusion-filtered pulse sequence (ledgpgp2s1d) (Figure 3.7), with 5 to 95 % of the maximum gradient intensity. A smoothed-square shaped gradient (SMSQ10.100) was used. The diffusion delay (Δ), diffusion gradient length (δ) and gradient strength (g) were optimised for each experiment and are specified in the corresponding figure caption.

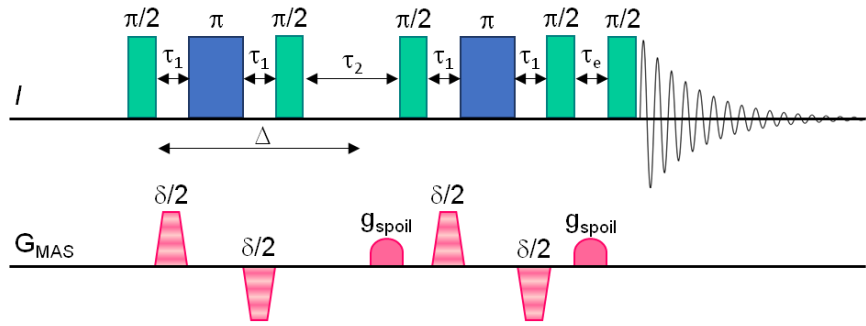


Figure 3.7. Representation of a PFG experiment with stimulated echo and longitudinal eddy current delay diffusion-filtered pulse sequence. Smoothed-square gradients with horizontal stripes correspond to pulsed-field gradients whose strength is varied during the experiment. Field gradients are short periods during which the applied magnetic field is made spatially inhomogeneous. All gradient pulses are trapezoidal shaped to compensate for the inability of instrumentation to generate perfect rectangular gradients. The gradient pairs are applied as bipolar gradients of opposite sign and separated by π r.f. pulses, an approach which reduces gradient artefacts, eddy currents and allows stronger overall gradients. The first $\pi/2$ pulse aligns all I magnetisation into the x,y -plane. The π pulse changes the direction of precession and refocuses chemical shifts, which is important in the presence of chemical exchange or spin diffusion. During the two τ_1 delays, the magnetisation is transverse, and therefore it is subject to T_2 relaxation. The second gradient of equal magnitude cancels the effects of the first and refocuses all spins, provided there was no change of position with respect to the direction of the gradient. During the τ_2 period, the magnetisation is aligned along the z -axis, and thus it is subject to T_1 relaxation. After the second $\pi/2$ pulse, the spins are in the z -axis so additional short gradient pulses, g_{spoil} , are added to destroy transverse magnetisation due to pulse imperfections. Eddy currents are generated in surrounding conducting surfaces by the rapid rise and fall of the gradient pulses. To prevent these effects a delay is necessary between the end of a gradient pulse and the start of spectral acquisition. During this eddy current delay (τ_e), magnetisation is stored in the z -direction and the eddy currents are allowed to decay. This sequence is less prone to T_2 artefacts because during the diffusion time (Δ) the magnetisation is in the z -axis. The stimulated echo sequence is also the method of choice for macromolecules.^{135, 168, 172, 186, 200}

Attenuated peak intensities are plotted against the b factor,

$$b = -\gamma^2 g^2 \delta^2 \left(\Delta - \frac{\delta}{3} \right).^{201} \quad \text{Equation 3.1}$$

Apparent self-diffusion coefficients (D) can be obtained from the mathematical fitting of the resulting curves to the mono-exponential Stejskal-Tanner function

$$I = I_0 e^{-D \gamma^2 g^2 \delta^2 \left(\Delta - \frac{\delta}{3} - \frac{\tau_e}{2} \right)} \quad \text{Equation 3.2}$$

where I is the observed intensity, I_0 is the unattenuated signal intensity and γ is the gyromagnetic ratio of the observed nucleus. Since bipolar gradients are used, a correction for the time τ_g between those bipolar gradients has to be applied.^{186, 200, 201}

3.11.3. Solution-state NMR spectroscopy

Solution-state NMR spectra were acquired at 11.7 T on a Bruker Avance I solution-state spectrometer equipped with a 5 mm $^1\text{H}/\text{X}/\text{Y}$ triple resonance probe head and a z-gradient coil reaching a maximum field gradient intensity of 34.1 G cm $^{-1}$, operating at 499.68 (^1H) and 125.65 MHz (^{13}C).

High-field solution-state NMR spectra were acquired at 18.8 T using a Bruker Avance III spectrometer equipped with a 5 mm $^1\text{H}/\text{X}/\text{Y}$ triple resonance probe head and a z-gradient coil reaching a maximum field gradient intensity of 49.5 G cm $^{-1}$, operating at 800.23 (^1H) and 201.24 MHz (^{13}C).

Gels were prepared by pipetting 600 μL of hot solutions into NMR tubes and allowed to gelate inside the tube. All experiments were acquired using a $\pi/2$ pulse length of 8.0 μs (^1H). Pulse delays were optimised for each experiment and are specified in the corresponding figure caption. The chemical shifts of ^1H and ^{13}C were referenced with respect to DSS or TMS inside a coaxial insert.

3.11.3.1. One-dimensional experiments

^1H single pulse experiments were acquired using the single pulse sequence shown in Figure 3.2.

3.11.3.2. Solvent suppression

^1H NMR spectra with solvent suppression were acquired using an excitation sculpting pulse sequence (Figure 3.8).

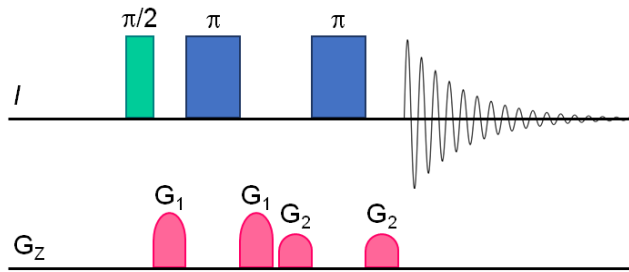


Figure 3.8. Representation of an excitation sculpting pulse sequence. It consists of a solvent-selective excitation profile (π pulse) embedded between two pulsed-field gradients. By applying the filter sequence twice with G_1 and G_2 not being correlated to each other, a flat baseline can be obtained.²⁰²

3.11.3.3. Longitudinal relaxation time

^1H longitudinal relaxation times (T_1) were determined using the standard inversion-recovery pulse sequence (Figure 3.9). 16 points were recorded with a recycle delay of 10 s and variable time delays (τ) ranging from 0.1 to 20 s.

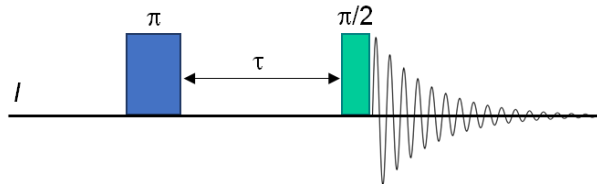


Figure 3.9. Representation of an inversion-recovery pulse sequence. The first π pulse inverts the magnetisation so that it lies along $-z$ -axis. Relaxation is then allowed to occur during the delay τ . The $\pi/2$ pulse converts it into transverse magnetisation for detection. During the set of experiments, the delay time τ is varied, which enables the remaining magnetisation to be plotted as a function of time delay.²⁰³

According to Bloch's theory, longitudinal relaxation follows first order kinetics. Hence, the evolution of peak intensities was fitted mathematically to the mono-exponential function

$$M_z(\tau) = M_0 \left[1 - 2e^{\left(\frac{-\tau}{T_1}\right)} \right] \quad \text{Equation 3.3}$$

where M_z is the z -component of magnetisation, M_0 is the equilibrium magnetisation and τ is the time delay.²⁰⁴

3.11.3.4. 2D ^1H - ^1H NOESY

2D ^1H - ^1H nuclear Overhauser effect spectroscopy (NOESY) NMR experiments were recorded using phase-sensitive 2D NOESY pulse sequence with symmetrical 3-9-19 WATERGATE²⁰⁵ (water suppression by gradient tailored excitation) for solvent suppression (noesygpph19) (Figure 3.10). Spectra were acquired with a recycle delay of 2 s, 32 scans and 16 points at variable mixing times (τ_m) ranging from 0.0025 to 1 s.

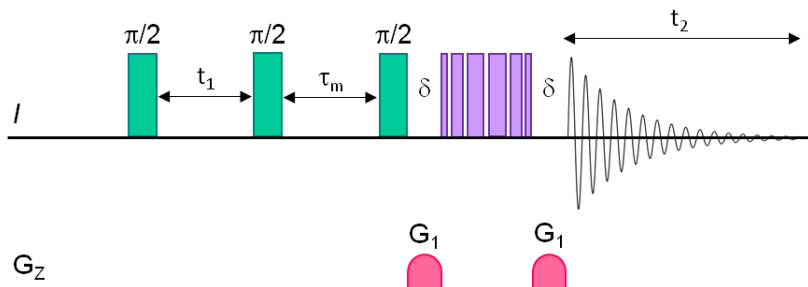


Figure 3.10. Representation of a 2D ^1H - ^1H NOESY NMR pulse sequence using WATERGATE²⁰⁵ 3-9-19 selective spin echo. The first $\pi/2$ pulse aligns all I magnetisation into the x,y -plane. During the evolution period, t_1 , chemical shifts and spin-spin couplings evolve. The second $\pi/2$ pulse aligns the y components of the two vectors, which are now labelled with their individual chemical shifts, into the z -direction. During the mixing period, τ_m , I spins are allowed to relax, show cross-relaxation and magnetisation is transferred. The final $\pi/2$ pulse realigns the vectors into the x,y -plane and creates transverse magnetisation for detection. WATERGATE²⁰⁵ 3-9-19 is a pulse train of symmetric pulses in the form $3\alpha-\tau-9\alpha-\tau-19\alpha-\tau-19\alpha-\tau-9\alpha-\tau-3\alpha$ with $26\alpha = \pi$ used for solvent suppression. The first sine-shaped gradient dephases all the resonances that have been excited by the first $\pi/2$ pulse. Then, the selective pulses reverse the sense of precession of all the spins of interest but not that of the solvent. The second sine-shaped gradient refocuses the I spins of interest whereas the solvent resonances dephase even further.^{172, 199}

Internuclear distances were calculated according to the initial rate approximation, which establishes that the evolution of the initial build-up of nOe enhancements with mixing time is approximately linear.¹⁵² The cross-relaxation rate can therefore be determined from the initial slope of the build-up curve (I_{IS} as function of τ_m), where the nOe enhancement (I_{IS}) is defined as the ratio between the intensity of the cross-peak at a certain mixing time and the intensity of the diagonal peak at zero mixing time ($I_{IS} = I_z \times I_{eq}$).¹⁴⁸ In turn, the cross-relaxation rate is proportional to the inverse sixth power of the internuclear distance (r_{IS}^{-6}), $\sigma_{IS} = \zeta r_{IS}^{-6}$. The observed nOe intensities have to be calibrated relative to a known internuclear distance.^{148, 152, 153}

3.11.3.5. 2D ^1H - ^1H COSY

2D ^1H - ^1H Homonuclear correlation spectroscopy (COSY) NMR experiments were recorded using magnitude-mode 2D COSY pulse sequence with gradients and purge pulses before the recycle delay (cosygpppqr) (Figure 3.11).

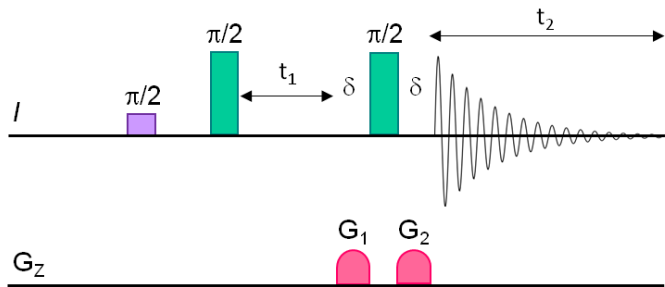


Figure 3.11. Representation of a 2D ^1H - ^1H COSY NMR pulse sequence. The $\pi/2$ purge pulse, indicated by the purple square pulse, consists of a long period of spin locking. Magnetisation not aligned along the spin locking axis will precess around the spin locking field and will dephase, as this purge pulse is used to suppress contributions from zero-quantum coherence. The first $\pi/2$ pulse transforms z -magnetisation into transverse magnetisation. The chemical shift of the direct dimension, f_2 , is modulated by the J -coupling of the indirect dimension, f_1 . Two gradient pulses of different strengths or durations are applied before and after the second $\pi/2$ pulse to select particular coherence transfer pathways.^{168, 172}

3.11.3.6. 2D ^1H - ^{13}C HSQC

2D ^1H - ^1H Heteronuclear single-quantum coherence spectroscopy (HSQC) NMR experiments were recorded using phase-sensitive improved-sensitivity 2D HQSC pulse sequence with echo/anti-echo coherence selection and gradients with improved sensitivity (hsqcetgpsi) (Figure 3.12).

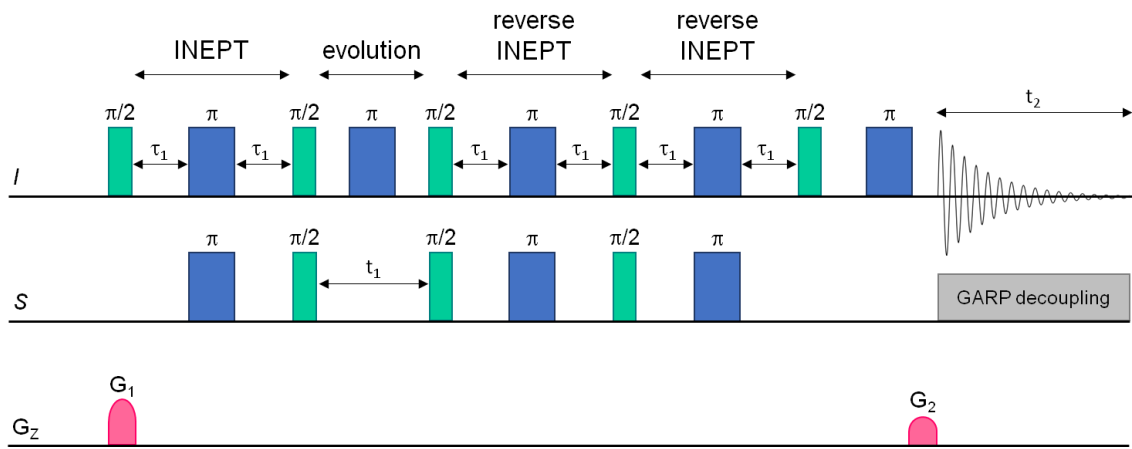


Figure 3.12. Representation of a 2D ^1H - ^{13}C HSQC NMR pulse sequence. The sequence starts with an INEPT transfer (insensitive nuclei enhanced by polarisation transfer) from I to S , which results in anti-phase magnetisation of S with respect to I . The editing period has the purpose of attributing different signs to CH and CH_3 , in comparison to CH_2 signals, and it is characterised by G_1 , the π pulse and the τ_1 delays. During the evolution period, t_1 , anti-phase magnetisation develops the S chemical shifts. The π pulse on I in the middle of t_1 applied over a period of time symmetrically distributed eliminates the $J(I,S)$ heteronuclear couplings in the f_1 dimension, when $t_1 = 1/(4J_{IS})$. Afterwards, a reverse INEPT transfer converts S magnetisation into in-phase I magnetisation. Unconventionally, there is the addition of a second reverse INEPT block in order to select both orthogonal components of the magnetisation present during t_1 and improve sensitivity. G_1 and G_2 are gradients for echo/anti-echo selection. Being an echo/anti-echo pulse sequence, the intensity of the refocusing gradient G_2 is inverted on alternated scans to obtain the N-(negative) and P-type (positive) data separately, which allows phase-sensitive spectra to be obtained. Acquisition is conducted with GARP²⁰⁶ decoupling.¹⁷²

3.11.3.7. STD NMR

Saturation transfer difference (STD) NMR experiments were performed using a pulse sequence with selective saturation of a given ^1H frequency by a train of 40 Gaussian pulses with the duration of 50 ms each and WATERGATE²⁰⁵ for solvent suppression (stddiffgp19.2) (Figure 3.13), acquired with a constant total experiment duration of 6 s.

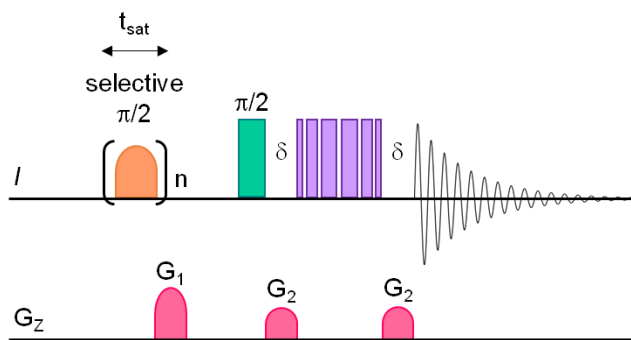


Figure 3.13. Representation of an STD NMR pulse sequence using WATERGATE²⁰⁵ 3-9-19 selective spin echo. During the saturation time, t_{sat} , I magnetisation is selectively saturated either on (STD_{on}) or off-resonance (STD_{off}) by a train of Gaussian pulses, indicated by the orange Gaussian-shaped pulse in brackets. The bandwidth of these 50 ms pulses is approximately 20 Hz, applied in a loop with $n = 40$, which results in a narrow-band irradiation. For every set of scans, the pre-irradiation frequency is changed from STD_{on} to STD_{off} (interleave mode) and the two spectra are stored separately. G_1 is a pulsed-field gradient that ensures that only z -magnetisation remains.^{158, 172, 196}

STD spectra were created by the subtraction of an on-resonance spectrum (STD_{on}), in which a spectral region was selectively saturated, to an off-resonance spectrum (STD_{off}), acquired with no selective saturation.^{158, 196} STD_{on} spectra were acquired at a saturation frequency of 0 or 1 ppm (where only resonances of the network can be encountered), whereas the STD_{off} saturation frequency was set for 40 ppm.¹⁵⁸ Interleaved acquisition of STD_{on} and STD_{off} spectra was performed as a pseudo-2D experiment to minimise artefacts caused by variations throughout the experiment.¹⁵⁸ Each pair of experiments was acquired at variable saturation times (t_{sat}) ranging from 0.25 to 6 s. Peak intensity in the difference spectrum relative to the signal intensity in the STD_{off} spectrum was used to determine the fractional STD response, η_{STD} ,

$$\eta_{\text{STD}} = \frac{I_0 - I_{\text{SAT}}}{I_0} \times 100 = \frac{I_{\text{STD}}}{I_0} \times 100 \quad \text{Equation 3.4}$$

where I_0 is the peak intensity from the STD_{off} spectrum, I_{SAT} is the peak intensity from the STD_{on} spectrum and I_{STD} is the peak intensity from the difference spectrum.¹⁵⁸ STD build-up curves were fitted mathematically to the mono-exponential function

$$\text{STD}_{(t_{\text{sat}})} = \text{STD}^{\max} (1 - e^{(-k_{\text{sat}} \cdot t_{\text{sat}})}) \quad \text{Equation 3.5}$$

where STD^{\max} is the maximum possible STD response at very long saturation times, k_{sat} is the saturation rate constant and t_{sat} is the saturation time. The initial slope values of the build-up curves, STD_0 , were obtained from the product $STD^{\max} \times k_{\text{sat}}$.¹⁹⁶

3.11.4. Two-dimensional experiments

In two-dimensional (2D) NMR experiments, the signal is recorded as a function of two time variables, t_1 and t_2 , and the resulting data is Fourier transformed twice to yield a 2D spectrum which is a function of two frequency variables, f_1 and f_2 .

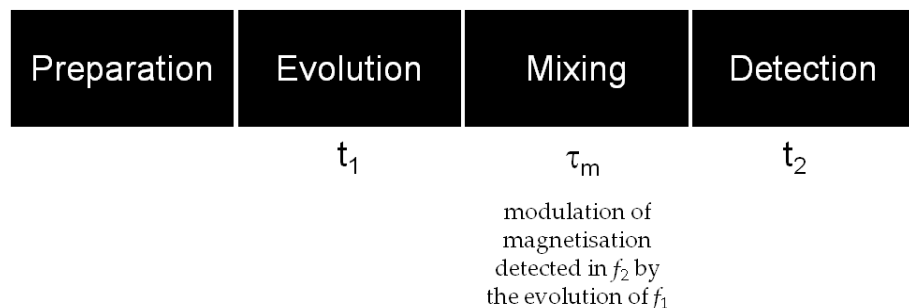


Figure 3.14. 2D NMR experiments start with the preparation time, in which the sample is excited. The resulting magnetisation is allowed to evolve during the evolution time, t_1 . During the mixing time, τ_m , there is modulation of magnetisation detected in f_2 by the evolution of the frequency of the second spin, f_1 . Finally, during the detection period, the signal is recorded as a function of the second time variable, t_2 . This pulse sequence is repeated cyclically and a free induction decay is recorded as a function of t_2 for increasing t_1 values.¹⁶⁸

3.11.5. Variable temperature

Variable temperature measurements were typically performed between 273 and 363 K at 5 K intervals, allowing equilibration of thermal conditions for 15 min before acquisition. Temperature control was accomplished with a FTS System cooling unit for solution-state experiments; and with a Bruker BCU-II chilling unit and through heating the bearing gas within the probe *via* a probe filament for solid-state measurements.

3.11.6. Data processing

NMR spectra were acquired and processed using Bruker Topspin 3.1.7 analysis software. All ¹⁹F, ¹³C and ¹⁵N spectra were fitted with 200, 60 or 0 Hz line broadening, respectively. Further processing was carried out with Origin 9.0, including fitting of ¹H T_1 decays, PFG intensities for determination of self-diffusion coefficients and fractional STD response build-up curves.

Chapter 4

4. Literature review on the structural motifs and self-assembly processes of phenylalanine

4.1. Introduction

The present chapter is an overview of the current knowledge on aggregation and gelation of phenylalanine in water, to put into context the following results chapters. *L*-Phenylalanine (Phe), (S)-2-amino-3-phenylpropanoic acid, is a natural amino acid that plays a significant role in several biological processes. Phe is also a key component in the synthesis of natural and synthetic products such as aspartame, peptides and medicines.^{55, 207-209} Furthermore, non-covalent interactions between Phe and other amino acids are essential in dictating peptide and protein aggregation, which is important in many pathological disorders. Examples include the formation of β -amyloid fibres, which have been linked to the development of Alzheimer's disease, type II diabetes and prion disorders.^{55, 207-209}

Recently, a relationship between the accumulation of Phe *in vivo* and its capability of self-assembling into stable aggregates inside human cells has been established.^{55, 74, 207-210} Accumulation of Phe in the human body has pathological implications, giving rise to a characteristic syndrome defined as phenylketonuria (PKU).^{55, 207-209} PKU is an autosomal recessive disease that originates from mutations in the gene coding for phenylalanine hydroxylase.^{55, 207-209} The absence of this enzyme leads to a significant accumulation of Phe in the plasma, brain tissue and cerebral fluids.²⁰⁷ Phe saturates the *L*-type amino acid transporter, depriving the brain of tyrosine, dopamine and epinephrine and hindering brain development.²⁰⁷ The resulting accumulation of micromolar concentrations of Phe leads to the formation of stable and toxic aggregates *in vivo*.^{207, 209} However, it has been defended that Phe serum levels (500 μ M) do not account for the high local concentrations,

which might be even higher in the regions of the brain associated with the neurotoxic effects.^{74, 211}

Phe self-assembles into long fibres that give rise to a supramolecular crystalline hydrogel at millimolar concentrations *in vitro*.^{207, 208, 212} Hydrogelation of Phe was first described in 2002 by Myerson *et al.* as producing a hydrogel containing crystals – the material was named a gel-crystal.²¹² To date, Phe is one of the smallest molecules known to form supramolecular hydrogels and it is of particular interest due to its crystalline gel state.²¹² The numerous new crystal structures, polymorphs, hydrates and gel forms described recently have increased the interest in the solid state behaviour of Phe.^{66, 213-215} Thus, this chapter summarises and provides a timeline for the most relevant information gathered to date on the early stages of self-assembly of Phe in water, the structure and dynamics of the resulting gel fibres and the solid state landscape of Phe.

4.2. Investigating early stages of self-assembly of Phe

The correlation between supramolecular aggregation of Phe and PKU exposed the need for investigating self-assembly processes of Phe in water. In the past decade, research groups focused mainly on the structure and dynamics of gels, disregarding the clarification of the initial stages of molecular assembly.⁴⁶ Hence, it was decided that this chapter should start by describing puzzling, but essential discoveries made on the early stages of aggregation of Phe. Unravelling dynamics of the initial steps of self-assembly of molecular gelators is critical to understand the final self-assembled structures.⁴⁶

Infrared spectroscopy studies performed on aqueous solutions of Phe in 2006 by Komorowska's group showed that association of Phe in water resulted in strong and stable aggregates due to the ability of Phe to promote reorientation of water molecules, called hydrophobic hydration.²¹⁰ This prevented water from surrounding the non-polar groups, enhanced the free energy of interaction and facilitated contact between solute molecules.²¹⁰

In 2012, Adler-Abramovich *et al.* performed electron diffraction studies in solutions of Phe in water (6 mM) and established that fibrils exhibited well-ordered motifs.²⁰⁷ The electron diffraction pattern of a single fibril (Figure 4.1a) was consistent with molecular dynamics simulations conducted at high pH and in the presence of counterions. The resulting low

stability structure showed a ladder-like arrangement with interspersed counterions (Figure 4.1b).²⁰⁷ Pairs of neighbouring molecules were closely involved in direct hydrogen bonds or salt-bridged polar interactions.²⁰⁷ Hence, the charged carboxyl termini faced each other and were bridged by counterions of opposite charge. Because of this arrangement, the hydrophobic aromatic rings were in contact with the surrounding water molecules, an energetically unfavourable situation.

Moreover, Adler-Abramovich *et al.* defended that PKU was closely related to the family of amyloid-based diseases and thus should have similar aetiology. This statement was based on the detected birefringence in microscopic studies and excitation shifts in Congo red and thioflavin T (ThT) fluorescence assays typical of amyloid fibrils.²⁰⁷ Pursuing the role of Phe in the symptoms linked to PKU, they proved that the high build-up of Phe in the hippocampus and the parietal cortex area of the brain resulted in the formation of supramolecular fibrillar structures that were responsible for Phe's cytotoxicity.²⁰⁷ They suggested that these fibrils interacted and were incorporated inside cells, as they could be found intracellularly after their incubation with Phe.²⁰⁷

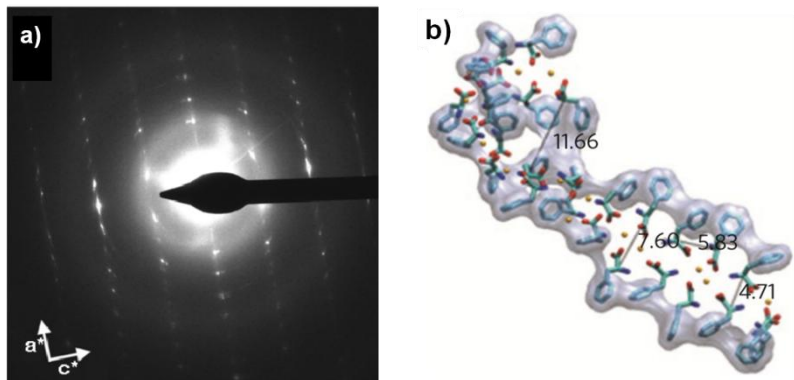


Figure 4.1. a) Electron-diffraction pattern of a single Phe fibril.²⁰⁷ b) Ladder-like structure of Phe aggregates obtained by molecular dynamics simulations conducted at high pH in the presence of counterions (yellow spheres).²⁰⁷

In 2013, Perween *et al.* refuted Adler-Abramovich and co-workers interpretation of thioflavin T fluorescence assays.⁵⁵ They defended that the characteristic ThT fluorescence was due to the parallel binding of ThT along the molecular axis of the fibrils, hence it did not necessarily imply formation of β -sheet assemblies. Their justification was supported by the lack of Congo red binding, the absence of an absorption band typical of β -sheet-like

structures between 1600 and 1700 cm⁻¹ in FTIR studies and no proof of the intercalation of ThT molecules in Phe fibres in confocal microscopy images.⁵⁵ By combining Congo red and ThT photoluminescence, FTIR and confocal microscopy, Perween *et al.* concluded that Phe fibres do not have amyloid-like features. In clear contradiction with the report by Adler-Abramovich *et al.* (2012),²⁰⁷ Perween *et al.* suggested that it is a network of strong hydrogen bonds and electrostatic interactions that is responsible for aggregation, attributing only a secondary role to π - π interactions between phenyl residues of adjacent monomers of Phe in the stabilisation of fibres.⁵⁵ They determined that Phe fibres can be obtained between 1 and 100 mM solutions of Phe in deionised water (pH = 7), giving rise to fibre widths between 300 to 800 nm and lengths in the order of several micrometers.⁵⁵

Later, Mossou *et al.* (2014) characterised water-free assemblies of Phe using synchrotron X-rays.⁶⁶ They came up with a crystal structure with a monoclinic space group *P21* with four molecules in the asymmetric unit (Figure 4.2a). This structure was composed of layers stabilised by alternating hydrophobic and hydrophilic interactions (Figure 4.2b).⁶⁶ The crystal packing assumed laterally displaced rings and edge-to-face ring interactions between layers, forming an angle of 45° between rings.⁶⁶ They proposed that a strong set of π - π stacking and hydrogen bonding interactions held the network together.⁶⁶ These interactions were considered significant in the self-assembly processes of Phe nanofilaments.⁶⁶

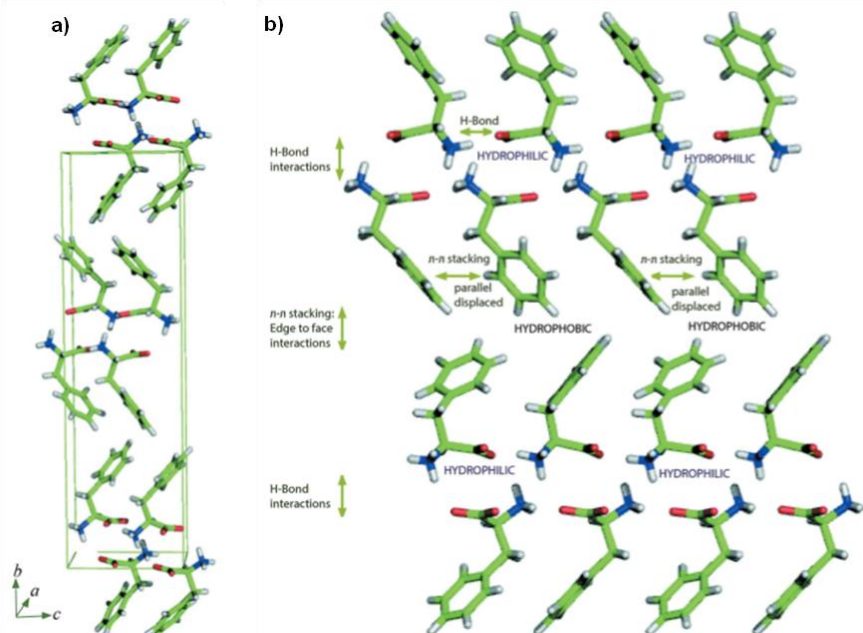


Figure 4.2. a) Monoclinic unit cell of Phe. b) Proposed interactions involved in the stabilisation of Phe fibres, composed of a bilayer of hydrophobic/hydrophilic interactions.⁶⁶

German *et al.* (2014) were mainly interested in understanding the structure of early stage assemblies of Phe. By conducting molecular dynamics simulations at physiological pH using a semi-empirical force field (OPLS-AA) as implemented in GROMACS²¹⁶, it was determined that tubular pore-like structures were dominant, with each layer consisting of four Phe molecules (Figure 4.3a). They defended that a more likely candidate for oligomer and fibril formation contained this four-fold symmetry in which molecular termini acted as an anisotropic driving force for vertical formation of nanotubes.^{66, 74, 207} However, they also found less stable aggregates similar to the crystal structure of the Phe monohydrate²¹⁴ (Figure 4.3b) or the previously proposed ladder-like form²⁰⁷ (Figure 4.1b) during the simulations.⁷⁴ The newly determined structure by German *et al.* (2014) was in agreement with the one determined by electron diffraction.^{74, 207} It was concluded that the small pore size (4.93 Å) of the proposed tubular structures did not allow water molecules to pass through. Hence, the cytotoxicity associated with Phe aggregates was not due to the formation of a water channel inserted in the cell membranes but it was more likely that Phe rings interacted with the aliphatic chains of the lipids, which would separate the polar head groups of the lipids and lead to membrane disruption.⁷⁴

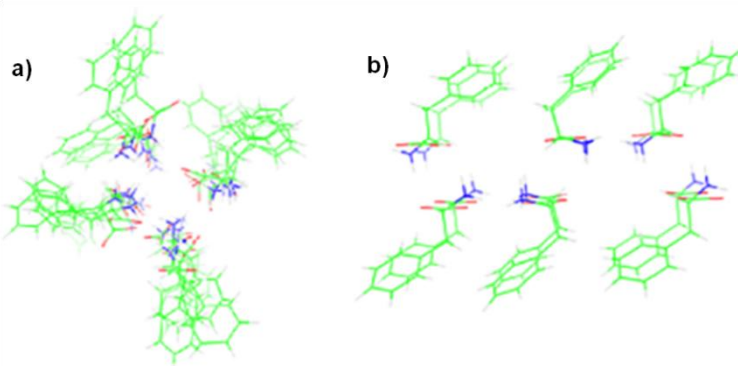


Figure 4.3. a) Lowest energy nanotubular structure ($-8434 \text{ kJ mol}^{-1}$) of Phe proposed by German *et al.*⁷⁴ and b) crystal structure of Phe monohydrate from reference ²¹⁴. Green atoms represent carbon, blue represent nitrogen, red represent oxygen and white represent hydrogen.⁷⁴

In 2015, Do *et al.* conducted ion-mobility mass spectrometry to study the structure of successively formed Phe oligomers that pre-empt fibre formation.²⁰⁹ Initially, they performed experiments in water and at neutral pH using a 6 mM concentration of Phe.²⁰⁹ Since German *et al.* (2014) had verified the presence of low abundance ladder-like

structures at neutral pH without counterions, and such structures were initially proposed by Adler-Abramovich *et al.* (2012) at high pH in the presence of counterions, Do *et al.* wanted to address this inconsistency and to clarify the mechanism of assembly in water at physiological conditions.²⁰⁹ In the presence of oligomers with a low number (n) of Phe molecules (n up to 20) structures resembled the single-tube model, whereas structures with medium-sized oligomers ($n = 20$ to 35) corresponded to double-tube models (Figure 4.4).²⁰⁹ The remaining data were better fitted by the tetra-tube model. In this model, Phe oligomers become more stable as size increases.²⁰⁹

The measurements at high pH (pH = 11) using ammonium acetate buffer revealed the presence of two octamer isomers. The dominant isomer was very similar to the one recorded in water (Figure 4.4), whereas the minor isomer was significantly larger and resembled the ladder-like structure obtained by Adler-Abramovich and co-workers. Do *et al.* confirmed the presence of this structure, but since the self-assembly of the latter was driven by non-zwitterionic NH₂ and COO⁻ terminal interactions, the resulting structures were relative unstable. In contrast with what was claimed by Adler-Abramovich and co-workers, the ion-mobility mass spectrometry data obtained by Do *et al.* indicated that counterions (NH₄⁺) disrupted these ladder-like structures and prompted rearrangement into the pore-like structures found at neutral pH.²⁰⁹ Overall, their results suggested that the aggregation pathway of Phe involved the formation of hollow tetrameric oligomers. These tetramer layers stacked on top of each other, building multiple core structures through lateral π -stacking interactions. The toxicity of these aggregates should arise from their hydrophobic outside surface, thus facilitating insertion and penetration into the cell membrane, coupled to their hydrophilic interior surfaces that had the potential to cause ion leakage.²⁰⁹

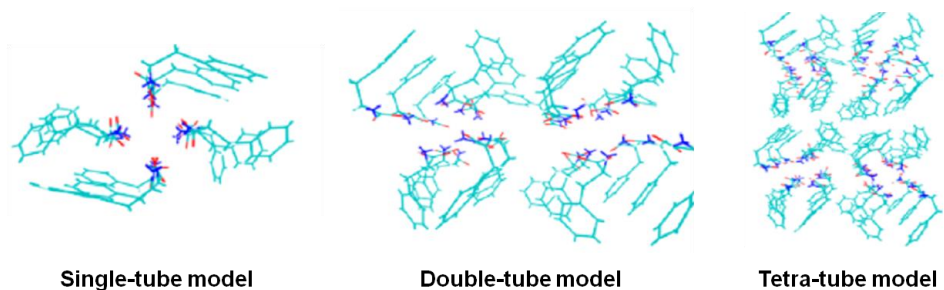


Figure 4.4. Representative structures of single, double and tetra-tube models.²⁰⁹

Griffith *et al.* (2015) found experimental evidence supporting German *et al.* and Do *et al.* proposed the cause for Phe's cytotoxicity. They investigated the interaction of Phe with a phospholipid monolayer.²¹⁷ Using a combination of surface-sensitive experimental techniques and molecular dynamics simulations, they established that Phe was able to intercalate itself into a 1,2-dipalmitoyl-sn-glycero-3-phosphocholine (DPPC) monolayer at the air/water interface (Figure 4.5).²¹⁷ Consequently, the presence of Phe affected surface tension, phase morphology and ordering of the DPPC film, which could greatly influence the permeability and stability of a cell membrane.²¹⁷ Furthermore, the conversion of the zwitterionic form into the neutral form when Phe was located in the hydrophobic region of the phospholipid layer was observed.²¹⁷ This represented a worse situation, as the neutral form of Phe would be able to penetrate deeper into the hydrocarbon core of the film and be incorporated fully into the membrane, cross the membrane and/or promote local aggregation of Phe.²¹⁷

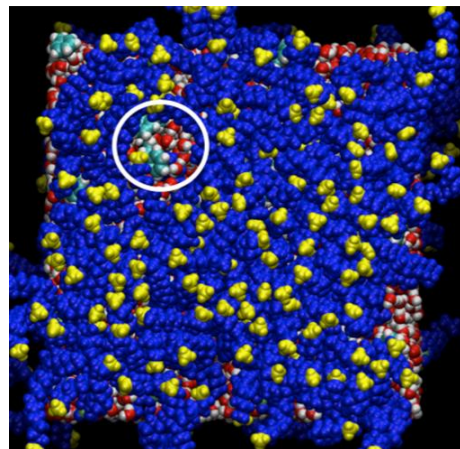


Figure 4.5. Top-view snapshot of a small-scale defect (circled in white) in a DPPC film from molecular dynamics simulations. DPPC molecules are coloured blue with terminal methyl groups coloured yellow. Water molecules are red and white and Phe molecules can be seen by their light blue aromatic rings.²¹⁷

4.3. Exploring gelation properties of Phe

Thakur and co-workers (2014) were the first group to investigate self-assembly of Phe in water at gel forming concentrations (300 mM).²⁰⁸ The zwitterionic features of Phe molecules suggested a pH-dependent self-assembly. Hence, white opaque hydrogels were prepared in water and phosphate-buffered saline at pH values of 2, 5.5, 7.4 and 9 (Figure 4.6a), with kinetics of gel formation slowing down at pH = 9.²⁰⁸ Similar fibre morphology

was identified at all pH values, but longer multi-nodal fibres were detected at a pH of 9.²⁰⁸ Variation of ionic strength had a more marked effect in fibre morphology, as increased ionic strength led to larger particle size from z-average measurements by dynamic light scattering. They proposed that this was due to salt-induced charge suppression, resulting in strong hydrophobic interactions.²⁰⁸ Despite recognising that previous studies assumed hydrogen bonding between $-\text{C=O}\cdots\text{HOOC}-$ and electrostatic interactions between $-\text{NH}_3^+ \cdots \text{O=C}-$ as being responsible for Phe aggregation,²¹⁰ Thakur and co-workers insisted that hydrophobic interactions directed self-assembly processes of Phe.²⁰⁸ They supported their hypothesis on concentration-dependent solution-state NMR studies of hydrogels of Phe, in which an upfield shift was observed for the aryl protons (Figure 4.6b). However, the rate of change of ¹H chemical shift values shown in their supporting information was more significant for the aliphatic than for the aryl protons (Figure 4.6c).²⁰⁸

Taking into account the pathological implications of intracellular accumulation of Phe, Thakur and co-workers investigated strategies to disrupt these stable fibrous aggregates. Equimolar racemic mixtures of *L*- and *D*-Phe led to formation of more stable racemate plaques instead.²⁰⁸ The cytotoxicity of these racemate plaques has not been evaluated yet, therefore their proposal as a therapeutic molecule in PKU remains doubtful. Up to date, a viable and less toxic alternative is still needed.

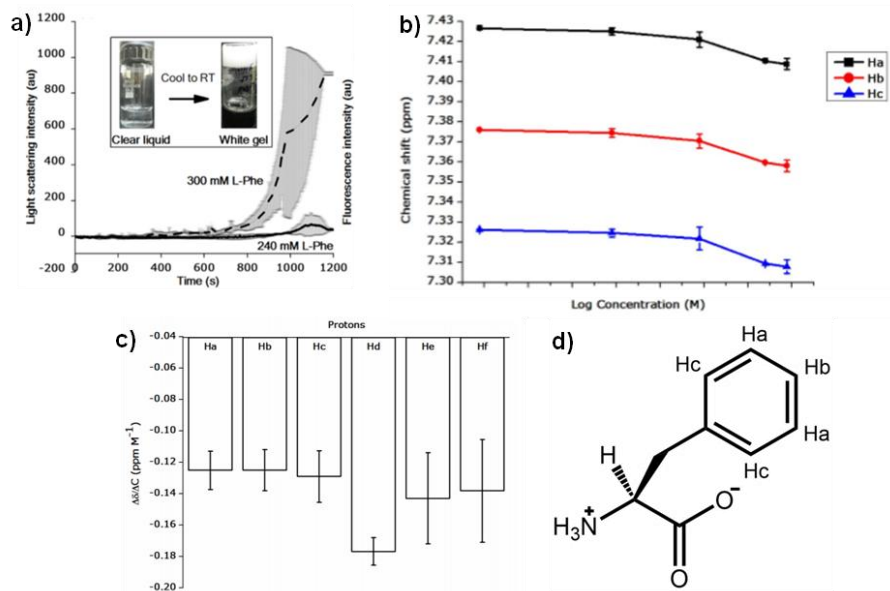


Figure 4.6. a) Kinetics of hydrogel formation of Phe from dynamic light scattering studies, with a photograph of a self-supporting gel (300 mM). The initial lag-phase might be due to nucleation events where molecules associate to form productive nucleus for further elongation into mature fibres, or the associated molecules are insensitive to light scattering. b) Variation of ^1H chemical shift of aryl protons with concentration of Phe and c) rate of change of ^1H chemical shift with respect to change in concentration ($\Delta\delta/\Delta C$) for all Phe protons. d) Molecular structure of Phe with assignment.²⁰⁸

4.4. Structural motifs of Phe gel fibres

The need for determining the crystal structures of the 20 essential amino acids has been recognised for some time.²¹³ The lack of reported crystal structures is often due to the difficulties in obtaining sufficiently large and good quality crystals suitable for single-crystal X-ray diffraction studies.²¹³ The crystallographic studies conducted by the groups of Harris, Gazit, Korter and Görbitz contributed significantly to the understanding of the crystalline packing motifs of Phe in the solid state (Table 4.1), using single-crystal and powder XRD studies, and computational approaches.^{66, 213-215} These groups proved the existence of a total of seven solid forms, which reflect the structural complexity of this essential amino acid (4 polymorphs, two hydrates and a racemic solid form).⁸²

Table 4.1. Crystallographic unit cells of Phe.²¹⁵

Form	I ²¹⁸	II ²¹⁵	II ²¹³	III ⁶⁶	IV ²¹⁵
space group	C2	P2 ₁	P2 ₁	P2 ₁	C2
<i>a</i> / Å	8.804	8.7829/8.7955	12.063	6.0010	9.6806
<i>b</i> / Å	6.041	5.9985/6.0363	5.412	30.8020	5.2362
<i>c</i> / Å	31.509	31.0175/31.5233	13.676	8.7980	15.8474
β / °	96.60	96.9220/96.6441	99.5976	90.120	96.291
<i>V</i> / Å ³	1667.6	1622.12/1622.40	880.3	1626.24	798.46
<i>Z'</i>	2	4	2	4	1
T / K	298	105/293	294	100	100

4.5. Aims of the project

Although a better understanding of the early stages of aggregation of Phe was gained, together with intermolecular interactions and structure of the gel fibres, the supramolecular packing motifs and dynamics of the resulting hydrogels remain unclear, a gap that is addressed in the following results chapters. Consequently, one of the main priorities when studying Phe was to determine the supramolecular packing motifs of the hydrogel network. Studies on this topic are discussed in Chapter 5 (section 5.2.4, page 157) and prove that Phe hydrogels have a very crystalline nature and the crystal structure of the gel fibres, determined directly on the gel fibres, corresponds to the monohydrate form of Phe.

Even though Mossou⁶⁶ and Thakur²⁰⁸ groups attributed considerable importance to hydrophobic interactions between phenyl rings in the formation of Phe fibrils, Perween *et al.* (2013)⁵⁵ contradicted their conclusions. With the purpose of clarifying these inconsistencies, experimental evidence is provided in Chapter 5 (section 5.2, page 149) that enables the conclusions to be drawn that the main driving force of gelation is the strong ionic interaction between the electrostatic ends of Phe.

Understanding hidden dynamics of molecular gels of Phe was one of the main goals of the project. It was found that dynamic processes of Phe were best understood in the presence of structurally diverse additive molecules, henceforth the effects of introducing amino acids are described in Chapter 6 (page 164), molecules that form fibres isostructural to those of Phe are discussed in Chapter 7 (page 186) and molecules that show concentration-dependent disruptive and gelation behaviours are shown in Chapter 8 (page 219).

Chapter 5

5. Gel-crystallisation of Phe: structure, dynamics and molecular-level characterisation

Findings from this chapter are partly published in

Nartowski, K. P.; Ramalhete, S. M.; Martin, P. C.; Foster, J. S.; Heinrich, M.; Eddleston, M. D.; Hayley, G. R.; Day, G. M.; Khimyak, Y. Z.; Lloyd, G. O., The plot thickens: gelation by phenylalanine in water and dimethyl sulfoxide. *Crystal Growth & Design*, 2017, 17(8), 4100-4109.

5.1. Introduction

The ability of Phe to self-assemble into organised supramolecular structures, giving rise to crystalline hydrogels under certain conditions, has caught the attention of several research groups.^{55, 74, 207-210, 212-214} Detailed description on this topic can be found in Chapter 4 (page 138), which summarises the up to date information on nucleation and growth of Phe into self-assembled structures.

This chapter highlights the relationship between gelation, crystallisation and dynamics of self-assembly of Phe in water. The gelation of Phe and its gel/crystal relationship are described, as well as the crystal structure predictions conducted for this relative simple compound. NMR studies were used to elucidate structure and dynamics of Phe molecules. The main purpose of this work was to provide guidance to future research into Phe assemblies, and possible treatments for phenylketonuria and diseases based on the formation of stable β -amyloid fibres.

Phe was also able to gelate DMSO, giving rise to transparent gels of low crystallinity. The resulting gels were structurally and dynamically different from hydrogels, denoting the

importance of solvent properties, but the description of organogels of Phe falls out of focus of this thesis. Findings related to DMSO gels can be found in reference ⁸².

This project resulted from the collaborative work between the groups of Dr. Gareth Lloyd (Heriot-Watt University), responsible for microscopy imaging, rheology measurements and diffraction studies and Professor Graeme Day (University of Southampton), who performed computational modelling experiments. My group conducted the characterisation of the gelation ability of Phe and of the resulting gel materials using NMR spectroscopy. Calculations of NMR parameters were conducted in collaboration with Dr. Karol Nartowski (University of East Anglia).

5.2. Results

5.2.1. Macroscopic and mechanical properties of Phe hydrogels

During the process of cooling of hot solutions of Phe, the formation of white, cloud-like centres was observed, followed by growth and entanglement of fibres, ultimately leading to the formation of white opaque hydrogels (CGC = 212 mM) (Figure 5.1b). Above a certain concentration of Phe in water (605 mM), the process of gelation occurred simultaneously with crystallisation of the anhydrous form I. This point was taken as the maximum concentration, below which only pure gelation occurs with no visible presence of crystallisation of the anhydrous form. Fast quenching of the solutions was essential to ensure gelation, as lowering the temperature gradually led to the formation of solid precipitates. It should also be noted that racemic mixtures prevented gelation and promoted crystallisation instead, as reported by Thakur and co-workers.⁸²

Similarly to Thakur, it was observed that hydrogels were rheologically weaker upon changing the pH away from its isoelectric point, $pI = 5.48$ (*i.e.*, by adding HCl or NaOH and measuring the pH of the solution with a pH meter) or by the addition of salt. Gels became metastable upon the addition of NaCl (above 100 mg / 5 ml) preferring the formation of the crystalline anhydrous form I.

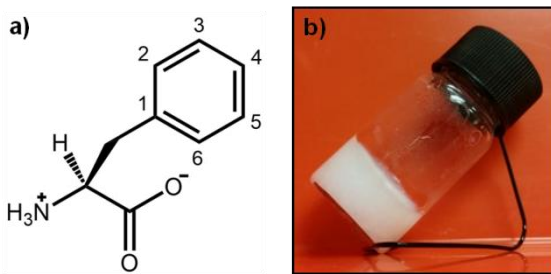


Figure 5.1. a) Molecular structure of *L*-phenylalanine, with numbered carbons. b) Hydrogel of Phe (303 mM).

The measurements of the rheological properties of hydrogels (Figure 5.2) provided clear evidence of the viscoelastic nature of the materials and the importance of defining these phases as gels. Frequency sweep rheometry with a small amplitude stress revealed the solid-like nature of the gels at 293 K, with the storage moduli, G' , being typically an order of magnitude greater than the loss moduli, G'' (Figure 5.2a). Concentrations of Phe higher than 303 mM exhibited G' values in the range of 10^5 Pa, unusually observed values that are characteristic of very strong gel materials.²¹⁹

The non-linear rheological response for the gels was also investigated using stress sweep experiments. The high elastic moduli values for the hydrogels revealed a robust material. The gels showed a G' value essentially constant below the critical value of oscillatory torque (“yield stress”), again showing a behaviour typical of a gelatinous material (Figure 5.2b).

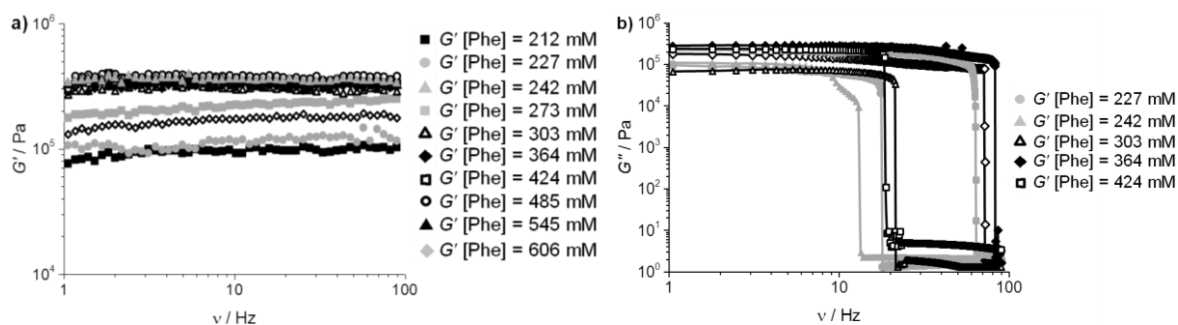


Figure 5.2. a) Frequency sweep and b) stress sweep experiments for different concentrations of Phe hydrogels. Lines between points were added to help guide the eye. Hot solutions (*ca.* 0.5 mL) were pipetted into a 150 μm gap (cone and plate geometry). All samples were subjected to frequency sweeps in the range of 0.1 to 100 Hz and applied stress of 700 Pa, as well as stress amplitude sweeps in the range of 500 to 10000 Pa.

5.2.2. Morphology of the gel-crystals

Microscopic analysis of the hydrogels showed the presence of thin fibres with an average width of 440 nm and 0.2–2 mm diameters (Figure 5.3a,b), which is consistent with the fact that the gels are opaque and that the fibrous nature can be observed with the visible eye. The fibrous nature of the hydrogel was also confirmed through imaging by electron microscopy (Figure 5.4a).

Since the phenomenon of Phe hydrogelation had been described previously as “gel-crystallisation” by Myerson,²¹² diffraction studies were performed on the gel samples to understand why this may be the case. This revealed that the dry and wet hydrogels were considerably crystalline in nature, with no indications of amorphous or semi-crystalline phases ([Phe] = 303 mM). TEM diffraction images of dried samples (Figure 5.4b) also revealed a single phase of excellent crystallinity.

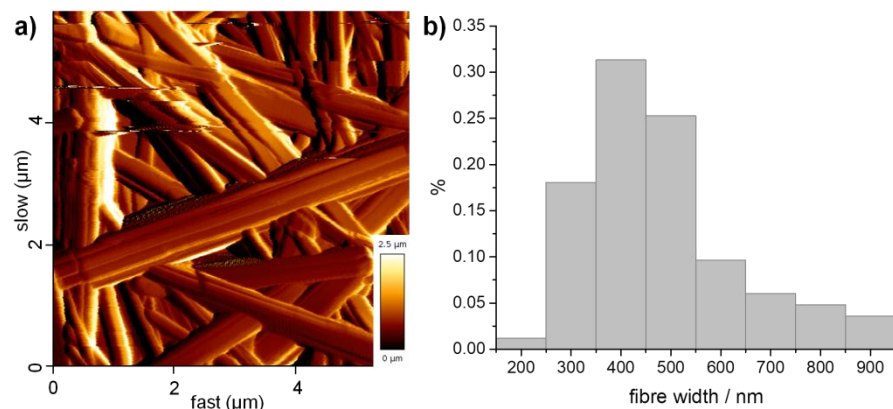


Figure 5.3. a) AFM image of the dry hydrogel of Phe, highlighting the entanglement of a fibrous network. b) Histogram of measured widths in AFM experiments for the hydrogel of Phe, with an average width of 437 ± 16 nm.

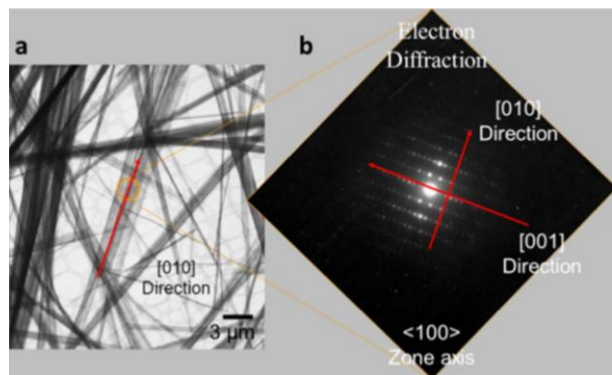


Figure 5.4. The determination of the hydrate structure of the hydrogel allows for **a)** the morphology of the fibres by TEM to be confirmed and **b)** the molecular packing in these fibres determined by electron diffraction. Zone axis electron diffraction of the fibres indicates the growing direction to be the [010] crystallographic direction.

Initial attempts to identify this phase were unsuccessful until the PXRD data produced by Harris and co-workers in 2013 confirmed the material to be the hydrate phase of Phe.²¹³ It was then possible to confirm this phase by obtaining single-crystal data sets of both the monohydrate and hemi-hydrate forms of Phe from fibres pulled directly from the gels. I believe the process of isolating the fibre from the gelation mixture can result in dehydration of the hydrate phase to give a crystal of the hemi-hydrate form, also reported by Harris *et al.*²¹³ Hence, solid-state NMR studies were performed directly on the hydrogel phase and were in agreement with spectra presented by Harris and co-workers for the Phe monohydrate (Figure 5.5).²¹³ This enabled to confidently assign this material as the monohydrate crystal form of Phe utilising chemical shift calculations with CASTEP. These experiments are described below (section 5.2.4, page 157).

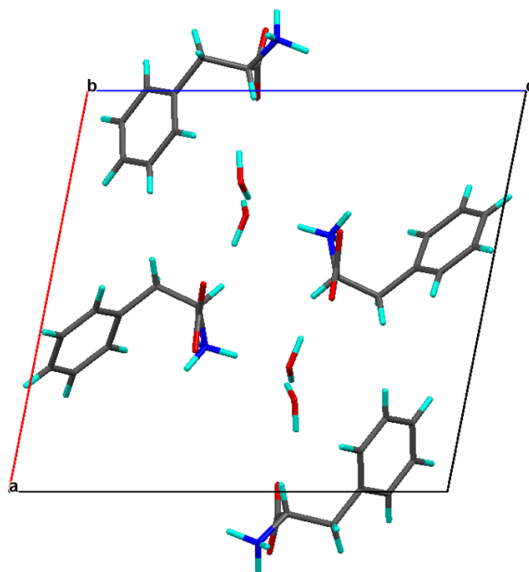


Figure 5.5. Unit cell of Phe monohydrate shown along the a axis (CCDC Number 1532251). The unit cell presented monoclinic metric symmetry, with the following refined parameters: $a = 13.112(14)$ Å, $b = 5.409(5)$ Å, $c = 13.849(14)$ Å, $\beta = 102.985(4)$ Å, ($V = 957.11(17)$ Å 3) and $Z = 4$. The space group was assigned as $P2_1$.²¹³

When the molecular packing of Phe in the hydrogel form was identified, it allowed for analysing the morphological characteristics of self-assembly and attempts to understand why Phe shows preference for forming fibrous assemblies. Prof. Graeme Day's groups performed Bravais–Friedel–Donnay–Harker (BFDH) crystal morphology calculations, which indicated a needle habit (Figure 5.6a,b). The non-growing faces of the morphology were [100] and [001], which represent the hydrophobic faces. This, however, did not fully explain the “extreme” needle/fibre morphology. Intermolecular supramolecular interaction analyses of the crystal structure also did not divulge any clear unidirectional interactions, such as hydrogen bonding, π - π stacking or van der Waals interactions.

However, the electrostatic potential Hirshfeld surface analysis of Phe molecules of the monohydrate structure exposed the anisotropic character of the molecules (Figure 5.6c,d). This clearly confirmed that Coulombic interactions are an important intermolecular force in determining fibre morphology. The influence of electrostatics in the form of Coulombic interactions is sometimes underestimated, even though they can make a dominant contribution to intermolecular interactions, and their strong directionality often makes them structure determining.^{220–223} This was confirmed by face indexing the fibres by electron diffraction in TEM experiments. The electron diffraction patterns obtained matched the calculated patterns from the monohydrate crystal structure. The direction of

the long axis of the fibres could be attributed to the [010] direction of the monohydrate structure. This [010] direction corresponds to the stacking of the positive and negative charges of the zwitterionic Phe molecules in an expected $+/-/+/-$ arrangement.

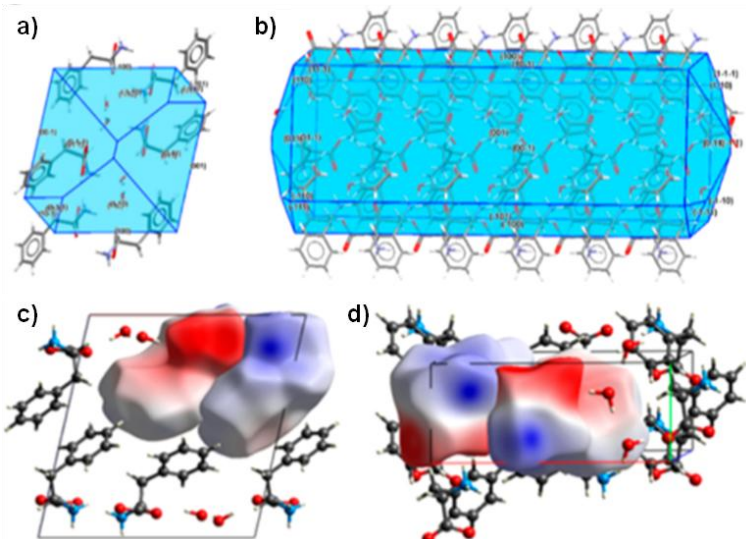


Figure 5.6. a,b) BFDH crystal morphology calculation indicated a needle habit of Phe monohydrate. Analysis of the crystal structure indicated that c) the electrostatics (shown here as the electrostatic potential Hirshfeld surface) are a significant interaction for the stacking of Phe in this anisotropic manner, with π - π stacking, hydrogen bonding and van der Waals interactions complementing the $+/-/+/-$ stacking in the [010] direction. Figure c) shows the structure viewed down [010] and d) is shown viewed down the [001] with *b* axis coloured green, *a* axis red and *c* axis blue.

5.2.3. Computational modelling of structure of Phe fibres

As the solid matrix of the hydrogel is clearly crystalline in nature, Prof. Day's group conducted CSP calculations to investigate the structural landscape of Phe. CSP calculations were performed in the common Sohncke space groups with $Z' = 1$ and 2, taking into account the conformational flexibility of the molecule. Lattice energy calculations were also performed on the known $Z' = 4$ forms I and III for comparison of their stabilities to the $Z' = 1$ and $Z' = 2$ landscape of structures.

The results demonstrated a very rich structural landscape (Figure 5.7). It was found that the known $Z' = 4$ polymorphs were more stable than any of the predicted structures, 2.6 kJ mol^{-1} below the most stable $Z' = 2$ predicted structure. The low symmetry packing in these polymorphs seemed to be driven by a reduction of the lattice energy, which could not be

achieved within the constraints of smaller ($Z' = 1$ and $Z' = 2$) asymmetric units. However, it was also noticed that forms I and III lattice energy minimised to the same structure. These structurally very similar assemblies did not correspond to different energy minima on the energy surface described by the methods used here. Amongst the predicted structures, several low energy $Z' = 1$ structures and a large number of possibilities with $Z' = 2$ were found, with a slight energetic preference for $Z' = 2$. The known form II was located as one of the lowest energy predicted structures, 3.5 kJ mol^{-1} above the lowest energy prediction and 6 kJ mol^{-1} above forms I and III. To compare the conformationally disordered form IV with the predicted structures, Day's group lattice energy minimised three ordered versions of form IV, each with one of the side chain conformations seen in the observed structure. The resulting lattice energy minima corresponded to structures that were found in the $Z' = 1$ prediction results and are highlighted in Figure 5.7. These ordered structures were all at lower density than the observed disordered structure and also outside of the normal energetic range of polymorphism, demonstrating the importance of disorder in the close packing and stability of form IV.

The calculated lattice energy ($-252.0 \text{ kJ mol}^{-1}$) of the hydrate was 83.8 kJ mol^{-1} lower than that of forms I and III. This stabilisation provided to the lattice by water was approximately double water's vaporisation enthalpy, so greatly exceeded the cost of removing water from its pure phase. This suggested that the hydrate is the thermodynamically stable form in the presence of water. For comparison, water was removed and re-optimised the structure. The resulting "computationally dehydrated" structure corresponded to one of the high energy predicted $Z' = 1$ structures. The results showed that the stability of the hydrate is dominated by the hydrogen bond interactions involving the lattice water. This was reflected in the contributions to the lattice energy: the lattice energy of the hydrate is more than 93 % electrostatic, compared to 73 % (forms I and III) and 74 % (form II) in the known anhydrous polymorphs. At this point, it should be noted that the Phe monohydrate crystal structure was determined to be the thermodynamically most stable form in the presence of water.

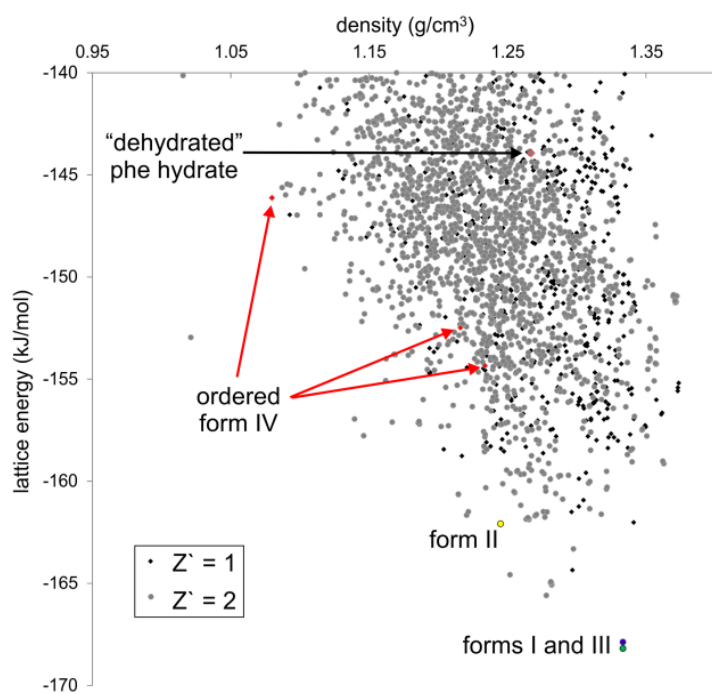


Figure 5.7. Calculated energy landscape of Phe. $Z'=1$ and $Z'=2$ predicted crystal structures are indicated as grey circles and black diamonds, respectively. The known forms I, II and III, as well as a number of ordered versions of form IV, are indicated. Also highlighted is the structure resulting from *in silico* dehydration of the monohydrate form found in the hydrogel.

The packing motif of the crystal structures determined for Phe contained a distinct AB bilayered pattern of a hydrophobic layer consisting of the phenyl groups and a hydrophilic layer consisting of hydrogen bonding and electrostatic interactions between the negatively charged carboxylate groups and positively charged ammonium cation groups (Figure 5.8), which together formed the zwitterionic component of the amino acids.

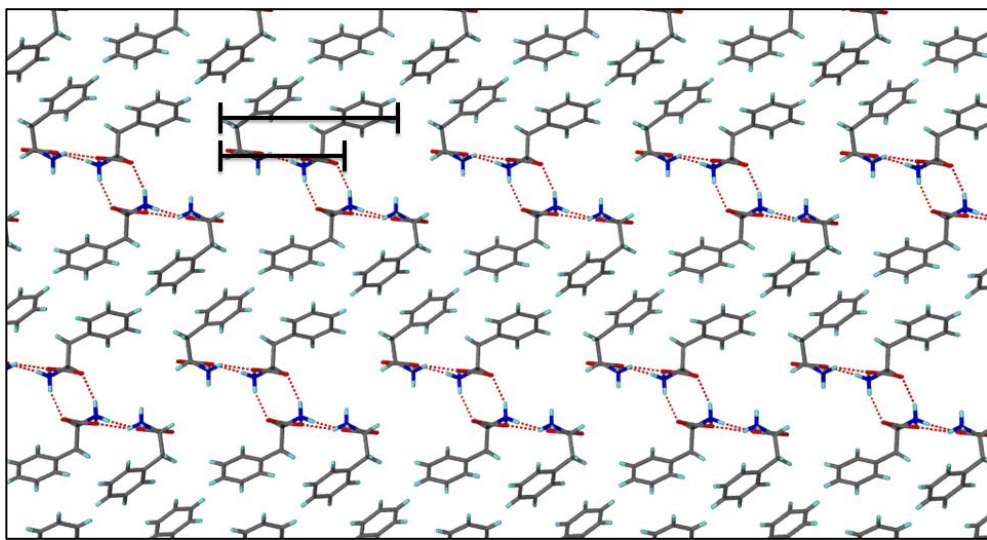


Figure 5.8. Packing of dimers of Phe shown down the *b* axis, with water molecules removed for clarity. Dimer stacks are interacting with each other except *via* hydrogen bonding and π - π interactions. What is also clear is that the dimer stacks are anisotropic with the hydrophilic section shorter than the hydrophobic region.

5.2.4. Structural studies using NMR spectroscopy

^1H - ^{13}C CP/MAS solid-state NMR experiments of hydrogels provided information on the rigid components, which are characterised by strong heteronuclear dipolar couplings that efficiently transfer magnetisation between ^1H and ^{13}C spins.⁵⁰ ^1H - ^{13}C CP/MAS NMR spectra of the Phe hydrogel showed a characteristic splitting for each carbon site (Figure 5.9) indicating the presence of two non-equivalent molecules in the crystal structure. These data matched the spectrum published by Harris *et al.* for the high humidity material (Phe monohydrate phase).²¹³ This was further corroborated by PXRD results and CASTEP calculations of the solid-state NMR parameters for a geometry optimised Phe monohydrate crystal structure (Figure 5.10).

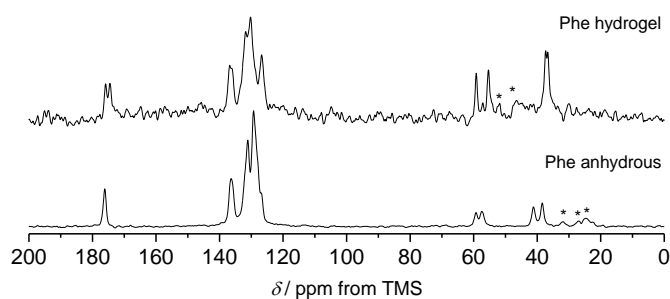


Figure 5.9. ^1H - ^{13}C CP/MAS solid-state NMR spectra of anhydrous Phe and Phe hydrogel acquired with MAS rates of 10.5 or 8 kHz and 2048 or 8192 scans, respectively. All experiments were conducted with a recycle delay of 20 s and $\pi/2$ pulse lengths of 3.2 μs (^1H) and 3.0 μs (^{13}C), using a 400 MHz solid-state NMR spectrometer. Asterisks represent spinning sidebands.

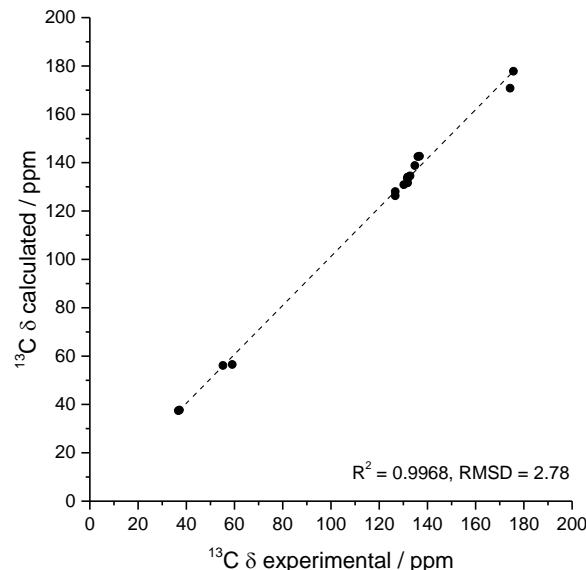


Figure 5.10. Experimental ^{13}C chemical shift values for Phe hydrogel derived from the spectra acquired at an MAS rate of 8 kHz *vs.* calculated chemical shifts for the Phe monohydrate that give best agreement with both NMR and PXRD data from the hydrogel.

5.2.5. Monitoring self-assembly of Phe in water using NMR

It has been shown using vibrational spectroscopy that electrostatic interactions between $-\text{COO}^- \cdots \text{NH}_3^+$ motifs are key in Phe self-assembly.^{207, 209, 210} However, recently, it has been hypothesised that there are significant contributions of hydrophobic interactions between phenyl rings in the formation of Phe fibrils.^{66, 208} I was interested in ascertaining the main driving force of fibre formation, which from the crystallographic characterisation appeared to be the electrostatic interactions. In order to gain a better understanding of Phe self-assembly in water and provide strong experimental evidence to clarify the

existing contradictions, the process of Phe aggregation was studied over a wide range of concentrations. Solution-state ^1H NMR spectra of Phe gels in D_2O showed substantial broadening of the peaks (Figure 5.11), which is related to short T_2 relaxation times together with increased ^1H - ^1H dipolar interactions within aggregating, solid-like structures.

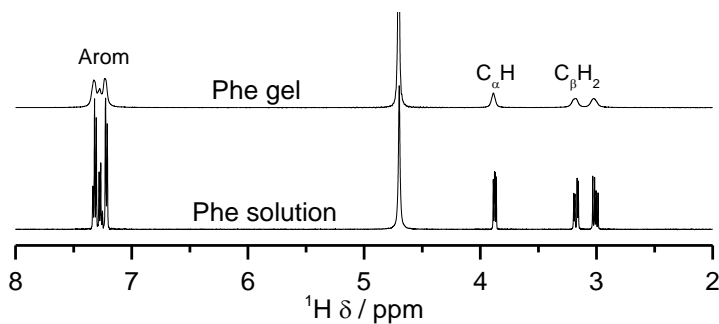


Figure 5.11. ^1H solution-state NMR spectra of a solution and hydrogel of Phe. The high intensity peak at 4.7 ppm is due to residual water and exchangeable protons. Experiments were conducted with a recycle delay of 2 s, using a 500 MHz solution-state NMR spectrometer.

It was clear that the local environment of the aromatic region of the aggregating species was left practically unchanged during saturation-induced self-assembly (Figure 5.12a). Substantial changes in the chemical shift values of aliphatic protons proved unambiguously the importance of the aliphatic region in Phe self-assembly. This was corroborated by the structural studies of the Phe monohydrate, the building block of the gel fibrils, where short contact interactions between aromatic rings of Phe are negligible.

As ^1H NMR is a quantitative analytical method, CGC was confirmed and the ratio between Phe species dissolved in the pools of solvent and Phe bound to the rigid gel network was determined. A linear increase in the intensity of NMR peaks was observed in the range of Phe concentrations from 17 to 200 mM (Figure 5.12b). When the concentration of Phe reached the CGC and a gel was formed, saturation was evident with no further increase of the intensity of NMR peaks even when increasing solute concentration. As it is well known for LMWG, formation of supramolecular structures does not require all molecules to be incorporated in the gel network (Table 5.1), but a certain concentration needs to be reached to drive the spontaneous process of fibril formation.^{46, 148} Based on this, the NMR-based CGC in water was determined at *ca.* 212

mM. Phe formed a supersaturated solution in the range of concentrations from *ca.* 160 to 200 mM, which produced a gel in the NMR tubes at the air/water interface after three weeks of storage.

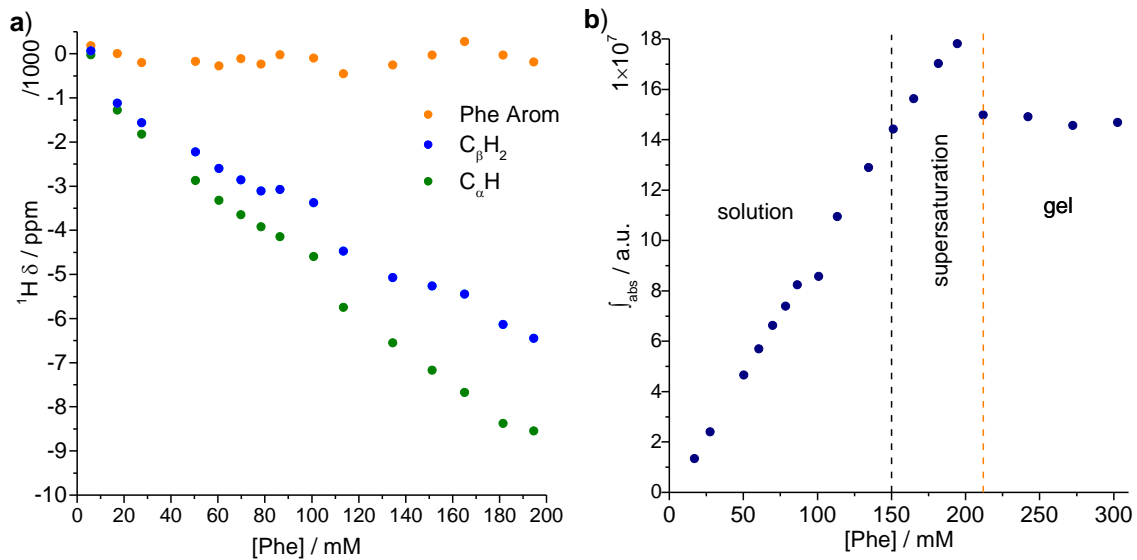


Figure 5.12. **a)** Variation of ${}^1\text{H}$ NMR chemical shifts (δ) with concentration of Phe in water. **b)** Dependence of ${}^1\text{H}$ NMR peak intensity on the concentration of Phe in D_2O . Three different stages during the gelation process can be identified based on intensities of the peaks, *i.e.* solution, supersaturated solution and gel phase. The orange line indicates the NMR-determined CGC. All experiments were conducted with a recycle delay of 10 s, using a 500 MHz solution-state NMR spectrometer.

Table 5.1. Concentration of Phe in solution and in gel phases based on ${}^1\text{H}$ NMR peak intensities.

$[\text{Phe}]_{\text{total}} / \text{mM}$	$[\text{Phe}]_{\text{gel phase}} / \text{mM}$	$[\text{Phe}]_{\text{solution}} / \text{mM}$
212	52	160
242	83	159
272	116	156
303	146	157

Kinetics of self-assembly of the Phe hydrogel (303 mM) was monitored through the acquisition of several ${}^1\text{H}$ solution-state NMR spectra at room temperature, immediately after cooling down a hot solution of Phe. Very sharp and intense peaks of Phe were recorded three minutes after quenching (Figure 5.12b). Gradually, these peaks became broader and less intense, until a plateau was reached after 24 h, a trend consistent with gelation.¹⁴⁷ Changes in intensity of peaks indicated that *ca.* 50 % of Phe molecules formed

the rigid hydrogel fibres (Table 5.1). No chemical shift variations were detected throughout gelation, an observation that has been reported previously for other gel systems,^{147, 224} and has been justified by the presence of fast exchange processes between free gelator molecules and those partially immobilised onto the gel fibres.²²⁵

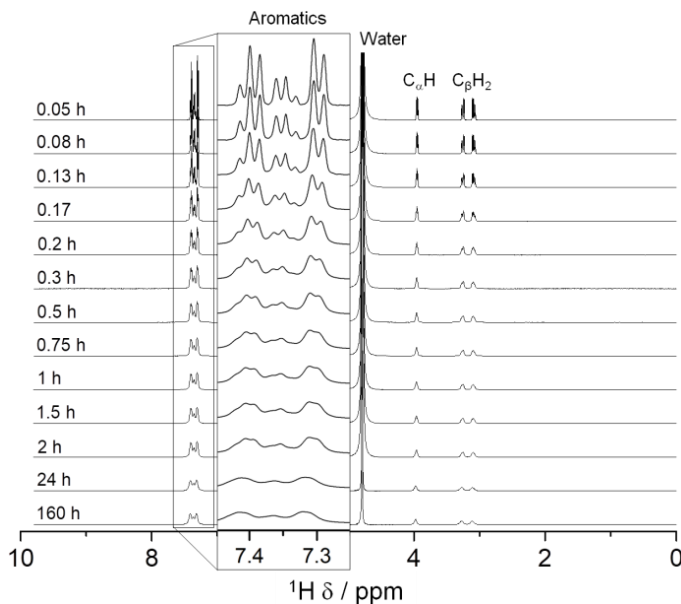


Figure 5.13. Kinetics of gelation of Phe monitored by the acquisition of ^1H solution-state NMR spectra over time, immediately after cooling down a hot solution of Phe (measured at 298 K). All experiments were conducted with a recycle delay of 10 s, using a 500 MHz solution-state NMR spectrometer.

The dependence of ^1H T_1 relaxation times with increasing concentration of Phe in water and throughout the gel-to-solution transition of the hydrogel provided a further insight towards the mechanism of fibre formation. Prior to gelation, differences in local dynamics were observed between the protons of the aromatic group, C_αH and C_βH_2 protons (Figure 5.14). There was a clear difference in the relaxation times for different ^1H sites in the solution. The long relaxation times (*ca.* 3.0 s) of the protons of the aromatic group and C_αH protons were contrasted by the three-fold shorter relaxation times of neighbouring C_βH_2 protons. Upon formation of the gel, ^1H T_1 relaxation times for different ^1H sites became similar. This corresponded to averaged values resulting from a strong network of ^1H - ^1H dipolar couplings (spin diffusion), as a result of restricted mobility of the gelator molecules, and exchange phenomena of Phe molecules between solution and gel states. Bouquet-Bonnet *et al.* (2012) reported a similar observation for single-component organogels of a derivative of phenylalanine and naphthalimide.¹⁴⁸ The increase in the T_1

relaxation time with increasing concentration of Phe in the gel state reflected aggregation of the amino acid prior to fibre growth.

VT NMR measurements of ^1H T_1 times indicated the Phe hydrogel was in the “fast tumbling regime”, also corroborated by the decreased line widths with increasing temperature. Three distinct stages in the temperature-dependent transformation of the hydrogel were identified. During stage I, the sample was in the gel state and ^1H T_1 times of Phe were similar for different ^1H sites. During stage II, a heterogeneous distribution of T_1 times typical of Phe solutions was observed, reflecting the disassembly of the network and the presence of more Phe molecules in the solution state. The process of the molecular gel-to-solution transition, T_{gel}^{*} ,¹⁵⁰ (here at 313 K) usually occurs at temperatures below the macroscopically determined T_{gel} ($T_{\text{gel}} = 323.6\text{--}326.6$ K). T_{gel}^{*} reflects the temperature above which the dissolution of the fibres starts occurring, which pre-empts the loss of structural integrity, translated by T_{gel} . This temperature marked the beginning of stage III, after which the distribution of ^1H T_1 times increased further and resulted in an overall increase of T_1 times for aromatic and C_αH protons. The dispersion of these values increased with temperature as the dissolution of the supramolecular network weakened ^1H - ^1H dipolar couplings, making the spin diffusion mechanism less efficient. However, ^1H T_1 times for C_βH_2 protons followed a different trend, with a rapid decay throughout the range of temperatures and a minimum at 326 K. This minimum possibly reflected the point after which ^1H T_1 values corresponded mainly to fast tumbling molecules dissolved in solution.

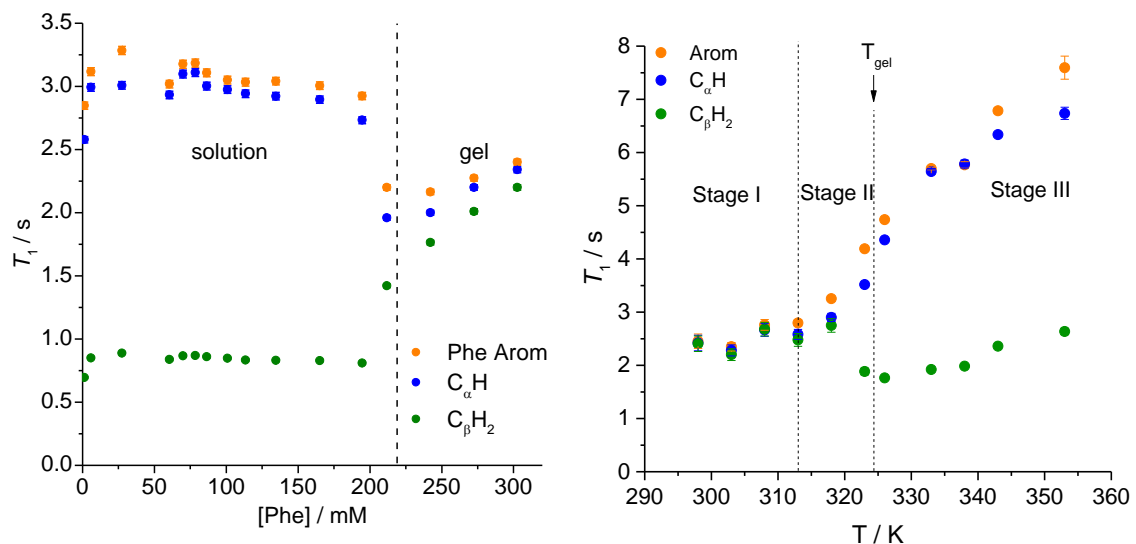


Figure 5.14. a) Evolution of ^1H solution-state T_1 relaxation times of different regions of Phe as a function of concentration in D_2O . **b)** ^1H T_1 times of hydrogels of Phe (303 mM), recorded from 298 to 353 K. All experiments were conducted with a recycle delay of 10 s, using a 500 MHz solution-state NMR spectrometer.

5.3. Concluding remarks

The “gel-crystallisation” phenomenon described by Myerson was corroborated by the determination of the gel fibres as being the crystalline monohydrate form of Phe. CSP data clearly showed that the structural landscape of Phe is very rich and that all solid forms may not have been characterised yet. NMR characterisation, coupled to crystallography, showed how the electrostatics of the zwitterionic Phe molecule, together with hydrogen bonding and hydrophobic interactions, lead to anisotropic assembly and fibre formation at the isoelectric point.

One key experiment in understanding dynamics of solutions and hydrogels is the determination of the dependence of ^1H T_1 times with increasing concentration of Phe and at variable temperature. Under the presence of strong homonuclear dipolar couplings (in the gel state) there is similarity of ^1H T_1 times for different proton sites due to spin diffusion. In the presence of mainly fast tumbling molecules (in the solution state), a dispersion of ^1H T_1 values is observed with each proton presenting its own relaxation profile. Since the strength of the dipolar couplings dictate the evolution of T_1 values with concentration and temperature, it was therefore possible to monitor molecular level variations induced by the gradual processes of aggregation and throughout gel-to-solution transitions.

Chapter 6

6. Supramolecular amino acid based hydrogels: probing the contribution of additive molecules using NMR spectroscopy

Findings from this chapter are partly published in

Ramalhete, S. M.; Nartowski, K. P.; Sarathchandra, N.; Foster, J. S.; Round, A. N.; Angulo, J.; Lloyd, G. O.; Khimyak, Y. Z., Supramolecular amino acid based hydrogels: probing the contribution of additive molecules using NMR spectroscopy. *Chemistry-A European Journal* 2017, 23 (33), 8014-8024.

6.1. Introduction

The understanding gained of the crystal packing of Phe fibres, non-covalent driving forces and dynamic processes of self-assembly of Phe (Chapter 5, page 148) enabled opportunities for tuning supramolecular gelation of Phe to be explored. The introduction of co-gelators or non-gelating additive molecules has been reported previously in other gel systems to create an extra level of control and therefore to allow tailoring of the physical properties of gels through modifications to their supramolecular structure.^{51, 92} Possible co-gelators or non-gelating additive molecules in the form of related hydrophilic and hydrophobic amino acids (Figure 6.1) were added to hydrogels of Phe. Reversible interactions between complimentary amino acids occur in nature (hydrogen and disulfide bonds, salt bridges and hydrophobic interactions) and their importance has been demonstrated in many biological processes, such as protein folding, protein-protein and protein-ligand interactions. These essential building blocks of life have their function dictated by the type of amino acids and interactions participating in their stabilisation.^{38, 43,}

Furthermore, this chapter describes the development of an NMR-based analytical approach to gain insight into the general mechanisms of supramolecular gelation, with these multi-component hydrogels used as a proof of concept. Besides NMR spectroscopy, complimentary techniques able to probe larger scales of organisation were used, such as microscopy, rheology and diffraction methodologies, to aid in the interpretation and validation of the NMR findings.

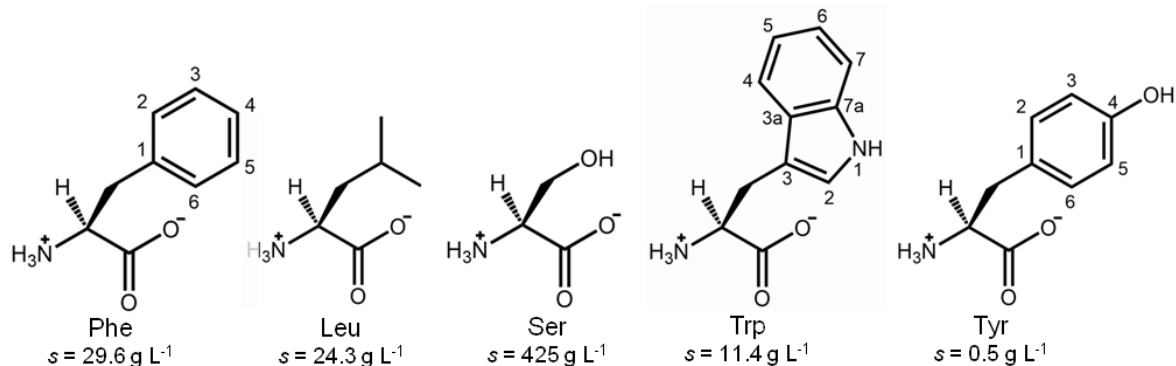


Figure 6.1. Zwitterionic structures of the amino acids in study with the corresponding solubilities in water at 298 K. Tyr is less soluble than Phe since the additional hydroxyl group interacts with nearby hydroxyl and carboxylate groups, resulting in stronger Tyr-Tyr than Tyr-water interactions.²²⁶

6.2. Results

6.2.1. Macroscopic observations and fibre morphology determination

The hydrogelation ability of these structurally diverse amino acids (Figure 6.1) was tested. Suspensions of *L*-leucine (Leu), *L*-serine (Ser), *L*-tryptophan (Trp) and *L*-tyrosine (Tyr) formed clear solutions in water when heated. When quenched, all formed crystalline precipitates in the range of 5 to 500 mM. Despite Tyr being able to form supramolecular fibres⁵⁵, it showed no tridimensional ability of fully entrapping water.

Suspensions of Phe mixed with these non-gelating additives (total concentration of 303 mM) were heated and quenched, resulting in white opaque hydrogels obtained from the mixtures Phe/Leu (5:1), Phe/Ser (5:1), Phe/Trp (5:1) and Phe/Tyr (5:1). pH values were monitored upon the addition of other amino acids to suspensions of Phe, due to the importance of pH in dictating non-covalent interactions and, therefore, self-assembly. Despite small differences were found between pure and mixed systems, these did not significantly affect the outcome of self-assembly (Table 6.1). T_{gel} values of hydrogels of Phe

were also not affected considerably upon the introduction of these additive molecules. These temperatures were in the range of 322 to 327 K for all hydrogels (Table 6.2).

Table 6.1. pH values of suspensions of Phe, Phe/Leu (5:1), Phe/Ser (5:1), Phe/Trp (5:1) and Phe/Tyr (5:1), and corresponding dissociation constants (pK_a) and isoelectric points (pI).²²⁷

Suspension	pH	pI	pK_a^1	pK_a^2	pK_a^3
Phe	6.5	5.48	Phe: 2.18	Phe: 9.09	-
Phe/Leu	6.5	5.98	Leu: 2.32	Leu: 9.58	-
Phe/Ser	6.4	5.68	Ser: 2.13	Ser: 9.05	-
Phe/Trp	6.5	5.66	Trp: 2.38	Trp: 9.34	-
Phe/Tyr	6.3	5.66	Tyr: 2.24	Tyr: 9.04	Tyr: 10.10

Table 6.2. Gel-to-solution transition temperatures (T_{gel}) of hydrogels of Phe, Phe/Leu (5:1), Phe/Ser (5:1), Phe/Trp (5:1) and Phe/Tyr (5:1).

Hydrogel	T_{gel} / K
Phe	323.6 – 326.6
Phe/Leu	323.5 – 324.5
Phe/Ser	323.5 – 324.1
Phe/Trp	322.2 – 326.9
Phe/Tyr	324.8 – 325.0

6.2.2. Resistance of gel fibres to deformation

Similarly to the pure Phe hydrogel (Chapter 5, section 5.2.1, page 149), when frequency sweeps were performed with a small amplitude stress, a phase angle of *ca.* 10° was recorded, showing a solid-like behaviour. Since G' values for the majority of these hydrogels were in the order of 10^5 Pa and were typically two to five times greater than the G'' values (Figure 6.2a), a relationship characteristic of robust gels, the elastic nature of the mixed gel materials was confirmed.

Similar G' values were obtained for the hydrogels of Phe, Phe/Leu and Phe/Tyr ($G' \approx 2.0 \times 10^5$ Pa), indicating the presence of Tyr or Leu did not modify the response of the hydrogel fibres to stress considerably. However, significant differences between these systems and the hydrogels of Phe/Trp and Phe/Ser were identified. The addition of Trp increased the storage modulus ($G' = 3.5 \times 10^5$ Pa), indicative of a rheologically stronger network. In contrast to Trp, the addition of Ser decreased severely the resistance of the hydrogel to deformation ($G' = 7.5 \times 10^4$ Pa).

During stress sweep experiments, all hydrogels showed a typical G' value, essentially constant below the critical value of oscillatory torque (“yield stress”). At this stress point, the sample started to flow or there was slippage between the interface of the rheometer and the hydrogel. Hence, no trends or conclusions could be drawn from these data. Hydrogel materials often exude water (syneresis) resulting in uncontrollable slippage, thus inconsistent data were obtained (Figure 6.2b).

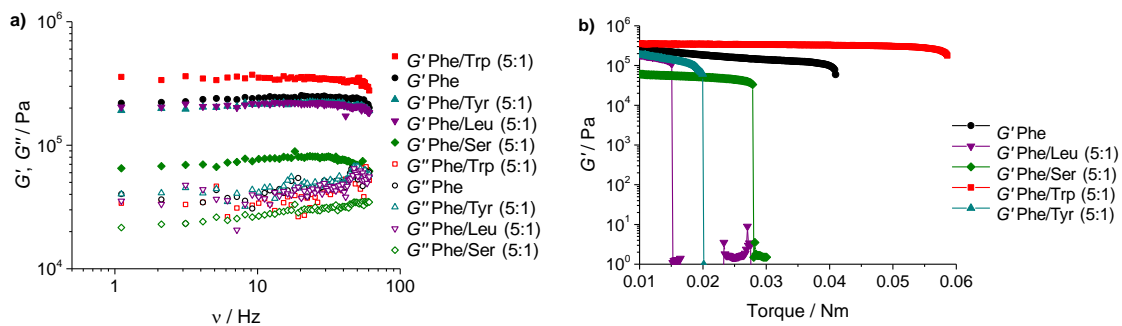


Figure 6.2. Storage (G') and loss (G'') moduli at **a)** increasing frequency sweeps and **b)** increasing stress sweeps for the hydrogels of Phe, Phe/Ser (5:1), Phe/Leu (5:1), Phe/Trp (5:1) and Phe/Tyr (5:1). Measurements of storage and loss moduli of supramolecular hydrogels were reproducible with an error of 10.7 %. Lines are guides for the eyes. Hot solutions (*ca.* 1.5 mL) were pipetted into a 300 μ m gap (cone and plate geometry). All samples were subjected to frequency sweeps in the range of 0.1 to 100 Hz and applied stress of 700 Pa, as well as stress amplitude sweeps in the range of 500 to 10000 Pa.

6.2.3. Structural characterisation of the fibrous network

The crystalline nature of the hydrogel fibres was revealed by the presence of diffraction peaks in PXRD patterns of single and multi-component hydrogels (Figure 6.3). All patterns exhibited a broad low intensity hump centred at $28^\circ 2\theta$, assigned to water molecules.²²⁸ When the gels were dried, this “halo” peak disappeared.

It was determined in Chapter 5 (page 148) that pure hydrogels of Phe self-organise into the monohydrate phase of Phe. Very similar diffraction patterns were recorded for multi-component hydrogels, indicating the presence of the Phe monohydrate form as the building block of the mixed hydrogel fibres, despite the introduction of additive molecules. Additional diffraction peaks were identified in the PXRD patterns of Phe/Tyr gels (Figure 6.3), attributed to needle-like crystals of Tyr immersed in a very dense fibrous Phe network. These were also detected by polarised light microscopy and SEM (Figure

6.4). Despite Tyr being poorly soluble in water (0.451 g L^{-1} at 298 K) – which prevented full dissolution at 55 mM – the same molar concentrations were used to match the studies performed with the other amino acids.

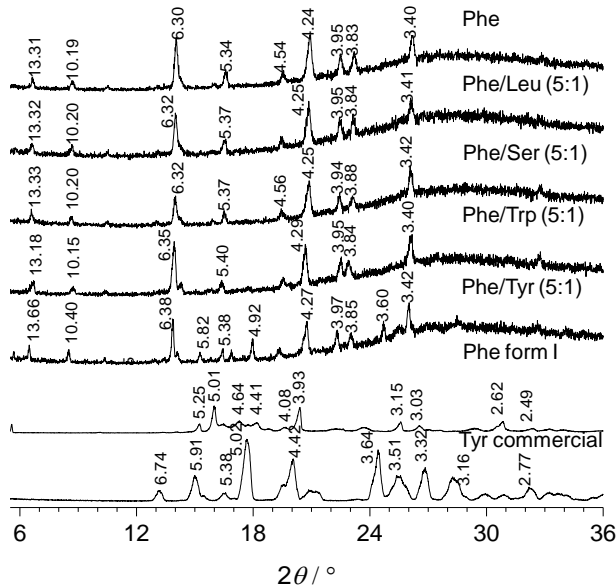


Figure 6.3. PXRD patterns of the hydrogels of Phe, Phe/Leu (5:1), Phe/Ser (5:1), Phe/Trp (5:1) and Phe/Tyr (5:1) and reference solid powders of the anhydrous form I of Phe and the commercially available Tyr (CSD ref. LTYROS02)²²⁹.

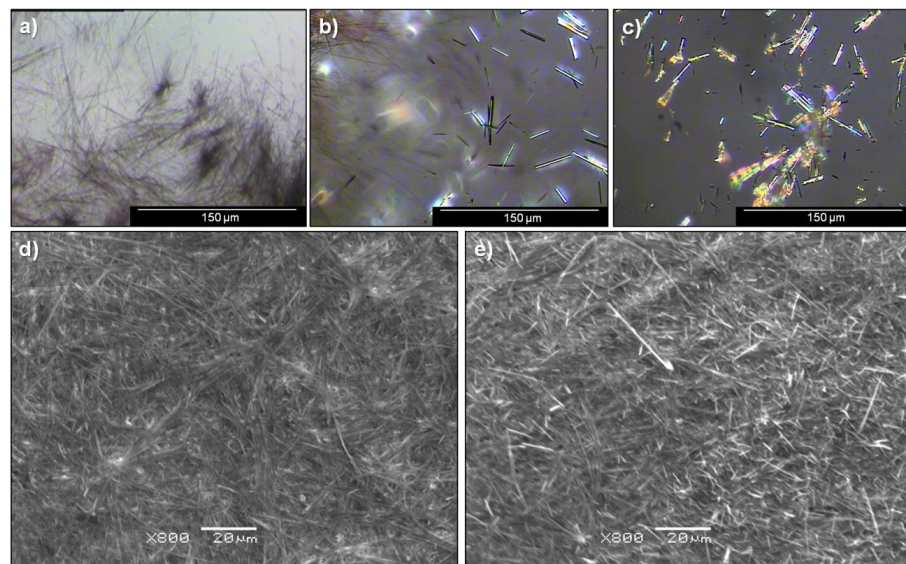


Figure 6.4. Polarised light microscopy images of hydrogels of **a**) Phe and **b**) Phe/Tyr (5:1) (303 mM), and **c**) polarised light microscopy images of the commercially available Tyr (CSD ref. LTYROS02)²²⁹. SEM images of the dry hydrogels of **d**) Phe and **e**) Phe/Tyr (5:1) (303 mM). Insoluble white needle-like crystals of Tyr can be seen immersed in a network of entangled thin fibres.

¹H-¹³C CP/MAS spectra acquired on both wet and dry hydrogels were very similar (Figure 6.5). Not surprisingly, the spectra of dry hydrogels presented a significant improvement in signal-to-noise ratio due to increased percentage content of the gelator during the measurements. Upon introduction of additives, similar chemical shift values and splitting patterns were observed for all Phe peaks when comparing with the pure Phe hydrogel (Table 6.3), confirming that the Phe monohydrate form was maintained as the supramolecular structure forming the hydrogel fibres, which is in excellent agreement with PXRD data.

The additional peaks detected for hydrogels of Phe/Trp and Phe/Tyr were assigned to Trp and Tyr carbons, respectively (Figure 6.5). Significant broadening of Trp and Tyr peaks was observed in the hydrogels as compared to the sharp peaks of the reference crystalline powders of Trp and Tyr, an indication of the participation of these molecules in less ordered structures. In dry hydrogels of Phe/Tyr, the Tyr peaks appeared as much sharper resonances with chemical shift values identical to the reference solid powder of Tyr. This is consistent with microscopy and PXRD patterns, indicating the existence of a fraction of crystalline Tyr in the gel matrix. Upon drying, this fraction increased as Tyr precipitates out of solution.

¹H-¹³C CP/MAS NMR spectra of hydrogels of Phe/Leu and Phe/Ser did not exhibit any carbon peaks for Leu or Ser, an indication these remained in a highly mobile state. Overall, these findings strongly suggested Leu and Ser were not incorporated in the rigid elements of the fibrous networks.

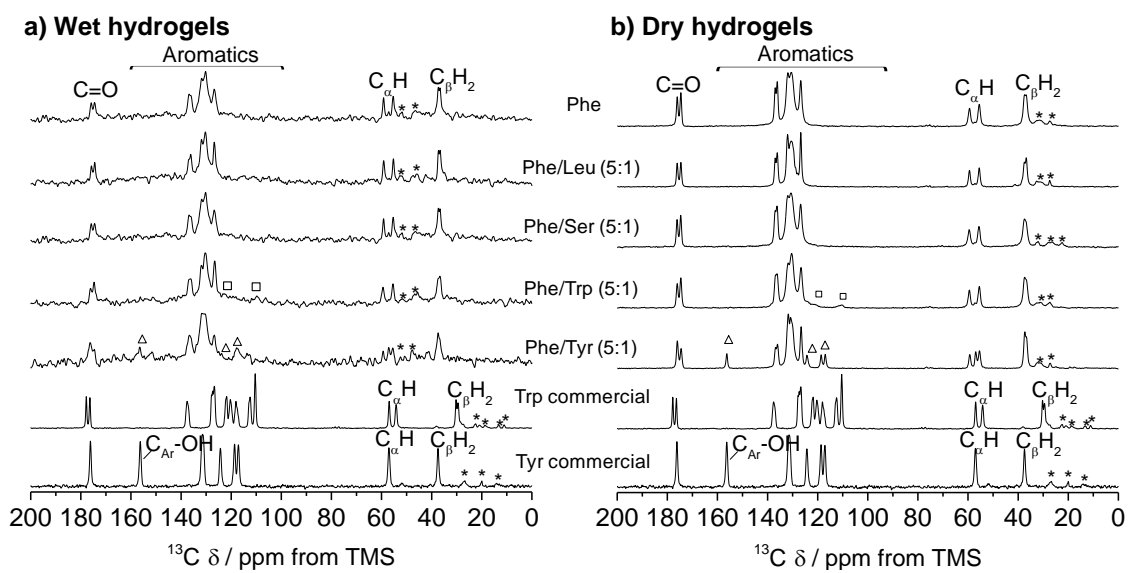


Figure 6.5. ^1H - ^{13}C CP/MAS NMR spectra of **a)** wet and **b)** dry hydrogels of Phe, Phe/Leu (5:1), Phe/Ser (5:1), Phe/Trp (5:1) and Phe/Tyr (5:1) acquired with MAS rates of 8.5 kHz and 8192 scans (wet gel samples) or 10 kHz and 2048 scans (dry gel samples); and reference solid powders of the commercially available Trp (CSD ref. QQQBTO03)²²⁹ and Tyr (CSD ref. LTYROS02)²²⁹ acquired with MAS rates of 10.5 kHz and 2048 scans. All experiments were conducted with a recycle delay of 20 s and $\pi/2$ pulse lengths of 3.2 μs (^1H) and 3.0 μs (^{13}C), using a 400 MHz solid-state NMR spectrometer. Rectangles and triangles highlight the presence of rigid elements of Trp and Tyr, respectively. Spectra of reference solid powders of commercially available Leu and Ser are not shown since insoluble components of Leu or Ser were not observed in the mixed materials. Asterisks represent spinning sidebands.

Table 6.3. ^{13}C chemical shifts from ^1H - ^{13}C CP/MAS NMR spectra of dry hydrogels of Phe, Phe/Leu (5:1), Phe/Ser (5:1), Phe/Trp (5:1) and Phe/Tyr (5:1).

^{13}C δ / ppm from TMS					
	Phe	Phe/Leu	Phe/Ser	Phe/Trp	Phe/Tyr
C=O	176.0	176.0	176.0	176.0	176.0
	174.5	174.6	174.5	174.6	174.5
Tyr C₄-OH	-	-	-	-	156.3
	136.9	136.9	136.8	136.7	136.8
	136.1	136.1	136.1	136.2	136.1
Phe Aromatics	132.0	131.8	131.8	131.7	131.8
	130.5	130.5	130.5	130.3	130.8
	126.7	126.7	126.7	126.6	126.6
Tyr C_{3,5}	-	-	-	-	124.3
Trp Aromatics	-	-	-	120.8	-
Tyr C_{2,6}	-	-	-	-	118.6
Tyr C₁	-	-	-	-	117.0
Trp Aromatics	-	-	-	110.5	-
Phe C_αH	59.4	59.4	59.4	59.4	59.3
	55.5	55.5	55.5	55.5	57.0
Phe C_βH₂	37.4	37.3	37.3	37.4	55.5
	36.7	36.8	36.8	36.7	37.4

6.2.4. Investigation of semi-solid components by PFG HR-MAS NMR

PFG HR-MAS NMR experiments were conducted for single and multi-component hydrogels, but the relative small dimensions of the molecules under study prevented differentiation between the rigid moieties incorporated in the gel fibres from the mobile regions water-exposed.

In an attempt to distinguish between free gelator molecules and oligomeric aggregates, which presence in equilibrium in solution has been reported previously in valine-based organogels¹⁴⁷, apparent self-diffusion coefficients (D) were determined. Detailed description of the determination of apparent self-diffusion coefficients from PFG HR-MAS experiments can be found in Chapter 3, section 3.11.2.2, page 128. These D values usually differ from those calculated from solution-state experiments, since diffusion of molecules is affected by sample rotation.¹⁴⁰ The resulting curves were best fitted to a mono-exponential function (Figure 6.6), reflecting the presence of a single molecular diffusion regime (D values can be found in Table 6.4).

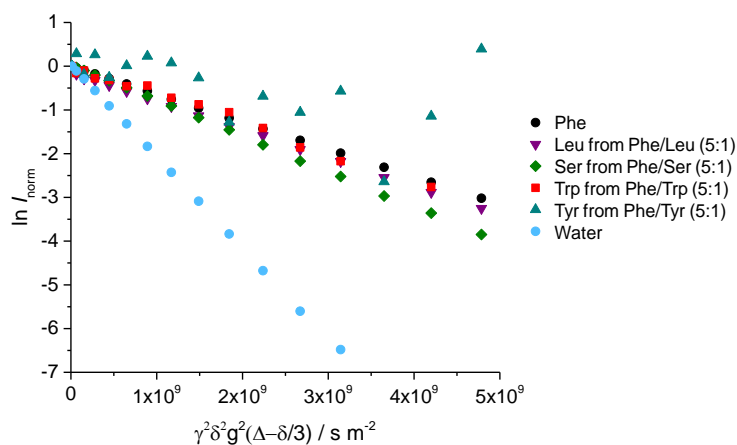


Figure 6.6. Evolution of ^1H PFG HR-MAS NMR normalised peak intensity with increasing gradient strength of hydrogels of Phe, Phe/Leu (5:1), Phe/Ser (5:1), Phe/Trp (5:1) and Phe/Tyr (5:1), acquired with MAS rates of 1 kHz at 298 K. Tyr presented poor signal-to-noise, preventing accurate determination of peak intensity. All experiments were conducted with 5 to 95 % of the maximum gradient intensity (G_{\max} = of 49.5 G cm^{-1}), a diffusion delay of 70 ms and a diffusion gradient of 1 ms, using a 400 MHz HR-MAS NMR probe head.

The values of apparent self-diffusion coefficients for water and Phe were very similar for all hydrogels and are consistent with those reported for supramolecular gels.^{140, 230} In hydrogels of Phe/Leu and Phe/Trp, the D values for Leu and Trp were in the same range as Phe ($D \approx 7.0 \times 10^{-10} \text{ m}^2 \text{ s}^{-1}$). In contrast to this, a higher apparent self-diffusion coefficient was determined for Ser, in the hydrogels of Phe/Ser. This indicated that Ser exists mainly as free mobile molecules in the pools of solvent. Tyr presented poor signal-to-noise (due to significant overlap with Phe aromatic peaks and Tyr poor water solubility), preventing accurate determination of its apparent self-diffusion coefficient.

Table 6.4. Apparent self-diffusion coefficients (D) calculated from PFG HR-MAS NMR experiments of hydrogels of Phe, Phe/Leu (5:1), Phe/Ser (5:1), Phe/Trp (5:1) and Phe/Tyr (5:1), acquired with MAS rates of 1 kHz at 298 K.

Hydrogel	Phe		Water		Additive molecule	
	$D \times 10^{10} / \text{m}^2 \text{ s}^{-1}$	$\delta \times 10^{10}$	$D \times 10^9 / \text{m}^2 \text{ s}^{-1}$	$\delta \times 10^{10}$	$D \times 10^{10} / \text{m}^2 \text{ s}^{-1}$	$\delta \times 10^{10}$
Phe	6.98	0.13	2.28	0.01	-	-
Phe/Leu	7.14	0.17	2.44	0.06	7.42	0.03
Phe/Ser	8.47	0.03	2.27	0.01	8.12	0.11
Phe/Trp	6.96	0.24	2.31	0.09	7.35	0.23
Phe/Tyr	7.24	0.13	2.26	0.05	3.50	1.09 ^a

^aOverlapped with Phe, preventing accurate determination

6.2.5. Dynamics of molecules in solution assessed by ^1H NMR spectra

The consequences of introducing additive molecules were reflected even at early stages of self-aggregation, as the kinetics of gelation of Phe (monitored by the evolution of peak intensity and line broadening with time) were modified to different extents in multi-component hydrogels (Figure 6.7).

Upon gel formation, 40 to 50 % of Phe gelator molecules became NMR “silent” in multi-component hydrogels (Table 6.5) and were therefore considered to be structural components of the fibres. However, caution should be exercised when comparing different samples, as the calculation of the fraction of ^1H peak intensity and variation of FWHM are highly dependent on the time of acquisition of the initial spectrum and on the kinetics of gelation (which can be affected by sample volume, temperature and diameter of the NMR tube). 24 h ageing of these hydrogels led to reduced peak intensities for Trp and Tyr (Figure 6.8). However, no significant peak variations were identified for either Leu or Ser. Interestingly, the intensity of Phe peaks increased upon the addition of Ser, in hydrogels of Phe/Ser, indicating that the presence of Ser in solution led to increased concentrations of Phe molecules in solution.

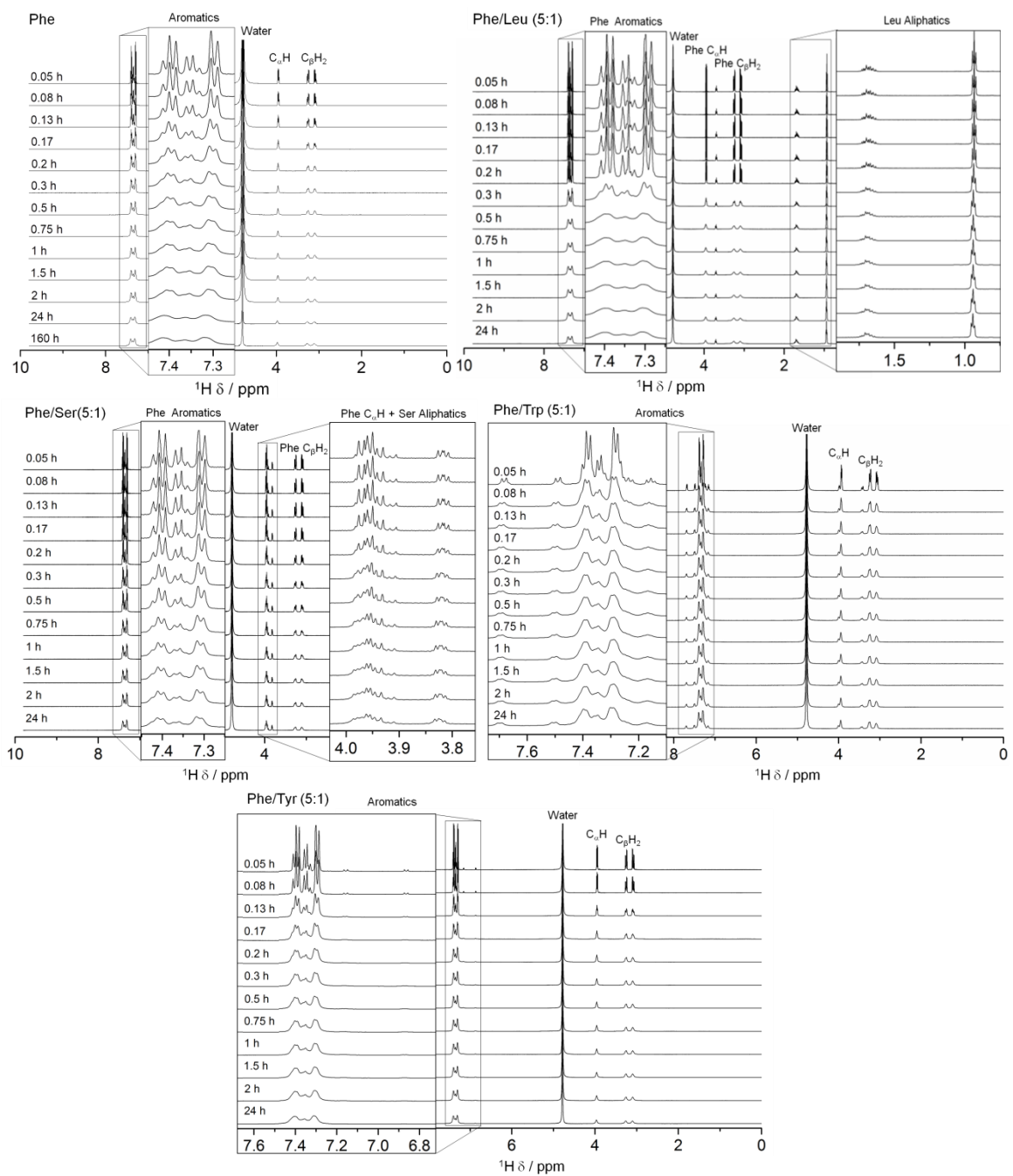


Figure 6.7. Kinetics of gelation monitored by the acquisition of ^1H solution-state NMR spectra over time, immediately after cooling down hot solutions of Phe, Phe/Leu (5:1), Phe/Ser (5:1), Phe/Trp (5:1) and Phe/Tyr (5:1) (303 mM) (measured at 298 K). Phe, Trp and Tyr peak ^1H become broader as a consequence of gelation, whereas Leu and Ser ^1H peaks remained sharp even after the hydrogel is formed. All experiments were conducted with a recycle delay of 10 s, using a 500 MHz solution-state NMR spectrometer.

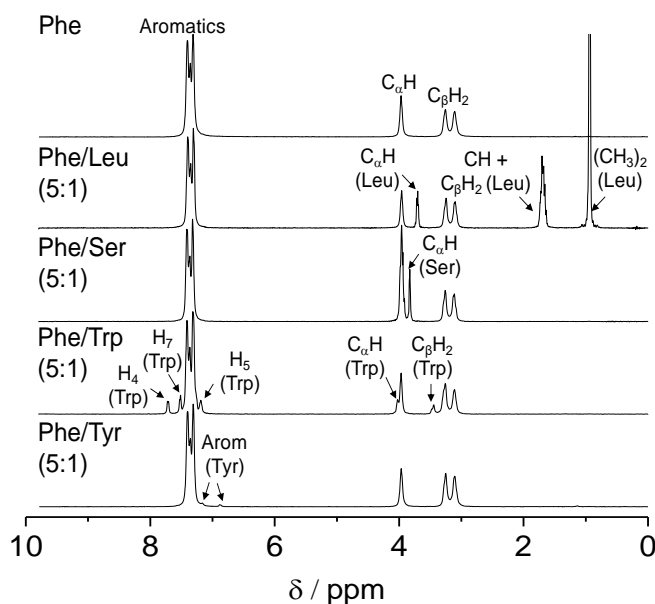


Figure 6.8. ^1H solution-state NMR spectra of hydrogels of Phe, Phe/Leu (5:1), Phe/Ser (5:1), Phe/Trp (5:1) and Phe/Tyr (5:1) acquired 24 h after quenching hot solutions (303 mM) measured at 298 K. Tyr peaks displayed much lower intensities than expected according to the composition, as Tyr precipitates under the experimental conditions. All experiments were conducted with a recycle delay of 10 s, using a 500 MHz solution-state NMR spectrometer.

Table 6.5. Fraction of ^1H peak intensity (\int_{gel}) of spectra acquired 24 h after quenching hot solutions of Phe, Phe/Leu (5:1), Phe/Ser (5:1), Phe/Trp (5:1) and Phe/Tyr (5:1) (303 mM), in comparison with the ^1H peak intensity of spectra acquired immediately (measured at 298 K).

	$\int_{\text{gel}} / \%$			Additive molecule				
	Phe Arom	Phe C α H	Phe C β H ₂					
Phe	61	59	60	-	-	-	-	-
Phe/Leu	50	51	49	Leu C α H 103	Leu CH+C β H ₂ 98	Leu (CH ₃) ₂ 99	-	-
Phe/Ser	68	80 ^a	67	Ser C α H 98	Ser C β H ₂ 80 ^a	-	-	-
Phe/Trp	56	58 ^b	53	Trp H ₄ 88 ^c	Trp H ₇ 115 ^c	Trp H ₅ 81	Trp C α H 58 ^b	Trp C β H ₂ 80
Phe/Tyr	56	56	55	Tyr Arom 61	-	-	-	-

^aOverlapped

^bOverlapped

^cBroad baseline due to Phe Arom peak

6.2.6. Identifying spatial correlations using 2D ^1H - ^1H NOESY NMR

The intermolecular interactions responsible for formation of the hydrogel network were probed using NOESY. Negative nOe enhancements (blue) were detected in 2D ^1H - ^1H NOESY NMR spectra for Phe protons in Phe hydrogels (Figure 6.9). This is characteristic of large molecules which transfer magnetisation efficiently through dipolar interactions.¹⁴⁸ Since these Phe-based hydrogel systems are composed exclusively of LMW species, these findings indicated that molecules in solution contain information from the fibrous network due to their fast dynamics of exchange on the NMR frequency time scale. The phenomenon of solution-state NMR spectra containing information from the hydrogel fibres due to fast molecular exchange between solution and gel states has been described previously^{147, 148} and was here further confirmed by the determination of a single diffusion regime (see section 6.2.4, page 171). Strong negative cross-peaks were also recorded between Phe and Trp or Tyr, supporting the hypothesis that Trp and Tyr were in close proximity with Phe due to their incorporation in the Phe/Trp and Phe/Tyr hydrogel fibres, respectively. No cross-peaks were observed between Phe and Ser in the hydrogel of Phe/Ser.

The presence of weak negative cross-peaks between Phe and Leu also indicated spatial proximity between both molecules. Despite this evidence for fast interaction of Leu with Phe at the gel/solution interfaces, the detection of positive spatial correlations between Leu protons (green), associated with small molecules, showed this molecule exists mainly in a free dissolved state. These findings were in agreement with the sharp Leu peaks (Figure 6.7) and the unmodified Leu peak integral (Table 6.5) observed after gelation. Hence, the absence of Leu peaks in ^1H - ^{13}C CP/MAS NMR spectra allowed us to confidently conclude these were interactions occurring merely at the gel/solution interfaces. This was in good agreement with the lower apparent self-diffusion coefficient determined for Leu in the hydrogel of Phe/Leu in comparison with solutions of Leu.

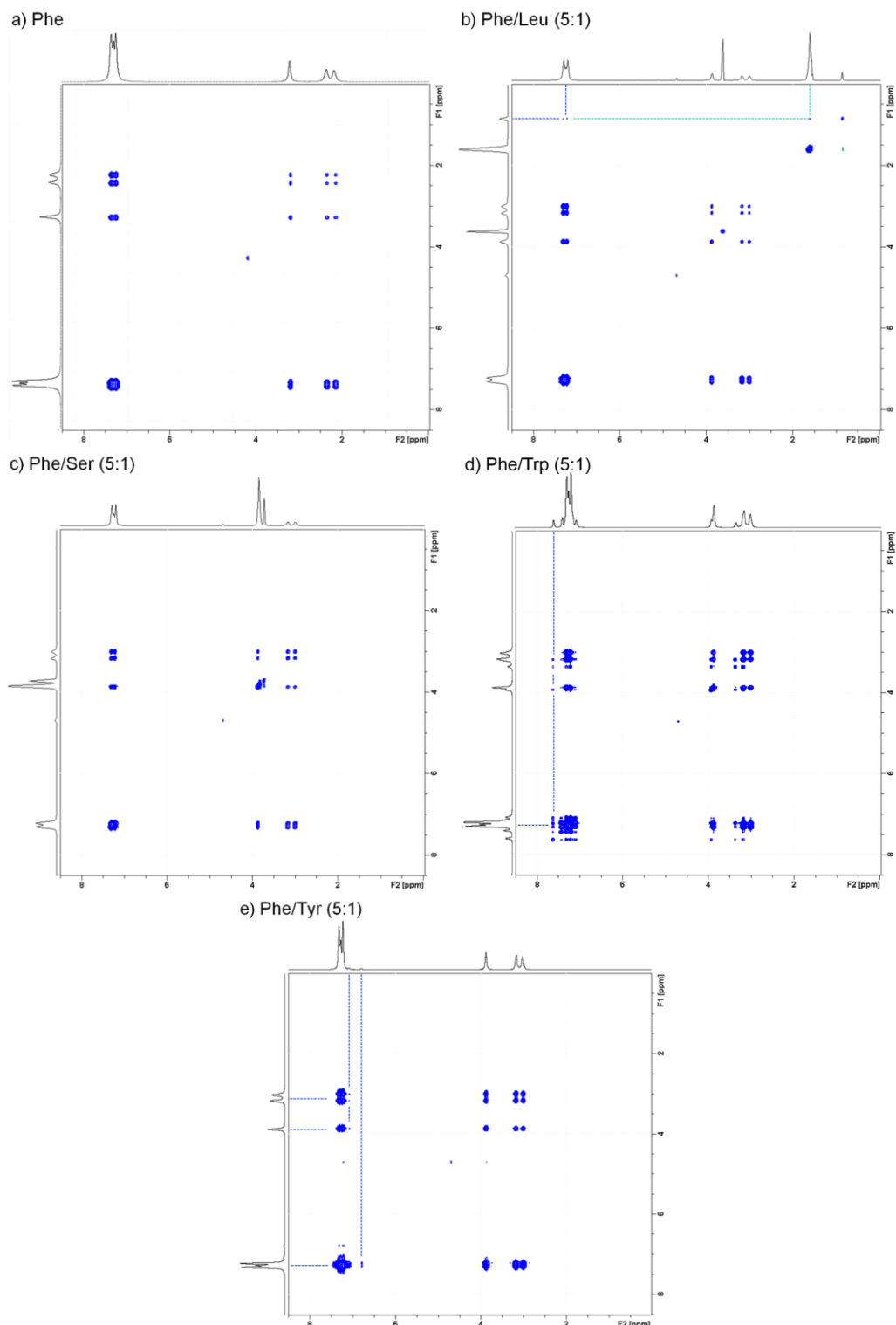


Figure 6.9. 2D ^1H - ^1H NOESY spectra of hydrogels of Phe, Phe/Leu (5:1), Phe/Ser (5:1), Phe/Trp (5:1) and Phe/Tyr (5:1) acquired with a mixing time of 0.5 s (measured at 298 K). Negative nOe enhancements (blue), characteristic of large molecules, indicate that free gelator molecules contain properties from the fibrous network. Blue dashed lines highlight intermolecular correlations between Phe and **b)** Leu, **d)** Trp and **e)** Tyr, which are absent in hydrogels of Phe/Ser (c). Positive nOe enhancements (green), characteristic of small molecules, are highlighted by green dashed lines and correspond to correlations between Leu molecules in solution (**b**). All experiments were conducted with a recycle delay of 2 s and 32 scans, using a 500 MHz solution-state NMR spectrometer.

6.2.7. Characterisation of gel/solution dynamics of exchange using ^1H T_1 measurements

The detailed description and rationalisation of the molecular events that condition the evolution of T_1 times with temperature in the pure Phe hydrogel can be found in Chapter 5 (section 5.2.5, page 158). Focusing on multi-component hydrogels, ^1H T_1 times of Phe determined at 298 K increased according to the following trend: Phe/Trp < Phe/Tyr \leq Phe \leq Phe/Leu < Phe/Ser (Figure 6.10). The strongest hydrogel, composed of Phe and Trp, presented the fastest relaxation rates for Phe Arom protons. Similarly, the weakest material, formed by Phe and Ser, contains the highest concentrations of dissolved Phe whose slower relaxation profiles contributed to a higher averaged ^1H T_1 value. ^1H T_1 relaxation times may therefore mirror the strength of the hydrogel fibres – although such a comparison should only be performed when discussing systems with similar composition.

For all hydrogels, Phe ^1H sites displayed an evolution of T_1 times with temperature similar to the single component system. Furthermore, ^1H T_1 times for Trp and Tyr presented similar dependence of temperature in hydrogels of Phe/Trp and Phe/Tyr, respectively. At low temperatures, ^1H T_1 times were similar for different ^1H sites followed by a gradual dispersion of values as temperature was increased. The evolution of ^1H T_1 times for Trp and Tyr throughout the gelation processes proved that these additive molecules were incorporated in the network at lower temperatures and started tumbling faster, as free molecules, as temperature was raised. Hence, T_1 findings strongly support the claim that Trp and Tyr are intimately associated with Phe within the solid elements of the 3D network and in equilibrium with free molecules dissolved in the isotropic pools of water (*i.e.* bulk solvent).

In hydrogels of Phe/Leu and Phe/Ser, a distribution of values similar to solutions was observed throughout the range of temperatures for Leu and Ser. In the gel state, Leu and Ser protons showed long T_1 values and narrow peak line widths in ^1H solution-state NMR spectra (Figure 6.8 and Figure 6.9), characteristic of fast molecular motions. These findings, in combination with the lack of peaks of Leu and Ser in CP/MAS NMR spectra, are strong indications that these additive molecules remain essentially dissolved in pools of water surrounded by Phe fibres.

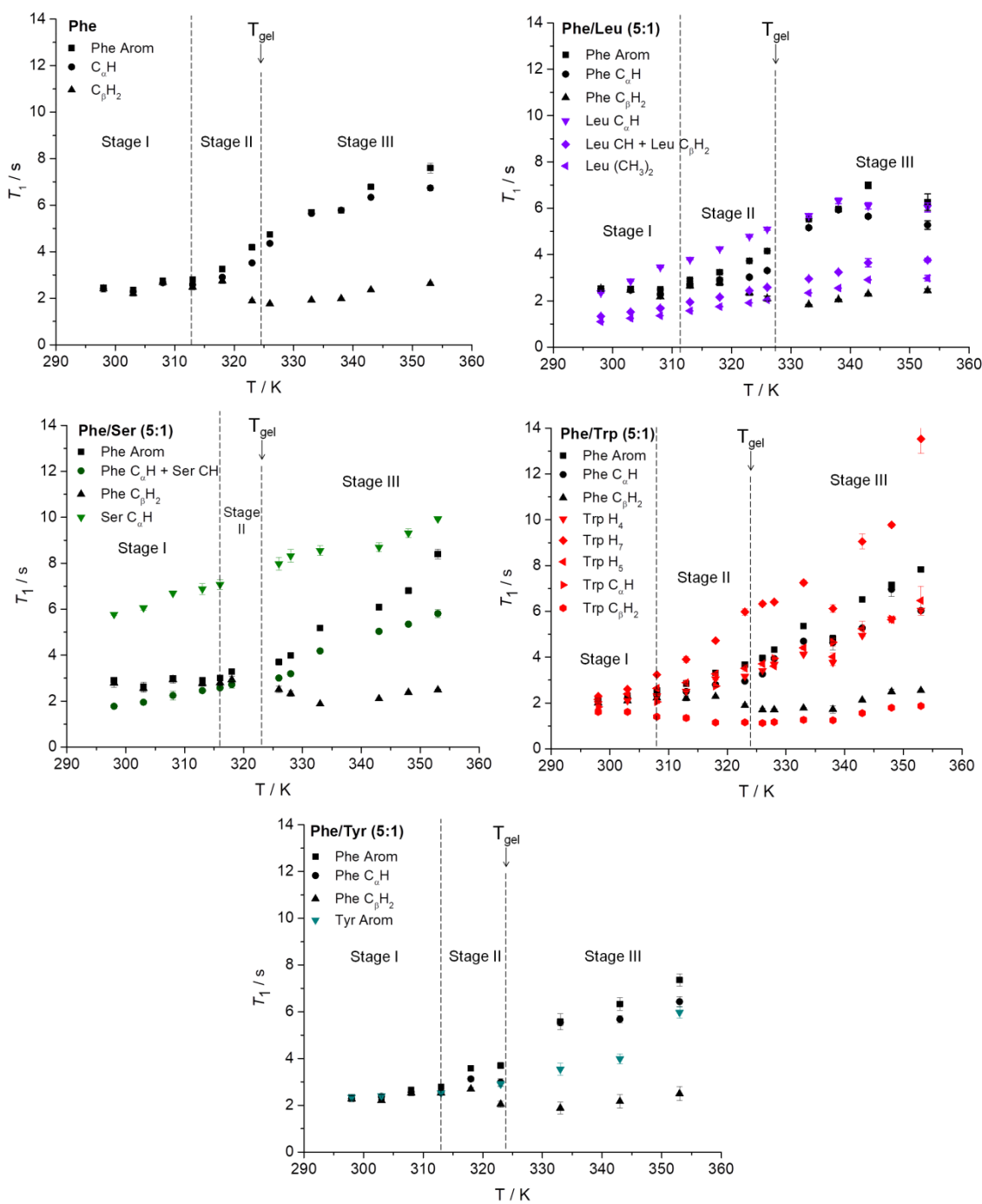


Figure 6.10. ^1H solution-state NMR T_1 times of Phe, Leu, Ser, Trp and Tyr in hydrogels of Phe, Phe/Leu (5:1), Phe/Ser (5:1), Phe/Trp (5:1) and Phe/Tyr (5:1), recorded from 298 to 353 K. All experiments were conducted with a recycle delay of 10 s, using a 500 MHz solution-state NMR spectrometer.

6.2.8. Investigation of binding processes to the fibrous network by STD NMR

Exchange phenomena between molecules incorporated in the hydrogel network and those dissolved in the isotropic solution phase can be elucidated using STD NMR experiments. The observed mono-exponential evolution of fractional STD response (η^{STD}) with saturation time (Figure 6.11a) supported the presence of fast exchanging processes (on the

NMR relaxation time scale) of Phe between free and bound states in the hydrogel of Phe. To analyse the experiments quantitatively, the initial slopes of the curves, STD_0 , were considered. This is also needed to avoid potential effects of differences in longitudinal relaxation times and rebinding processes on the accumulation of saturation.¹⁹⁶ No significant differences were observed between the STD_0 values of different proton sites of Phe, due to its relative small dimensions, which prevented us from drawing conclusions about specific structural details on the bound state.

STD NMR experiments were conducted also at variable temperature to monitor how exchange phenomena were affected throughout the gel-to-solution transitions. STD_0 for Phe protons decreased rather linearly with increasing temperature (Figure 6.11b). As the determined 1H T_1 times were longer at higher temperatures, this reduction cannot be explained in terms of saturation losses by longitudinal relaxation. The significant reduction in STD_0 observed was considered to reflect two processes: (i) the increase in the binding kinetics with temperature, reducing the fraction of bound species, and, more importantly, (ii) the gradual dissolution of the supramolecular network, reaching full dissolution at 338 K. This temperature was higher than the determined macroscopically T_{gel} value (*ca.* 325 K), since the former reflects the dissolution of the supramolecular network (that acts as a reservoir of magnetisation), whereas the latter describes the loss of structural integrity. Relaxation studies corroborated these findings, since 338 K was the temperature above which the distribution of 1H T_1 values started resembling that of solutions of Phe (Figure 6.10). At very high temperatures, molecules form a pure solution with individual molecules behaving isotropically and hence no STD signals are detected.

The ability of STD NMR to detect the exchange of gelator molecules between the network and the solution at temperatures above T_{gel} is particularly interesting. It is therefore proposed the application of variable temperature STD NMR experiments to supramolecular gels as a quick and robust tool to provide information at a molecular level on the different stages of dissolution of the 3D network. These results could pave the way for the use of STD NMR to understand non-covalent supramolecular assembly processes that occur through nucleation (*e.g.* aggregation, gelation or crystallisation) and current investigations are underway in my research group.

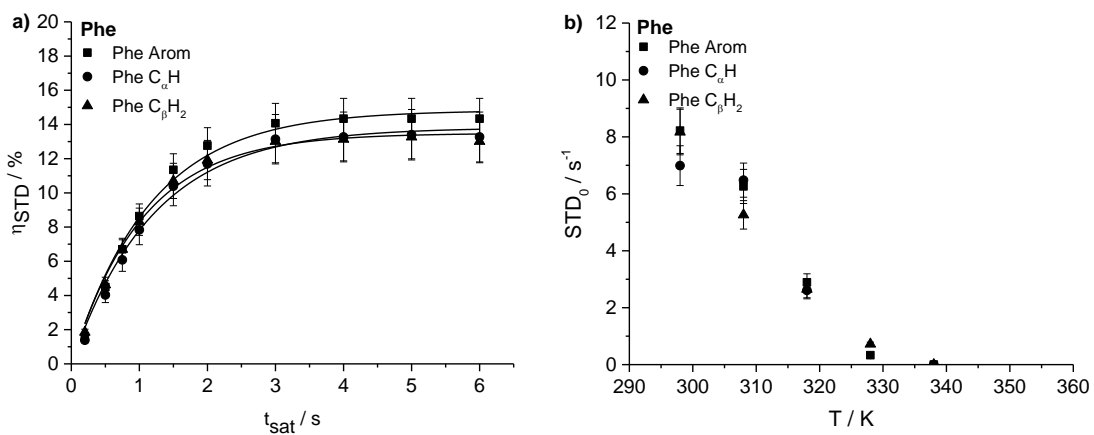


Figure 6.11. Build-up curves of fractional STD response (η_{STD}) in hydrogels of **a)** Phe measured at 298 K. **b)** Initial slope values recorded from 298 to 338 K upon saturation of the network in the hydrogel of Phe ($STD_{on} = 0$ ppm and $STD_{off} = 40$ ppm). STD parameters in these studies were reproducible with a mean error of 9.6 % as a result of three independent measurements. All experiments were conducted with a total experiment time of 6 s, using a 500 MHz solution-state NMR spectrometer.

The effect of introducing an additive was assessed through the evaluation of η_{STD} (Figure 6.12) and STD_0 in multi-component systems (Table 6.6). η_{STD} values of Phe protons decreased in all multi-component hydrogels in comparison with the hydrogel of Phe. In contrast to classical exchange processes in protein-ligand interactions (in which there is a determined number of binding sites decorating the surface of the protein), in a supramolecular system such a decrease in saturation transfer may be attributed to several phenomena, which are discussed below.

Lower values of η_{STD} might result from: (i) decreased binding strength of Phe, due to perturbations of the network structure from the binding of the additive, or (ii) from competition of the additive with Phe for the interaction sites, assuming the network interaction sites keep the same in the presence and in the absence of the additive. In both cases, there will be an increased amount of Phe in solution, which reduces the fraction of bound molecules, and hence the fractional STD response. On the other hand, slow exchange on the NMR relaxation time scale, associated with strong binding, would result in longer residence time in the network-bound state, lower accumulation of saturation in solution and, therefore, lower STD signals.

In the hydrogels of Phe/Trp and Phe/Tyr, Trp and Tyr aromatic protons displayed η_{STD} values in the same range as protons of Phe (Figure 6.12). These experiments provided

evidence supporting the claim that Trp and Tyr are in fast exchange between the free and network-bound states. More importantly, the similarity between η_{STD} values for Phe and Trp or Tyr can be interpreted in terms of the strength of binding of these additives to the network. Under these conditions, if Trp and Tyr had similar affinities for the network as Phe, their η_{STD} values would be much larger than the η_{STD} values of Phe. Their lower η_{STD} values, along with the reduction of η_{STD} values of Phe, suggested that Trp and Tyr were stronger binders to the network than Phe, accumulating lower saturation in solution. In this way, the combination of solid-state CP/MAS NMR findings, 1H T_1 measurements, nOe-based experiments and solution-state NMR spectral variations allowed us to conclude confidently that Trp and Tyr make part of the rigid components of the fibrous network.

The lower η_{STD} observed for Phe in hydrogels of Phe/Trp and Phe/Tyr could be interpreted incorrectly as an indication of an increase in the amount of Phe in the free state, resulting from the competitive binding between Phe and the additive. This is not the case for two reasons. Firstly, supramolecular gels do not have a well-defined number of interaction sites, unlike binding pockets in proteins. The hydrogel network is a dynamic assembly, and binding of additives will not just passively compete with Phe, but they can alter the structure and dynamics of the interaction sites. Secondly, this interpretation is contradictory to the presence of lower concentrations of Phe in solution (Table 6.5) and the enhanced resistance to deformation found for the hydrogel of Phe/Trp (Figure 6.2). Strengthening of supramolecular gel fibres is usually associated with an increased number of gel forming molecules, leading to formation of more fibres and interfibrillar connections. In light of these findings, lower η_{STD} for Phe occurs due to modification of the strength of the interactions of Phe with Trp or Tyr rich domains located in the gel fibres, resulting in different rates of exchange.

The low STD response recorded for Leu in the hydrogel of Phe/Leu (Figure 6.12) confirmed the weak interaction of Leu with the gel/solution interfaces, in agreement with the findings from NOESY experiments. Additionally, there was no evidence in CP/MAS NMR experiments of the incorporation of Leu in the rigid components of the network.

In the case of Ser-based hydrogels, the absence of η_{STD} for Ser indicated absence of binding to the network, in agreement with 1H solution-state NMR experiments in which Ser

protons appeared as sharp intense resonances with long T_1 times, suggestive of fast molecular tumbling. The increased amount of dissolved Phe observed in ^1H spectra of the hydrogel of Phe/Ser resulted in the decrease of η_{STD} values for Phe protons. Altogether, NMR experimental data on Phe/Ser hydrogels showed that Ser has disruptive effects on the Phe network, explaining the markedly lower G' value measured. Intriguingly, NOESY and STD NMR experiments showed that Ser does not interact with the Phe network in the gel state, even though Phe/Ser interactions have been described previously.²³¹ Since slower kinetics of formation of early stage aggregates was observed for the hydrogel of Phe/Ser hydrogel (Figure 6.7), it was assumed that the solubilising effect of Phe by Ser is likely to be predominant during the nucleation stage of the gelation process.

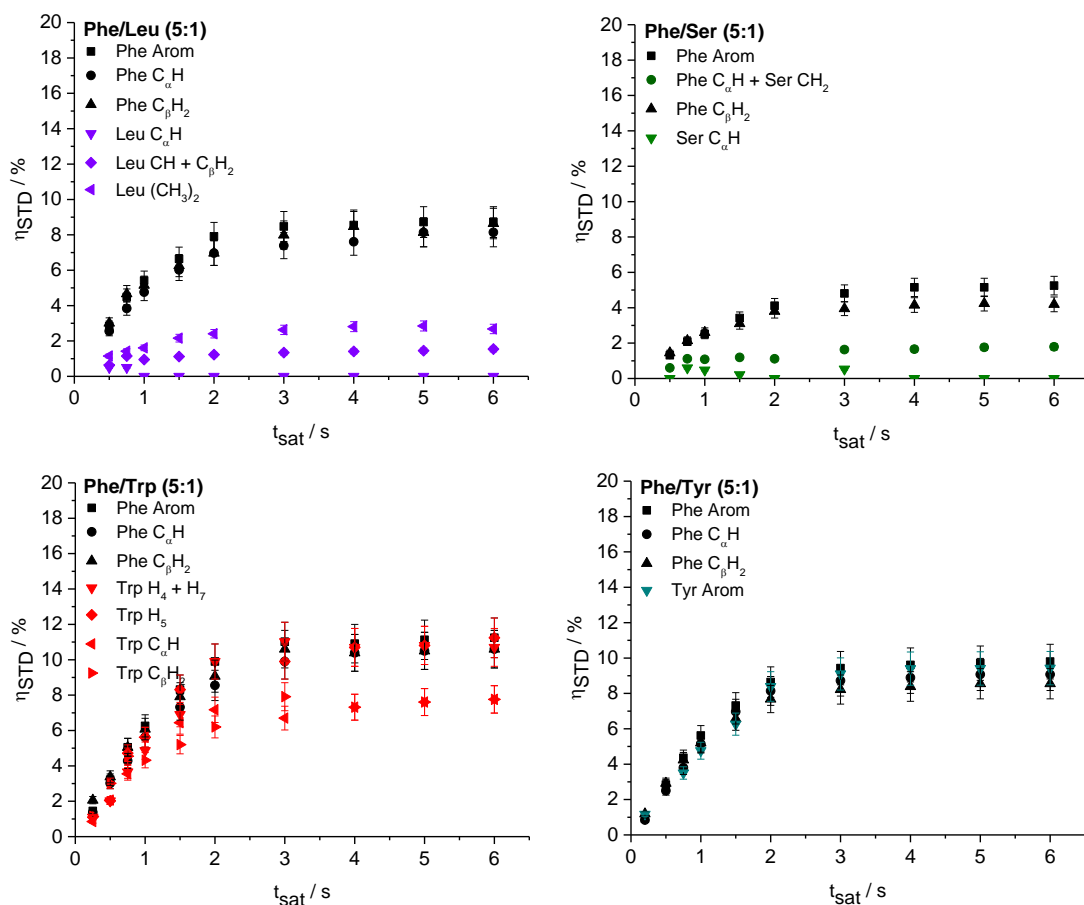


Figure 6.12. Build-up curves of η_{STD} in hydrogels of Phe/Leu (5:1), Phe/Ser (5:1), Phe/Trp (5:1) and Phe/Tyr (5:1), measured at 298 K (STD₀ = 0 ppm and STD_{off} = 40 ppm).

Table 6.6. Initial slope values of fractional STD response (STD_0) for the hydrogels of Phe, Phe/Leu (5:1), Phe/Ser (5:1), Phe/Trp (5:1) and Phe/Tyr (5:1), measured at 298 K ($STD_{on} = 0$ ppm and $STD_{off} = 40$ ppm).

	Phe Arom	Phe $C_\alpha H$	Phe $C_\beta H_2$	STD ₀ / s ⁻¹				Additive molecule
				Trp H ₄ 7.25	Trp H ₇ 7.25	Trp H ₅ 7.72	Trp C _α H 7.41	
Phe/Trp	8.26	7.77	7.93	Trp H ₄ 7.25	Trp H ₇ 7.25	Trp H ₅ 7.72	Trp C _α H 7.41	Trp C _β H ₂ 6.91
Phe/Tyr	9.22	7.47	9.21	Tyr Arom 7.01	-	-	-	-
Phe	12.80	11.52	12.90	-	-	-	-	-
Phe/Leu	8.14	7.03	7.93	Leu C _α H 0	Leu CH+C _β H ₂ 1.86	Leu (CH ₃) ₂ 2.67	-	-
Phe/Ser	3.54	1.53 ^a	3.93	Ser C _α H 0	Ser C _β H ₂ 1.53 ^a	-	-	-

^a Represents an averaged value between Phe C_αH and Ser C_βH₂.

6.3. Concluding remarks

The development of multi-component systems proved to be an elegant strategy to modify the rheological properties of the “gel-crystal” supramolecular system. The study emphasised the dynamic complexity of multi-component hydrogels: the effect of additive molecules on hydrogels might not result only from their interactions with the final gel product, but also from modifications introduced during nucleation and/or growth processes.

It was possible to correlate the strength of the gel with the composition of the gel fibres and solid-liquid interface in the presence of additive gelator molecules. Modification of the kinetics of gelation, due to interference with nucleation and fibre growth, changed the concentration of gelator molecules incorporated within the rigid structures. This indicated differences in the gelation mechanism of multi-component systems, which in turn altered the materials resistance to deformation. The addition of Ser resulted in weaker materials, due to an effectively lower concentration of Phe in the solid fibres. Contrarily, Trp was proven to contribute to stabilisation of the 3D network, as a higher content of molecules incorporated in the solid structures probably led to a higher number of fibres and interfibrillar cross-links, resulting in a material more resistant to deformation.

Solid and solution-state NMR experiments have provided mechanistic insights into the processes of supramolecular multi-component gel formation and the dynamics of the resulting materials. When assessing the impact of additive molecules on hydrogels by

means of STD NMR studies, observations from CP/MAS experiments should also be taken into account. If the additive molecule shows a build-up of saturation and peaks in CP/MAS spectra of hydrogels, they might be incorporated into the rigid fibres. If the additive molecule accumulates saturation in solution but no peaks are observed in CP/MAS experiments, there is no incorporation but weak interactions occur at the surface of the fibres. The combination of STD NMR and CP/MAS NMR was shown to be a very powerful approach to monitor the incorporation of additives into the hydrogel supramolecular fibrous network.

These studies have proven capable of providing an insight into the dynamics of soft materials, even when the solid component is crystalline. It was only the combination of solution, solid-state and HR-MAS NMR experiments that has enabled us to gain in-depth understanding of such complex, multiphasic soft materials. STD NMR experiments confirmed that all investigated supramolecular hydrogels were dominated by fast exchange processes between free and bound gelator molecules, characteristic of a highly dynamic environment. The application of the presented NMR-based approach enabled better understanding of the role of guest molecules, such as drugs, co-gelators or cells, in the self-assembly processes of supramolecular soft materials, which is of paramount importance in knowledge-based design of new functional systems.

Chapter 7

7. Investigating halogen effect on the solid-state packing of phenylalanine and the properties of the resulting multiple gelator hydrogels

Findings from this chapter are partly published in

Ramalhete, S.; Foster, J. S.; Green, H. R.; Nartowski, K. P.; Heinrich, M.; Martin, P.; Khimyak, Y. Z.; Lloyd, G. O., FDHALO17: Halogen effects on the solid-state packing of phenylalanine derivatives and the resulting gelation properties. *Faraday Discussions* **2017**, 203, 423-439.

Bearing in mind that different halides attached to the aromatic ring have had marked effects on gelation of Fmoc-Phe derivatives²³²⁻²³⁴, pentapeptides²³⁵, poly(benzyl ether) derived dendrons²³⁶ and bis(pyridyl urea) derivatives²³⁷ previously, it was decided to introduce halogen atoms into Phe to gain structural control over supramolecular gelation. With a number of potential sites for intermolecular interactions, namely π - π stacking, hydrogen bonding, hydrophobic effects and electrostatic interactions between the zwitterionic components of the compound, there were a number of chemical modifications that could be implemented to alter the resulting gelation properties. Studies on Phe hydrogelation described in Chapter 5 (page 148) highlighted that the electrostatic interactions drive the self-assembly process. These functional groups should not be modified since this might fully prevent gelation. Hence, the aromatic ring was the most appropriate chemical functionality to alter, enabling the acidity and distribution of the electronic cloud of the ring to be tailored by halogenation, since the hydrophobic effects, C-H \cdots π and π - π interactions provided a minor contribution to stabilisation of the 3D crystal structure.

The first part of this chapter focuses on the gelation of halogenated derivatives of Phe and the effect of the substituents on the outcome of gelation, fibre morphology and viscoelasticity of the network. The crystal structures of five halogenated derivatives were determined and the data was correlated with the tendency to form three-dimensional matrices.

The additional level of control gained over supramolecular gelation of Phe by the preparation of multi-component systems (Chapter 6, page 164) increased the interest in developing materials from two gelating molecules. Therefore, the second part of this chapter discusses multiple gelator hydrogels prepared from Phe and 4-fluoro-*L*-phenylalanine, which individually give rise to isostructural solid networks. It was evaluated how the isostructurality of the solid components dictates the packing of gel fibres and dynamics of the interfaces using microscopy, rheology, diffraction and NMR spectroscopy. Furthermore, the possibility of monitoring local environments of ¹⁹F nuclei, an abundant and sensitive NMR active spin, was very advantageous. The wide chemical shift range and high sensitivity of ¹⁹F nuclei enabled subtle changes in the local environments of mixed systems to be identified, and the presence of a single ¹⁹F nucleus per molecule of F-Phe avoided overlapping of multiple resonances.

7.1. Introduction

Halogenation of Fmoc-Phe derivatives by Ryan *et al.* (2010) and Pizzi *et al.* (2017) showed that self-assembly processes in water and mechanical properties of the resulting materials were highly dependent on the nature of the halogen and substitution position on the aromatic ring.²³²⁻²³⁴ They hypothesised that halides modified the electronic distribution around the aromatic group which, in turn, altered the strength of π - π interactions.²³² An important aspect to take into account in all these studies is the concept of halogen-halogen interaction and halogen bonding.²³⁸⁻²⁴⁵ This has been highlighted in a number of studies involving small molecule gelators.^{235-237, 246} In particular, the Br and I derivatives can often show significant halogen-based interactions that cause a stepped change in structural packing and properties.^{232-234, 238-245}

The gelation properties of a number of chirally pure Phe derivatives were thus determined (Figure 7.1): 4-fluoro-*L*-phenylalanine (F-Phe), 3,4-difluoro-*L*-phenylalanine

(2F-Phe), pentafluoro-*L*-phenylalanine (5F-Phe), 4-chloro-*D*-phenylalanine (Cl-Phe), 3,4-dichloro-*D*-phenylalanine (2ClPhe), 4-bromo-*L*-phenylalanine (Br-Phe), and 4-iodo-*L*-phenylalanine (I-Phe).

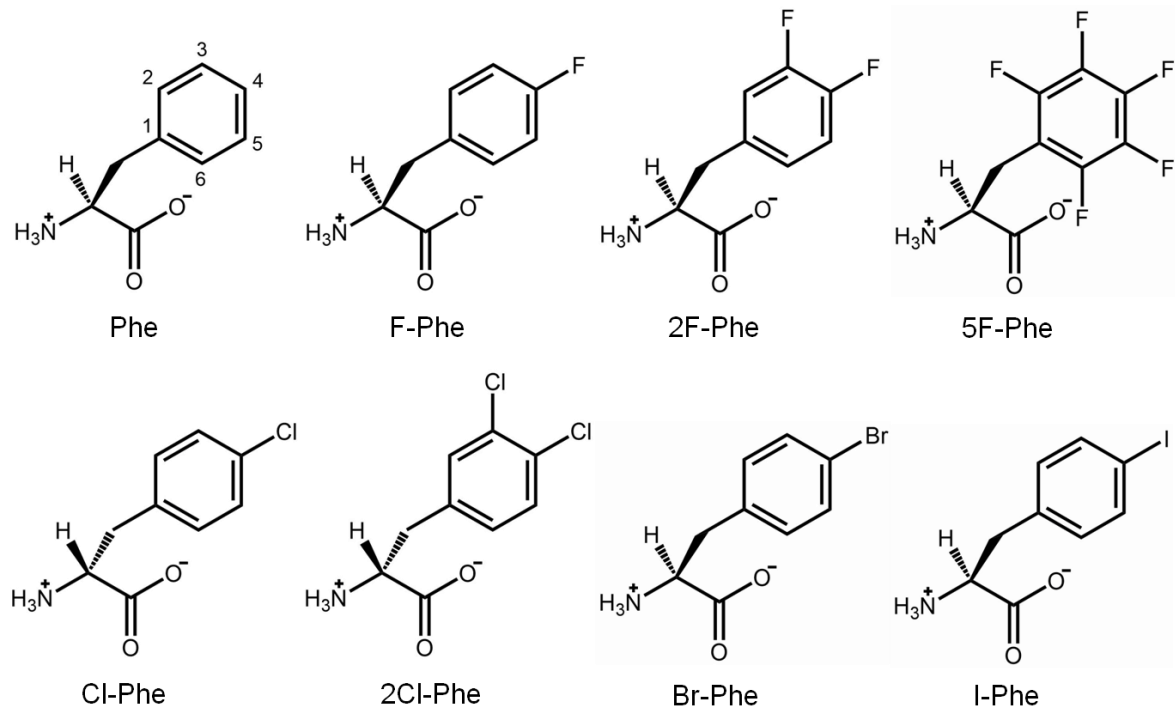


Figure 7.1. Molecular structure of the zwitterionic form of Phe with numbering of aromatic carbon atoms and the halogenated derivatives under study.

7.2. Results and discussion

7.3. Part I – Halogenated derivatives of Phe

7.3.1. Macro and microscopic characterisation of hydrogels

The majority of these halogenated derivatives of Phe were found to yield gels in water (Figure 7.2). Br-Phe and I-Phe did not produce stable hydrogels, most probably due to their very poor water solubilities. In the case of Br-Phe, the compound was found to form a gel, but the hydrogels were very unstable, whereas I-Phe was not able to produce gels at all in water. This behaviour was different to that found for the Fmoc-Phe derivatives, where gelation still occurred for Br and I derivatives, as the hydrophobic Fmoc group is a strong driving force of gel formation.²³²⁻²³⁴

The determination of CGC *via* the vial inversion test showed a general decrease of the CGC value with increasing molecular mass of Phe derivatives (Table 7.1). Lower molar concentrations were needed to prompt fibre formation in comparison with the parent compound Phe, due to their lower water solubilities. Generally, a more hydrophobic group decreases the CGC, as shown in the Fmoc-Phe series of compounds.²³²⁻²³⁴ Despite the lowering of the molar CGC trends with the increase of molecular weight, the CGC values as % of weight/volume only decreased slightly. Moreover, F-Phe formed gels significantly faster than Phe, a phenomenon observed previously for the electron-deficient derivatives of Fmoc-Phe.²³⁴

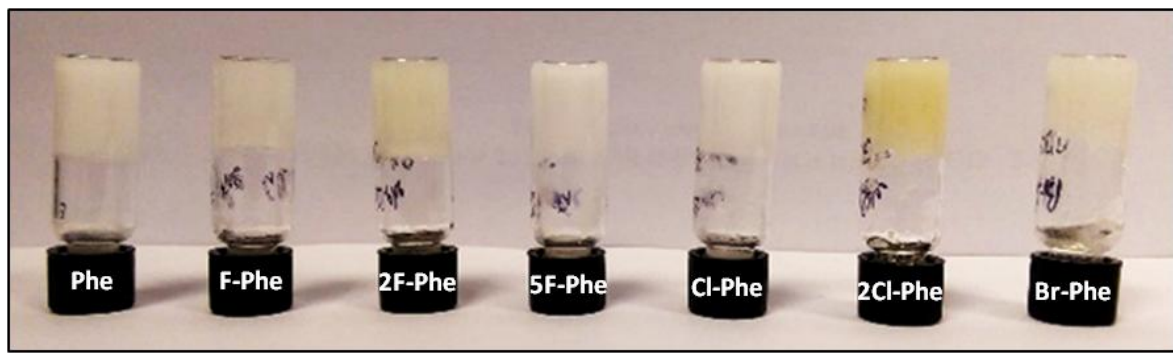


Figure 7.2. Photographs of hydrogels of Phe and its halogenated derivatives.

Table 7.1. Gelation results, critical gelation concentration (CGC), water solubility (s_{water}) and molar mass (M) of Phe and its halogenated derivatives at 298 K.

Compound	Product	CGC / mM	$s_{\text{water}} / \text{g L}^{-1}, 298 \text{ K}$	$M / \text{g mol}^{-1}$
Phe	Gel	210	29.60	165.19
F-Phe	Gel	160	18.59	183.18
2F-Phe	Gel	140	2.08	201.17
5F-Phe	Gel	80	0.33	477.38
Cl-Phe	Gel	100	0.96	199.63
2Cl-Phe	Gel	85	0.24	234.08
Br-Phe	Metastable gel	40	0.47	244.09
I-Phe	Insoluble/precipitate	-	0.15	291.09

The morphology of the hydrogels was assessed by performing SEM on dried samples and gave clear fibrous morphology (Figure 7.3). The size of these fibres was found to be in the range from 600 to 2000 nm wide.

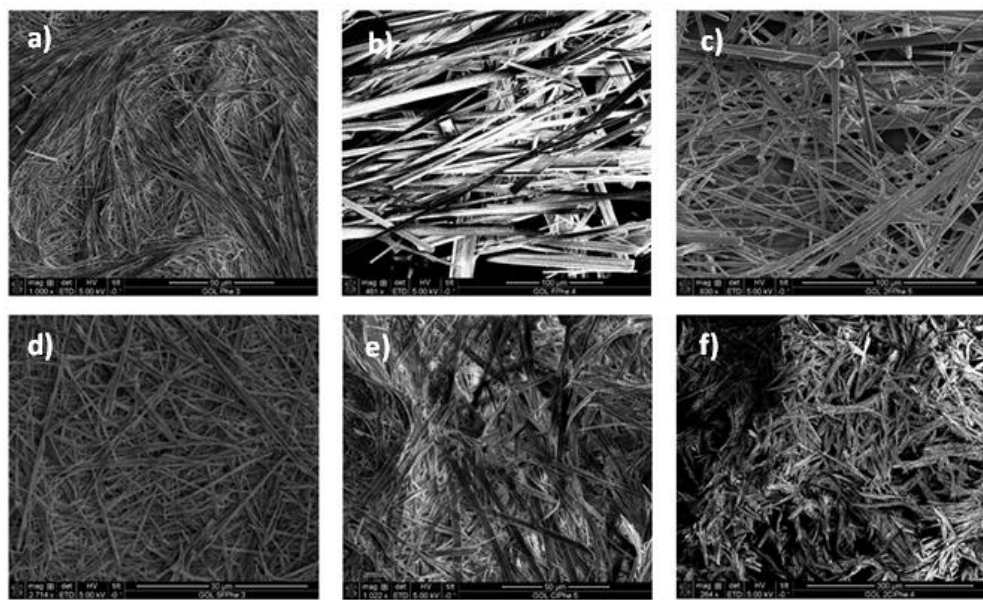


Figure 7.3. SEM images of dry hydrogels of a) Phe, b) F-Phe, c) 2F-Phe, d) 5F-Phe, e) Cl-Phe and f) 2Cl-Phe (100 mM).

7.3.2. Viscoelastic properties of hydrogels

Similarly to the hydrogel of Phe, these hydrogels often collapsed under mechanical manipulation with a spatula, extruding the majority of the water. The large size of the fibres and crystalline rigidity of the hydrogels can partly explain this behaviour. The determination of viscoelastic parameters allowed us to assess the strength of the fibres. When frequency sweeps were performed with a small amplitude stress on a number of different samples, the solid-like nature at 293 K was reflected in the phase angle (δ) formed between the phases of stress and strain, which was always below 10°. The storage moduli (G') of all materials were in the order of 10^5 Pa ($G' \approx 5.0 \times 10^5$ Pa) and these values were typically one order of magnitude greater than the loss moduli (G'') ($G'' \approx 2.5 \times 10^4$ Pa) (Figure 7.4), a property of robust gels, demonstrating the elastic behaviour of these materials. The values of storage moduli in the range of 10^5 Pa are a rare example of very strong supramolecular gel materials.²¹⁹

The trend of lowering the CGC within the hydrogels upon the addition of halogenated groups was partially matched by the trends in the G' values. The G' values increased with increase in the fluoro addition from F-Phe to 2F-Phe, and finally to 5F-Phe. This could be explained by different partitioning of the compounds between solution and solid components in the gels. The more hydrophobic and less soluble the compound, the more

of it is likely to be included into the solid component of the gel (the fibres), thus increasing the mass of the solid network (and the number of interfibrillar cross-links) and potential gel strength.

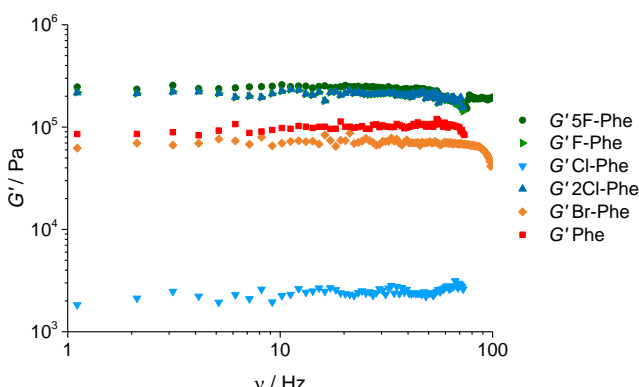


Figure 7.4. Evolution of storage modulus (G') in frequency sweep experiments for Phe, F-Phe, 2F-Phe, 5F-Phe, Cl-Phe, 2Cl-Phe and Br-Phe. Hot solutions (*ca.* 1 mL) were pipetted into a 500 μm gap (parallel plate geometry). All samples were subjected to frequency sweeps in the range of 0.1 to 100 Hz and applied stress of 500 Pa.

7.3.3. Structural characterisation of the rigid fibres

Since X-ray crystallography offers a valuable insight into formation of ordered hydrogel structures, Dr. Gareth Lloyd (Heriot-Watt University) conducted crystallography studies on these halogenated Phe compounds. This provided an excellent opportunity to study the solid state phase of colloidal materials, as the fibres are crystalline in nature. Single-crystal data were obtained by removing single fibrous crystals from the gel solutions.

All the crystal forms were found to be hydrates. The $Z' = 2$ leads to two non-equivalent molecules in the asymmetric unit of each structure. The bilayer arrangement was found in all the materials studied. The F-Phe, 2F-Phe, Cl-Phe gel forming phases were all found to be isostructural to the known form of Phe monohydrate and the published structure of 3-fluorophenylalanine monohydrate.^{247, 248} This could be best evidenced by looking at their packing motifs (Figure 7.5). The isostructurality of the gel forming crystals allows for analysis of the predominant interactions and of the subtle variations between different halogens. The anisotropic assembly resulting in fibre formation occurs due to the electrostatic interactions of the positive and negative components of the Phe derivatives down the *b* axis of all the structures. The crystal structures of 2Cl-Phe and 5F-Phe phases are yet to be determined.

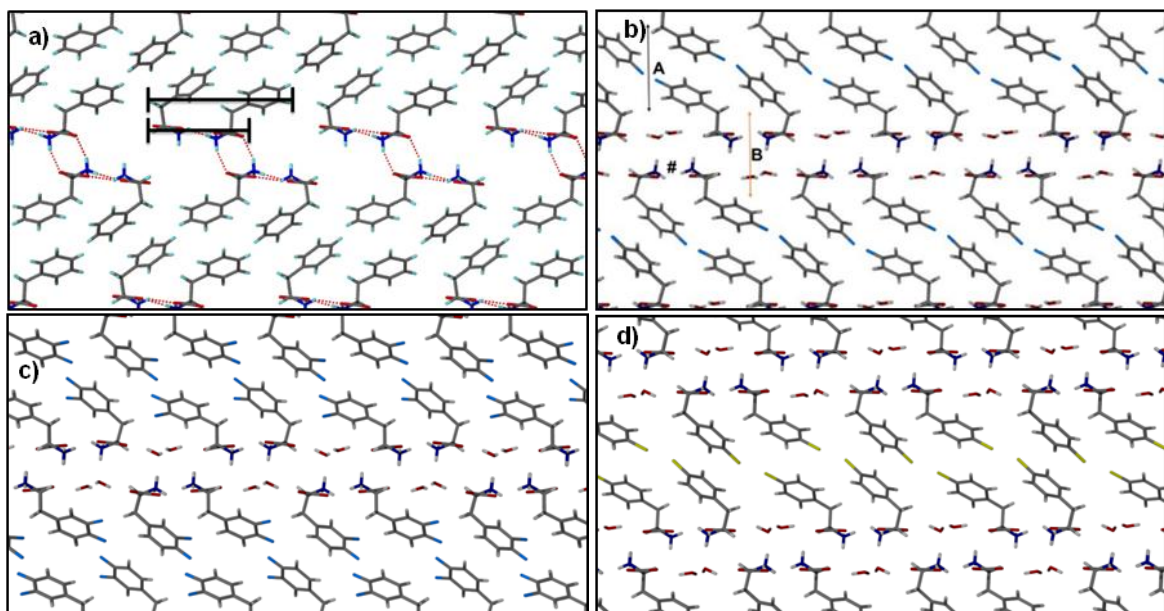


Figure 7.5. Packing motif of the **a)** Phe, **b)** F-Phe, **c)** 2F-Phe and **d)** Cl-Phe fibres. **a)** Packing of dimers of Phe shown down the *b* axis and with water guests removed for clarity. **b)** A (hydrophobic) and B (hydrophilic) layers are indicated, # is highlighting the dimer formation between the zwitterionic groups. Dimer stacks are not interacting with each other except for some hydrogen bonding and π - π interactions. It is also clear that the dimer stacks are anisotropic with the hydrophilic section shorter than the hydrophobic region.

Hirshfeld surface analyses of the monohydrate structures revealed there were no significant changes in the interactions between the molecules with regards to hydrogen bonding and electrostatic interactions (Figure 7.6a,b). The clear difference occurred in the hydrophobic region of the phenyl groups. The fluoro groups appeared only to increase the polarisation of the aromatic group and did not interact with each other significantly. Increased fluorination escalated the polarisation of the aromatic group and caused disruption of the hydrophobic packing motif. The chlorine atoms in the Cl-Phe monohydrate structure interacted with each other forming a halogen-halogen interaction with an angle (148.6(3) $^\circ$) considerably smaller than the ideal linear arrangement (180 $^\circ$) for strong halogen-halogen bonds. It could therefore be ascertained that this type I halogen-halogen interaction did not disrupt the hydrophilic layer interactions. The electrostatic potential surface indicated that the π negative potential could still interact with the electropositive potential of the C-H groups of the methylene group.

In clear contrast, the Br-Phe monohydrate structure isolated from an aged hydrogel was found to be isostructural to the known I-Phe monohydrate form (this was designated as monoclinic form I³²). Hydrogen bonding, molecular conformations and electrostatic

interactions were similar. The $Z' = 1$ leads to one non-equivalent molecule in the asymmetric unit of each structure. These structures contained type II halogen-halogen interactions (Figure 7.6c,d). The halogen-halogen interactions are more significant in these structures when compared to the interactions found in the Cl-Phe structure.

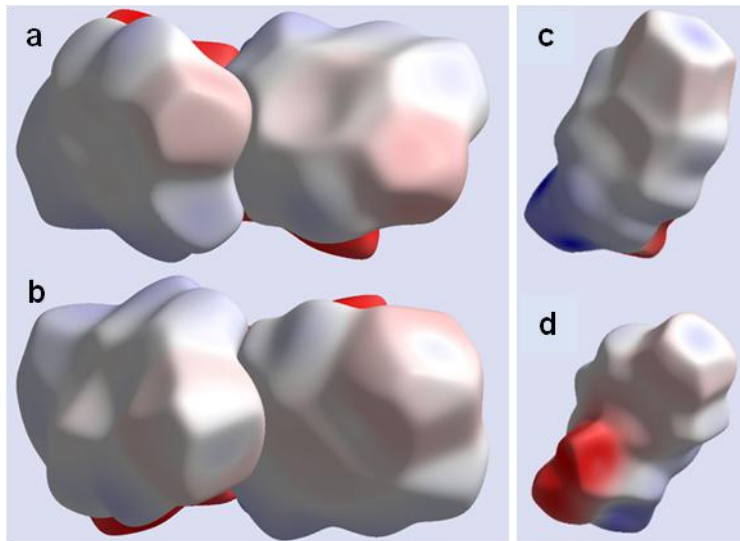


Figure 7.6. Electrostatic potential Hirshfeld surfaces of the **a)** F-Phe and **b)** Cl-Phe derivatives with the asymmetric unit (ASU) of the respective monohydrate crystal structures. Halogenation of the aromatic ring resulted in increased polarisation of the hydrophobic groups and this could be viewed by the blue “hue” of the hydrogen edges of the aromatic groups and the red “hue” of the central carbon rings. The “sigma” hole of the chloro (circular “white” region of the red area) could be viewed in both molecules of the Cl-Phe ASU. Electrostatic potential Hirshfeld surfaces of the **c)** I-Phe and **d)** Br-Phe derivatives. The halogen-halogen interactions are shown clearly with the “sigma hole” indicated by the blue area surrounded by white at the tips of the halogen groups. The sigma hole interacts with the electrostatically negative regions of the halogen groups perpendicularly, as expected for a type II halogen-halogen interaction.

7.3.4. Concluding remarks

It was shown that halogenation of the aromatic ring of Phe can result in the variation of the hydrogelation properties to a great extent. Upon addition of halogen atoms, gelation in water resulted in crystalline phases and in a general improvement in gelation ability, due to a decrease in solubility. The viscoelastic properties were typical of very robust molecular gels. Analyses of the crystal structures revealed isostructural behaviour with changes in the interactions between aromatic groups of Phe, fluoro and chloro derivatives. The halogen functionality was found to be driving changes in the packing motifs, and

therefore, dictate gelation ability. With an increase in the strength of the halogen-halogen interactions, the crystal packing motifs changed, most notably when Br or I were positioned in the *para*-position of the aromatic group. There was a stepped change with the addition of Br resulting in the gels becoming metastable. With the iodo functionality, the gelation ability was fully lost.

7.4. Part II – Multiple gelator hydrogels of Phe and F-Phe

7.4.1. Characterisation of morphologic and viscoelastic properties

Mixtures of Phe and F-Phe with different ratios and concentrations (Table 7.2) were heated up and immediately quenched as described in the experimental section (Chapter 3, section 3.2, page 120). For comparison purposes, the overall molar concentration was maintained at 303 mM, which corresponds to the concentration at which the pure monohydrate form of Phe can be obtained.

Table 7.2. Molar concentrations and ratios of Phe and F-Phe used to prepare single and multiple gelator hydrogels.

	[Phe] / mM	[F-Phe] / mM
Phe	303.0	-
Phe/F-Phe (5:1)	252.5	50.5
Phe/F-Phe (2:1)	202.0	101.0
Phe/F-Phe (1:1)	151.5	151.5
Phe/F-Phe (1:2)	101.0	202.0
Phe/F-Phe (1:5)	50.5	252.5
F-Phe	-	303.0

The resulting hydrogels (Figure 7.7b) were composed of hair-like structures assigned to Phe fibres (Figure 7.7a) co-existing with thicker needle-like structures that most likely corresponded to F-Phe fibres (Figure 7.7c). The gelation ability of these mixtures was only dependent on the overall mass concentration, as a minimum of 3 % (w/v) was the determining factor for hydrogel formation. Similar G' values were obtained for pure and mixed hydrogels (Figure 7.8), indicating comparable response of the hydrogel fibres to external stress.

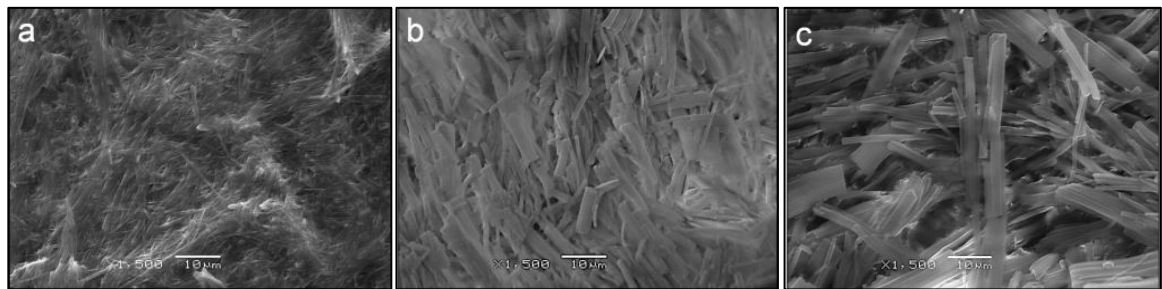


Figure 7.7. SEM images of dry hydrogels of **a)** Phe, **b)** Phe/F-Phe (1:1) and **c)** F-Phe (303 mM).

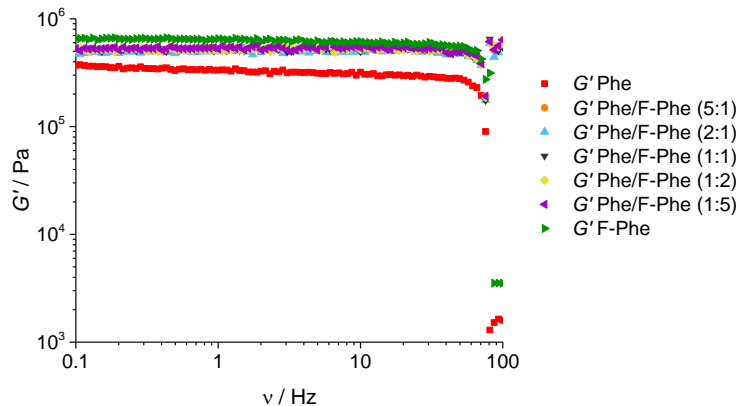


Figure 7.8. Evolution of storage (G') and loss (G'') moduli in frequency sweep experiments for Phe, Phe/F-Phe (5:1), Phe/F-Phe (2:1), Phe/F-Phe (1:1), Phe/F-Phe (1:2), Phe/F-Phe (1:5) and F-Phe hydrogels (303 mM). Hot solutions (*ca.* 1 mL) were pipetted into a 500 μ m gap (parallel plate geometry). All samples were subjected to frequency sweeps in the range of 0.1 to 100 Hz and applied stress of 500 Pa.

7.4.2. Structural characterisation of the rigid fibres

The crystalline nature of the fibres of multiple gelator hydrogels was confirmed by the presence of diffraction peaks in their PXRD patterns (Figure 7.9). PXRD patterns of pure and mixed materials were sufficiently similar to suggest two possibilities: self-sorting occurred resulting in two separate crystalline phases; or a crystalline solid solution (co-assembly) was formed. Careful analysis of the PXRD patterns revealed no clear evidence of self-sorting, which would result in two distinct sets of peaks for the separate structures. Instead, the PXRD patterns of each mixed phases appeared to correspond to a pure phase that contributed as major component. For the 1:1 mixture, the pattern resembled that of F-Phe.

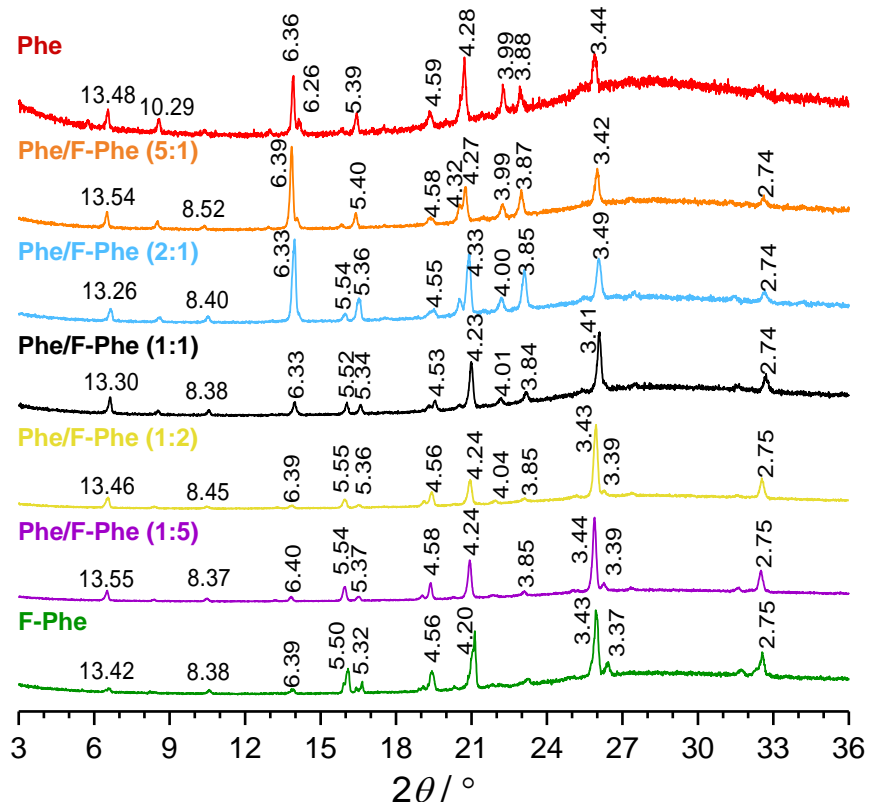


Figure 7.9. PXRD patterns of Phe, Phe/F-Phe (5:1), Phe/F-Phe (2:1), Phe/F-Phe (1:1), Phe/F-Phe (1:2), Phe/F-Phe (1:5) and F-Phe hydrogels.

Further analysis of the XRD patterns through Pawley refinement²⁴⁹ revealed a continuum of the unit cell parameters that was more consistent with a solid solution than with a self-sorted mixing of structures (Figure 7.10). Kitaigorodsky's guidelines on crystalline solid solutions can be summarised into the following: miscibility of the two compounds is required, which often occurs best between the principles of size and shape similarity; and generally the compounds should be good matches in terms of isoelectronicity and isostructurality.²⁵⁰⁻²⁶⁰ It is not unusual to observe formation of solid solutions when two compounds form isostructural crystalline phases and molecules are of similar size.²⁵⁰⁻²⁶⁰ As it is shown in Figure 7.11, the overlay of the two structures revealed that the packing motifs were very similar (isostructural) and the addition of the fluoro group did not alter the unit cell size significantly. Unfortunately, PXRD data were not detailed sufficiently to truly determine the extent of homogeneity of the phases produced, so NMR was used to determine the characteristics of the mixed phases.

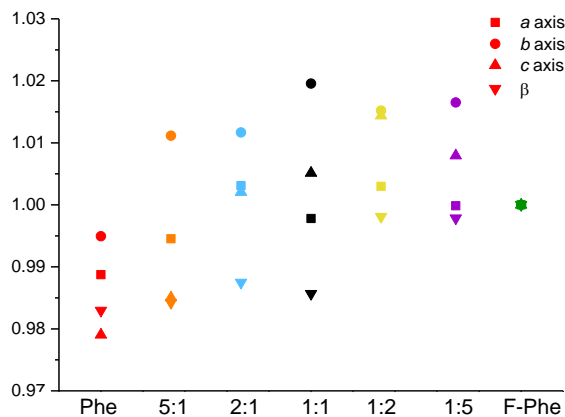


Figure 7.10. Unit cell parameters (normalised to the F-Phe monohydrate phase) determined from the PXRD patterns of Phe, Phe/F-Phe (5:1), Phe/F-Phe (2:1), Phe/F-Phe (1:1), Phe/F-Phe (1:2), Phe/F-Phe (1:5) and F-Phe hydrogels utilising a Pawley fit. The mixtures do not indicate the presence of two components but rather a mixed solid solution with related changes to the unit cells of the structures.

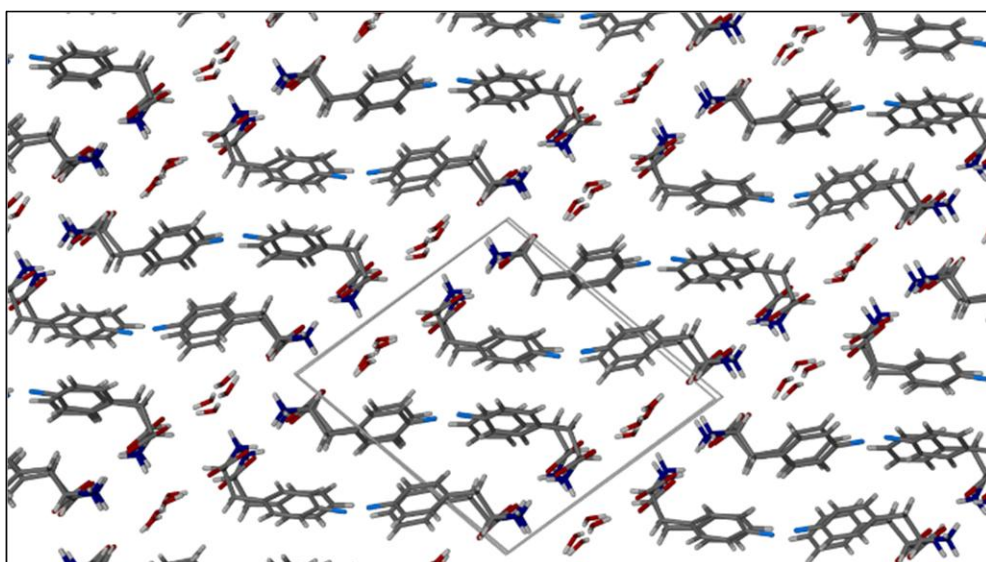


Figure 7.11. Overlay of the molecular packing of Phe²¹³ and F-Phe²⁶¹ crystal structures shown along the b axis of the unit cell of the monohydrate forms, which shows their isostructurality. The Phe structure has been transformed to match the F-Phe by moving the origin of the unit cell one half the length of the a axis along the a axis direction. The unit cell of the monohydrate form of Phe (CCDC Number 1532251) presented monoclinic metric symmetry (space group $P2_1$), with the following refined parameters: $a = 13.112(14)$ Å, $b = 5.409(5)$ Å, $c = 13.849(14)$ Å, $\beta = 102.985(4)$ Å, ($V = 957.11(17)$ Å³) and $Z = 4$.²¹³ The unit cell of the monohydrate form of F-Phe presented monoclinic metric symmetry (space group $P2_1$), with the following refined parameters: $a = 13.303(14)$ Å, $b = 5.443(6)$ Å, $c = 14.015(15)$ Å, $\beta = 104.048(5)$ Å, ($V = 988.02(18)$ Å³) and $Z = 4$.

^1H - ^{13}C CP/MAS solid-state NMR experiments were conducted to investigate the structure of the rigid gel fibres. ^1H - ^{13}C CP/MAS NMR spectra acquired for Phe and F-Phe hydrogels (Figure 7.12) showed two magnetically non-equivalent environments per carbon site, consistent with the presence of two molecules in the asymmetric unit of the monohydrate form.

Similar peak splitting was observed in ^1H - ^{13}C CP/MAS spectra of the mixed gels (Figure 7.12), indicating the crystal structure of these fibres was maintained, in agreement with the findings from diffraction studies. However, the observed line broadening and peak asymmetry indicated a certain degree of tridimensional disorganisation within the mixed hydrogel fibres. The variation of the Phe/F-Phe ratio had the most considerable effect on the ^{13}C chemical shifts and line widths of the following carbon sites: C_1 (Phe), C_1 (F-Phe) and C_βH_2 (Phe and F-Phe). This was most likely due to their proximity to the *para*-substituent, being sensitive to the presence of nearby ^1H and/or ^{19}F atoms. More specifically, when the concentration of F-Phe was increased, ^{13}C peaks of carbon C_1 (Phe) became broader and more deshielded due to the close proximity of this carbon site with electronegative fluorine atoms. Similarly, when the concentration of Phe was increased, the inverse evolution of spectral features was observed for ^{13}C peaks of carbon C_1 (F-Phe) as the presence of nearby Phe molecules had a shielding effect on this proximal carbon. These initial results showed that chemical shifts and line widths of Phe and F-Phe ^{13}C peaks changed accordingly to the nature of the surrounding molecules, which pointed towards Phe and F-Phe molecules being in close proximity in the rigid components of the mixed hydrogels. These trends were more evident in ^1H - ^{13}C CP/MAS spectra of dry hydrogels (Figure 7.13 and Table 7.3).

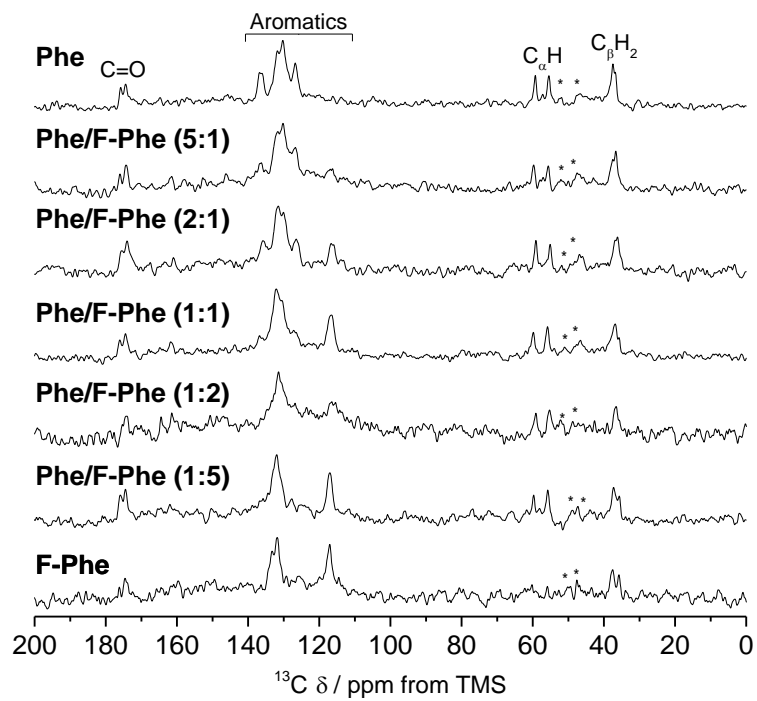


Figure 7.12. ^1H - ^{13}C CP/MAS NMR spectra of Phe, Phe/F-Phe (5:1), Phe/F-Phe (2:1), Phe/F-Phe (1:1), Phe/F-Phe (1:2), Phe/F-Phe (1:5) and F-Phe hydrogels (303 mM), acquired with an MAS rate of 8.5 kHz using a 400 MHz solid-state NMR spectrometer.

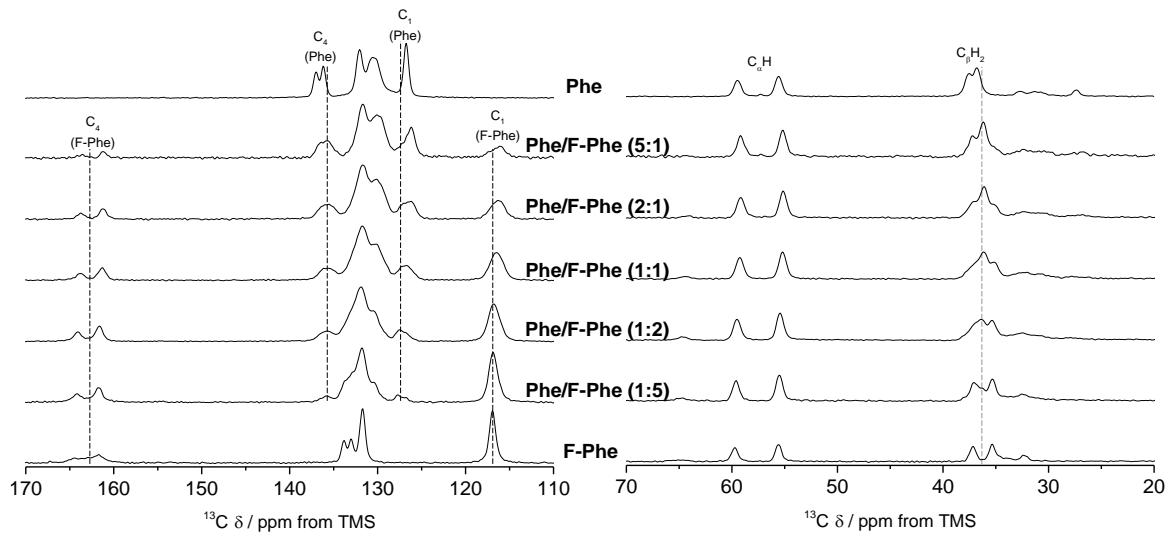


Figure 7.13. Amplification of the aromatic and aliphatic regions of ^1H - ^{13}C CP/MAS NMR spectra of Phe, Phe/F-Phe (5:1), Phe/F-Phe (2:1), Phe/F-Phe (1:1), Phe/F-Phe (1:2), Phe/F-Phe (1:5) and F-Phe dry hydrogels, acquired with an MAS rate of 10 kHz, using a 400 MHz solid-state NMR spectrometer.

Table 7.3. ^{13}C chemical shifts from ^1H - ^{13}C CP/MAS NMR spectra of Phe, Phe/F-Phe (5:1), Phe/F-Phe (2:1), Phe/F-Phe (1:1), Phe/F-Phe (1:2), Phe/F-Phe (1:5) and F-Phe dry hydrogels.

^{19}F δ / ppm from TMS							
	Phe	Phe/F-Phe (5:1)	Phe/F-Phe (2:1)	Phe/F-Phe (1:1)	Phe/F-Phe (1:2)	Phe/F-Phe (1:5)	F-Phe
C=O	176.0	176.1	176.1	176.2	176.1	176.1	176.3
	174.5	174.7	174.6	174.7	174.6	174.6	174.6
F-Phe C ₄ -F	-	164.0	164.1	164.0	164.1	164.2	161.7
	-	161.6	161.6	161.7	161.7	161.8	-
Aromatics	136.9		136.2	136.0	135.9	136.0	136.0
	136.1						-
	132.0	132.0	132.0	132.1	132.0	131.9	133.9
	130.5	130.6	-	-	-	-	133.1
	-	-	-	-	-	-	131.9
F-Phe C ₁	126.7	126.6	126.9	127.5	127.7	127.7	-
	-	116.5	116.7	116.9	116.8	116.9	117.1
C _α H	59.4	59.6	59.6	59.6	59.6	59.7	59.8
	55.5	55.6	55.5	55.6	55.5	55.6	55.7
C _β H ₂	37.5	37.6	37.4	-	-	37.2	-
	36.8	36.6	36.5	36.5	36.4	36.3	37.4
	-	-	35.6	35.6	35.4	35.4	36.7

^{19}F is a sensitive nuclear spin with an isotopic abundance of 100 % and can reveal a wealth of structural information.²⁶² Hence, the local environments of this nucleus were monitored for the different Phe/F-Phe ratios used in single and multiple gelator hydrogels. Single-pulse ^{19}F NMR spectra of all hydrogels presented a sharp peak at -114.5 ppm corresponding to the isotropic pools of dissolved F-Phe molecules (Figure 7.4), whereas significant line broadening was observed in experiments performed on dry hydrogels caused by the considerable anisotropy of ^{19}F chemical shift and strong dipolar couplings between ^{19}F and ^1H spins.

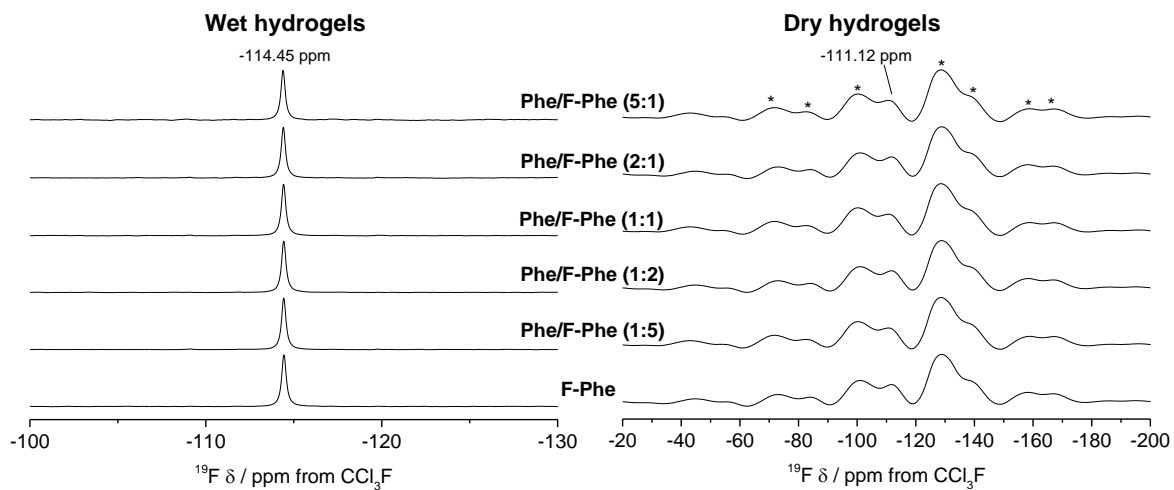


Figure 7.14. ^{19}F NMR spectra of Phe/F-Phe (5:1), Phe/F-Phe (2:1), Phe/F-Phe (1:1), Phe/F-Phe (1:2), Phe/F-Phe (1:5) and F-Phe wet and dry hydrogels, acquired with MAS rates of 1 or 10 kHz, respectively, using a 400 MHz solid-state NMR spectrometer. Asterisks represent spinning sidebands.

Experiments at the UK 850 MHz solid-state NMR Facility enabled us to achieve a significant increase in resolution (Figure 7.15) due to both high B_0 field and faster MAS rates available. The application of heteronuclear decoupling during acquisition of ^1H - ^{19}F CP/MAS NMR spectra was also beneficial for recording well-resolved spectra (Figure 7.16). High-field ^1H - ^{19}F CP/MAS NMR spectra of dry hydrogels of F-Phe showed two peaks at -112.9 and -114.7 ppm, as expected for the monohydrate form due to $Z' = 2$. As the concentration of Phe was increased, these peaks broadened and gradually disappeared. This was accompanied by the appearance of additional broad peaks at *ca.* 116.8 ppm. These peaks were assigned to ^{19}F s of F-Phe molecules in new molecular environments, probably in close proximity to Phe. In combination with single pulse ^{19}F experiments acquired without heteronuclear decoupling of ^1H s, these findings confirmed the formation of fibres composed of both Phe and F-Phe, consistent with co-assembly mechanisms of formation of mixed gelator hydrogels.

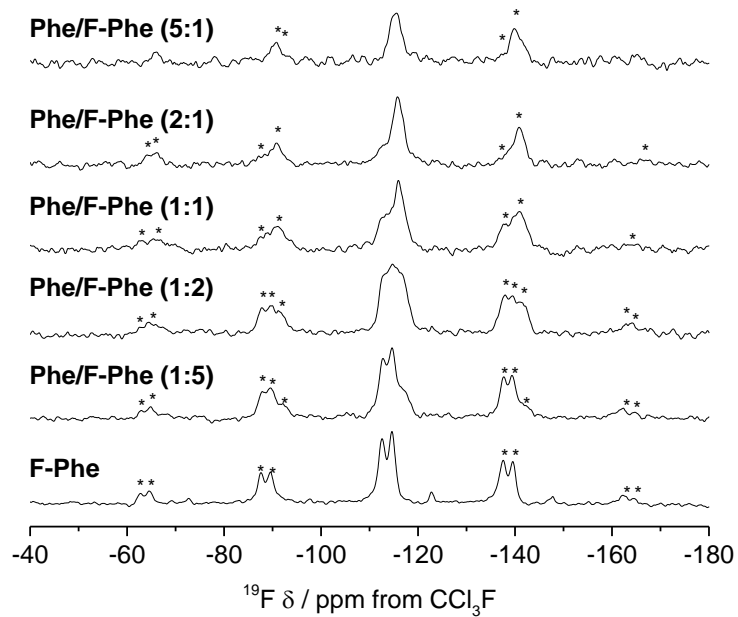


Figure 7.15. ¹⁹F MAS NMR spectra of Phe, Phe/F-Phe (5:1), Phe/F-Phe (2:1), Phe/F-Phe (1:1), Phe/F-Phe (1:2), Phe/F-Phe (1:5) and F-Phe dry hydrogels (303 mM), acquired with an MAS rate of 20 kHz using an 850 MHz solid-state NMR spectrometer with an 8.5 mm MAS probe head. Asterisks represent spinning sidebands.

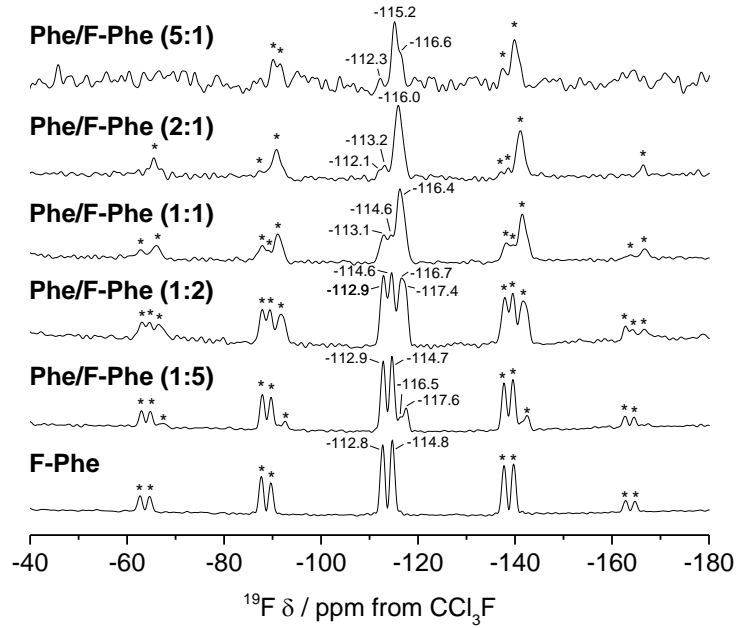


Figure 7.16. ¹H-¹⁹F CP/MAS NMR spectra of Phe, Phe/F-Phe (5:1), Phe/F-Phe (2:1), Phe/F-Phe (1:1), Phe/F-Phe (1:2), Phe/F-Phe (1:5) and F-Phe dry hydrogels (303 mM), acquired with an MAS rate of 20 kHz using an 850 MHz solid-state NMR spectrometer with an 8.5 mm MAS probe head. Numbers represent chemical shift values given in ppm. Asterisks represent spinning sidebands.

^1H - ^{19}F - ^{13}C double CP/MAS spectra only showed the ^{13}C covalently bound to the fluorine group ($\text{C}_4 = 161.32$ ppm) (Figure 7.17). Even though the optimum contact time was being used (2.0 ms, optimised for ^{19}F - ^{13}C conducted at lower fields), there was inefficient transfer of magnetisation from ^{19}Fs to ^{13}Cs through space, possibly reflecting that fluorine is located far from other carbons.

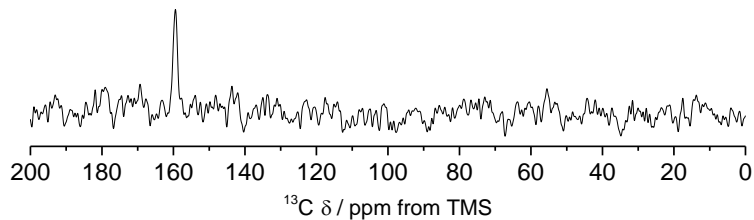


Figure 7.17. ^1H - ^{19}F - ^{13}C double CP/MAS spectra of the dry hydrogel of Phe/F-Phe (1:1) performed with a contact time of 2.0 ms using an MAS rate of 20 kHz using an 850 MHz solid-state NMR spectrometer with an 2.5 mm MAS probe head.

1D ^{19}F - ^1H NOESY high-field experiments were performed with fully hydrated samples, as ^1H NMR peaks were considerably broadened in dry hydrogels. A positive nOe enhancement (typical of fast tumbling molecules) was detected between ^{19}F and the nearby protons $\text{H}_{3,5}$ (6.55 ppm), showing only free gelator molecules could be detected using this methodology.

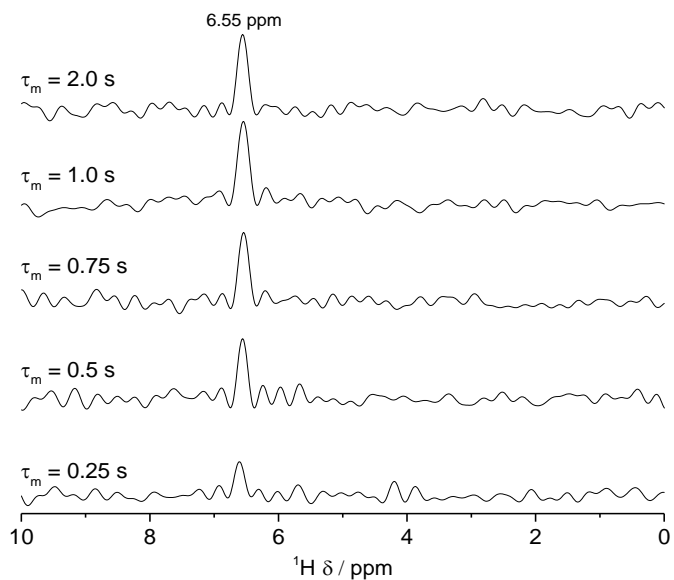


Figure 7.18. 1D ^{19}F - ^1H HOESY spectra of the wet hydrogel of Phe/F-Phe (1:2) performed under static conditions, acquired using an 850 MHz solid-state NMR spectrometer with an 8.2 mm MAS probe head.

Therefore, fast MAS experiments were conducted with the purpose of increasing resolution in the ^1H dimension and allow identifying ^1H - ^1H spatial contacts. However, ^1H spectra remained significantly broadened (Figure 7.19a), reflecting the presence of very strong homonuclear dipolar couplings that cannot be averaged out even at MAS rates of 75 kHz. Consequently, 2D ^1H - ^1H NOESY and 2D ^1H - ^1H Back-to-Back homonuclear double-quantum MAS recoupling (BABA) (Figure 7.19b,c) of Phe/F-Phe dry hydrogel mixtures did not have sufficient resolution for concluding on spatial proximity in the solid state.

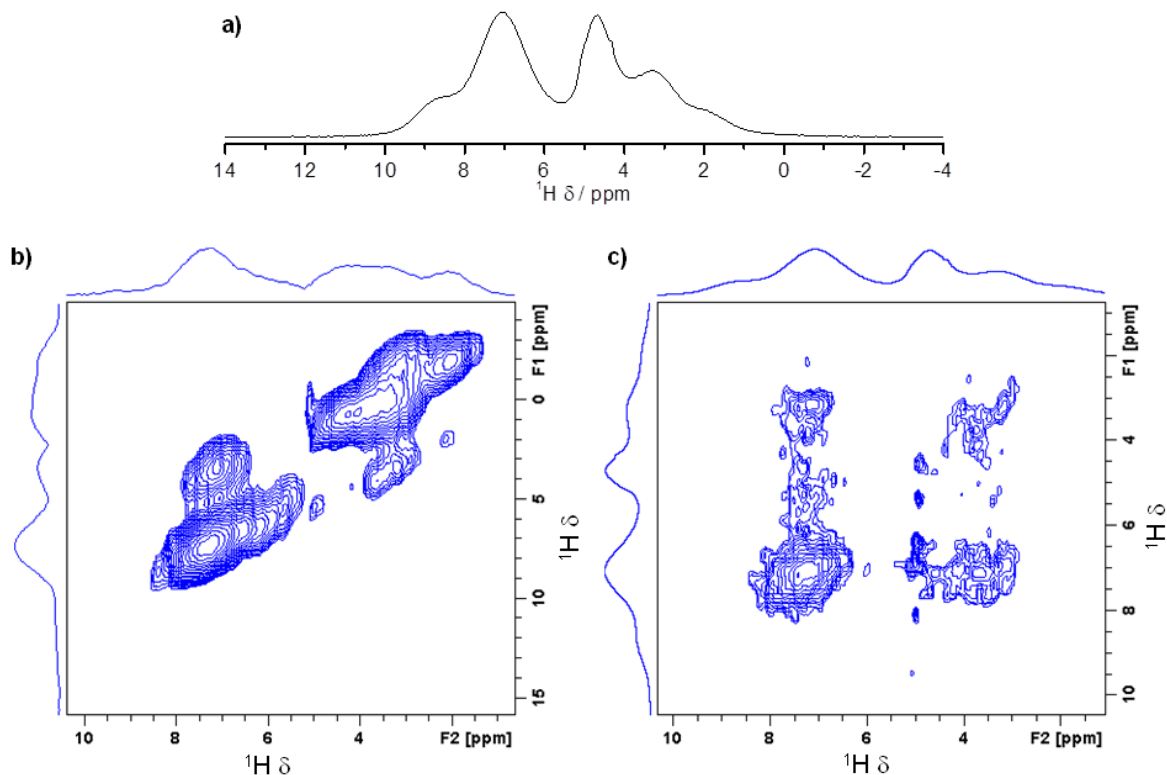


Figure 7.19. a) ^1H NMR, b) 2D ^1H - ^1H BABA and c) 2D ^1H - ^1H NOESY spectra of the dry hydrogel of Phe/F-Phe (1:1) performed using an MAS rate of 75 kHz using an 850 MHz solid-state NMR spectrometer with an 1 mm MAS probe head.

Despite the vast range of techniques available, the challenging features of this system (as strong homonuclear ^1H - ^1H couplings, low concentration of gelators and inefficient ^{19}F - ^{13}C through-space transfer of magnetisation) did not allow spatial connectivities in the solid state to be ascertained.

7.4.3. Investigation of gel/solution interfaces using HR-MAS

^1H PFG HR-MAS NMR spectra of Phe and F-Phe-based hydrogels showed intense peaks for all ^1H sites after the application of a 95 % diffusion filter ($G_{\text{eff}} = 45.7 \text{ G cm}^{-1}$) (Figure 7.20). For supramolecular gels, after the application of the diffusion filter, the resulting ^1H peaks probably correspond to the less mobile molecules ‘locked’ onto the surface of the fibres that did not diffuse in the period of the experiment.

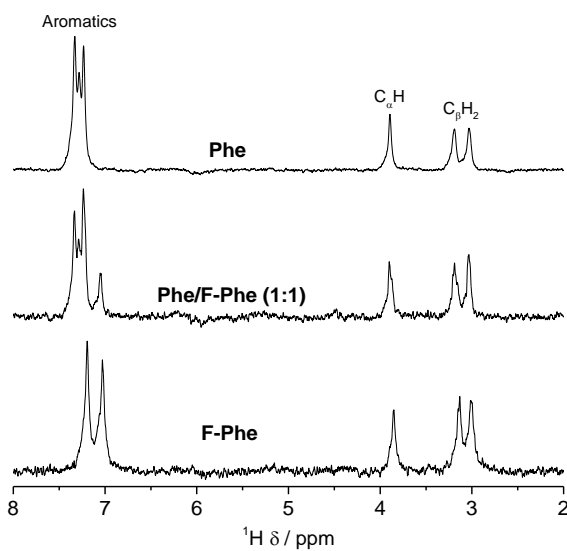


Figure 7.20. ^1H PFG HR-MAS NMR spectra of Phe, Phe/F-Phe (1:1) and F-Phe hydrogels with an effective field of 45.7 G cm^{-1} (95 % diffusion filter), measured at 298 K and an MAS rate of 1.5 kHz using an 800 MHz HR-MAS NMR probe head.

Apparent self-diffusion coefficients (D) were determined from the evolution of peak intensities in ^1H PFG HR-MAS NMR experiments. Despite the structural heterogeneities present in supramolecular gels, all curves were best fitted to a mono-exponential function (Figure 7.21), reflecting the presence of a single molecular diffusion regime.¹⁸³ It was previously discussed that Phe molecules experience exchange processes between the surface of the gel fibres and the pools of water (Chapter 6, section 6.2.7, page 178). The single value of diffusion coefficient is therefore the average between solution and gel species, as the dynamics of exchange is fast compared with the diffusion time scale. For the Phe hydrogel, a D_{Phe} value of $8.17 \times 10^{-10} \text{ m}^2 \text{ s}^{-1}$ was determined (Table 7.4). In F-Phe hydrogels, F-Phe molecules presented higher D values ($D_{\text{F-Phe}} = 1.03 \times 10^{-09} \text{ m}^2 \text{ s}^{-1}$), which are characteristic of fast tumbling molecules.^{140, 230} This indicated mainly free gelator molecules were detected. Interestingly, in multiple gelator hydrogels, Phe and F-Phe molecules presented intermediate D values, with only subtle differences being recorded between pure and mixed materials ($D_{\text{Phe}} = 9.21 \times 10^{-10} \text{ m}^2 \text{ s}^{-1}$ and $D_{\text{F-Phe}} = 9.02 \times 10^{-10} \text{ m}^2 \text{ s}^{-1}$). To better interpret these variations, solution-state NMR experiments were carried out.

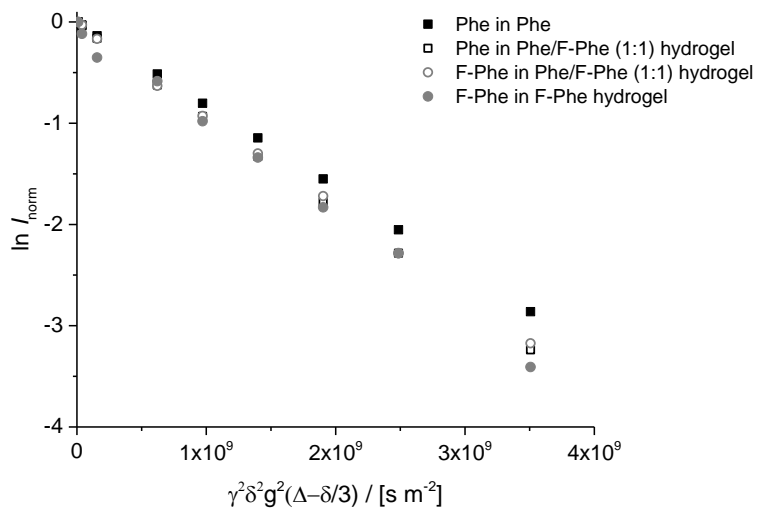


Figure 7.21. Evolution of ^1H PFG HR-MAS NMR normalised peak intensity with increasing gradient strength for Phe and F-Phe in Phe, Phe/F-Phe (1:1) and F-Phe hydrogels measured at 298 K and an MAS rate of 1.5 kHz.

Table 7.4. Apparent self-diffusion coefficients (D) of Phe and F-Phe molecules determined from variable gradient ^1H PFG HR-MAS NMR experiments of Phe, Phe/F-Phe (1:1) and F-Phe hydrogels were measured at 298 K with an MAS rate of 1.5 kHz.

Hydrogel	$D \times 10^{10}$ Phe / $\text{m}^2 \text{s}^{-1}$	$\delta \times 10^{12}$	$D \times 10^{10}$ F-Phe / $\text{m}^2 \text{s}^{-1}$	$\delta \times 10^{12}$
Phe	8.17	2.72	-	-
Phe/F-Phe (1:1)	9.21	6.50	9.02	8.05
F-Phe	-	-	10.3	34.1

7.4.4. Dynamics of gelator molecules in solution

Kinetics of self-assembly of single and multiple gelator systems was monitored through the acquisition of several ^1H NMR spectra, at room temperature, throughout gelation of hot solutions of pure and mixed systems (Figure 7.22). For the pure Phe hydrogel, the process of self-assembly of Phe molecules into gradually larger and less mobile structures could be monitored. ^1H peaks became broader and less intense, which was consistent with gelation.¹⁴⁷ However, kinetics of hydrogelation was very fast for the pure F-Phe hydrogel, with incorporation of the majority of molecules into NMR “silent” components before the acquisition of the first ^1H spectra (*ca.* 3.5 min). Similarly fast kinetics of gelation were found in mixed hydrogels, which prevented monitoring the details of their early stages of self-assembly. These studies proved that halogenation of the aromatic ring has a great impact on the kinetics of nucleation and supramolecular aggregation in water.

Broad peaks were recorded 24 h after quenching of hot solutions of pure and mixed materials, without significant chemical shift variation (Figure 7.23). Their ^1H NMR peak intensities were compared to elucidate dynamics of molecules in solution. In the pure hydrogel of Phe, very intense peaks were recorded. In the previous work presented in Chapter 6 (page 164), these peaks were attributed to the free gelator molecules as well as molecules exchanging between gel/solution states. Interestingly, despite total concentration of F-Phe being maintained at 303 mM, ^1H peak intensity in the pure F-Phe hydrogel was considerably lower. The decreased concentration of dissolved gelator molecules showed that the incorporation of gelator molecules within the network occurred to a greater extent in mixed hydrogels with higher concentrations of F-Phe. This is linked to F-Phe lower water solubility. These findings are also consistent with the lower molar CGC values determined for the hydrogel of F-Phe (in comparison with the hydrogel of Phe) (Table 7.1).

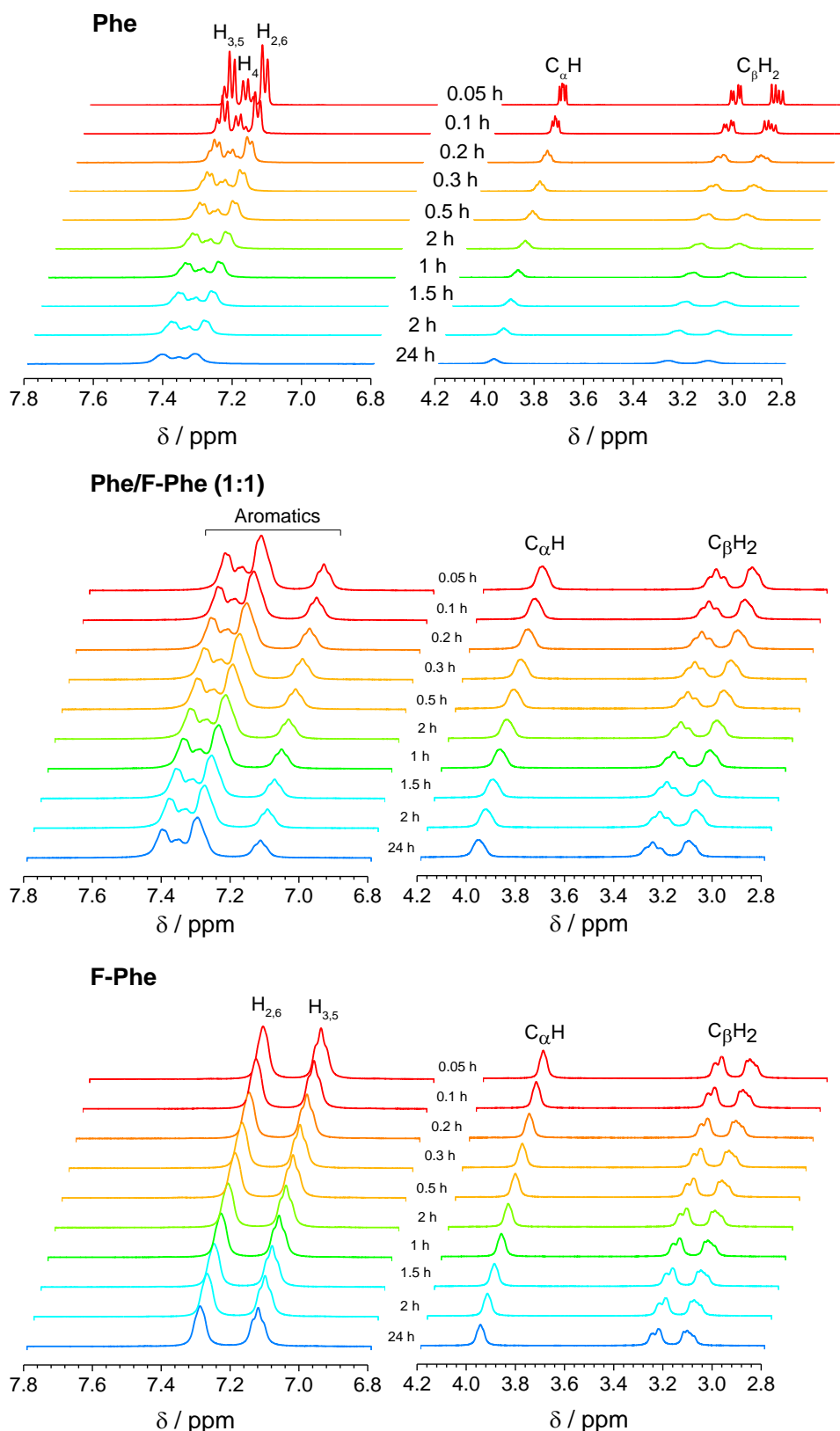


Figure 7.22. Kinetics of gelation monitored by the acquisition of ^1H solution-state NMR spectra over time, immediately after cooling down a hot solution of Phe, Phe/F-Phe (1:1) and F-Phe (303 mM) measured at 298 K.

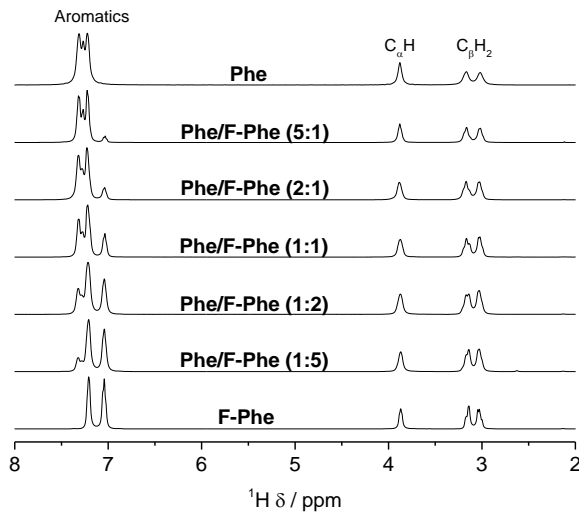


Figure 7.23. ^1H solution-state NMR spectra of Phe, Phe/F-Phe (5:1), Phe/F-Phe (2:1), Phe/F-Phe (1:1), Phe/F-Phe (1:2), Phe/F-Phe (1:5) and F-Phe hydrogels (303 mM) measured at 298 K.

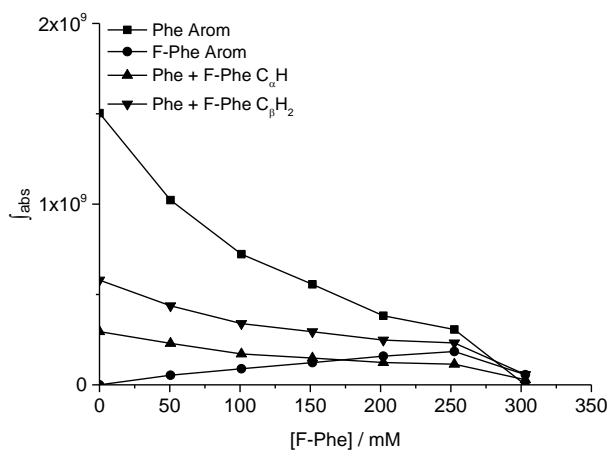


Figure 7.24. ^1H solution-state NMR peak intensity (I_{abs}) of Phe and F-Phe Arom, C_αH and C_βH_2 sites in Phe, Phe/F-Phe (5:1), Phe/F-Phe (2:1), Phe/F-Phe (1:1), Phe/F-Phe (1:2), Phe/F-Phe (1:5) and F-Phe hydrogels (303 mM) recorded 24 h after quenching hot solutions, measured at 298 K.

Due to the thermoreversible nature of these hydrogels, it was important to monitor the evolution of ^1H T_1 times with temperature to understand the changes that occur throughout the gel-to-solution transitions. In the Phe hydrogel, ^1H T_1 times were similar for different Phe ^1H sites at 298 K (Figure 7.25). As temperature was raised above T_{gel}^* (molecular gel-to-solution transition), a dispersion of ^1H T_1 times similar to solutions of Phe was observed (Table 7.5). This phenomenon is fully discussed in Chapter 6, section 6.2.7, page 178.

A different evolution of ^1H T_1 times with temperature was recorded for the pure F-Phe hydrogel. In the gel state, at low temperatures, the distribution of ^1H T_1 times corresponded to solutions of F-Phe (Table 7.5). These values increased linearly with temperature (Figure 7.25). These data confirmed that only fast tumbling free gelator molecules were being detected throughout the range of temperatures, in agreement with the shorter D values from HR-MAS studies. This was corroborated further by the detection of positive cross-peaks, characteristic of small molecules,²⁶³ in the 2D ^1H - ^1H NOESY NMR spectrum of the F-Phe hydrogel (Figure 7.27).

Not surprisingly, in multiple gelator hydrogels, Phe and F-Phe displayed intermediate T_1 times at 298 K (Figure 7.26). ^1H T_1 values were similar for different ^1H sites at higher concentrations of Phe, whereas a dispersion of ^1H T_1 times was observed when F-Phe was more abundant. These results can be interpreted in terms of modified dynamics of exchange, which would affect the averaging of ^1H s local molecular motions. ^1H T_1 values are a balance between all the species present and depend on the strength of homonuclear dipolar couplings. In hydrogels dominated by fast exchanging processes (on the NMR frequency time scale), as those with higher contents of Phe, the measured T_1 values correspond to a multiplicity of environments: fast tumbling molecules dissolved in the pools of solvent, and those that have contacted with the surface of the gel fibres and hence have restricted mobility. This leads to the efficient transfer of magnetisation *via* the strong ^1H - ^1H dipolar couplings, resulting in similar T_1 times.⁸² In contrast to this, at higher amounts of F-Phe the dynamics of exchange was slowed down and this balance was altered. Consequently, the proportion of NMR “silent” molecules increased. These conclusions were supported by the fact that T_1 times for these gels presented a distribution of values as in solutions of Phe or F-Phe (Table 7.5). However, the dispersion of T_1 times was narrower in gels, when comparing with solutions, because of the presence of a rigid network in the gel state that restricts freedom of movement. In conclusion, the detection of intermediate T_1 values most likely arises from the spatial proximity between Phe and F-Phe, which affected the strength of intermolecular interactions at the interfaces and, therefore, modulated dynamics of exchange between gel and solution states.

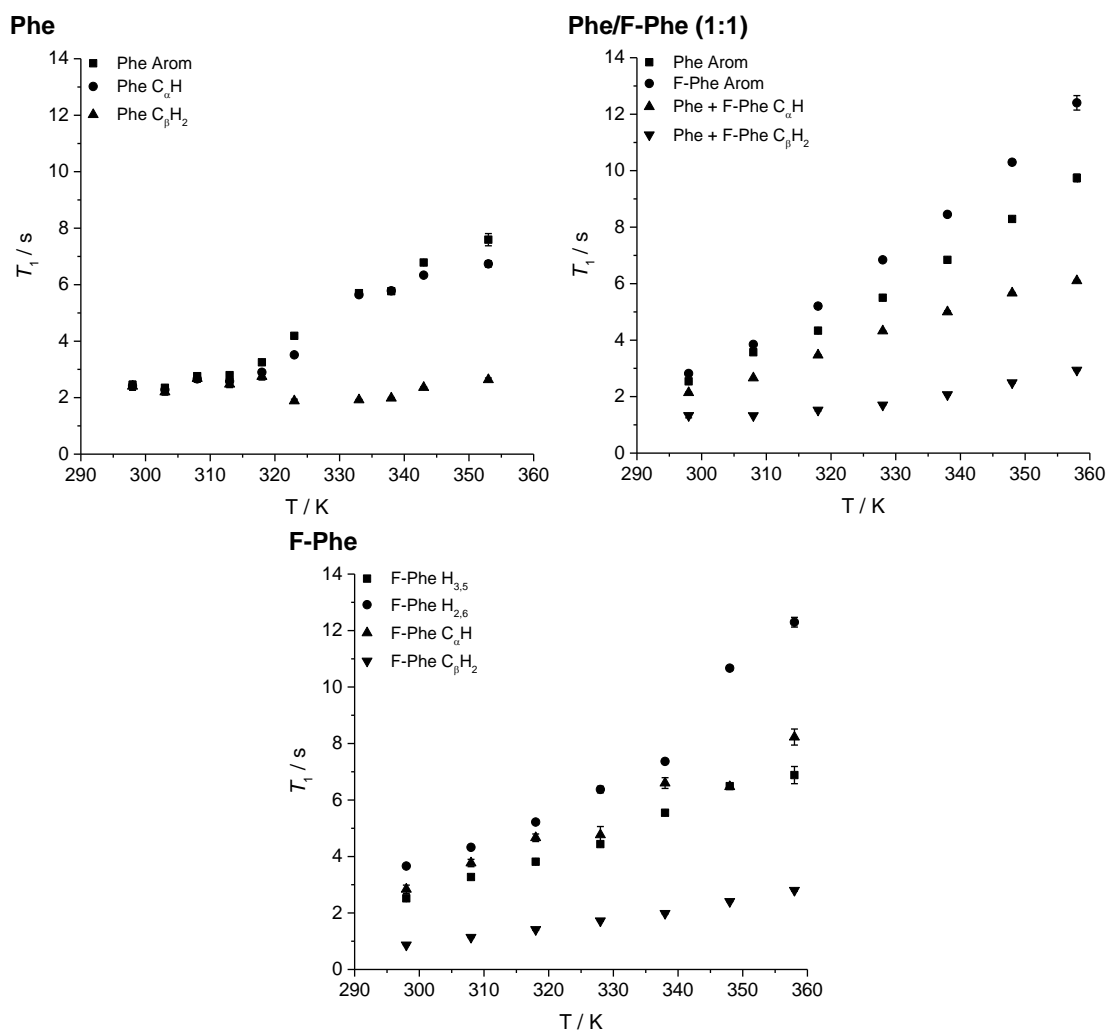


Figure 7.25. ^1H solution-state T₁ times of Phe and F-Phe Arom, C_αH and C_βH₂ in Phe, Phe/F-Phe (5:1), Phe/F-Phe (1:1), Phe/F-Phe (1:5) and F-Phe hydrogels (303 mM) recorded between 298 and 358 K.

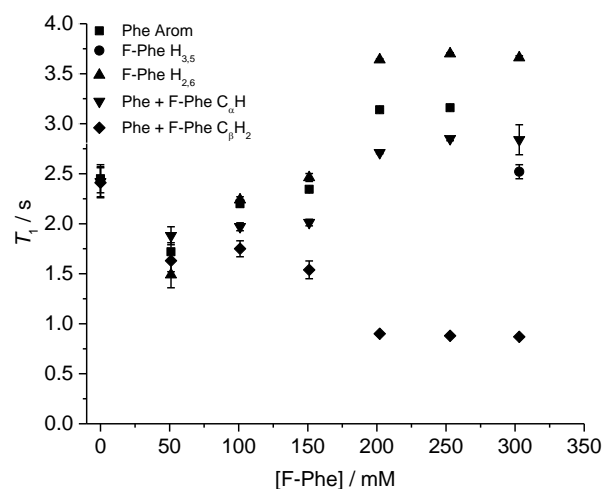


Figure 7.26. Comparison of ^1H T₁ times of Phe and F-Phe Arom, C_αH and C_βH₂ in Phe, Phe/F-Phe (5:1), Phe/F-Phe (2:1), Phe/F-Phe (1:1), Phe/F-Phe (1:2), Phe/F-Phe (1:5) and F-Phe hydrogels (303 mM) recorded at 298 K.

Table 7.5. ^1H solution-state NMR longitudinal relaxation times T_1 for Phe and F-Phe solutions (101 mM) measured at 298 K, with error values in parenthesis.

$^1\text{H} T_1 / \text{s}$					
		Arom		C_αH	C_βH_2
Phe		F-Phe $\text{H}_{3,5}$	F-Phe $\text{H}_{2,6}$		
Phe (solution)	2.07 (0.02)	-	-	2.20 (0.03)	0.63 (0.01)
F-Phe (solution)	-	2.75 (0.03)	3.73 (0.02)	2.90 (0.04)	0.85 (0.02)

Negative cross-peaks, characteristic of medium to large aggregates,²⁶³ were detected between F-Phe molecules and between Phe and F-Phe protons in the 2D ^1H - ^1H NOESY NMR spectrum of the Phe/F-Phe (1:1) hydrogel (Figure 7.27). The negative correlations between the aromatic groups of Phe and F-Phe shown in this map of connectivities pointed towards close contacts between Phe and F-Phe in the slow motion limit, reflecting interactions occurring at the surface of the fibres. Similarly, the negative nOe enhancements found between F-Phe protons showed that slowly tumbling molecules of F-Phe interact with each other at the interfaces, contrasting with the positive correlations found for the fast tumbling F-Phe molecules in solution of pure F-Phe systems.

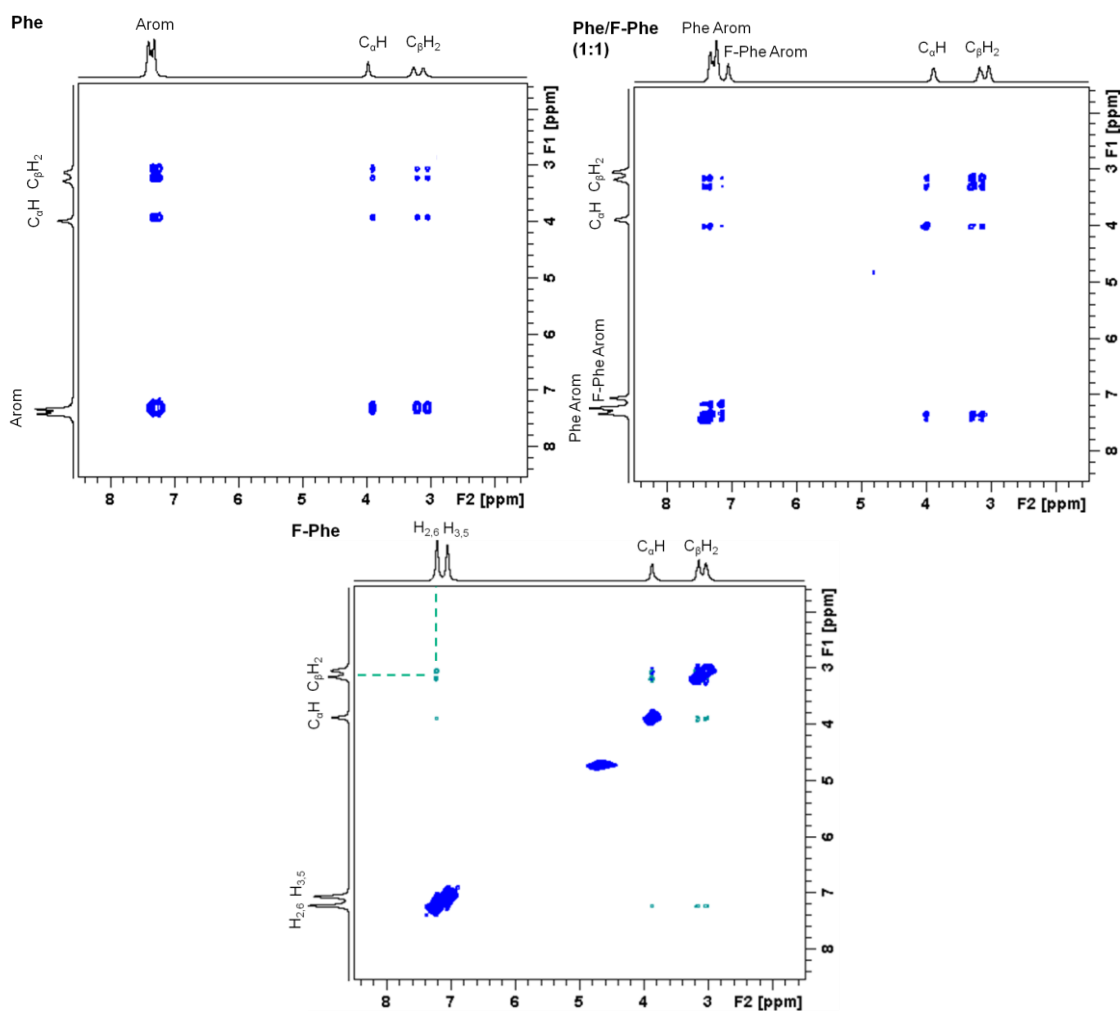


Figure 7.27. 2D ^1H - ^1H NOESY spectra of the hydrogels of Phe, Phe/F-Phe (1:1) and F-Phe acquired with a mixing time of 0.5 s. The green dashed lines highlight a positive nOe enhancement between the aromatic and aliphatic protons of F-Phe molecules.

7.4.5. Monitoring exchange phenomena at the interfaces

Exchange phenomena between molecules incorporated in the hydrogel network and those dissolved in the isotropic solution phase can be elucidated using STD NMR experiments. A mono-exponential evolution of saturation was recorded for the Phe hydrogel, resulting from the fast exchange between gel and solution states (explained in detail in Chapter 6, section 6.2.8, page 179).

In contrast to the Phe hydrogel, no peaks were detected in the STD spectrum of the F-Phe hydrogel at 298 K. The lack of accumulation of saturation in solution can reflect either strong binding processes (associated with very slow exchange phenomena on the NMR frequency time scale), or lack of exchange. Considering the dynamic nature of supramolecular hydrogels,¹⁴⁷ it was concluded that F-Phe molecules strongly interacted

with the surface of the fibres. With the purpose of modifying the rate of exchange between gel and solution states, STD NMR experiments were conducted at variable temperature. No signals were detected in the STD spectra acquired between 298 and 338 K. The exchange rate could not be increased significantly without promoting dissolution of the supramolecular network (which occurred at 335 K), proving the exchange of F-Phe between gel and solution states is slow and the interaction of F-Phe with the surface of the fibres is very strong. In summary, the observation of shorter diffusion rates, a linear evolution of ^1H T_1 values with temperature, the presence of positive cross-peaks in 2D ^1H - ^1H NOESY experiments and the absence of STD signals in VT difference spectra for the pure F-Phe hydrogel pointed towards the detection of mainly free molecules due to a system dominated by very slow exchange phenomena of F-Phe molecules between the fibres and the isotropic solutions on the NMR frequency time scale.

In multiple gelator hydrogels, a mono-exponential build-up of saturation was recorded for both Phe and F-Phe molecules (Figure 7.28). The initial build-up rates recorded for Phe protons were lower than those in the pure Phe hydrogel (Figure 7.29). This was a consequence of slower exchange rate of Phe in multiple gelator hydrogels (in comparison with the pure Phe system), leading to a decreased amount of saturation accumulated in solution for Phe molecules. F-Phe protons also showed a mono-exponential accumulation of saturation in mixed systems, in contrast to pure F-Phe hydrogels. This means the dynamics of exchange for F-Phe molecules was fastened in mixed materials, which allowed F-Phe receiving saturation and accumulating it in solution. These observations are discussed below in the light of all the previous findings.

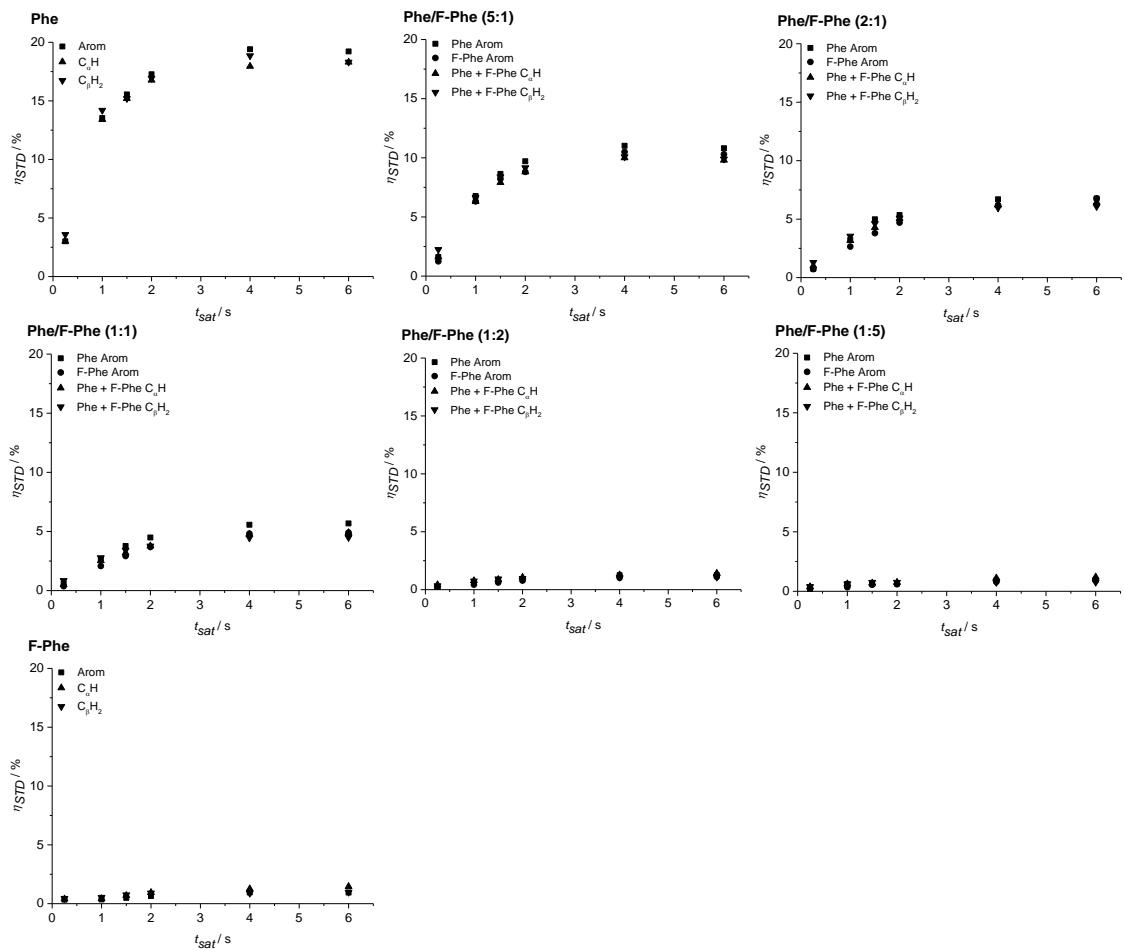


Figure 7.28. Build-up curves of fractional STD response (η_{STD}) in Phe, Phe/F-Phe (5:1), Phe/F-Phe (2:1), Phe/F-Phe (1:1), Phe/F-Phe (1:2), Phe/F-Phe (1:5) and F-Phe hydrogels (303 mM) ($STD_{on} = 1$ ppm and $STD_{off} = 40$ ppm), measured at 298 K.

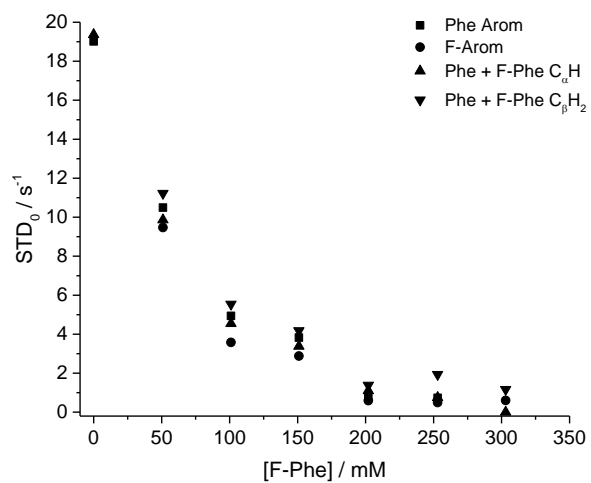


Figure 7.29. Initial slope values (STD_0) versus [F-Phe] in Phe, Phe/F-Phe (5:1), Phe/F-Phe (2:1), Phe/F-Phe (1:1), Phe/F-Phe (1:2), Phe/F-Phe (1:5) and F-Phe hydrogels (303 mM) ($STD_{on} = 1$ ppm and $STD_{off} = 40$ ppm), measured at 298 K.

Overall, in mixed systems, Phe and F-Phe molecules displayed intermediate values of apparent self-diffusion coefficients, ^1H T_1 relaxation times and fractional STD responses when comparing to those recorded for pure hydrogels. These were an average of the multiple exchange phenomena present at the interfaces: $[\text{Phe}]_{\text{solution}}/[\text{Phe}]_{\text{fibre}}$ weak interaction, $[\text{Phe}]_{\text{solution}}/[\text{F-Phe}]_{\text{fibre}}$ and $[\text{F-Phe}]_{\text{solution}}/[\text{Phe}]_{\text{fibre}}$ intermediate strength interactions, and $[\text{F-Phe}]_{\text{solution}}/[\text{F-Phe}]_{\text{fibre}}$ strong interaction. These findings showed that Phe's rate of exchange was slowed down when interacting with F-Phe at the interfaces. Fluorination of the aromatic group created increased polarisation which resulted in an electron poor aromatic ring, promoting stronger interactions between F-Phe and the more electron rich Phe aromatic group. The presence of stronger interactions between Phe and F-Phe molecules than between two Phe dimers probably explains the differences observed in the dynamics of exchange at the fibre/solution interfaces.

7.5. Concluding remarks

As it has been shown in the first part of this chapter, the introduction of a fluoro group to Phe resulted in general improvement of gelation ability due to a decrease in the solubility of the derivative in water. The packing of molecules was determined to correspond to the monohydrate form. In this second part, the dynamics of molecular exchange at the interfaces was found to be considerably different for F-Phe relative to Phe. The observation of shorter diffusion rates, a linear evolution of ^1H T_1 values with temperature, the presence of positive cross-peaks in 2D ^1H - ^1H NOESY experiments and the absence of STD signals for the pure F-Phe hydrogel pointed towards a system dominated by very slow exchange phenomena of F-Phe molecules at the fibre/solution interfaces (on the NMR frequency time scale). This slower dynamics of exchange and faster kinetics of gelation was consistent with the strong intermolecular interactions experienced between F-Phe molecules.

Since Phe and F-Phe gels formed isostructural solid components, it was considered important to understand how the preparation of multiple gelator hydrogels affected gel formation. It was found that the viscoelastic properties of single and multiple gelator hydrogels of Phe and F-Phe were very similar. Diffraction studies and ^{13}C NMR spectra showed that mixed materials largely preserved the supramolecular arrangements of the

fibrous structures of the pure hydrogels. Moreover, the continuum of the unit cell parameters found for variable ratio Phe/F-Phe pointed towards formation of co-assembled fibres. These mixed fibres were characterised as a crystalline solid solution of Phe and F-Phe that retained the monohydrate form. It is not unusual to observe formation of solid solutions when two compounds form isostructural crystalline phases and the molecules are of similar size. However, the detection of extra ^{19}F peaks in mixtures provided experimental evidence of the formation of new molecular environments within the rigid components. These high-field ^{19}F NMR studies proved, at a molecular level, that Phe and F-Phe were very intimately mixed in the solid state and that fibres were composed of both gelators, supporting the interpretation of the diffraction data.

Structural findings were consistent with the variations recorded for solution-state and HR-MAS NMR parameters of multiple gelator hydrogels. The observation of intermediate values of self-diffusion, longitudinal relaxation times and fractional STD response can be explained by the spatial proximity between both gelators. This affects the strength of intermolecular interactions and helps explaining the intermediate dynamics of exchange in mixed materials. Very dynamic processes of interaction occur between the surface of the fibres and both types of gelators. Consequently, this changes the rates of exchange between gel and solution environments, ultimately leading to modification of the dynamics of the entire system. Hence, these studies proved that the variation of composition and tridimensional organisation of the gel fibres has an effect on the interfacial properties of the gel. Even though the formation of co-assembled fibres from isostructural gelators has been described for urea derivatives⁹⁴ the study did not take into account the effects on the dynamic properties of the interfaces. Altogether, these experiments proved that multiple gelator hydrogels of Phe and F-Phe with isostructural packing motifs showed a tendency to form crystalline solid solution fibres composed of both gelator molecules. The potential utility of solid solutions lies on the possibility of modulation of their physicochemical properties, such as the demonstrated enhanced pharmacokinetic profile of an antiparasitic and antiviral drug molecule, nitazoxanide, in a solid solution formed from co-crystals.²⁶⁴

Chapter 8

8. Understanding concentration dependent disruptive effects of aminophenylalanine on phenylalanine-based hydrogels using NMR spectroscopy

8.1. Introduction

In this chapter, the findings regarding self-assembly of 4-amino-*L*-phenylalanine (NH₂-Phe) (Figure 8.1) and its interactions with Phe in solution and in solid state are discussed. While exploring the interaction of Phe with several additive molecules, it was discovered that NH₂-Phe was also able itself to form supramolecular hydrogels. More interestingly, it exhibited a concentration-dependent behaviour of disrupting and modifying the Phe tridimensional network. The possibility of disrupting the Phe network has biologic relevance, due to the pathological implications of the intracellular accumulation of stable and toxic Phe aggregates (more details can be found in Chapter 4, page 138). Henceforth, this chapter describes the study of single and multi-component hydrogels of Phe and NH₂-Phe, in order to understand the gelation/crystallisation outcomes and to pinpoint the interactions responsible for the disruption of Phe hydrogels upon the addition of NH₂-Phe.

Due to the complexity of the Phe/NH₂-Phe materials, some important features should be highlighted. When preparing multiple gelator hydrogels, a variety of behaviours can be observed depending on how intimately the gelators interact with each other. There can be formation of individualised self-sorted networks of the pure gel fibres; formation of co-assembled fibres that acquire the supramolecular organisation of one of the possible crystal structures; or formation of mixed fibres with entirely new architectures.^{17, 51, 93} The structural similarity between both gelators under study on this chapter and the potential to form non-covalent interactions with each other is expected to lead to the preferential formation of co-assembled networks. This statement does not mean that self-sorting is not

possible nor that it is not formed to a certain extent. Despite the basicity of the arylamine group, this amine is able to participate in hydrogen bonding, possibly being able to create stable intermolecular interactions that may promote structural rearrangement of the assemblies. Furthermore, the duality of effects observed for the interaction between Phe and NH₂-Phe, with prevention of gelation at low concentrations of NH₂-Phe and multiple gelator gelation at high concentrations of NH₂-Phe, showed there is a delicate balance between aggregation and disaggregation processes that dictate the gelation outcomes. Formation of mixtures of structurally different molecules makes understanding of gelation outcomes more challenging, but considerably more interesting.

With the goal of understanding the mechanisms of disruption and gelation the resulting materials were characterised using microscopy, rheology, X-ray diffraction and NMR spectroscopy, methodologies which are able to probe different regimes of mobility, levels of self-organisation and intermolecular connectivities.

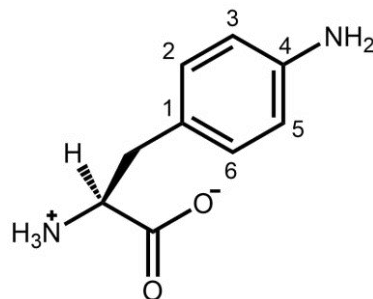


Figure 8.1. Molecular structure of zwitterionic NH₂-Phe.

8.2. Results and Discussion

8.2.1. Macroscopic and morphologic characterisation of hydrogels

When Phe and NH₂-Phe were mixed in water, different products were obtained depending on the concentration and molar ratio of these gelators (Table 8.1, Figure 8.2). For comparison purposes, the concentration of Phe was maintained at 303 mM, which corresponds to the concentration at which a hydrogel composed of the pure monohydrate form of Phe can be obtained.

Table 8.1. Molar ratio and concentration of Phe and NH₂-Phe in the suspensions and hydrogels under study.

Molar ratio / Phe:NH ₂ -Phe	[Phe] / mM	[NH ₂ -Phe] / mM
Phe	303	0
1:0.05	303	15
1:0.1	303	30
1:0.15	303	45
1:0.2	303	60
1:0.3	303	90
1:0.4	303	120
1:1	303	303
1:2	303	606
NH ₂ -Phe	0	606

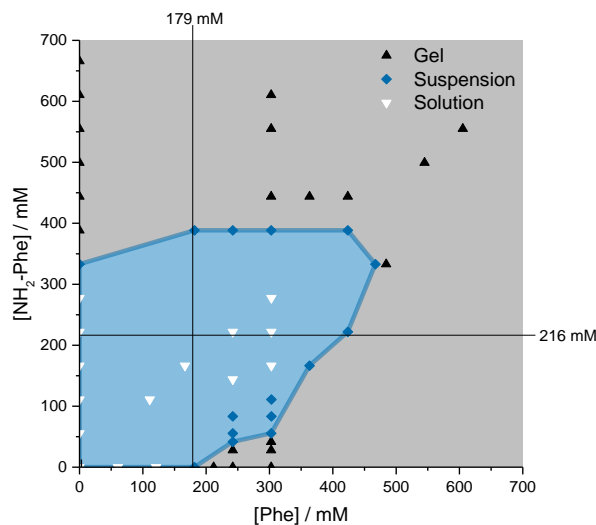


Figure 8.2. Phase diagram of the products obtained depending on the concentration and molar ratio of Phe and NH₂-Phe in water. Water solubility of Phe (179 mM) and NH₂-Phe (216 mM, experimentally determined) at 298 K are highlighted with black lines.

Phe gives rise to white opaque hydrogels (Figure 8.3a) composed of long hair-like fibres (Figure 8.4a) at concentrations higher than 212 mM. When small amounts of NH₂-Phe were added (up to 1:0.2) a brownish colouration appeared, but the self-sustaining properties of the material were maintained (Figure 8.3b). Between the ratios of 1:0.2 and 1:0.4, a heterogeneous sample was obtained containing white “fluffy” structures in suspension. These samples exhibited flow when inverted. When the concentration of NH₂-Phe was increased further, thin white particles were observed in the suspension (Figure 8.3c). Above the 1:1 ratio, these particles were fully dissolved and a clear brown solution was obtained (Figure 8.3d). Mixing both molecules above their individual critical

gelation concentrations ($\text{CGC}_{\text{Phe}} = 212 \text{ mM}$ and $\text{CGC}_{\text{NH}_2\text{-Phe}} = 388 \text{ mM}$) resulted in brown hydrogels containing white crystalline structures (Figure 8.3e and Figure 8.4b). The white elements were attributed to the long hair-like fibres due to Phe, interpenetrated with shorter and wider needle-like crystals of $\text{NH}_2\text{-Phe}$ (Figure 8.4b). Since co-assembly and self-sorting occur at the molecular and supramolecular levels, it is not possible to determine their presence simply by observing fibre morphology.⁹⁶

$\text{NH}_2\text{-Phe}$ is also able to self-assemble independently in water into organised structures, yielding brown opaque crystalline hydrogels (Figure 8.3f) composed of wide needle-like fibres (Figure 8.4c) at concentrations superior to 388 mM. The gelation process of $\text{NH}_2\text{-Phe}$ was found to be considerably slower than that of Phe and very dependent on the quenching and agitation rates. Hydrogels were obtained successfully only when the hot solutions were cooled immediately in an ice bath with constant agitation, as slow cooling rates and lack of agitation favoured precipitation of crystalline needle-like components over gel formation. The tridimensional motifs of these needles matched the crystal structure of the $\text{NH}_2\text{-Phe}$ gel fibres, confirmed by solid-state NMR (Figure 8.8).

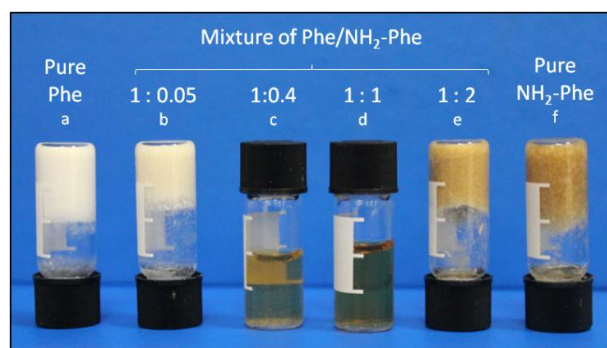


Figure 8.3. Images of hydrogels of **a**) Phe (303 mM), **b**) Phe/ $\text{NH}_2\text{-Phe}$ (1:0.05), **e**) Phe/ $\text{NH}_2\text{-Phe}$ (1:2) and **f**) $\text{NH}_2\text{-Phe}$ (606 mM), **c**) suspension of Phe/ $\text{NH}_2\text{-Phe}$ (1:0.4) and **d**) solution of Phe/ $\text{NH}_2\text{-Phe}$ (1:1). Commercially available $\text{NH}_2\text{-Phe}$ is brown, giving rise to coloured materials.

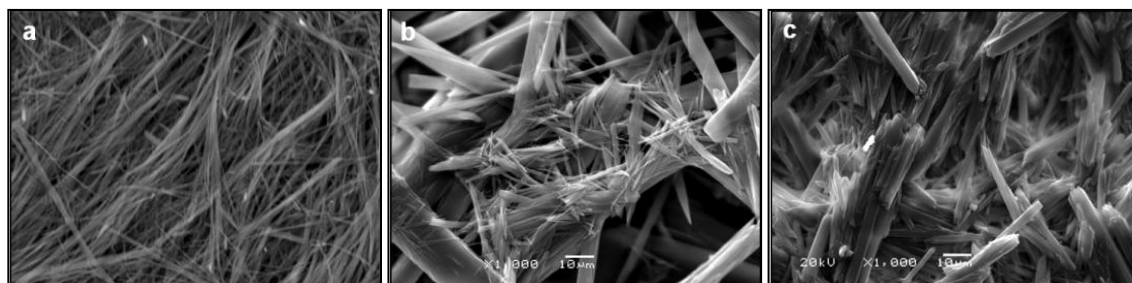


Figure 8.4. SEM images of **a**) Phe (303 mM), **b**) Phe/ $\text{NH}_2\text{-Phe}$ (1:2) and **c**) $\text{NH}_2\text{-Phe}$ (606 mM) dry hydrogels. The average width of the needle-like fibres of $\text{NH}_2\text{-Phe}$ was 25.3 μm (ranging between 2.6 and 47.9 μm).

8.2.2. Mechanical properties of hydrogels

The phase angle measured in rheology studies was below 10° for pure hydrogels, reflecting the solid-like nature of these materials.¹¹ The storage moduli (G') for Phe and NH₂-Phe hydrogels were in the order of 10⁵ Pa ($G'_{\text{Phe}} = 4.7 \times 10^5$ Pa and $G'_{\text{NH}_2\text{-Phe}} = 5.1 \times 10^5$ Pa) and these values were one order of magnitude greater than the loss moduli (G'') ($G''_{\text{Phe}} = 3.2 \times 10^4$ Pa and $G''_{\text{NH}_2\text{-Phe}} = 3.1 \times 10^4$ Pa) (Figure 8.5), values characteristic of robust gels.⁴³

Interestingly, weaker gel fibres with lower resistance to deformation were found for the mixed hydrogel Phe/NH₂-Phe (1:2). The higher values of phase angle ($\delta > 10$) in combination with the lower elastic response ($G'_{\text{Phe/NH}_2\text{-Phe}} = 2.7 \times 10^5$ Pa) and higher inelastic response ($G''_{\text{Phe/NH}_2\text{-Phe}} = 7.1 \times 10^4$ Pa) for this hydrogel compared to the pure materials pointed towards a less rigid system. The variations in the bulk properties of the pure and mixed gels reflected differences in their molecular and supramolecular level arrangements.

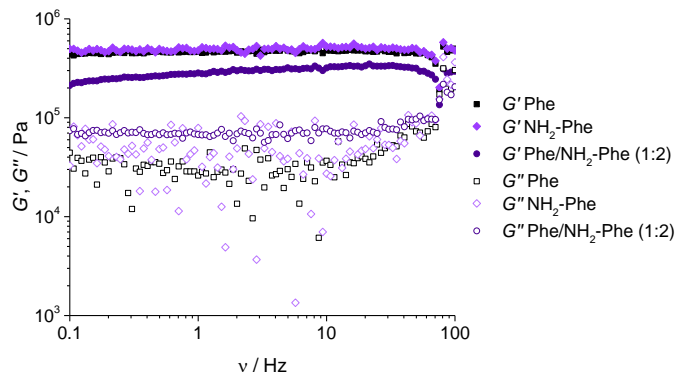


Figure 8.5. Storage (G') and loss (G'') moduli for Phe (303 mM), Phe/NH₂-Phe (1:2) and NH₂-Phe (606 mM) hydrogels in frequency sweep experiments. Hot solutions (*ca.* 1 mL) were pipetted into a 500 μm gap (parallel plate geometry). All samples were subjected to frequency sweeps in the range of 0.1 to 100 Hz and applied stress of 500 Pa.

8.2.3. Determination of the structure of the gel fibres

Using single-crystal X-ray diffraction experiments, the crystal structure of pure NH₂-Phe fibres was determined (Figure 8.6). The unit cell presented monoclinic metric symmetry (space group $P2_1$), with the following refined parameters: $a = 5.9813(9)$ \AA , $b = 11.3702(15)$ \AA , $c = 14.985(2)$ \AA , $\beta = 93.681(8)$ \AA , ($V = 1017.01$ \AA^3) and $Z = 4$. The good agreement between

the ^{13}C chemical shift values measured experimentally (Table 8.2) and those predicted using CASTEP¹⁶² for NH₂-Phe hydrogels (Figure 8.7) allowed us to confidently confirm the molecular packing motif within the gel fibres. This asymmetric unit is different from that of the monohydrate form of Phe composing the gel fibres. CASTEP calculations were performed by Dr. Karol Nartowski from the University of East Anglia. Further details on NMR measurements are given below.

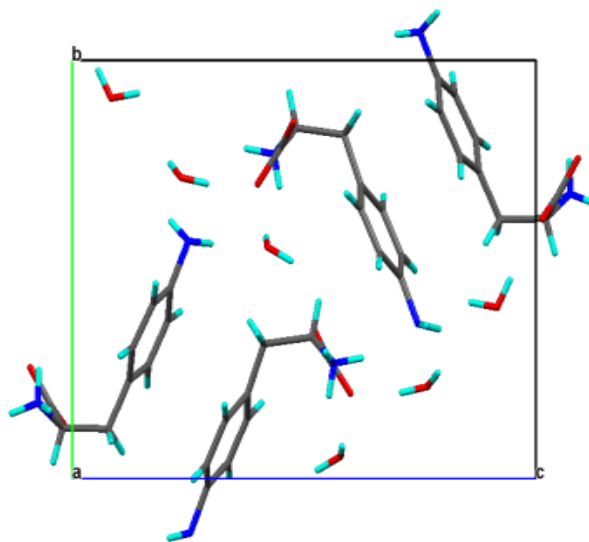


Figure 8.6. Unit cell of NH₂-Phe shown along the *a* axis.

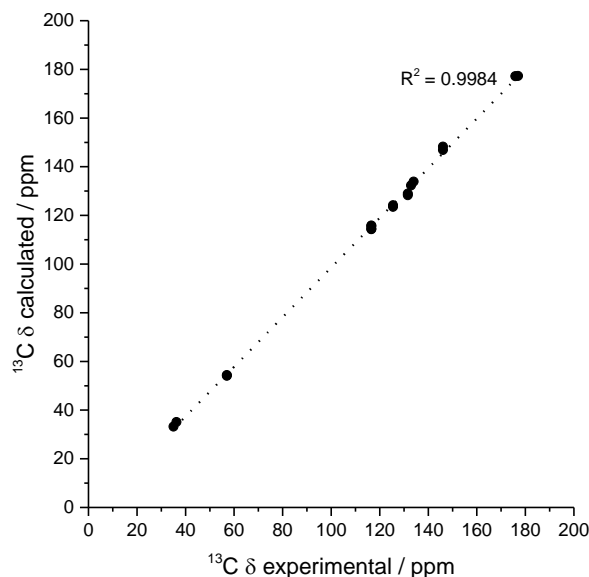


Figure 8.7. Experimental ^{13}C chemical shift values for the NH₂-Phe (606 mM) dry hydrogel derived from the ^1H - ^{13}C CP/MAS NMR spectrum acquired with an MAS rate of 10 kHz *vs.* calculated values for the predicted structure. Calculated isotropic chemical shieldings were converted to chemical shifts by matching the calculated and observed chemical shift of the CH₃ carbon.

Cross-polarisation NMR experiments rely on efficient transfer of polarisation from ^1H s to strongly dipolar coupled ^{13}C nuclei and only rigid components satisfy this condition. The addition of low concentrations of $\text{NH}_2\text{-Phe}$ to Phe hydrogels did not affect the tridimensional molecular arrangement of Phe gel fibres, as PXRD patterns and ^1H - ^{13}C CP/MAS NMR spectra of hydrogels (Figure 8.8) were very similar to those of the pure Phe. The spectra acquired on wet gel samples showed that Phe forms the rigid phases of these mixtures (1:0.1 and 1:0.2), without the identification of any peaks belonging to $\text{NH}_2\text{-Phe}$. It is important to note that 50 to 65 % of $\text{NH}_2\text{-Phe}$ molecules were not detectable by solution-state NMR (Table 8.4), but were also too mobile to be observed by CP/MAS. These data proved the existence of semi-solid components that exist in both solid and liquid environments. At this point, it should be highlighted that quantitative interpretation of NMR data needs to be treated with caution, as a full account of the presence of dynamic semi-solid structures remains a challenge. This is a feature common to supramolecular gels, discussed in detail in the general discussion chapter (Chapter 10, section 10.6, page 273).

Regarding the suspensions formed at higher concentration of $\text{NH}_2\text{-Phe}$ – Phe/ $\text{NH}_2\text{-Phe}$ (1:0.4) – the tridimensional arrangements of the suspended particles (Figure 8.3c) were very similar to the monohydrate form of Phe (Figure 8.8) and contained peaks from $\text{NH}_2\text{-Phe}$ (highlighted in the figure).

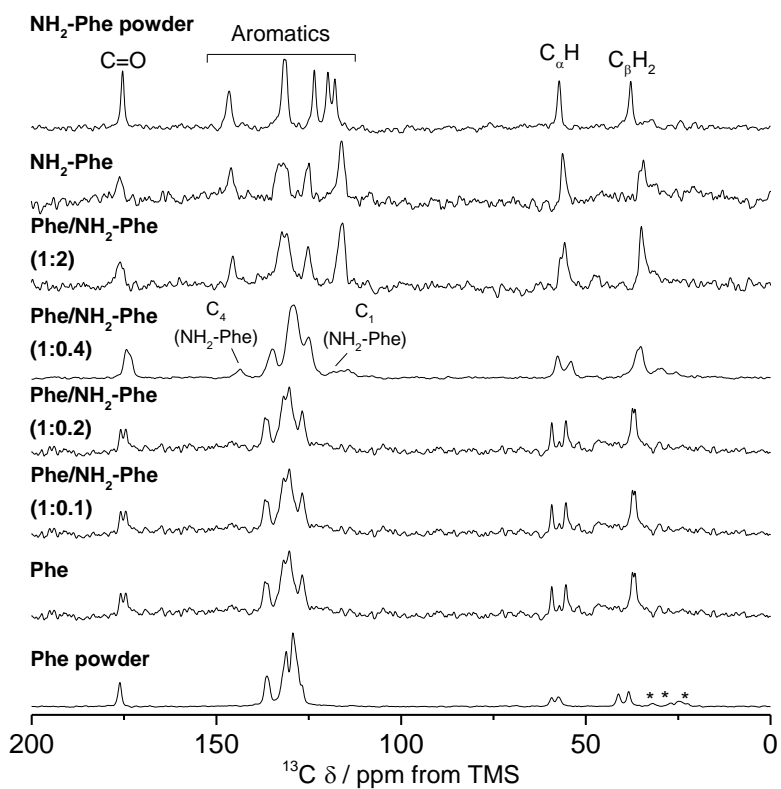


Figure 8.8. ^1H - ^{13}C CP/MAS NMR spectra of Phe (303 mM), Phe/NH₂-Phe (1:0.2), Phe/NH₂-Phe (1:0.4), Phe/NH₂-Phe (1:2) and NH₂-Phe (606 mM) hydrogels acquired with an MAS rate of 8.5 kHz and 8192 scans; Phe/NH₂-Phe (1:0.4) dry particles removed from suspension and dried, and Phe and NH₂-Phe solid reference powders acquired with an MAS rate of 10 kHz and 8192 scans. All experiments were conducted with a recycle delay of 20 s and $\pi/2$ pulse lengths of 3.2 μs (^1H) and 3.0 μs (^{13}C), using a 400 MHz solid-state spectrometer. Asterisks represent spinning sidebands.

A further increase in the concentration of NH₂-Phe led to different results. The PXRD pattern of the mixed Phe/NH₂-Phe (1:2) hydrogel was very similar to the one of pure NH₂-Phe (Figure 8.9), suggesting a similar supramolecular arrangement to that in the NH₂-Phe hydrogel. The presence of NH₂-Phe in a higher concentration seemed to impose its tridimensional crystal organisation on the mixed hydrogel. In combination with the evolution of ^1H - ^{13}C CP/MAS spectra with variable ratio of gelators (Figure 8.8), these data showed a structure-determining gelation behaviour, in which the most abundant gelator dictates the final supramolecular arrangement. Despite this, some differences between the Phe/NH₂-Phe (1:2) and the pure NH₂-Phe hydrogels were identified in CP/MAS spectra (Figure 8.10) and are discussed below.

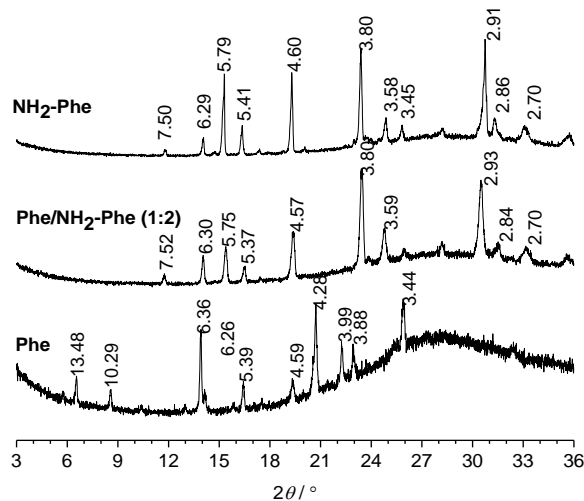


Figure 8.9. PXRD patterns of Phe (303 mM), Phe/NH₂-Phe (1:2) and NH₂-Phe (606 mM) hydrogels.

The ¹H-¹³C CP/MAS NMR spectrum of this hydrogel was not a simple superposition of both spectra of pure hydrogels (Figure 8.11). Instead, chemical shift variation was observed for the carbonyl, aromatic and C_βH₂ carbons (Figure 8.10, Table 8.2). Moreover, the peaks of the aromatic carbons of mixtures were significantly broadened with different peak line shapes in comparison with those of single gelator hydrogels. The existence of Phe peaks in this mixed Phe/NH₂-Phe (1:2) hydrogel confirmed its presence within the solid components and indicated that Phe is not just in the mobile state, *i.e.* dissolved in solution (Figure 8.10). These low intensity peaks highlighted in the figure (C₁ = 116.43 ppm and C₄ = 136.01 ppm) might not represent the totality of ¹³C environments for Phe. The heterogeneity of the mixed system probably leads to a multiplicity of environments, and some ¹³C peaks of Phe might be underneath the more intense ¹³C signals from NH₂-Phe. These studies showed that the supramolecular organisation of NH₂-Phe is not dominant as suggested by PXRD data, but both molecules are intricately modifying each other's packing motifs.

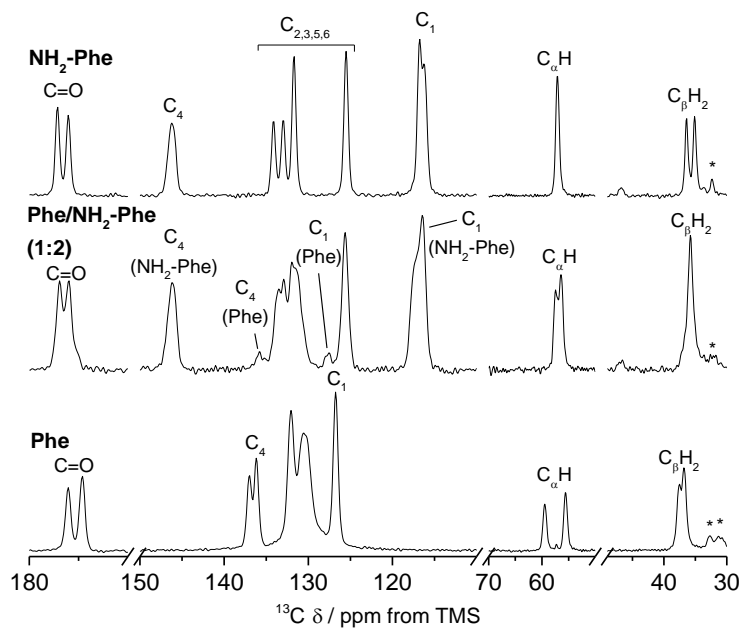


Figure 8.10. Amplification of ^1H - ^{13}C CP/MAS NMR spectra of Phe (303 mM), Phe/NH₂-Phe (1:2) and NH₂-Phe (606 mM) dry hydrogels acquired with an MAS rate of 10 kHz and 2048 scans. All experiments were conducted with a recycle delay of 20 s, $\pi/2$ pulse lengths of 3.2 μs (^1H) and 3.0 μs (^{13}C), using a 400 MHz solid-state spectrometer. Asterisks represent spinning sidebands.

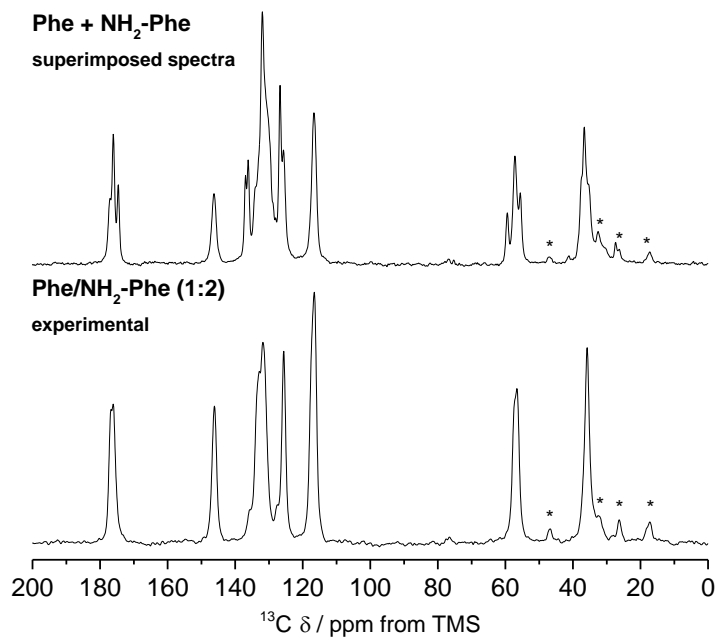


Figure 8.11. Experimental ^1H - ^{13}C CP/MAS NMR spectra of Phe/NH₂-Phe (1:2) dry hydrogel sample and modelled spectra from the superimposition of spectra of pure Phe and NH₂-Phe dry hydrogel samples.

Table 8.2. ^{13}C chemical shift values (δ) from ^1H - ^{13}C CP/MAS NMR spectra of Phe and $\text{NH}_2\text{-Phe}$ reference solid powders and Phe (303 mM), Phe/ $\text{NH}_2\text{-Phe}$ (1:0.2), Phe/ $\text{NH}_2\text{-Phe}$ (1:0.4), Phe/ $\text{NH}_2\text{-Phe}$ (1:2) and $\text{NH}_2\text{-Phe}$ (606 mM) dry hydrogel samples.

^{13}C δ / ppm from TMS							
Phe reference solid powder		Phe	Phe/ $\text{NH}_2\text{-Phe}$ (1:0.2)	Phe/ $\text{NH}_2\text{-Phe}$ (1:0.4)	Phe/ $\text{NH}_2\text{-Phe}$ (1:2)	NH ₂ -Phe	NH ₂ -Phe reference solid powder
C=O	176.1	176.0	176.1	176.3	176.8	177.1	175.3
		174.6	175.2	175.4	175.9	176.0	
C ₄ (NH ₂ -Phe)	-	-	-	145.5	146.1	146.2	146.5
C ₄ (Phe)	136.3	136.9	137.8	136.9	136.0	-	-
	-	136.1	136.2	-	-	134.1	131.7
Arom	131.0	131.9	132.7	-	132.9	132.9	131.1
	129.3	130.5	130.8	130.9	131.8	131.7	-
C ₁ (Phe)	126.7	126.7	126.3	126.9	127.6	-	-
						119.8	117.9
C ₁ (NH ₂ -Phe)	-	-	-	116.2	116.4	116.7	
	59.2	59.4	58.7	59.6	56.4	57.1	57.1
C _α H	57.4	55.5	56.3	55.8			
	41.1	37.4	37.2	38.0	35.7	36.4	37.8
C _β H ₂	38.36	36.7	36.4	36.9		35.1	

^{15}N is an NMR-active nucleus very sensitive to changes in the local environments of N-bearing groups and geometry of hydrogen bonds, therefore it contains specific structural information.²⁶⁵ Due to its low NMR sensitivity,²⁶⁵ ^{15}N -labelled Phe was used when monitoring local variations of $^{15}\text{NH}_3^+$ motifs in single and multiple gelator hydrogels.

High-field ^{15}N NMR spectra of the Phe hydrogel (Figure 8.12) showed two peaks (39.9 and 44.4 ppm), most likely corresponding to $^{15}\text{NH}_3^+$ terminal groups of the two molecules per asymmetric unit of the monohydrate form. Regarding the Phe/ $\text{NH}_2\text{-Phe}$ hydrogel, the considerable variation in ^{15}N peak intensities of the peaks at 40.2 and 44.7 ppm reflected that these nitrogen atoms were structurally different in the mixed hydrogel. These peaks were considerably broadened in comparison with ^{15}N peaks from the pure Phe hydrogel with the appearance of additional ^{15}N environments at 40.9 and 42.8 ppm. These data showed there was an increased distribution of possible orientations of magnetically non-equivalent Phe moieties due to the presence of considerably less ordered fibres. In the presence of the co-gelator $\text{NH}_2\text{-Phe}$, Phe has to adapt and acquire new tridimensional

arrangements as it cannot purely self-assemble into its monohydrate form. Therefore, Phe molecules might exist in a multiplicity of environments in the mixed hydrogel: within fibres arranged as the monohydrate form of Phe, forming fibres organised as the crystal motif of NH₂-Phe, and taking part of fibres with supramolecular arrangements different from both pure gels. This was consistent with the broad and asymmetric ¹³C peaks observed in the ¹H-¹³C CP/MAS NMR spectra of these systems (Figure 8.10). The variations observed between the organisation of pure and mixed gel systems showed fibres of both networks were composed of structurally different supramolecular assemblies.

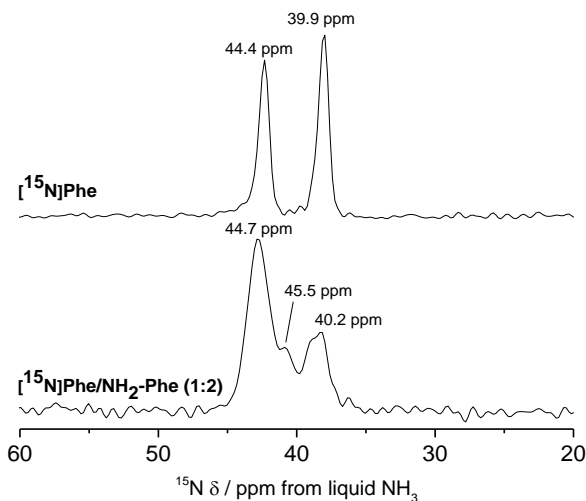


Figure 8.12. ¹H-¹⁵N CP/MAS NMR spectra of ¹⁵N-labelled ^{[13}C]/[¹⁵N]-Phe (303 mM) and ^{[13}C]/[¹⁵N]-Phe/NH₂-Phe dry hydrogel samples, acquired with MAS rates of 10 kHz and 1024 scans. All experiments were conducted with a recycle delay of 20 s and $\pi/2$ pulse lengths of 4.0 μ s (¹H) and 3.0 μ s (¹³C), using an 850 MHz solid-state NMR spectrometer.

One of the challenges in determining the tridimensional organisation of this mixed system is the fact that Phe/NH₂-Phe (1:2) hydrogel has twice the concentration of NH₂-Phe, but only a fraction of the fibres is detected *via* ¹⁵N-labelled Phe. Future work should focus on understanding ¹⁵N environments of NH₂-Phe molecules and compare them with those in pure NH₂-Phe hydrogel fibres. However, ¹⁵N-labelled NH₂-Phe is not yet available and ¹⁵N NMR experiments of semicrystalline materials require very long experimental times, which are not compatible with the use of high-field facilities for limited periods. Hence, indirect observation of these groups will be attempted using ¹H-¹⁵N HSQC HR-MAS experiments.

8.2.4. Investigation of intermolecular interactions responsible for aggregation and network disruption

Understanding the dynamics of disruption and identifying the structure of the gel products might shed a light on the composition of the solid-state components that preempt formation of the multiple gelator systems. The quantitative ability of ^1H solution-state NMR experiments was taken advantage of and it was determined that the particles suspended in the Phe/NH₂-Phe (1:0.4) suspension contained an equimolar composition of Phe and NH₂-Phe (1:1) (Figure 8.13). Interestingly, when studying spatial correlations between both molecules in the suspension and solution regimes, no cross-peaks were found between Phe and NH₂-Phe in the 2D ^1H - ^1H NOESY spectrum (Figure 8.14). The interaction between both gelator molecules, if any, might be very short-lived and do not allow cross-relaxation processes to occur. There might be formation of a very dynamic complex of Phe/NH₂-Phe in solution that is not detectable on the NMR time scale. The fact that these gelators do not form stable aggregates that would tend to precipitate out of solution might arise from weak interactions between Phe and NH₂-Phe in solution.

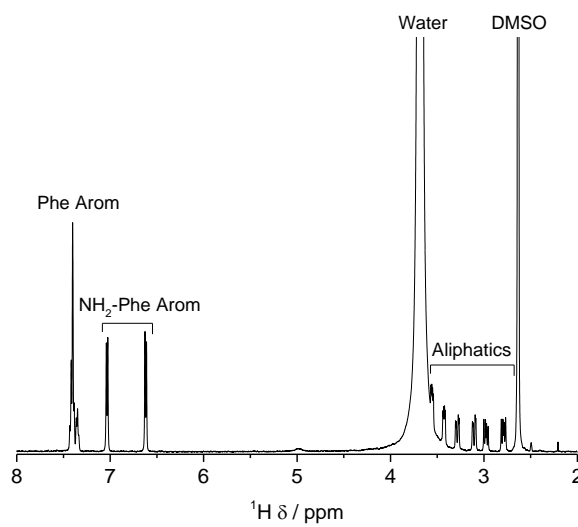


Figure 8.13. ^1H solution-state NMR spectra of Phe/NH₂-Phe (1:0.4) particles removed from suspension, dried and dissolved in DMSO-d₆. Experiments were conducted with a recycle delay of 10 s, using a 500 MHz solution-state NMR spectrometer.

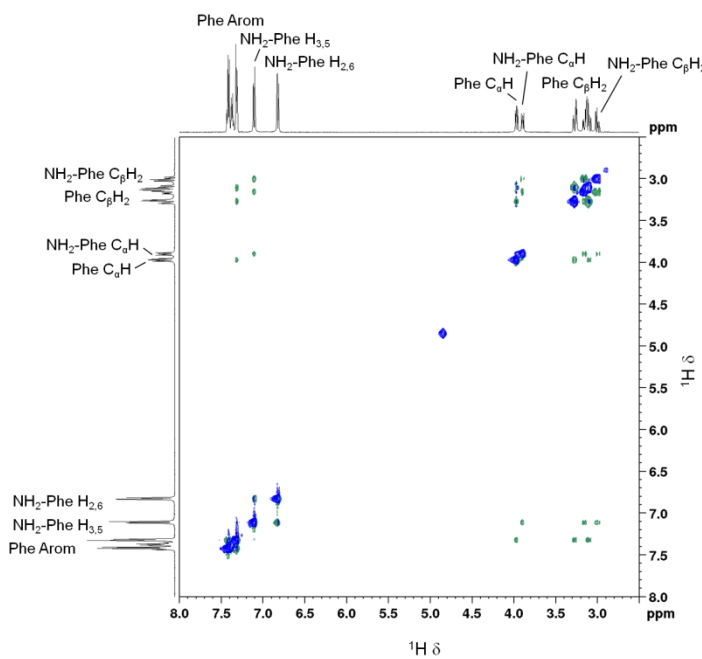


Figure 8.14. 2D ^1H - ^1H NOESY NMR spectrum of Phe/NH₂-Phe (1:1) solution, measured with a mixing time 1 s at 298 K. Experiments were conducted with a recycle delay of 2 s and 16 scans, using a 500 MHz solution-state NMR spectrometer.

Experiments monitoring chemical shift values of Phe with the gradual addition of NH₂-Phe were unsuccessful as working at gel forming conditions did not provide a clear trend of the modification of local ^1H environments. These are complex systems composed of several processes occurring in equilibrium, such as self-assembly, disassembly and exchange between gel/solution states. These processes contribute differently for chemical shift modulation. The mechanism of disruption was therefore investigated *via* dilution studies of the Phe/NH₂-Phe (1:0.15) hydrogel. Several ^1H NMR spectra were acquired at variable concentration to identify which proton sites were most affected by the disaggregation processes. The most significant chemical shift variation was observed for C_αH and C_βH₂ protons of both Phe and NH₂-Phe (Figure 8.15), indicating that the aliphatic region of both molecules was the most involved in formation of new intermolecular bonds. Thus, these findings provided evidence that NH₂-Phe participates in pre-gelation aggregation processes of the tridimensional network and does not merely remain dissolved in pools of solvent.

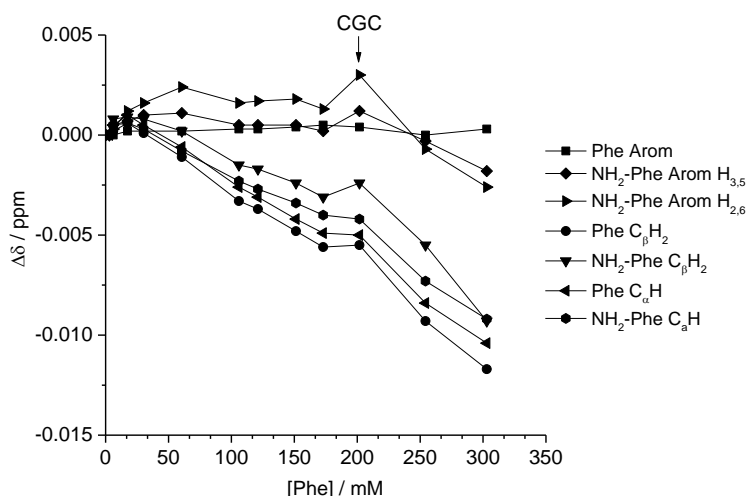


Figure 8.15. Chemical shift variation ($\Delta\delta$) in ^1H NMR spectra recorded during dilution studies of the Phe/NH₂-Phe (1:0.15) hydrogel, measured at 298 K.

The 2D ^1H - ^1H NOESY NMR spectrum acquired on the gel state of the same hydrogel Phe/NH₂-Phe (1:0.15) presented negative cross-peaks, characteristic of medium-to-large molecules,²⁶³ between all protons (Figure 8.16). It is important to highlight there was detection of intermolecular cross-peaks between Phe and NH₂-Phe molecules. This contrasted with NOESY experiments conducted in suspensions, in which only positive (typical of small molecules) and intramolecular nOe enhancements were detected. The map of through-space connectivities in the gel state allowed interproton distances to be calculated (Table 8.3). In combination with the evolution of nOe enhancements with mixing time (Figure 8.17) these data enabled the conclusion to be drawn that the closest interaction occurred between NH₂-Phe aliphatic protons and Phe C_αH. NH₂-Phe and Phe probably interact with each other in solution *via* their electrostatic moieties, suggesting the mechanism of disruption of Phe dimers⁸² occurs *via* the aliphatic region of both molecules. This is plausible, as electrostatic interactions are the driving force of gelation of Phe, and there was an initial indication that the electrostatics are key in driving the formation of unidirectional assemblies of NH₂-Phe (described in Chapter 5, section 5.2.5, page 158).

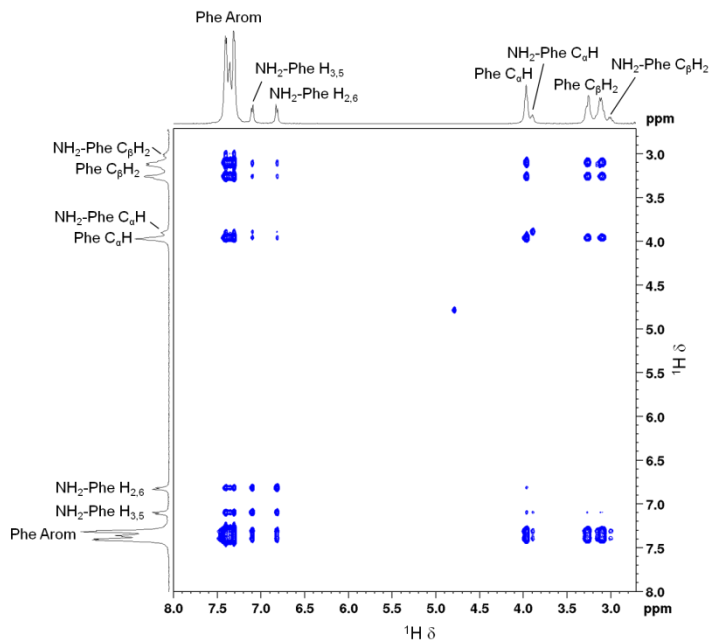


Figure 8.16. 2D ^1H - ^1H NOESY NMR spectrum of Phe/NH₂-Phe (1:0.15) hydrogel with a mixing time 0.5 s, measured at 298 K.

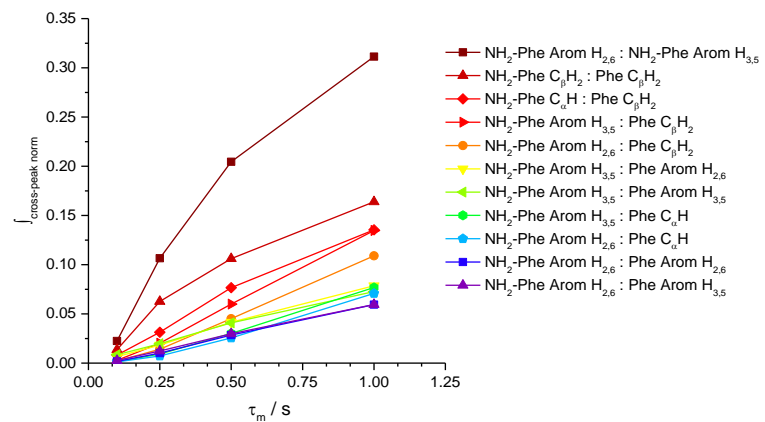


Figure 8.17. Evolution of normalised cross-peak intensity ($J_{\text{cross-peak norm}}$) with mixing time in 2D ^1H - ^1H NOESY NMR spectra of Phe/NH₂-Phe (1:0.15) hydrogel. Colour represents the degree of nOe enhancement.

Table 8.3. Interproton distances calculated from 2D ^1H - ^1H NOESY NMR spectrum of Phe/NH₂-Phe (1:0.15) hydrogel with a mixing time 0.01 s, measured at 298 K, using the H_{2,6}-H_{3,5} distance from NH₂-Phe as reference. Average errors of 7 % were assumed as for fast tumbling molecules in viscous solvents.²⁷

Correlation	r / Å	δ / Å
NH₂-Phe Arom H_{2,6} : NH₂-Phe Arom H_{3,5}	2.28 ^a	-
NH₂-Phe C_βH₂ : Phe C_βH₂	2.48	0.20
NH₂-Phe Arom H_{3,5} : Phe Arom H_{3,5}	2.68	0.21
NH₂Phe C_αH : Phe C_βH₂	2.70	0.22
NH₂-Phe Arom H_{3,5} : Phe Arom H_{2,6}	2.80	0.22
NH₂-Phe Arom H_{3,5} : Phe C_βH₂	3.23	0.26
NH₂-Phe Arom H_{2,6} : Phe Arom H_{3,5}	3.24	0.26
NH₂-Phe Arom H_{2,6} : Phe C_βH₂	3.37	0.27
NH₂-Phe Arom H_{2,6} : Phe Arom H_{2,6}	3.50	0.28
NH₂-Phe Arom H_{3,5} : Phe C_αH	3.60	0.29
NH₂-Phe Arom H_{2,6} : Phe C_αH	3.68	0.29

^a Distance used as reference

8.2.5. Characterisation of dynamics of disruption and gel formation

^1H NMR was used to monitor self-assembly processes of Phe in the presence of NH₂-Phe. ^1H NMR peaks of Phe and NH₂-Phe became broader and less intense throughout the gelation process of a hot solution of Phe/NH₂-Phe (1:0.1) (Figure 8.18), consistent with aggregation and formation of network components which are “silent” in solution-state NMR.¹⁴⁷ Interestingly, NH₂-Phe protons showed reduced peak intensities, a strong indication that *ca.* 35 % of NH₂-Phe molecules were entrapped into the rigid gel fibres (Table 8.4).

As the concentration of NH₂-Phe in Phe hydrogels was raised increased peak intensity for Phe protons was recorded, reflecting a higher concentration of Phe dissolved in solution (Figure 8.19 and Table 8.4). Sharp and intense ^1H peaks revealed the molecular variations associated with formation of a suspension at Phe/NH₂-Phe (1:0.3), exhibiting spectral features characteristic of isotropic solutions.

Phe/NH₂-Phe (1:0.1)

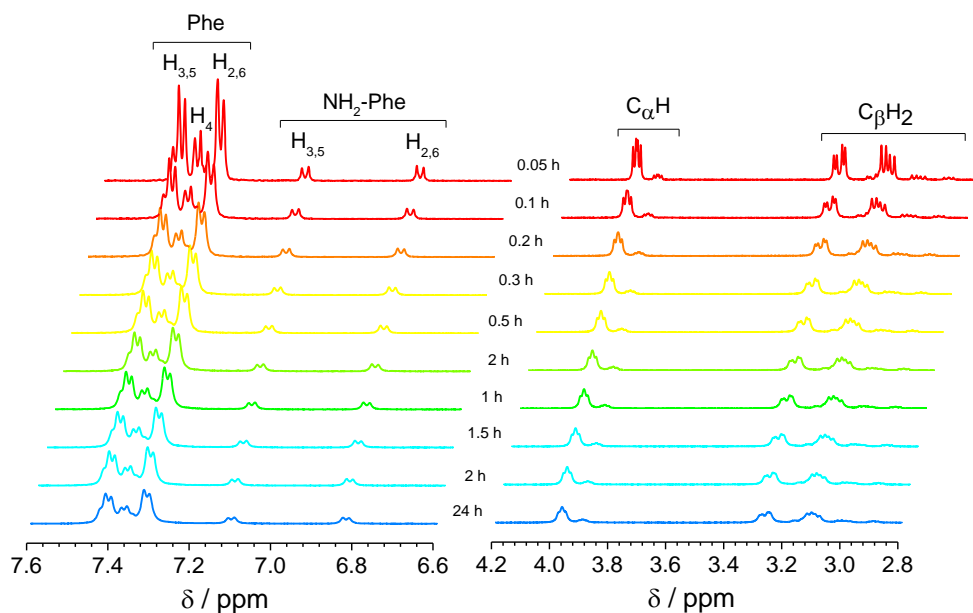


Figure 8.18. Kinetics of gelation monitored by the acquisition of ¹H NMR spectra with time, immediately after cooling down a hot solution of Phe/NH₂-Phe (1:0.1) with gradual formation of a hydrogel, measured at 298 K.

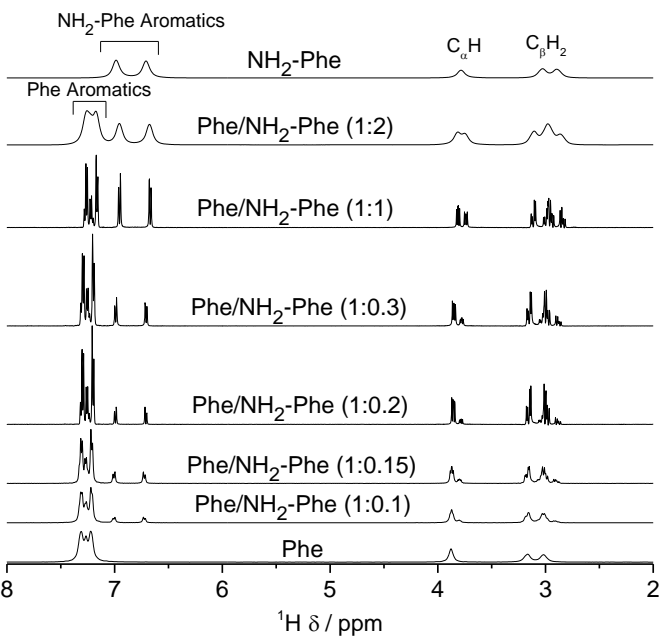


Figure 8.19. ¹H solution-state NMR spectra of Phe (303 mM), Phe/NH₂-Phe (1:0.1), Phe/NH₂-Phe (1:0.15), Phe/NH₂-Phe (1:0.2), Phe/NH₂-Phe (1:2) and NH₂-Phe (606 mM) hydrogels, Phe/NH₂-Phe (1:0.3) suspension and Phe/NH₂-Phe (1:1) solution measured at 298 K.

Table 8.4. Concentration of dissolved gelator molecules calculated from ^1H solution-state NMR peak intensity for Phe (303 mM), Phe/NH₂-Phe (1:0.05), Phe/NH₂-Phe (1:0.15), Phe/NH₂-Phe (1:0.2), Phe/NH₂-Phe (1:0.55), Phe/NH₂-Phe (1:2) and NH₂-Phe (606 mM) hydrogels, measured at 298 K.

	[Phe] in solution		[NH ₂ -Phe] in solution	
	%	mM	%	mM
Phe	47	142	-	-
Phe/NH₂-Phe (1:0.05)	50	152	90	3
Phe/NH₂-Phe (1:0.1)	55	167	65	4
Phe/NH₂-Phe (1:0.15)	61	185	56	22
Phe/NH₂-Phe (1:0.2)	76	230	51	28
Phe/NH₂-Phe (1:0.55)	88	267	63	105
Phe/NH₂-Phe (1:2)	40	121	40	242
NH₂-Phe	-	-	20	121

^1H longitudinal relaxation times (T_1) were monitored throughout the gel-to-solution transitions of these thermoreversible materials. ^1H T_1 times were similar for different ^1H species in the Phe hydrogel (Figure 8.20), a behaviour associated with the presence of strong homonuclear dipolar couplings and fast exchange processes occurring between gel and solution states. The resulting ^1H T_1 values are averaged out for molecules in both environments (this phenomenon is fully discussed in Chapter 6, section 6.2.7, page 178). The increase of ^1H T_1 times with temperature for all hydrogels under study corresponded to the “fast tumbling regime”, also corroborated by the decreased line widths with increasing temperature.

When NH₂-Phe was added to the Phe hydrogel at low concentrations, ^1H T_1 times were similar for different ^1H sites of NH₂-Phe (Figure 8.21). The similarity of ^1H T_1 values proved that Phe and NH₂-Phe were strongly dipolar coupled and exchanging between gel and solution states. After the addition of 40 mM of NH₂-Phe (molar ratio of 1:0.15), such similarity between T_1 values for different groups was lost, with full distribution of T_1 times typical of solutions when the concentration of NH₂-Phe was above 55 mM (molar ratio of 1:0.2). Above this concentration, the system consisted predominantly of the fast tumbling molecules of Phe and NH₂-Phe dissolved in isotropic pools of solvent. This was a consequence of the disruption of the supramolecular network, in agreement with the sharp and intense peaks detected in the corresponding ^1H spectrum (Figure 8.19).

Similarly, the distribution of ^1H T_1 times in pure NH₂-Phe and mixed Phe/NH₂-Phe hydrogel, in the gel state, was similar to solutions of NH₂-Phe (Figure 8.20). This pointed

towards Phe and NH₂-Phe being mainly dissolved throughout the range of temperatures. This dispersion of values was more marked for the pure NH₂-Phe system. These results reflected different dynamics of exchange of molecules between the gel and solution environments for the pure NH₂-Phe and mixed gels when compared with the pure Phe material. The time scale of these exchange phenomena is discussed below taking into account all findings.

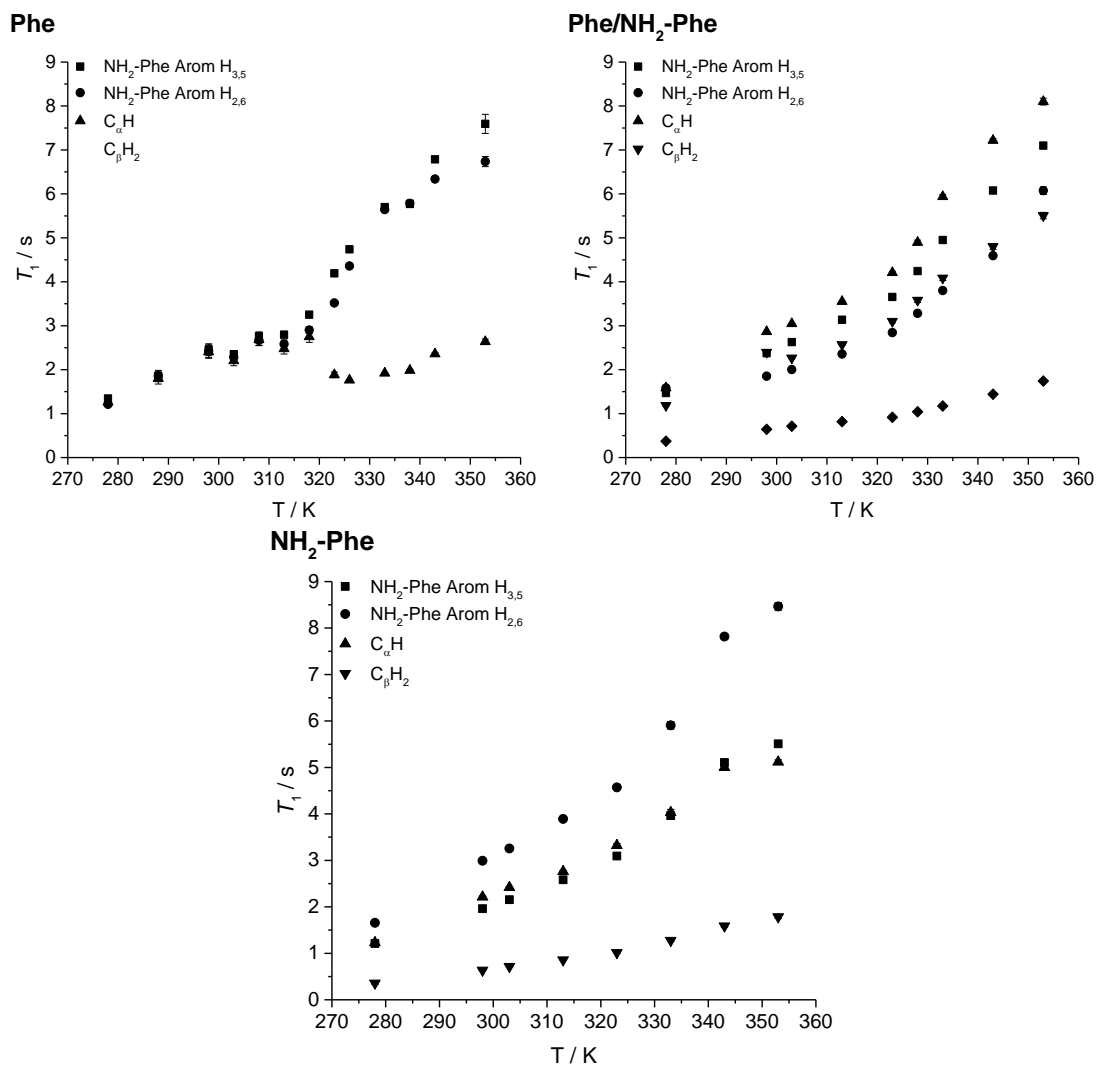


Figure 8.20. ¹H longitudinal relaxation times (T_1) for Phe Arom, NH₂-Phe Arom, C_αH and C_βH₂ of Phe (303 mM), Phe/NH₂-Phe (1:2) and NH₂-Phe (606 mM) hydrogels measured between 278 and 328 K. Experiments were conducted with a recycle delay of 10 s, using a 500 MHz solution-state NMR spectrometer.

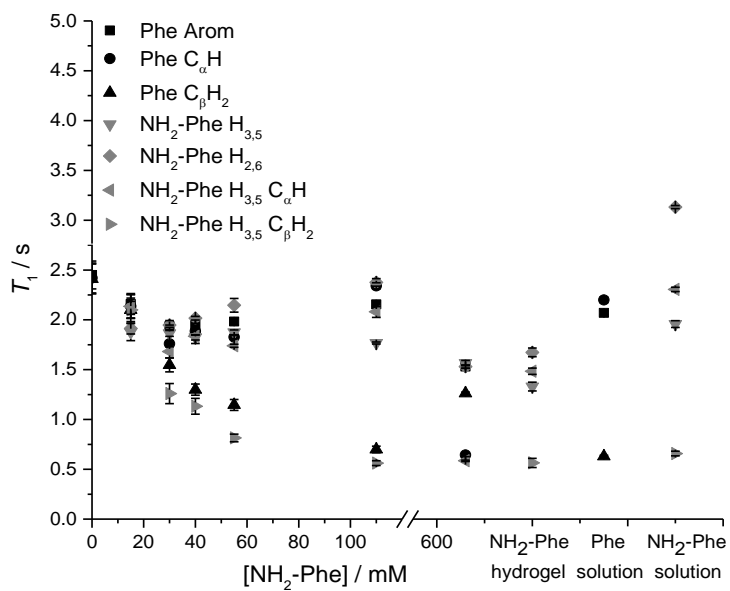


Figure 8.21. ^1H solution-state longitudinal relaxation times (T_1) of Phe hydrogels with variable concentration of $\text{NH}_2\text{-Phe}$, Phe/ $\text{NH}_2\text{-Phe}$ (1:2) and $\text{NH}_2\text{-Phe}$ (606 mM) hydrogels, and Phe (100 mM) and $\text{NH}_2\text{-Phe}$ (100 mM) solutions.

Table 8.5. ^1H solution-state NMR longitudinal relaxation times (T_1) for Phe and $\text{NH}_2\text{-Phe}$ solutions (101 mM) measured at 298 K, with error values in parenthesis.

		$^1\text{H} T_1 / \text{s}$						
		Arom			C α H		C β H ₂	
		Phe	$\text{NH}_2\text{-Phe H}_{3,5}$	$\text{NH}_2\text{-Phe H}_{2,6}$	Phe	$\text{NH}_2\text{-Phe}$	Phe	$\text{NH}_2\text{-Phe}$
Phe (solution)		2.07 (0.02)	-	-	2.20 (0.03)	-	0.63 (0.01)	-
$\text{NH}_2\text{-Phe}$ (solution)		-	1.96 (0.03)	3.13 (0.02)	-	2.31 (0.02)	-	0.66 (0.02)

STD NMR experiments were carried out to assess these dynamics of exchange at the gel/solution interfaces. A mono-exponential evolution of build-up of saturation in solution was observed for the Phe hydrogel (Figure 8.22), resulting from fast exchange between gel and solution states on the NMR relaxation time scale, previously discussed in Chapter 6 (section 6.2.8, page 179).

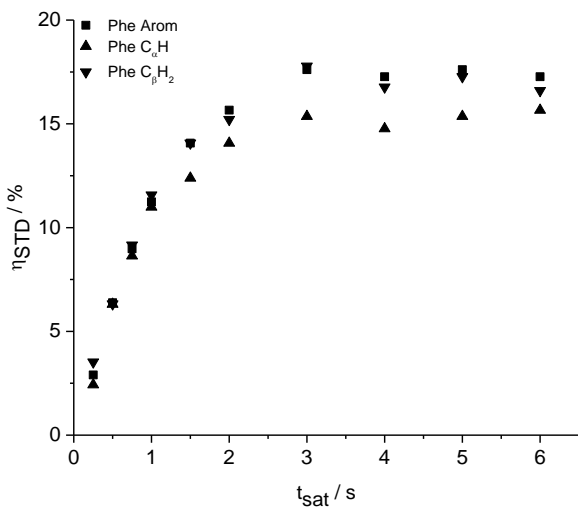


Figure 8.22. Evolution of fractional STD response (η_{STD}) for Phe hydrogels measured at 298 K, using a 500 MHz solution-state NMR spectrometer ($\text{STD}_{\text{on}} = 1 \text{ ppm}$).

The initial slope for fractional STD response decreased gradually as higher concentrations of $\text{NH}_2\text{-Phe}$ were introduced (Figure 8.23). More importantly, no build-up of saturation was detected at concentrations of $\text{NH}_2\text{-Phe}$ above 55 mM (molar ratio of 1:0.2). Since STD NMR experiments rely on the transfer of saturation from a large supramolecular network, which acts as a reservoir of magnetisation, to protons in close proximity, these studies proved that the supramolecular network loses its structural integrity at molar ratios higher than Phe/ $\text{NH}_2\text{-Phe}$ (1:0.2). This was consistent with ^1H longitudinal relaxation findings and with the loss of structural integrity observed macroscopically. These experiments allowed the “breaking point” of the network to be determined at a molecular level.

Low initial build-up values were observed in the pure $\text{NH}_2\text{-Phe}$ ($\text{STD}_0 = 0.46 \text{ s}^{-1}$) and mixed Phe/ $\text{NH}_2\text{-Phe}$ hydrogels ($\text{STD}_0 = 0.03 \text{ s}^{-1}$) (Figure 8.23). These values indicated an inefficient transfer of saturation at the interfaces or poor accumulation of saturation by molecules returning to solution. This can occur when molecules interact very fast with the surface of the fibres and have short residence time that prevents the efficient transfer of saturation; or when molecules participate in very strong interactions at the interface, remain longer at the gel surfaces and therefore do not accumulate as much saturation in solution. During VT STD measurements, the transfer of saturation was more efficient when molecular motions were slowed down (Figure 8.24 and Figure 8.25) translating

longer residence times at the interfaces at lower temperatures. Henceforth, these data clearly showed that, at 298 K, NH₂-Phe molecules have considerably fast dynamics of exchange on the NMR relaxation time scale, due to formation of weak intermolecular interactions, which is consistent with NH₂-Phe decreased gelation ability and higher water solubility. Regarding Phe in multiple gelator hydrogels, as Phe exhibited lower STD values than those recorded in the pure Phe hydrogel, it could be assumed that the rate of exchange between free and bound states of Phe was fastened in the presence of the co-gelator NH₂-Phe, as a consequence of the weaker intermolecular interactions formed between Phe and NH₂-Phe.

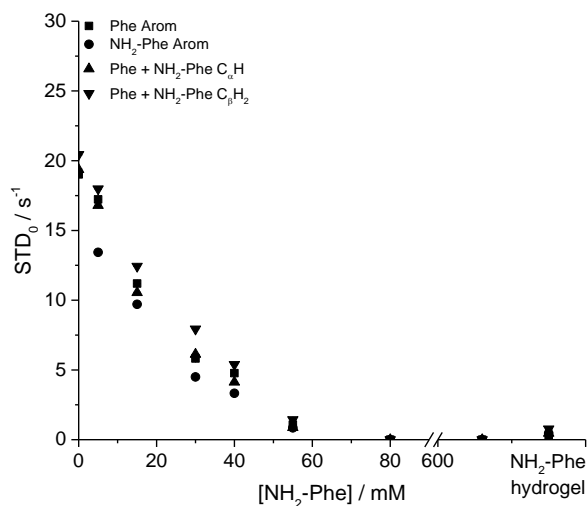


Figure 8.23. Initial slope of build-up curves (STD₀) of Phe hydrogels with increasing concentrations of NH₂-Phe, measured at 298 K, using a 500 MHz solution-state NMR spectrometer (STD_{on} = 1 ppm).

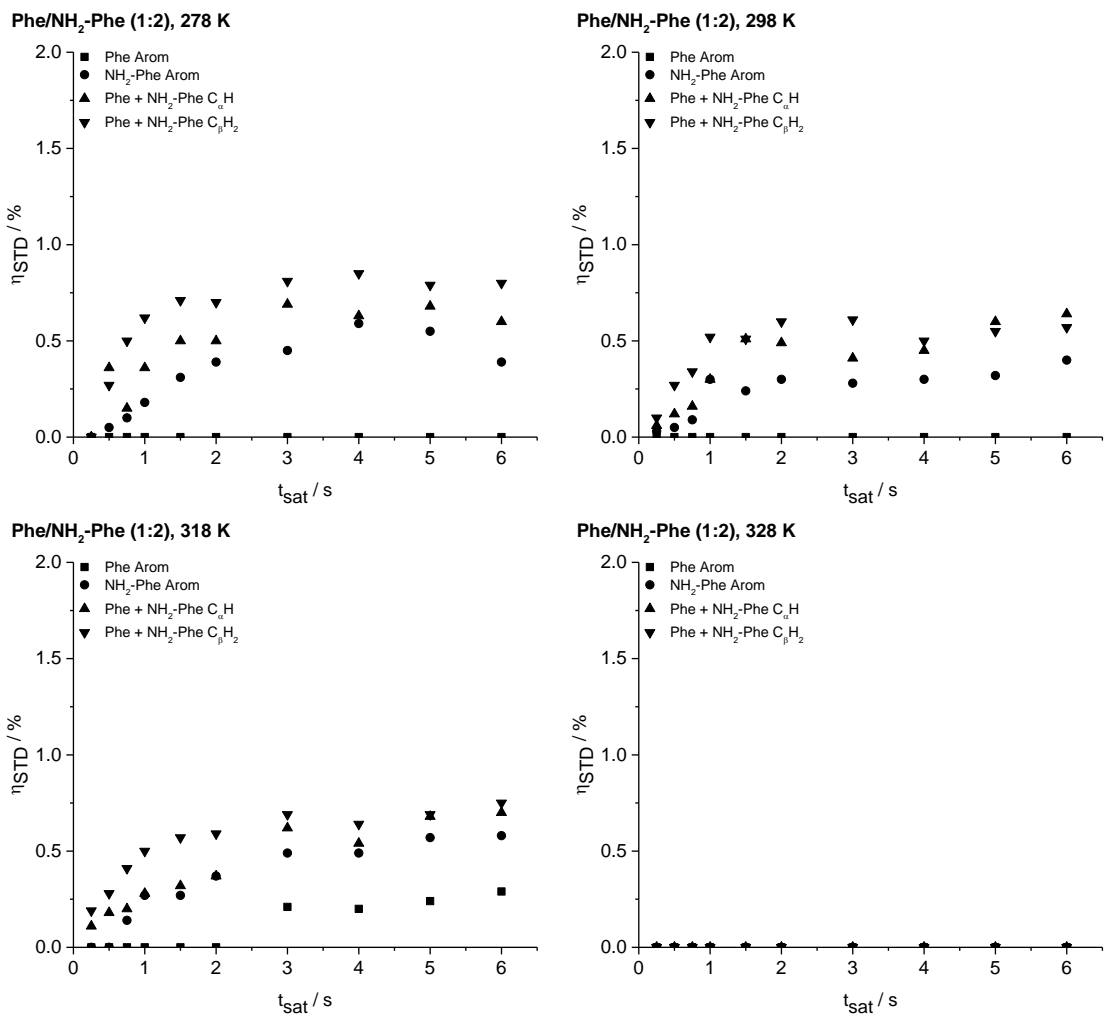


Figure 8.24. Evolution of fractional STD response (η_{STD}) for Phe/NH₂-Phe (1:2) hydrogels measured between 278 and 328 K, using a 500 MHz solution-state NMR spectrometer ($STD_{on} = 1$ ppm).

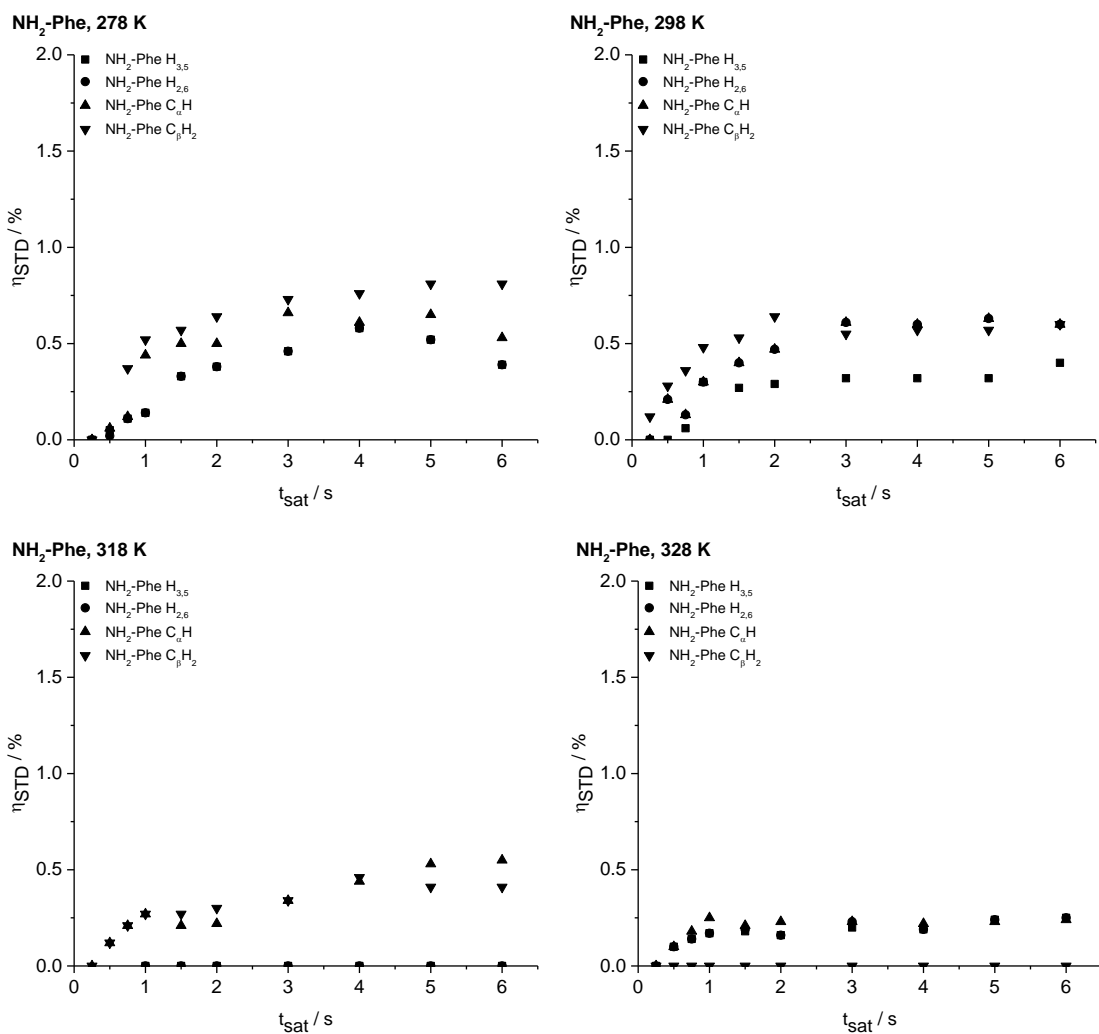


Figure 8.25. Evolution of fractional STD response (η_{STD}) for $\text{NH}_2\text{-Phe}$ hydrogels measured between 278 and 328 K, using a 500 MHz solution-state NMR spectrometer ($\text{STD}_{\text{on}} = 1 \text{ ppm}$).

8.3. Concluding remarks and future work

It was found that $\text{NH}_2\text{-Phe}$ is able to independently self-assemble in water and to give rise to strong brown gels above 388 mM. The tridimensional ordering of the needle-like crystalline fibres was determined using single-crystal and PXRD diffraction methods. The structure was in very good agreement with solid-state NMR experiments. These fibres were composed of *ca.* 80 % of gelator molecules, with the rest being dissolved in solution or partially trapped at the fibre interfaces. The dynamics of exchange was faster than that of the pure Phe hydrogel, as weaker intermolecular interactions between $\text{NH}_2\text{-Phe}$ molecules were formed. With the purpose of determining the predominant intermolecular interactions dictating self-assembly of $\text{NH}_2\text{-Phe}$, future work aims to generate an interaction energies framework using CrystalExplorer.

When Phe and NH₂-Phe were mixed in water, different products were obtained depending on the concentration and molar ratio of the gelator molecules. Hydrogelation of Phe could be prevented when Phe was mixed with NH₂-Phe at molar ratios between 1:0.2 and 1:2 (Phe/NH₂-Phe), with either a suspension or solution being formed. ¹H NMR and longitudinal relaxation studies indicated that, as the concentration of NH₂-Phe was increased, there was gradual dissolution of Phe assemblies. The resulting sharp and intense ¹H NMR peaks were accompanied by a distribution of ¹H *T*₁ times resembling those of solutions. These features became more marked above the ratio of 1:0.2 ([NH₂-Phe] = 55 mM and [Phe] = 303 mM). At this point, the considerable dissolution of the network promoted by NH₂-Phe led to the disappearance of the STD NMR response. This was attributed to the absence of a supramolecular structure capable of accumulating and transferring saturation, in agreement with the loss of structural integrity of the gel.

The assembly at higher concentrations of NH₂-Phe led to a different scenario. NH₂-Phe was mixed with Phe at gel forming concentrations ([Phe] > 212 mM and [NH₂-Phe] > 388 mM) and multiple gelator hydrogels of Phe/NH₂-Phe were obtained. Their tridimensional arrangements seemed to be dominated by the packing motif of NH₂-Phe, as diffraction experiments showed great similarity between the crystalline components of NH₂-Phe and Phe/NH₂-Phe hydrogels. However, investigation of local molecular environments by solid-state NMR spectroscopy showed a multiplicity of environments for both gelator molecules. The line broadening observed in ¹H-¹³C CP/MAS spectra and the presence of additional ¹⁵N peaks for Phe provided evidence of formation of new environments for both gelators in the mixed fibres. These fibres were organised in a less ordered fashion, when comparing with the molecular arrangement of the pure hydrogels. The above mentioned faster dynamics of exchange at the gel/solution interfaces resulted from these structural variations that modulated the properties of the surface of the fibres. The mixtures of Phe/NH₂-Phe were very complex to understand due to the presence of disordered multi-component gel fibres with most likely the presence of heterogeneous domains.

While studying both disruption and gelation phenomena, it was found that NH₂-Phe was involved in pre-gelation aggregation. NH₂-Phe manifested its disruption effects in early nucleation processes of Phe, modulating kinetics of gelation of Phe. This was attributed to the interference of NH₂-Phe with the electrostatic interactions between Phe dimers, which

are the anisotropic forces of self-assembly of Phe. Such interference by NH₂-Phe resulted in the formation of a clear brown solution at a ratio of 1:1. These data provided indirect evidence of the interaction between both gelator molecules in solution and onto the surface of the mixed hydrogel fibres. It is the affinity of Phe for NH₂-Phe, and *vice-versa*, that is behind the presence of both molecules in the solid fibres.

Despite significant progress being made towards understanding structures of multiple gelator hydrogels prepared from Phe and NH₂-Phe, through the application of the combined computational, diffraction and NMR approach presented in this chapter, the crystal structures of the mixed gel fibres and the patterns of interactions in such systems still present some challenges. It is proposed that the acquisition of high-field ¹⁵N solid-state spectra of multiple gelator hydrogels takes place using ¹⁵N-labelled NH₂-Phe when this labelled amino acid derivative becomes available. Indirect observation of unlabelled NH₂-Phe environments at the surface of the rigid gel fibres might be possible by performing ¹H-¹⁵N HSQC experiments in dry gel samples using HR-MAS spectroscopy.

Chapter 9

9. Substituent interference on supramolecular assembly of urea gelators: synthesis, structure prediction and NMR

Findings from this chapter are partly published in

Piana, F.; Case, D. H.; Ramalhete, S. M.; Pileio, G.; Facciotti, M.; Day, G. M.; Khimyak, Y. Z.; Angulo, J.; Brown, R. C.; Gale, P. A., Substituent interference on supramolecular assembly in urea gelators: synthesis, structure prediction and NMR. *Soft matter* **2016**, *12* (17), 4034-4043.

An NMR-based methodology was developed and optimised in the previous chapters to create a reliable approach of fully characterising supramolecular gels. The present chapter tests this strategy on structurally and dynamically different materials.

9.1. Introduction

Hanabusa,²⁶⁶ van Esch and Kellogg^{123, 133, 267} have extensively exploited the urea tape motif as a building block to obtain new supramolecular gelator molecules. Urea is the molecular equivalent of a Velcro® type hook-and-loop²⁶⁸ (Figure 9.1) and, for this reason, it is able to promote molecular unidirectional self-association and form supramolecular assemblies.²⁶⁷⁻²⁶⁹ For this purpose, molecular features of an urea derivative were varied systematically throughout this work. The main focus of this work was to help understand the relationship between molecular and self-assembled structure, with the purpose of contributing to the rational design of new gel-based materials. Furthermore, the present work helped validate the NMR-based methodological approach on a structurally different molecule.

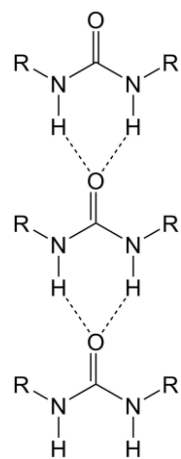


Figure 9.1. Schematic representation of the urea tape motif.

The present chapter resulted from the collaborative work between the groups of Professor Philip Gale (University of Southampton), responsible for the synthesis of gelator molecules, gelation studies and microscopy imaging; Professor Graeme Day (University of Southampton), who performed molecular modelling calculations; and my group, who conducted the characterisation of the resulting gel materials using powder X-ray diffraction and NMR spectroscopy.

9.2. Results and Discussion

9.2.1. Gelation studies

Prof. Philip Gale's group systematically varied head substituents and tail length of an urea-based scaffold (Figure 9.2). Eighteen *N*-aryl-*N'*-alkyl urea gelators were synthesised. It was found that gelators bearing short alkyl chains did not form any gels due to their high solubility, indicating that solute-solvent interactions prevailed over solute-solute interactions. The initial motivation for investigating different aromatic substitutions stemmed from the potential ability of electron withdrawing or donating substituents to tune the acidity of the urea group. Upon substitution of the aromatic head group with an electron withdrawing group ($-\text{NO}_2$), cooperative hydrogen bonding between urea functional groups was expected to be reinforced, leading to more acidic NH groups and consequently improving gelation. However, the opposite was observed for long chain gelator molecules and better gelation performance was reported in the presence of the electron donating group $-\text{OCH}_3$ instead. These observations indicated that it is a balance

of effects that dictate gelation, related to alkyl chain length, substituent electron withdrawing/donating ability and, perhaps, less intuitive substituent effects.

In order to isolate the contribution of $-\text{NO}_2$ and $-\text{OCH}_3$ head substituents on gelation ability, two representative gelator molecules (**1** and **2**) (Figure 9.2) underwent comprehensive thermo-mechanical, molecular modelling and NMR characterisation. Prof. Philip Gale's group performed gel formation studies in fifteen solvents, selected to cover a wide range of polarities. Solvent polarity did not directly affect gelation performance, despite reported evidence on other systems.⁵² Hence, more comprehensive studies were conducted with solvents with variable polarities: toluene, tetralin and DMSO.

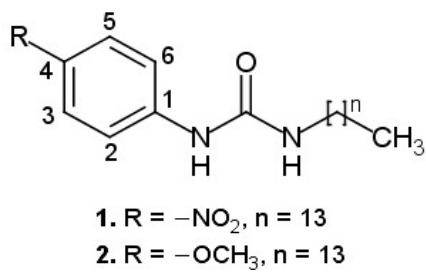


Figure 9.2. Schematic representation of the investigated gelator structures.

CGC values for gelator **1** were higher than for gelator **2** (Table 9.1), reflecting that the latter had increased tendency to self-assemble. T_{gel} values obtained by DSC were 348 K for organogel **1** and 359 K for organogel **2**, showing the network formed by gelator **2** was thermally more stable. Rheological tests reflected their solid-like behaviour, and demonstrated that the strength of the materials increased from **1** to **2** (Figure 9.3). Furthermore, environmental scanning electron microscopy (ESEM) showed morphological differences in xerogels obtained from gels **1** and **2** (Figure 9.4), with xerogel **1** showing a disorganised network. The thermo-mechanical and morphologic differences identified between both systems reflected the influence of the head group in conditioning the supramolecular packing of gelator molecules, similarly to what was observed with halogenated derivatives of phenylalanine (Chapter 7, page 186).

Table 9.1. Critical gelation concentration (CGC) values for organogels **1** and **2**.

Gelator	CGC / mg mL ⁻¹		
	Toluene	Tetralin	DMSO
1	20	20	50
2	5	5	50

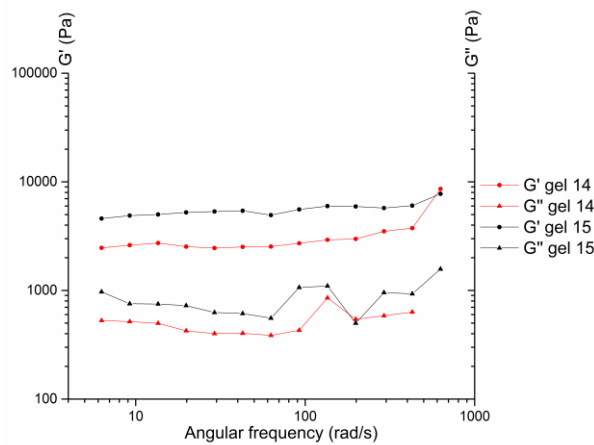


Figure 9.3. Storage (G') and loss (G'') moduli with angular frequency sweeps of organogels **1** and **2** in toluene (20 mg mL⁻¹).

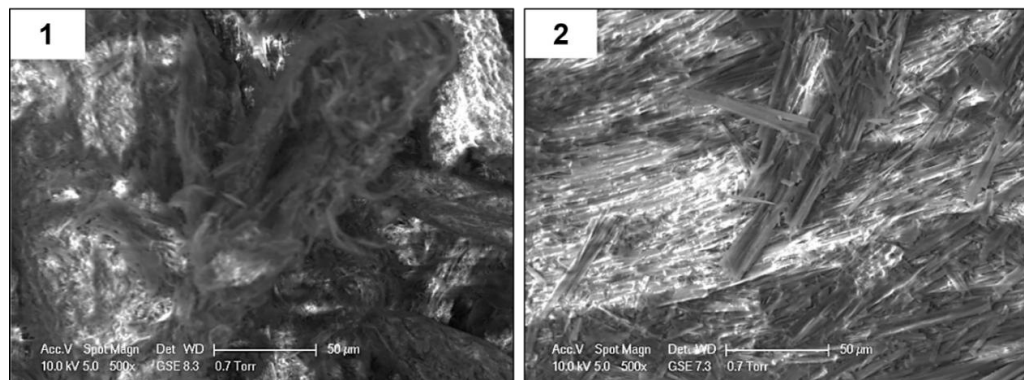


Figure 9.4. Environmental SEM images at 500x magnification of xerogels obtained from gels **1** and **2** (20 mg mL⁻¹) in toluene.

9.2.2. Investigating the effects of the addition of head groups by molecular modelling

To help interpret the observed differences in gelation between **1** and **2**, Prof. Graeme Day's group performed electronic structure calculations on both isolated molecules, as well as CSP calculations.

To investigate the inductive effect of the head substituent, single molecule DFT calculations were performed using DMol3 at the B3LYP/DNP level of theory to assess the electrostatic potential around **1** and **2**. These calculations revealed a slightly more positive electrostatic potential at the polar hydrogen atoms of the urea in **1** compared to **2**, as shown in Figure 9.5, and a more negative electrostatic potential in the π -electron region of the aromatic ring for **2**. These differences reflected the expected influence of the electron withdrawing or donating substituents. However, the most prominent difference between the molecules was the introduction of a region of negative charge at the $-\text{NO}_2$ substituent in gelator **1**. The oxygen atoms in the $-\text{NO}_2$ group of **1** are particularly accessible; hence they are positioned to easily compete with the urea oxygen as hydrogen bond acceptors for the protons of the urea group. Similarly, the oxygen of the $-\text{OCH}_3$ substituent in gelator **2** also introduced a region of negative charge, but one that was much weaker and was shielded to some extent by the steric impedance of the methyl group.

The observed differences in the electrostatic potential are significant, as they can promote disruption of the urea “zipping”, which is associated with favourable gelation properties.²⁶⁸ In a study of the effects of anions on urea gelators, Steed *et al.* (2012) have reported that anions of sufficient hardness could disrupt this pattern.²⁶⁹ Therefore, the increased acidity of the urea hydrogen atoms have the potential to enhance the formation of urea tapes in **1**, while the presence of competing hydrogen bond acceptors can disrupt their formation.

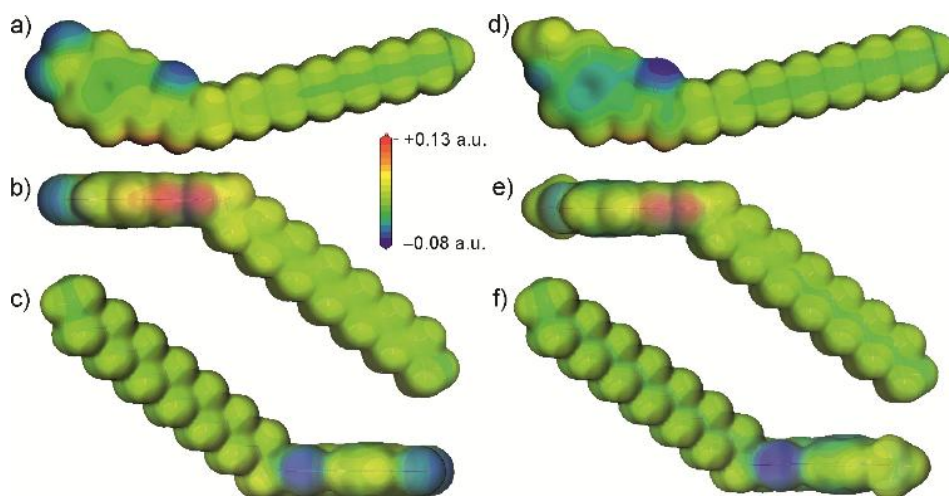


Figure 9.5. Calculated molecular electrostatic potentials of **1** (a-c) and **2** (d-f). The potentials are plotted on the 0.02 a.u. electronic isodensity surface. The red patches of positive electrostatic potential in b) and e) correspond to the urea hydrogen atom positions. c) and f) show the view down the urea oxygen atom, highlighting its negative electrostatic potential.

The purpose of performing CSP calculations was to explore the balance of these competing effects and the overall influence of the aromatic substituents on the preferred intermolecular arrangement of these molecules and their influence on solid-state packing. Prof. Graeme Day's group applied CSP methods to take advantage of the developments that have been made in this area over the past few years²⁷⁰⁻²⁷² in predicting the preferred solid-state assembly of organic molecules using a global search of the lattice energy surface. This global optimisation approach provides an unbiased assessment of molecular packing possibilities in a solid-state environment, unlike other recent molecular modelling studies of gel structure based on assumed supramolecular arrangements^{273, 274}, conformational sampling of small molecular clusters²⁷⁵ or dynamical simulations of pre-arranged fibre models.^{276, 277}

Prof. Graeme Day's group performed both rigid-molecule and flexible-molecule searches. The initial calculations displayed a clear difference in the predicted crystal packing behaviours of gelators **1** and **2**. The low energy predicted structures of gelator **2** displayed hydrogen bonding between urea groups, predominantly forming the unidimensional urea chains or tapes (Figure 9.6d,f) that are associated with fibre formation. The $-\text{OCH}_3$ did not participate in hydrogen bonding. In contrast, the low energy structures of **1** lacked the $\text{N}-\text{H}\cdots\text{O}_{\text{urea}}$ hydrogen bonding linking urea into one-dimensional chains or tapes (Figure 9.6a,b). The CSP results suggested that the urea tape formation was disrupted by the presence of the $-\text{NO}_2$ group, which acted preferentially as a hydrogen bond acceptor.

To verify that these findings were not biased by the simplification of using rigid molecular geometries in the crystal structure search, further CSP calculations were performed with flexibility of the molecular geometry allowed during structure generation and lattice energy minimisation. These flexible-molecule calculations did not change the overall conclusions from the initial calculations: hydrogen bonded urea tapes dominated the low energy structures of **2**, while the low energy structures of **1** were dominated by urea hydrogen bonded to $-\text{NO}_2$. Only small variations were observed in the angle and length of these intermolecular interactions by giving the molecule freedom to distort from its ideal geometry.

For gelator **1**, a slight reorientation of the alkyl chain allowed the alignment of both $-\text{NO}_2$ oxygen atoms with urea hydrogen atoms, forming a double hydrogen bond, as shown in

Figure 9.6a. This interaction was found in the overall lowest energy predicted structures of **1** and provided significant stabilisation of molecules. The total energy of the best structure involving the double hydrogen bond (Figure 9.6a) was 9 kJ mol⁻¹ lower than the lowest energy structure involving only one --NO_2 oxygen in hydrogen bonding (Figure 9.6b). The lowest energy predicted crystal structure of **1** that displayed the urea hydrogen bond tape motif was a further 13 kJ mol⁻¹ higher in energy (Figure 9.6c), outside the energetic range that would be observable in small molecule crystal structures.⁴⁴ This gave an indication of the strength of oxygen atoms on the --NO_2 group to interfere with the urea-tape packing motif.

For gelator **2**, the influence of molecular flexibility on the predictions was subtler. Here, freedom of the molecule to distort from its gas phase geometry led to some low energy structures with planar urea tapes (Figure 9.6e), whereas these interactions were twisted or buckled in the best structures generated with the rigid gas phase geometry (Figure 9.6d,f).

The difference in lattice energies of the most stable predicted structures of each gelator (-198.8 kJ mol⁻¹ for **1** *vs.* -176.7 kJ mol⁻¹ for **2**) further highlighted the strength of the urea $\cdots\text{O}_2\text{N}$ interaction. The calculated lattice energies of the lowest energy urea-tape structures of each molecule, as shown in Figure 9.6c *vs.* Figure 9.6d, were remarkably similar. Various types of interactions were present in these systems, including hydrogen bonding and van der Waals interactions, which could be maximised by stacking of the aromatic rings and aligning of molecular tails. Consequently, all of the low energy structures in the CSP were densely packed. It was observed, though, that in the systems of gelator **2** all of the types of interactions were associated within a pair of neighbouring molecules, *i.e.*, they had a tendency to align tails, urea groups and aromatic groups in series, a behaviour that is thought to be associated with the formation of a self-assembled fibrillar network (SAFiN) in gels. Contrarily, for gelator **1**, there was instead a strong interaction between the urea and the --NO_2 group of molecules, but these two molecules could not then align their tails and arrange aromatic groups into π -stacks (Figure 9.6a,b). These CSP results suggested that, rather than the acidity of the urea group determining the difference in behaviour of **1** and **2**, it was the compromise between sources of strong interaction that may have caused the differing observations in gel formation.

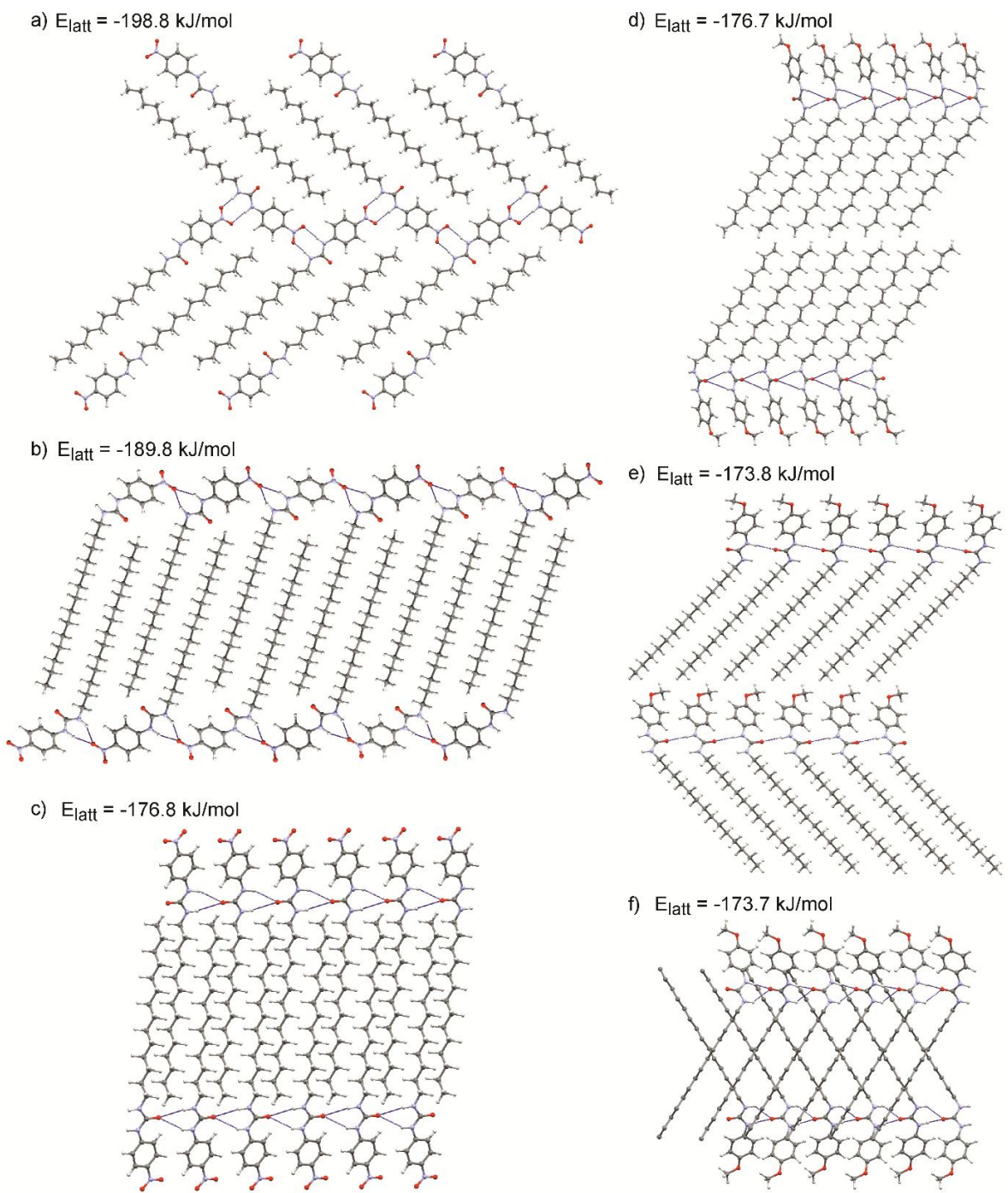


Figure 9.6. Molecular packing in representative low energy predicted crystal structures of **1** (**a, b, c**) and **2** (**d, e, f**), with the corresponding calculated lattice energies of each structure. **a)** and **d)** are the global minimum energy crystal structures that have been located for each molecule. Hydrogen bonds are shown as dashed blue lines. Hydrogen atoms on the alkyl chains are hidden in **(f)** for clarity.

9.2.3. Determination of the packing motifs of the gel fibres

PXRD studies were conducted to find experimental evidence to support the previous conclusions. The observation of diffraction peaks in PXRD patterns (Figure 9.7) acquired on gel samples without removing any amount of solvent confirmed the presence of semicrystalline structures, attributed to the gel fibres.

The comparison between the simulated and observed diffraction patterns must take into account the expected discrepancies between the lattice parameters of modelled structures and packing in the gel fibres, which are usually a few percent in lattice parameters, as well as differences in reflection intensities caused by orientation of the gel fibres. Nevertheless, several of the predicted crystal structures for each molecule were identified as giving similar simulated diffraction patterns to those observed from the gels (Figure 9.7). The simulated patterns are not expected to match perfectly the observed patterns as these are not well-ordered crystals.

Diffraction data supported the conclusions from structure prediction calculations: for gelator **2**, those structures that included hydrogen bond urea tapes gave similar PXRD patterns, whereas urea-nitro hydrogen bonding was present in all structures of gelator **1** that gave good agreement with the experimental diffraction pattern. These included the lowest energy predicted structures of each molecule (Figure 9.6a: $-198.8 \text{ kJ mol}^{-1}$ for **1** and Figure 9.6e: $-176.8 \text{ kJ mol}^{-1}$ for **2**).

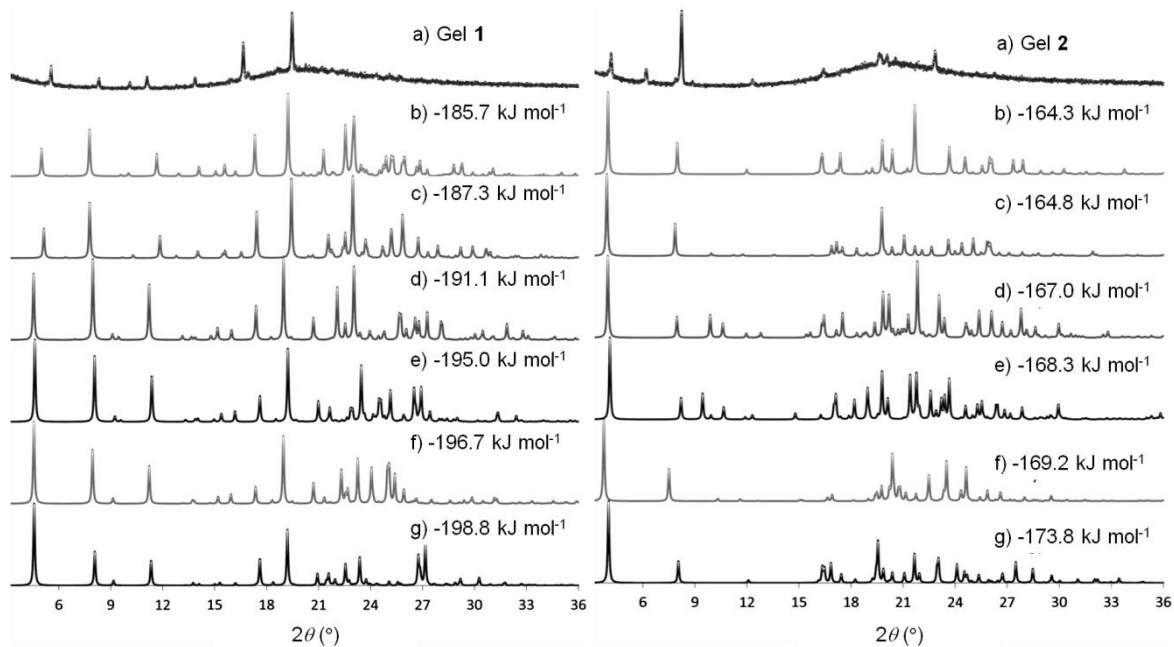


Figure 9.7. PXRD patterns of a) the organogel samples of **1** and **2** in DMSO (30 mg mL⁻¹), compared to b-g) the simulated diffraction patterns from the six lowest energy predicted crystal structures, all of which contained urea-nitro (N-H···O) hydrogen bonding for **1** and urea-urea hydrogen bonding for **2**. The simulated patterns from the predicted structures are labelled by their calculated lattice energies.

9.2.4. Assessment of the local environments of rigid components of gels by NMR

The multiphasic character of these materials required both solution and solid-state NMR spectroscopy to probe mobile and rigid components of the gel network, respectively. NMR studies were carried out with organogels and xerogels prepared from DMSO to avoid overlapping of aromatic peaks with solvent peaks from toluene and tetralin.

¹H-¹³C CP/MAS NMR experiments were used to study the molecular packing of the gel fibres. Despite the presence of high contents of solvent which was expected to lead to increased mobility and reduced efficiency of polarisation transfer, I was able to acquire ¹H-¹³C CP/MAS NMR spectra of organogels **1** and **2** (Figure 9.8 and Figure 9.9, respectively). The detection of peaks in ¹H-¹³C CP/MAS NMR spectra of these gels was indicative of a rigid 3D fibrous network, with densely packed molecules as predicted by molecular modelling studies. These are rare examples of supramolecular gels in which ¹H-¹³C CP/MAS NMR peaks were detectable without any physical modification of the organogel samples, *i.e.* removing any amount of the solvent or lowering the temperature.^{129, 132, 278}

For organogels **1** and **2**, aliphatic carbons appeared as sharp resonances, while low intensity peaks were observed for the aromatic and carbonyl carbons (and $-\text{OCH}_3$ carbon in organogel **1**) in the spectra measured at 298 K and 1 kHz MAS rate, as shown Figure 9.8a and Figure 9.9a. The presence of sharp peaks was in agreement with the semicrystalline fibres identified in PXRD experiments. Lowering the temperature to 288, 283, 278 and 273 K enabled us to record ^1H - ^{13}C CP/MAS NMR spectra at higher MAS rates, as shown in Figure 9.8b-g and Figure 9.9b-g. This led to significant narrowing of the aromatic and carbonyl carbons (and $-\text{OCH}_3$ carbon in organogel **2**), with spinning sidebands present in accordance with the specific MAS rate. No significant differences were observed for the chemical shift values in the spectra acquired at lower temperatures.

Regarding organogel **1**, the ^1H - ^{13}C CP/MAS NMR spectrum of frozen organogel **1** acquired at an MAS rate of 8 kHz (Figure 9.8g) presented a single peak per carbon, indicative of one magnetic environment for each carbon site. Peaks at 125.7 and 117.2 ppm resulted from overlapped resonances of carbons C_2 and C_6 , and C_3 and C_5 , respectively, as predicted by solid-state DFT calculations. The variation of chemical shift values between the reference solid powder **1** (Figure 9.8h) and the resulting organogel suggested the molecular organisation of the gel fibres was different from the original solid powder.

In contrast to organogel **1**, frozen organogel **2** acquired at an MAS rate of 8 kHz (Figure 9.9g) showed several peaks per carbon in the aromatic region, indicating the same carbon experienced different magnetic environments in different molecules. These results suggested the presence of multiple symmetrically independent gel molecules in the structure. Structures with multiple independent molecules ($Z' > 1$) are not uncommon in molecular crystals and it is not surprising that this phenomenon carries over to gel fibre packing.²⁷⁹ This observation reflects the symmetry of molecular packing and does not imply a less organised structure. However, this finding does mean that the packing in the organogel **2** fibres cannot be perfectly described by any one of the predicted crystal structures, since the molecular modelling studies were conducted considering only one molecule in the asymmetric unit ($Z' = 1$). ^{13}C chemical shifts for the aromatic carbons of gelator **2** were significantly shielded in comparison with gelator **1** (except C_4 , which was directly bonded to an oxygen), supporting the DFT predictions of a more negative electrostatic potential in the π -electron region of the aromatic ring. Furthermore, the similarity in chemical shift values of the reference solid powder **2** (Figure 9.9h) and the

resulting organogel pointed towards a self-assembled network with a 3D organisation similar to that of the crystalline powder.

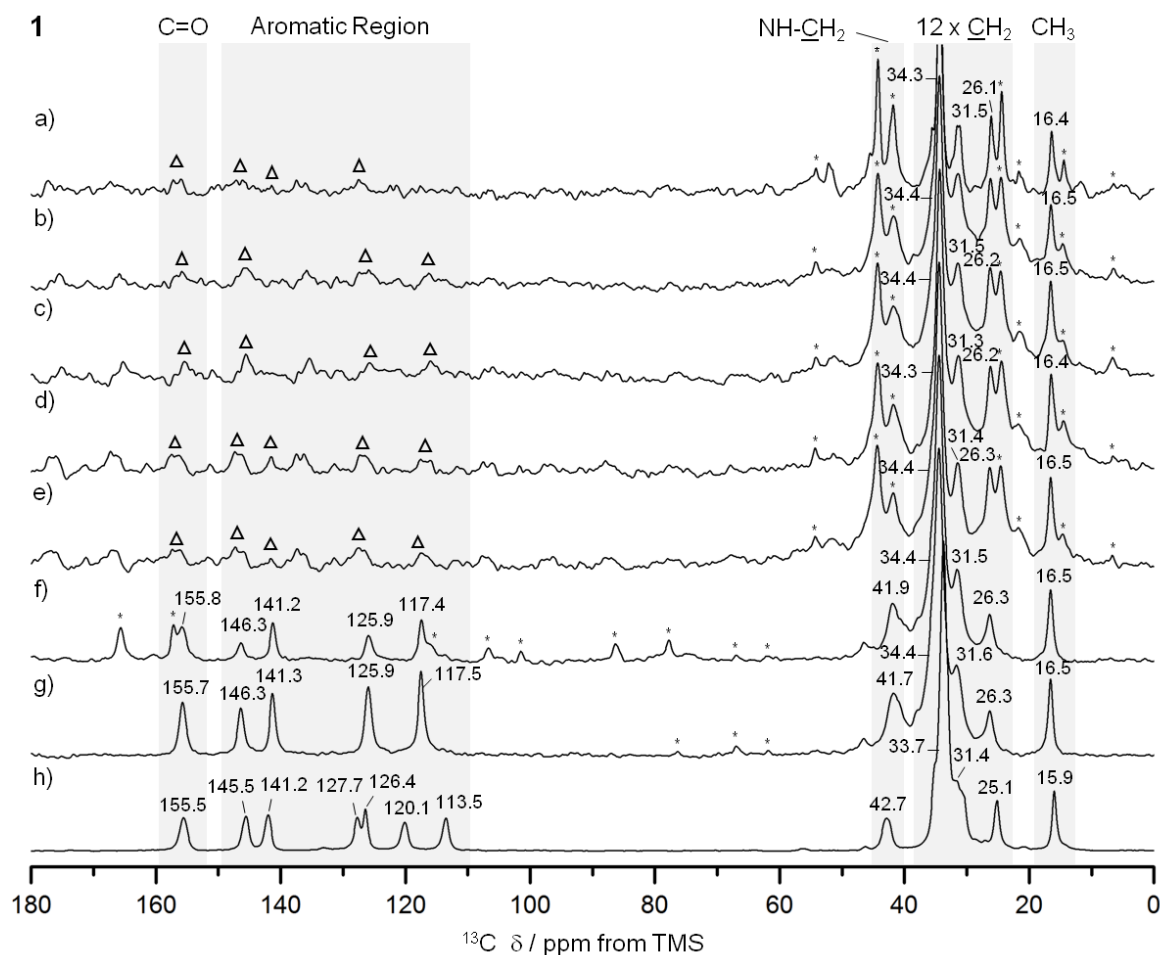


Figure 9.8. ¹H-¹³C CP/MAS NMR spectra of organogel **1** (30 mg mL⁻¹ in DMSO-*d*₆) acquired **a**) at 298 K and 1 kHz MAS rate; frozen gel samples acquired at **b**) 288 K, **c**) 283 K and **d**) 278 K and 1 kHz MAS rate; frozen gel samples acquired at 273 K and **e**) 1 kHz, **f**) 4 kHz and **g**) 8 kHz MAS rates; and **h**) reference solid powder measured at 298 K and 10 kHz MAS rate. All experiments were acquired with a recycle delay of 20 s, 1024 scans and $\pi/2$ pulse lengths of 4.0 μ s (¹H) and 3.0 μ s (¹³C), using a 400 MHz solid-state NMR spectrometer. Low-resolution aromatic peaks are highlighted with triangles and spinning sidebands with asterisks.

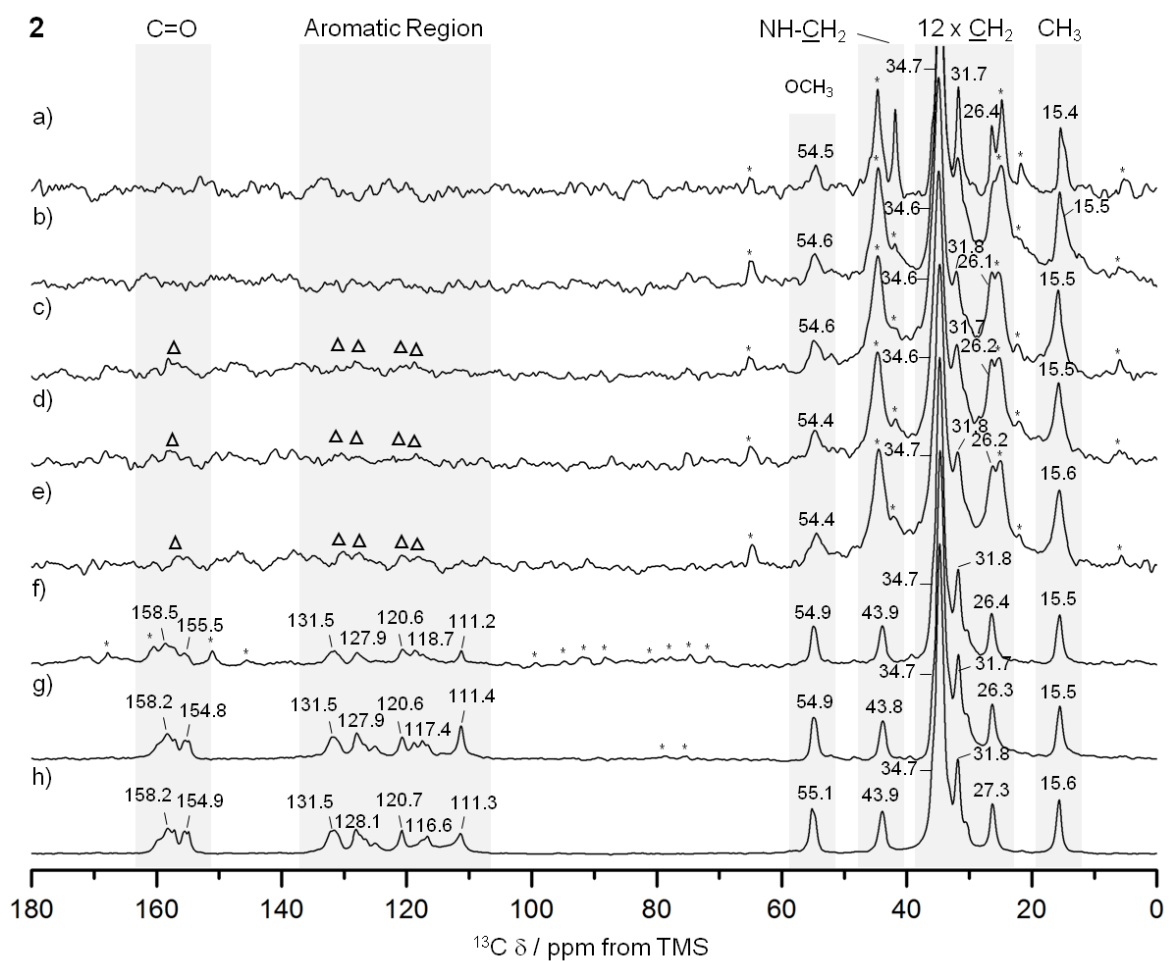


Figure 9.9. ^1H - ^{13}C CP/MAS NMR spectra of organogel **2** (30 mg mL $^{-1}$ in $\text{DMSO-}d_6$) acquired **a**) at 298 K and 1 kHz MAS rate; frozen gel samples acquired at **b**) 288 K, **c**) 283 K and **d**) 278 K and 1 kHz MAS rate; frozen gel samples acquired at 273 K and **e**) 1 kHz, **f**) 4 kHz and **g**) 8 kHz MAS rates; and **h**) reference solid powder measured at 298 K and 10 kHz MAS rate.

NMR chemical shielding calculations were then carried out by Prof. Day's group on sets of the lowest energy predicted crystal structures of gelators **1** and **2** using CASTEP¹⁶² and the GIPAW²⁸⁰ methodology. These gave reasonable agreement with the gel X-ray diffraction patterns (Figure 9.7). Despite the similarities in intermolecular interactions, reasonable variation was found in the chemical shifts predicted from the selected structures (Table 9.2 and Table 9.3). Amongst these structures, the simulated ^{13}C chemical shifts for the lowest energy predicted structures (-198.8 kJ mol $^{-1}$ for **1**, reported in Figure 9.6a, and -176.8 kJ mol $^{-1}$ for **2**, reported in Figure 9.6e) were found to be in best agreement with the ^{13}C chemical shift values observed for gel fibres (Figure 9.10), with RMSD (predicted – observed) of 1.8 ppm for **1** and 1.4 ppm for **2**. These deviations were as low as those seen in comparing observed ^{13}C chemical shifts with those predicted from known

single-crystal structures of small organic molecules.²⁸⁰ These results strongly supported the relevance of the predicted structures in interpreting the properties of the two gelators.

Table 9.2. Experimental ¹³C chemical shift values (δ) for frozen organogel 1 measured at 298 K and an MAS rate of 8 kHz *vs.* calculated values for the six lowest energy predicted crystal structures.

Assignment	Reference solid powder	Gel 273 K 8 kHz	Organogel 1 ¹³ C δ / ppm from TMS					
			-198.84	-196.70	-195.02	-191.14	-187.27	-185.73
Carbonyl	155.5	155.7	149.2	151.4	153.0	152.2	148.5	148.7
C₁	145.5	146.3	148.8	149.9	152.2	150.9	148.4	147.7
C₄	141.2	141.3	137.7	137.5	139.7	138.0	135.4	135.7
C₂	127.7	125.9	127.7	129.5	130.9	129.9	126.6	126.0
C₆	126.4		126.9	128.1	129.0	128.2	126.1	125.7
C₃	120.1	117.5	118.8	118.8	120.0	118.3	116.0	117.0
C₅	113.5		118.1	117.4	122.0	120.2	117.2	116.8
NHCH₂	42.7	41.7	41.4	41.7	42.1	41.5	40.3	38.5
11 x CH₂	33.7	34.4	33.9	34.2	35.5	35.4	32.5	33.0
CH₂CH₃	25.1	26.3	26.1	27.5	29.1	28.3	24.9	24.9
CH₃	15.9	16.5	16.5	16.5	16.5	16.5	16.5	16.5
RMSD	-	-	1.83	2.13	2.62	2.33	2.57	2.37

Table 9.3. Experimental ^{13}C chemical shift values (δ) for frozen organogel **2** measured at 298 K and an MAS rate of 8 kHz *vs.* calculated values for the six lowest energy predicted crystal structures.

Assignment	Reference solid powder	Gel 273 K 8 kHz	Organogel 2 ^{13}C δ / ppm from TMS						
			Calculated structures / kJ mol^{-1}						
			-173.78	-173.69	-169.17	-168.26	-167.00	-164.75	-164.33
Carbonyl	155.5	154.8	153.6	155.2	156.9	155.9	157.7	154.4	158.9
C₄	158.2	158.2	155.2	156.7	157.2	157.1	160.8	155.9	158.4
	157.1	157.0							
C₁	131.6	131.5	130.9	131.9	135.5	132.6	136.0	135.0	134.4
C₂	128.1	127.9	123.2	127.5	130.2	125.6	126.1	125.6	127.6
	125.0	125.0							
C₆	120.7	120.7	122.1	121.5	125.4	124.9	125.1	122.9	124.5
C₃	116.6	118.8	116.9	121.3	121.8	121.2	123.1	121.6	121.8
		117.4							
C₅	111.3	111.3	110.1	117.4	116.2	116.3	119.0	112.9	115.3
OCH₃	55.1	54.9	54.9	56.1	58.6	59.2	61.0	57.6	59.1
NHCH₂	43.9	43.8	40.9	42.7	45.9	42.1	46.8	42.7	44.6
11 x CH₂	34.7	34.7	34.7	34.1	35.2	35.3	38.7	35.5	38.2
CH₂CH₃	26.3	26.3	26.3	22.7	30.4	29.2	34.1	30.4	31.6
CH₃	15.6	15.5	15.5	15.5	15.5	15.5	15.5	15.5	15.5
RMSD	-	-	1.44	1.84	2.64	3.19	4.44	1.92	3.43

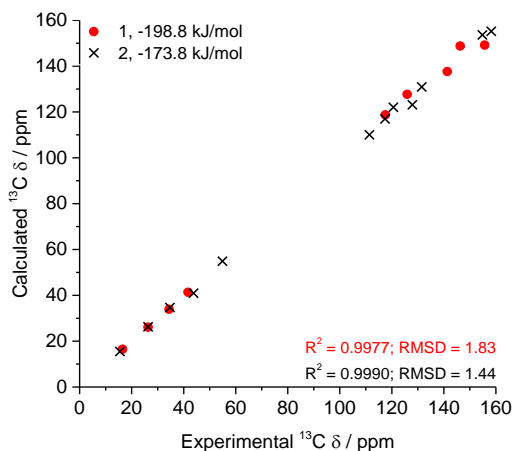


Figure 9.10. Experimental ^{13}C chemical shift values (δ) for frozen gels **1** and **2** measured at 298 K and an MAS rate of 8 kHz *vs.* calculated values for the predicted structures that give best agreement with both NMR and PXRD studies from the gel. Calculated isotropic chemical shieldings were converted to chemical shifts by matching the calculated and observed chemical shift of the CH_3 carbon in gel. The structures for gelators **1** and **2** correspond to those reported in Figure 9.6a and e, respectively.

The increased resolution obtained for the aromatic and carbonyl carbons (and $-\text{OCH}_3$ carbon in organogel **2**) upon spinning at higher MAS rates, with no significant changes for the aliphatic carbons, strongly indicated that chemical shift anisotropy was considerable for the aromatic and carbonyl carbons (and $-\text{OCH}_3$ carbon in organogel **2**), even in the gel state. The solid-state DFT calculations of NMR parameters performed for the low energy predicted crystal structures confirmed that the anisotropy of the shielding tensors for the aromatic and carbonyl carbon atoms was much larger (in the range from 108 to 192 ppm) than for the aliphatic carbons (in the range from 19 to 43 ppm) for both gelators, supporting the previous conclusions. The $-\text{OCH}_3$ carbon in organogel **2** was narrower than the aromatic carbons, but the peak sharpened as a result of spinning faster, in agreement with the DFT calculated intermediate anisotropy of the shielding tensor (*ca.* 70 ppm). Hence, the significantly broadened peaks detected for the aromatic and carbonyl carbons at low MAS rates in ^1H - ^{13}C CP/MAS NMR spectra of gels **1** and **2** were most likely due to the high values of chemical shift anisotropy for these carbon sites.

9.2.5. Investigation of the local environments of mobile components of gels by NMR

The increased acidity of the urea group predicted for gelator **1** using DFT calculations was confirmed by the downfield ^{15}N chemical shift observed in solution for the urea nitrogen atoms of organogel **1**, in comparison with organogel **2** (Table 9.4). This deshielding effect was a consequence of a nearby electron withdrawing nitro head group. ^{15}N chemical shift values of solutions and gels did not show any significant difference, due to the detection of mainly free gelator molecules in both samples, which prevented any conclusions to be drawn on the environment of NH groups in the gel state.

Table 9.4. Experimental ^{15}N NMR chemical shift values (δ) from 2D ^1H - ^{15}N HSQC experiments for gelators and organogels **1** and **2** (30 mg mL $^{-1}$ in DMSO-d $_6$) measured at 298 K with a recycle delay of 2 s and 8 scans, using an 800 MHz solution-state NMR spectrometer.

		^{15}N δ / ppm from liquid NH_3	
		Gel	Solution
1	NH_a	130.71	130.71
	NH_b	112.26	112.26
2	NH_a	125.39	125.39
	NH_b	101.63	101.63

9.2.6. Identification of spatial connectivities in the gel state

2D ^1H - ^1H NOESY solution-state NMR experiments provided information on spatial connectivities between molecular regions in aggregated states.¹²³ Cross-peaks in 2D ^1H - ^1H NOESY spectra of gels **1** and **2** displayed the same phase as the diagonal peaks (Figure 9.11) indicative of negative nOe enhancements, which are characteristic of large molecules. Since these systems are exclusively formed of small gelator molecules (< 400 Da), these negative enhancements can be attributed to medium-to-large supramolecular aggregates,²⁶³ which are the building blocks required for gel formation. Therefore, NOESY experiments allow the probe of interactions responsible for determining the gel network.

As shown in Figure 9.11, the cross-peaks between the $-\text{CH}_3$ protons of the alkyl chain and the aromatic and urea ones were identified in organogel **1**, whereas they were not detected for gel **2**. The presence of such cross-peaks in organogel **1** revealed close proximity between the end of the aliphatic chain, the benzene ring and the urea moiety (Table 9.5) belonging either to the same or to surrounding molecules. Such an arrangement was suggested by CSP calculations, indicating that the urea $\text{H}\cdots\text{O}_2\text{N}$ interaction led to interdigitation of the aliphatic chains, as shown in Figure 9.6a,b, which placed the end of the chain near to the aromatic rings of neighbouring molecules. Furthermore, intermolecular cross-peaks between distant NH_a and H_c or H_d (Figure 9.11) suggested proximity of the aromatic ring to another molecule with a different orientation.

Conversely, the absence of cross-peaks between the alkylic $-\text{CH}_3$ protons, the aromatic, the urea and the $-\text{OCH}_3$ sites in organogel **2** confirmed a well-aligned network in which the long aliphatic chains were positioned separately from aromatic and urea groups. In addition, the absence of cross-peaks between NH_a and H_c or H_d was also in agreement with the predicted, well-defined stacking of the aromatic rings in the 3D network of organogel **2**.

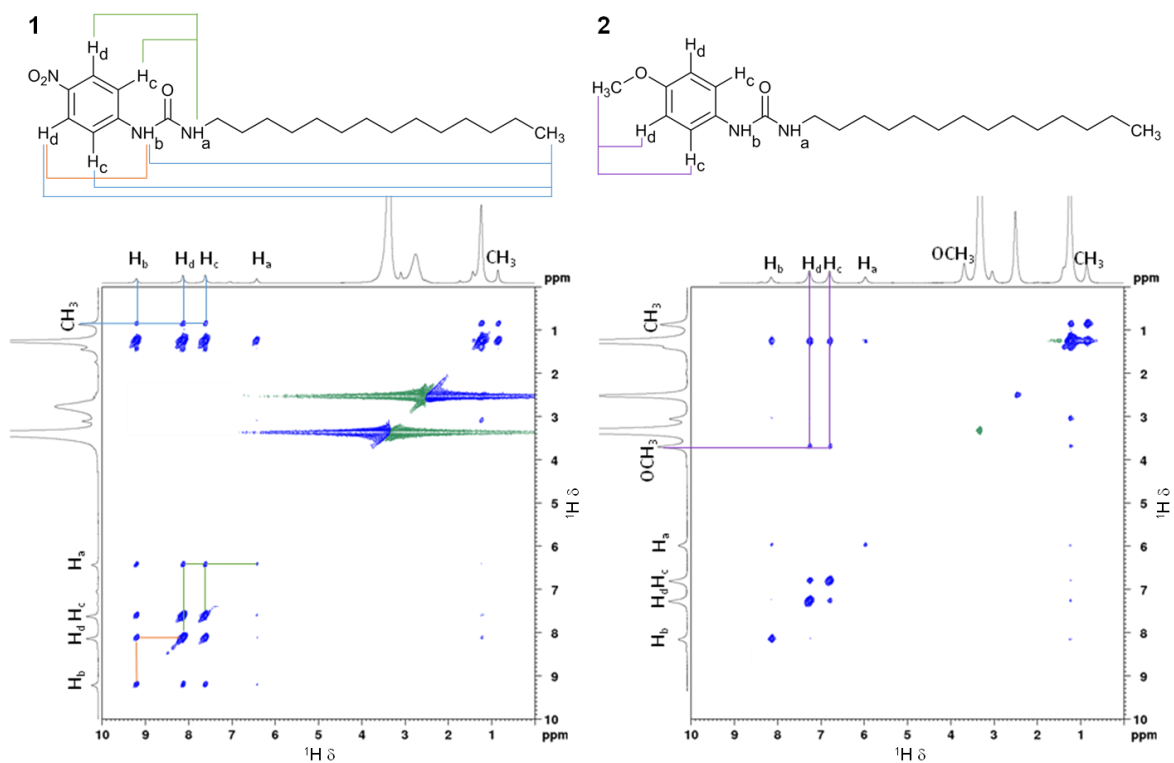


Figure 9.11. 2D ^1H - ^1H NOESY spectra of organogels **1** and **2** (30 mg mL $^{-1}$ in DMSO-d_6) measured at 298 K with a mixing time of 0.5 s, a recycle delay of 2 s and 32 scans, using an 800 MHz solution-state NMR spectrometer. Relevant cross-peaks have the corresponding spatial connectivity assigned (coloured lines).

The cross-peaks observed between the $-\text{CH}_2$ and the aromatic protons in organogel **2** (Figure 9.11) do not contain structural information, as they resulted from indirect nOe enhancements caused by a network of strong ^1H - ^1H dipolar couplings (spin diffusion), only observable at long mixing times (Figure 9.12).

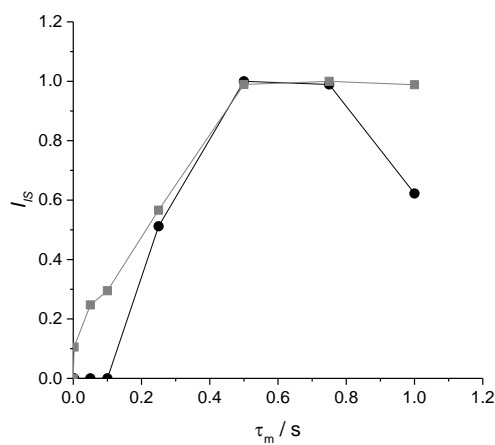


Figure 9.12. Evolution of normalised nOe enhancements (I_{ls}) with mixing time (τ_m) for the cross-peaks between $\text{H}_c\text{-H}_a$ (grey squares) and $\text{NH}_2\text{-H}_a$ (black circles) in organogel **2**, highlighting the characteristic lag time of indirect nOe enhancements.

Internuclear distances were thus calculated (Table 9.5) according to the initial rate approximation, which is described in Chapter 2, section 2.3.16.3, page 116. This methodology establishes that the initial build-up of nOe enhancements with mixing time is approximately linear.¹⁵² The relationship between nOe intensity and internuclear distance allowed the observed nOe intensities to be calibrated relative to a known internuclear distance (H_c–H_d) within the supramolecular system.^{148, 152, 153}

Table 9.5. Intermolecular distances calculated from initial rates of nOe build-up curves with mixing time, using the H_c–H_d distance as reference.

Pair of protons	Organogel 1			Organogel 2		
	σ_{IS} / s^{-1}	$\delta / \%$	r / Å	σ_{IS} / s^{-1}	$\delta / \%$	r / Å
H _c / H _d (ref) ^a	0.99	0.155	2.49	0.40	0.106	2.47
NH _a / NH _b	0.44	0.051	2.85	0.37	0.071	2.50
CH ₃ / H _c	0.04	0.005	4.24	-	-	-
CH ₃ / H _d	0.05	0.004	4.11	-	-	-
CH ₃ / NH _a	0.06	0.004	4.03	-	-	-
CH ₃ / NH _b	0.04	0.014	4.31	-	-	-
NH _a / H _c	0.09	0.030	3.74	-	-	-
NH _a / H _d	0.11	0.039	3.58	-	-	-
NH _b / H _c	0.24	0.063	3.16	-	-	-
NH _b / H _d	0.15	0.021	3.40	-	-	-

^a Distance used as reference

9.3. Concluding remarks

I believe the main aim of this work was met since molecular level understanding of differences observed in gelation performance of urea gelators with electron-withdrawing (–NO₂) or electron-donating (–OCH₃) head substituents was provided. Critical gelation concentration values revealed remarkable gelation performance in the presence of the electron donating group –OCH₃, in comparison with the –NO₂ head group. Gelator **2** showed increased tendency to self-assemble, increased strength of gel fibres and a more fibrillar network, in clear contrast with the analogue **1**. The thermo-mechanical and morphologic differences identified between both systems reflected the influence of the head group in the supramolecular packing of the corresponding gelator molecules.

DFT calculations revealed a slightly more positive electrostatic potential at the polar hydrogen atoms of the urea group in **1** compared to **2**. This increased acidity of the urea

hydrogen atoms had the potential to enhance the formation of urea tapes in **1**. However, the introduction of a region of negative charge at the $-\text{NO}_2$ substituent consequently made oxygen atoms from this group particularly accessible. This allowed them to compete with the urea oxygen as hydrogen bond acceptors for the protons of the urea group. CSP calculations showed that the low energy structures of **1** lacked the $\text{N}-\text{H}\cdots\text{O}_{\text{urea}}$ hydrogen bonding. Instead, urea-nitro hydrogen bonding was present in all structures of gelator **1** that matched the observed powder diffraction pattern. The chemical shifts generated from these calculated structures were in excellent agreement with the experimentally determined ^{13}C chemical shifts from CP/MAS solid-state NMR studies. Moreover, the presence of cross-peaks in NOESY spectra of organogel **1** between the $-\text{CH}_3$ protons of the alkyl chain and the aromatic and urea ones revealed close proximity between the end of the aliphatic chain, the ring and the urea moiety belonging either to the same or to surrounding molecules. This provided experimental evidence that the $\text{NO}_2\cdots\text{H}_{\text{urea}}$ strong interaction led to interference of urea tape formation by the $-\text{NO}_2$ group. This was responsible for disrupting the order of supramolecular packing and giving rise to a rheologically weaker and less organised material.

Contrarily, a more negative electrostatic potential in the π -electron region of the aromatic ring was found for gelator **2** in DFT studies. The low energy predicted structures from CSP calculations of gelator **2** displayed hydrogen bonding between urea groups, predominantly forming unidimensional urea tapes, and showed a tendency to align tails, urea groups and aromatic groups in series. All structures that produced simulated patterns similar to PXRD patterns included hydrogen bonded urea tapes. The chemical shifts generated from these calculated structures were in excellent agreement with the experimentally determined ^{13}C chemical shifts from CP/MAS solid-state NMR studies. In addition, the absence of cross-peaks in 2D NOESY spectra of organogel **2** between the alkylic $-\text{CH}_3$ protons, the aromatic, the urea and the $-\text{OCH}_3$ sites proved a well-aligned network was formed, in which the long aliphatic chains were positioned separately from the aromatic and urea groups, which explained the gel increased strength and thermal stability.

Henceforth, I suggest that the availability of substituent groups to form competing interactions must be considered in any programme of rationally designed self-assembling building blocks.

Chapter 10

10. General discussion and conclusions

Despite the wide range of existing and potential applications of supramolecular gels, fundamental understanding of the mechanism of formation of their complex fibrous networks is still limited. In addition, the correlation between molecular structure of gelator, conditions of assembly and self-assembled structure remains unclear. Such knowledge is of paramount importance to predict behaviour, design and control the properties of these materials for specific applications.

One of the main challenges regarding the characterisation of supramolecular gels is how to efficiently probe and determine structure of such heterogeneous, disordered and dynamic materials. Herein, a general approach is presented for the study of supramolecular gels developed using gels of amino acids and urea derivatives as model materials, giving special emphasis to NMR spectroscopy.

10.1. Structure and dynamics of gel-crystallisation of Phe

To date, Phe is one of the smallest molecules known to form supramolecular hydrogels and it is of a particular interest due to its crystalline gel state.²¹² Although the groups of Gazit, Khushalani, Thakur, Bowers, Hansmann and Harris have contributed for a better understanding of the early stages of aggregation, intermolecular interactions and structure of the gel fibres of Phe, the supramolecular packing motifs and dynamics of the resulting hydrogels remain unclear.

The “gel-crystallisation” phenomenon described by Myerson²¹² was confirmed by the determination of the structure of the gel fibres as being the crystalline monohydrate form of Phe, using single-crystal and powder XRD and ¹H-¹³C CP/MAS solid-state NMR experiments performed directly on the hydrogel fibres. In addition, ¹H solution-state NMR chemical shift values, coupled to molecular modelling optimisations, showed how the electrostatic interactions of the zwitterionic Phe molecule lead to anisotropic assembly and consequently fibre formation, having hydrogen bonding and hydrophobic

interactions as secondary stabilising interactions. These findings contradicted previous reports by Thakur²⁰⁸ and Mossou⁶⁶. From a dynamic perspective, the evolution of ¹H peak intensities and ¹H T₁ relaxation times throughout aggregation processes at increasing concentration and at variable temperature revealed the formation of a supersaturated solution that immediately precedes gelation. Moreover, these studies showed Phe gels were dominated by fast exchanging processes of molecules at the interfaces (on the NMR relaxation time scale).

10.2. The effects of structural modifications of Phe

The understanding gained on the crystal packing of fibres, non-covalent driving forces and dynamic processes of self-assembly of Phe enabled strategies of controlling self-assembly processes and tuning gel properties of the resulting materials to be investigated. It was discovered that the introduction of substituents to the aromatic ring of Phe resulted in a significant variation of hydrogelation properties (Table 10.1). These structural variations had a large impact in kinetics of nucleation and supramolecular aggregation of Phe derivatives in water.

Table 10.1. Gelation results, critical gelation concentration (CGC) and water solubility (s_{water}) of Phe and its derivatives at 298 K, organised in descending order of gelation ability.

Compound	Product	CGC / mM	s _{water} / g L ⁻¹ , 298 K
NH ₂ -Phe	Gel	388	39.01
Phe	Gel	210	29.60
F-Phe	Gel	160	18.59
2F-Phe	Gel	140	2.08
Cl-Phe	Gel	100	0.96
2Cl-Phe	Gel	85	0.24
5F-Phe	Gel	80	0.33
Br-Phe	Metastable gel	40	0.47
Tyr (Phe-OH)	Insoluble/precipitate	-	0.45
I-Phe	Insoluble/precipitate	-	0.15

The introduction of a hydroxyl group to the *para*-position of Phe (Tyr) resulted in a poorly water soluble compound ($s_{\text{Tyr}} = 0.45 \text{ g L}^{-1}$ at 298 K), which fully prevented its hydrogelation. Despite Tyr not being able to create SAFiNs capable of entrapping the totality of the solvent, the ability of tyrosine to participate in unidirectional anisotropic interactions forming well-ordered fibrillar nanostructures has been reported previously.²⁸¹ This is consistent with the fact that tridimensional fibre branching and entanglement ultimately determines whether a self-supporting material is formed or, instead, the fibres precipitate out of solution.⁶⁸

The addition of halogen atoms resulted in a general improvement of the hydrogelation ability and the mechanical properties of the resulting gels, due to decreased water solubility. The increased strength of intermolecular interactions from Phe to fluoro and chloro derivatives was reflected by their faster kinetics of gelation, lower CGC values (Table 10.1) and slower dynamics of exchange at the gel/solution interfaces. The slower rates of exchange of F-Phe and Cl-Phe gelators relative to Phe was reflected by the observation of a dispersion of $^1\text{H} T_1$ times in the gel state (contrarily to Phe), coupled to the very low fractional STD response that decreased further as temperature was increased. Detailed description on how dynamics of exchange modulates $^1\text{H} T_1$ values and STD response is found below (sections 10.7 and 10.8, respectively). Regarding the bromo and iodo derivatives, there was a stepped change with the addition of Br or I to the *para*-position on the aromatic group, with the formation of dominant type II halogen-halogen interactions preventing formation of stable gel materials. This behaviour was different to that observed for the Fmoc-Phe derivatives, where gelation still occurred for Br and I derivatives, as the hydrophobic Fmoc group is a strong driving force of gel formation.²³²⁻²³⁴

In contrast to the fluoro and chloro derivatives of Phe, upon the addition of a strongly hydrophilic amine group to the *para*-position of the benzene ($\text{NH}_2\text{-Phe}$), there was a decline in the hydrogelation ability due to its increased water solubility ($s_{\text{NH}_2\text{-Phe}} = 39.01 \text{ g L}^{-1}$ at 298 K). This contributed to slower kinetics of fibre growth and resulted in the formation of much shorter fibres. The tridimensional ordering of these needle-like crystalline fibres was determined successfully using single-crystal XRD, and confirmed by solid-state NMR experiments. The dispersion of $^1\text{H} T_1$ times in the gel state and the detection of higher STD_0 values at lower temperature (278 K) pointed towards the dynamics of interfacial exchange of $\text{NH}_2\text{-Phe}$ being faster than that of the hydrogel of Phe.

In conclusion, an inverse relationship was found between solubility and rate of exchange. Molecular solubility affects the strength of solute-solute and solute-solvent interactions. The strength of these intermolecular interactions then modulates the “residence” times of molecules at the interfaces and, consequently, determines the rate of the dynamic exchange processes that occur between gel and solution environments. In general terms, these findings showed how molecular structure determines supramolecular organisation of the gel fibres which, in turn, impacts on the interfacial properties, such as relaxation profiles and mobility of interfacial molecules.

10.3. Multi-component hydrogels of Phe

The introduction of co-gelators or non-gelating additive molecules has been reported previously in other gel systems to create an extra level of control and to allow tailoring of the physical properties of gels.^{51, 92} Henceforth, non-gelating additive molecules were introduced to Phe hydrogels (Leu, Ser, Tyr and Trp) (Figure 10.1a,b,c), but also investigated the modulation of multiple gelation processes upon the addition of a gelator that forms fibres isostructural to the monohydrate form of Phe (F-Phe), or upon the introduction of a gelator that gives rise to fibres with a supramolecular organisation different from that of Phe (high concentrations of NH₂-Phe) (Figure 10.1c). It was also found that certain additives have the ability to fully prevent gelation of Phe (low concentrations of NH₂-Phe) (Figure 10.1d). The molecules studied covered a wide range of structural diversity and water solubility, although several features were common to all systems, which are described below.

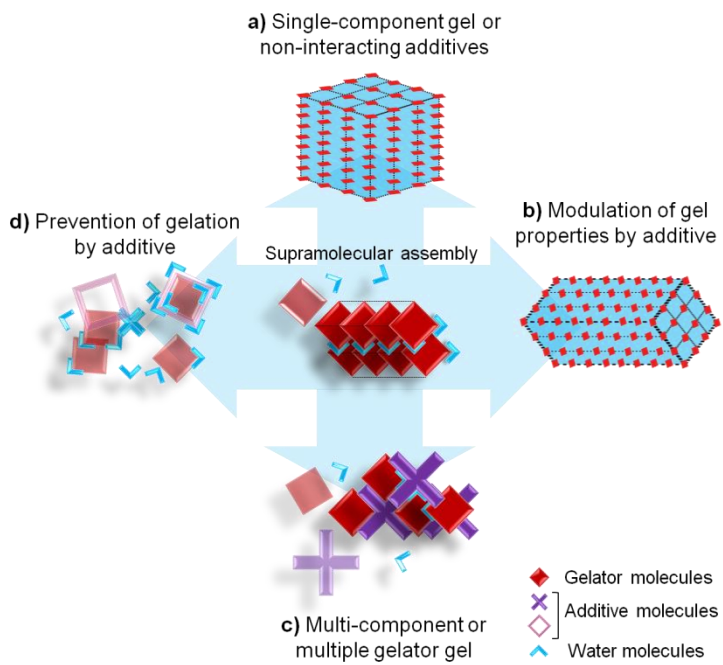


Figure 10.1. The introduction of additive molecules was investigated regarding their effects on the organisation of the 3D network. **a)** Representation of a single-component hydrogel (Phe) and introduction of a non-interacting additive (Leu). **b)** Modification of the gel properties resulted from the introduction of a partially disruptive additive (Ser). **c)** Representation of multi-component (Phe/Trp, Phe/Tyr) and multiple-gelator materials (Phe/F-Phe, Phe/NH₂-Phe). **d)** Gelation could be fully prevented upon the introduction of a disruptive additive (low concentrations of NH₂-Phe).

10.4. Tuning of rheological properties by preparation of multi-component hydrogels

Mechanical properties of gels are one of the most important features that determine the potential applications of the material. It was possible to alter the viscoelasticity of Phe hydrogels by the simple introduction of additive molecules, independently of their individual gelation abilities. The resulting mixed materials largely preserved the supramolecular arrangements of the fibrous structures of the pure hydrogels. The addition of Trp resulted in a higher content of molecules incorporated within the solid structures, detected by decreased ¹H peak intensities in solution-state NMR spectra and appearance of ¹³C peaks from the additive in ¹H-¹³C CP/MAS spectra. This most likely promoted the formation of an increased number of fibres and interfibrillar cross-links, which was reflected at larger scales by the formation of a material more resistant to deformation.

In contrast to this, the strength of Phe fibres decreased when the additive molecule (Ser or high concentrations of NH₂-Phe) led to an effectively lower concentration of Phe in the solid fibres. The evolution of ¹H peak intensities and line widths throughout the early stages of gelation processes of these mixed gels allowed the conclusion to be drawn that kinetics of gelation was slowed down in the presence of such additives. In addition, hydrogelation of Phe was fully prevented in the presence of NH₂-Phe at molar ratios between 1:0.2 and 1:1.3 (Phe/NH₂-Phe). All these data pointed towards the interference of Ser and NH₂-Phe with early nucleation and fibre-growth processes of Phe.

The aggregation processes of these mixtures were translated by variations on ¹Hs local magnetic environments, which were more marked for the aliphatic protons of Phe and NH₂-Phe, consistent with the very strong through-space nOe correlations observed. Thus, it was concluded that NH₂-Phe interferes with the electrostatic interactions occurring between Phe dimers, which are the anisotropic forces of self-assembly of Phe. This is plausible, as there is an initial indication from the analysis of the crystal structure of NH₂-Phe that electrostatic interactions play an important role in the formation of unidirectional assemblies of NH₂-Phe. To confirm that these are indeed the predominant intermolecular interactions dictating self-assembly of NH₂-Phe, it is aimed to generate an interaction energies framework using CrystalExplorer.

The potential that additive or guest molecules have in modulating mechanical properties of the gel fibres is very relevant in host-guest chemistry, particularly when supramolecular gels are used as biomedical vehicles for transporting drugs, growth factors and/or cells.

10.5. Modulation of the structure of the gel fibres and of interfacial dynamics in multiple gelator hydrogels

When two molecules capable of individually forming self-organised gel networks are mixed, the resulting multiple gelator materials can create several scenarios: formation of self-sorted separate orthogonal networks, formation of co-assembled fibres from intimately blended gelators, and/or formation of new architectures created due to the co-existence of both gelators.⁹⁴

Therefore, it was considered important to assess how the preparation of multiple gelator hydrogels from isostructural solid components (Phe and F-Phe) affected gel formation. The viscoelastic properties and supramolecular arrangements of the fibrillar structures of the pure and mixed hydrogels were very similar. A continuum of the unit cell parameters was determined from the PXRD patterns of the variable Phe/F-Phe ratios, which was consistent with the formation of co-assembled solid solution fibres. It is not unusual to observe formation of solid solutions when two compounds form isostructural crystalline phases and the molecules are of similar size. In addition, the detection of broad ^{13}C CP/MAS peaks and extra ^{19}F signals in mixtures confirmed the formation of new molecular environments within the rigid components. In combination with diffraction studies, the resolution gained using high-field ^{19}F NMR studies allowed it to be proved that Phe and F-Phe intimately interact in co-assembled fibres that retain the monohydrate form as the main building block.

Similarly, the self-assembly of mixtures of gelators that give rise to structurally different hydrogels (Phe and $\text{NH}_2\text{-Phe}$) was investigated. PXRD and ^1H - ^{13}C spectra of multiple gelator hydrogels of Phe/ $\text{NH}_2\text{-Phe}$ showed structure-determining gelation behaviour, in which the most abundant gelator dictates the supramolecular arrangement (one network templates the other). But when mixed at a 1:2 ratio (Phe/ $\text{NH}_2\text{-Phe}$), the crystal motifs of the mixed fibres were different from those of the pure gel fibres. The detection of broader ^{13}C CP/MAS peaks and additional $^{15}\text{NH}_3^+$ -Phe environments in the rigid fibres of multiple gelator hydrogels (when comparing with spectra acquired on the pure materials) resulted from an increased distribution of possible orientations due to the presence of considerably less ordered fibres. These data showed that the packing motifs of Phe were modified in the presence of the co-gelator $\text{NH}_2\text{-Phe}$, most likely resulting in co-assembled fibres structurally different from the supramolecular arrangements of the pure networks.

Summarising, strong experimental evidence was found for the mixed materials prepared from Phe and F-Phe or $\text{NH}_2\text{-Phe}$ that pointed towards formation of co-assembled gel fibres. This is not surprising, as Buerkle and Rowan (2012) proposed that similar gelator molecules present a thermodynamic preference to form mixed co-assemblies.⁵¹ However, it should be highlighted that PXRD and solid-state NMR studies only provide a general view of the several phenomena that might be present (co-assembly, self-sorting and/or new architectures). At the moment, it is still not possible to probe the existence of domains

nor the interaction between fibrils at larger length scales, as defended by Draper and Adams (2016).⁹⁶

Having a glance at the dynamic behaviour of these materials, multiple gelator hydrogels prepared from Phe, F-Phe and NH₂-Phe presented intermediate *D* values, ¹H *T*₁ times and fractional STD responses in solution-state and HR-MAS NMR experiments, when comparing with the values obtained for the pure materials. As discussed previously for Phe (section 10.2, page 267), such observations arise from the modification of the rate of exchange of molecules at the gel/solution interfaces. These findings highlighted the fact that the presence of co-assembled gel fibres has a strong effect in modulating the fibre/solution interfacial properties.

10.6. General strategy for the characterisation of supramolecular gels

The main outcome of these studies was the development of a general strategy for the characterisation of structurally and dynamically heterogeneous supramolecular gels. The protocol described below has been optimised for molecular gels and it was consistently validated by different molecular gelators in a variety of solvents, concentrations and self-assembly conditions. The applicability, advantages and limitations of each technique, which are highly dependent on the properties of the gel, were also discussed.

This methodology is based on the combination of microscopy, rheology, X-ray diffraction and computational techniques which help validate findings from NMR spectroscopy. The co-existence of different regimes of mobility (solid, semi-solid and liquid) was taken advantage of to utilise solution, solid-state and HR-MAS NMR experiments (Figure 10.2).

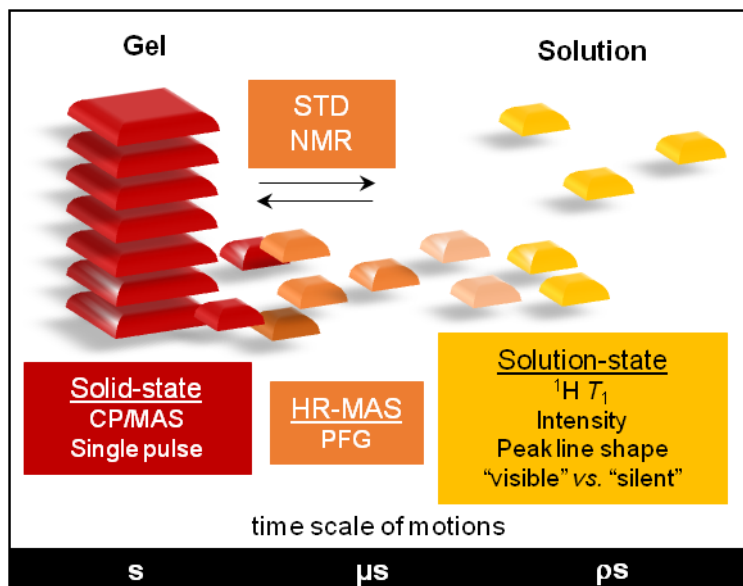


Figure 10.2. Schematic representation of the NMR methods optimised throughout these studies to probe different length scales of self-organisation and time scales of molecular motions in supramolecular gel materials.

Regarding the detection of rigid fibrous structures, the combination of NMR spectroscopy with computational and X-ray diffraction studies, designed as NMR crystallography, provided valuable insight into molecular level organisation, offering likely motifs of intermolecular packing and local structure in the gels. All the materials under study were composed of crystalline or semi-crystalline fibres. The presence of semi-ordered assemblies in supramolecular hydrogels is highly advantageous, as it enables the determination of the crystal structure by single-crystal XRD (for large and good quality crystals) and identification of the tridimensional organisation of the entire gel network by powder XRD. With this combined strategy, the crystal packing motifs of the crystalline hydrogel fibres of Phe, F-Phe, 2F-Phe, Cl-Phe and NH₂-Phe, and of the semi-crystalline organogel fibres of -NO₂ and -OCH₃ urea derivatives were confidently determined. However, this approach is not applicable when molecular gels lack well-ordered supramolecular structures, as the crystal structure prediction calculations generate perfectly crystalline arrangements. Even though first-principles computations have been optimised for small rigid molecules, their use in predicting organisation of complex flexible molecules has proven successful in surfactant-templated silicate frameworks without 3D periodicity.¹⁶¹ The combination of molecular dynamics and density function

theory calculations is now becoming an essential tool for the elucidation of structure of increasingly complex materials.

CP/MAS solid-state NMR experiments were used to detect the solid-like fibrous components without any physical modification of the gel samples, *i.e.* without removing any amount of the solvent or lowering the temperature. Despite the presence of high contents of solvent that were expected to lead to an increased mobility and a reduced efficiency of polarisation transfer, I was able to successfully acquire ^1H - ^{13}C CP/MAS NMR spectra on wet gel samples. ^1H - ^{13}C CP/MAS NMR spectra acquired on both wet and dry states showed similar chemical shift values and peak splitting patterns, proving that experiments conducted with dry samples can be indicative of the original structure of the hydrogel fibres, assuming validation is conducted on the native (wet) state using other methodologies.

The detection of semi-solid molecules at the interfaces between the solid fibres and the liquid pools of solvent required the use of PFG HR-MAS experiments. The small dimensions of the Phe derivatives became a limitation, as it was not possible to differentiate between the several motional regimes present in a molecule (solvent-exposed regions *vs.* regions deeply incorporated within the fibre). I believe this technique has its full potential in differentiating motional regimes of larger gelator molecules, as Iqbal *et al.* (2010) reported successful application of PFG HR-MAS in organogels of tetrapeptides.¹¹⁵

It should be noted at this point that when performing experiments under MAS the effects that the centrifugal forces have on the gel samples and NMR observables need to be considered, especially for rheologically weaker networks. Possible consequences include centrifugal disintegration of the sample, structural reorganisation of the network and local heating effects. Frictional heating affects molecular motions, consequently weakening dipolar couplings.¹⁴² Similarly, MAS modulates spin diffusion by averaging out of dipolar couplings, which modulates ^1H - ^{13}C CP/MAS, ^1H T_1 relaxation and nOe pathways, and promotes translational diffusion. Even though these factors do not prevent the attainment of good quality data, they should always be taken into account when interpreting data acquired under MAS.

Since only a fraction of gelator molecules is required for gel formation, ^1H solution-state NMR spectra of supramolecular gels frequently present well-defined peaks. These arise

from mobile molecules. To determine their structure and dynamics, one can rely on the characterisation of spectral variations, ^1H T_1 times and fractional STD response. The application of the last two experiments in molecular materials is discussed below in more detail (sections 10.7 and 10.8, respectively, pages 276 and 277). However, this approach has some limitations that should be accounted for during interpretation of data. The detection of good quality solution-state spectra is not always achievable, since the fraction of dissolved molecules can be below the limit of detection. In addition, determination of the concentration of molecules in solution is not always accurate in molecular gels. This is because NMR “silent” molecules are not necessarily within the rigid fibre (as they might exist in semi-solid interfacial regions) and the presence of dynamic exchange at the interfaces has the potential to give rise to a ^1H peak that is the average between both environments. The presence of molecules with these intermediate motions is manifested in solution-state NMR by the detection of considerably broadened ^1H peaks, which show similar ^1H T_1 times due to their strong homonuclear couplings and lead to the observation of negative intermolecular nOe correlations.

10.7. Interpretation of ^1H T_1 measurements in supramolecular gels

To understand dynamics of these materials, one of the key experiments is the determination of the dependence of ^1H T_1 times with increasing concentration of gelator and at variable temperature. VT NMR measurements of ^1H T_1 times indicated that Phe-based hydrogels were in the “fast tumbling regime”, also corroborated by the decreased line widths observed with increasing temperature.

Using ^1H T_1 times of Phe in solutions and hydrogels as an example, at low concentrations or at high temperatures (conditions in which a solution is present), there was a distribution of the relaxation times for different ^1H sites, which reflected differences in ^1H s local dynamics. The ^1H T_1 times of the aromatic and C_βH_2 protons were contrasted by the three-fold shorter T_1 values of neighbouring C_αH protons. This dispersion of T_1 values in solutions occurs because of the individual relaxation profiles of different protons. Upon the formation of the gel, ^1H T_1 relaxation times for different ^1H sites became similar. This reflected enhanced ^1H - ^1H spin diffusion as a result of restricted mobility of the gelator

molecules and corresponded to averaged values resulting from exchange phenomena of the gelator molecules between solution and gel states.

Moreover, three distinct stages in the temperature-dependent transformation of the hydrogel were identified. During stage I, the sample was in the gel state and ^1H T_1 times of Phe were similar for different ^1H sites. During stage II, a heterogeneous distribution of T_1 times typical of Phe solutions was observed, which reflected the disassembly of the network. As temperature was raised further, gradual dissolution of the fibres led to progressive destruction of the hydrogel, which finally resulted in the loss of structural integrity at the beginning of stage III. This temperature matched T_{gel} . The dispersion of these values increased with temperature as the dissolution of the supramolecular network weakened ^1H - ^1H dipolar couplings, making spin diffusion mechanisms less efficient.

More importantly, when assessing the incorporation of an additive molecule within the rigid fibres or determining if the additive contacted with the surface of the fibres, ^1H T_1 times enabled straightforward interpretation. A correlation between the distribution of ^1H T_1 times and the dynamics of exchange between gel and solution states was successfully established. Similar ^1H T_1 values are observed in the gel state for molecules experiencing fast exchange processes at the gel/solution interfaces (on the NMR time scale) (as Phe, Tyr and Trp). In contrast with this, a dispersion of ^1H T_1 values is observed in the gel state when there is detection of mainly free fast tumbling molecules. This can result from free molecules that do not participate in the formation of fibres (as Leu and Ser) or from molecules experiencing slow or very fast exchange processes at the gel/solution interfaces (on the NMR time scale) (as F-Phe, Cl-Phe and NH_2 -Phe). In conclusion, variations of ^1H T_1 times were correlated with molecular level events, highlighting the importance of longitudinal relaxation measurements in probing local molecular motions of dynamic soft materials.

10.8. Probing dynamic processes at the interfaces – the role of STD NMR

Saturation transfer difference NMR is becoming an increasingly important tool in the study of supramolecular gels.^{125, 149, 155, 156} STD NMR experiments have been used by Wallace *et al.* (2017) to characterise indirectly fibre surface properties, such as charge, hydrophobicity and ion-binding dynamics of hydrogels of *N*-functionalised dipeptides.¹⁵⁶

They measured and compared STD signals to assess the affinity of probe molecules for the gel fibres.¹⁵⁶ Similarly, STD NMR spectroscopy has been used to investigate the interaction of dopamine and related substances with amino acid based hydrogels.¹⁵⁵ These authors were also able to create a binding epitope of the interaction of these additives with the gelator molecules at the surface of the fibres.¹⁵⁵ In another study by Jiménez-Barbero and co-workers, STD NMR experiments were used to explore the molecular orientation of gelator molecules at the interfaces and the participation of solvent in aggregation processes of organogels prepared from *tert*-butyl esters of asparagine and tyrosine.²²⁵

Throughout the present work, the applicability of this technique has been expanded and its limitations in the study of molecular gels have been assessed. The evolution of fractional STD response with saturation time was found to be a powerful probe of the dynamics of exchange at the interfaces of supramolecular gels. When the rate of interfacial exchange is fast on the NMR relaxation time scale (as for the case of pure hydrogel of Phe), a mono-exponential evolution of the fractional STD response with saturation time is observed. When intermolecular interactions are strong and the dynamics of exchange is slowed down, the longer “residence” times of gelators locked onto the gel fibres prevents saturated molecules from returning to solution during the time of the experiment. This results in inefficient accumulation of saturation and leads to the detection of very low STD values, as in the case of the pure hydrogel of F-Phe. In contrast to this, when significantly weaker non-covalent interactions lead to much faster rates of exchange between gel and solutions, the transfer of saturation from the network to weakly bound molecules is inefficient and low fractional STD responses are also detected, which occurred in pure hydrogels of NH₂-Phe. Henceforth, VT STD NMR studies can help clarifying the regime present, due to the dependence of rates of exchange on temperature.

In addition, it was noticed that when assessing the effect of additive molecules on hydrogels by means of STD NMR, observations from CP/MAS experiments should also be taken into account to clarify whether the additive is found within the rigid gel fibres. For example, Leu additive showed a dispersion of ¹H T_1 times in the gel state typical of additives that remain fully dissolved. But this additive received some saturation from the gel network (low fractional STD values) and presented negative intermolecular nOe correlations with Phe. Henceforth, this combined approach helped understanding that

Leu weakly interacted with the gel/solution interfaces, but there was no incorporation of this additive within the rigid components of the network.

The main limitation of STD NMR in the study of multi-component hydrogels of Phe was the small dimensions of the gelator and additives molecules involved, which prevented us from drawing conclusions about specific structural details on the bound state. Larger gelator molecules are advantageous in STD NMR studies as it becomes possible to understand preferential binding and solvation patterns.

Concluding, STD NMR experiments can be applied to assess the above mentioned exchange phenomena at the gel/solution interfaces, with particular potential for the identification of the role of gelator, solvent, additive and disruptive molecules in the processes of self-assembly of multi-component supramolecular materials. This technique will most likely become widely used in the investigation of dynamics of exchange, binding preferences, solvent exposure and role of guest molecules in supramolecular self-assembled materials.

10.8.1. Proposed mechanism of transfer of saturation in molecular gels

From the present studies, it was proposed the following pathway of transfer of saturation throughout supramolecular networks in STD NMR experiments (Figure 10.3). The network was considered the supramolecular entity that can be saturated selectively. Such saturation is then transferred *via* n_{OE} throughout the network and finally intermolecularly passed over to the bound gelator molecules. Dissociation of the weakly bound molecules from the network into the pools of water results in accumulation of saturation in the isotropic solution phase for molecules that exchange faster than their relaxation rates (Figure 10.3). This accumulation occurs due to the much longer T_1 times for unbound fast tumbling molecules than for bound slow tumbling molecules.¹⁵⁷ In this way, the STD difference spectrum will only exhibit signals of protons of gelator molecules that, being in solution, have been in contact with (and hence received saturation from) the fibrous network.

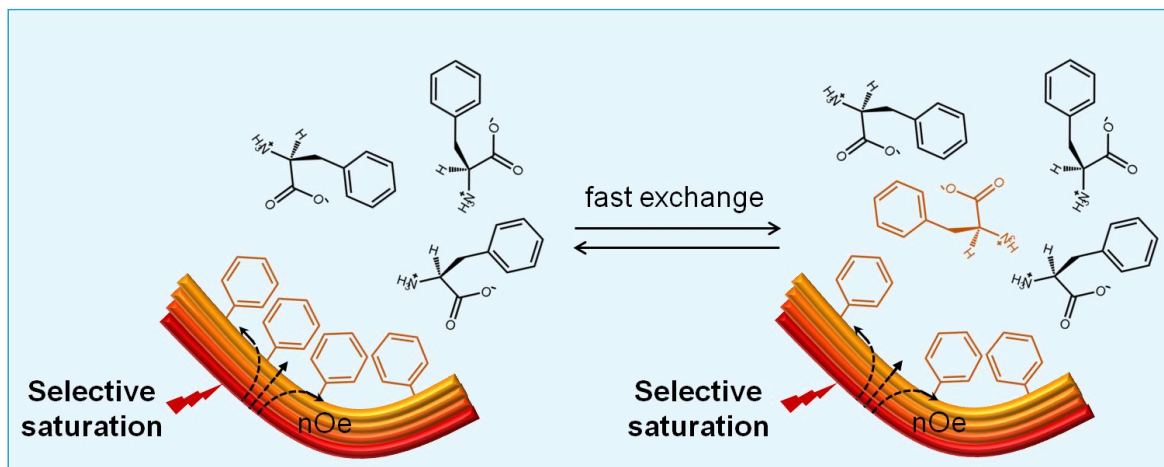


Figure 10.3. Proposed mechanism for the transfer of saturation in supramolecular gels during STD NMR experiments. Gelator molecules forming the network (bound state, left) are in fast exchange with those in the bulk solution phase (free state, right), allowing accumulation and detection of saturation in solution.

10.9. Overall conclusions

- ◆ Structural modifications of the aromatic group of Phe had a great impact on supramolecular aggregation. A strong correlation was found between solubility in water, strength of intermolecular interactions, kinetics of gelation and dynamics of exchange at the gel/solution interfaces.
- ◆ The development of multi-component systems proved to be an elegant strategy to modify the rheological properties of supramolecular systems. Additive molecules showed the potential to change the mechanical properties of the resulting multi-component hydrogels, independently of the gelation ability of the additive. A direct correlation was found between the strength of the network and the concentration of gelator molecules incorporated within the rigid fibrous structures. The present studies emphasised the dynamic complexity of multi-component gels: the additive molecules can create different patterns of interactions with the gels, thus having the potential to modify the properties of gel/solution interfaces. It was consistently observed that supramolecular reorganisation of gel fibres resulted in modification of interfacial properties, more specifically, in modulation of the dynamics of molecular exchange between fibre and solution environments. These findings are particularly relevant when supramolecular gels are developed as biomedical vehicles.

- ◆ Detailed understanding of the structure, local mobility and dynamics of interfacial processes across a range of length and time scales of multiphasic materials was achieved with the combination of rheology, microscopy, X-ray diffraction, computational and NMR spectroscopic methods. Single-crystal and powder XRD, and solid-state NMR measurements conducted directly on the gel fibres proved to be a reliable approach of determining the tridimensional organisation of rigid and crystalline fibres. Variations of ^1H longitudinal relaxation times were correlated with molecular level events, highlighting the importance of these measurements in probing local molecular motions of dynamic soft materials. Moreover, the understanding of saturation transfer difference NMR experiments has been expanded, with special focus in their applicability for the study of exchange dynamics and binding processes at the interfaces of supramolecular soft systems. Such a combined approach is essential in understanding the complexities of supramolecular soft materials.
- ◆ The application of the presented approach enables a better understanding of the role of guest molecules, such as co-gelators, non-gelating additives, cells or drugs, in the self-assembly and disassembly processes of molecular solids, which is of paramount importance in knowledge-based design of new functional materials. This NMR-based strategy is applicable to related fields of science and technology, enabling the determination of molecular mobility, dynamic processes and structural organisation in host-guest chemistry, colloidal science, supramolecular chemistry and interface technology.

11. References

1. Menger, F. M., Supramolecular Chemistry And Self-assembly Special Feature: Supramolecular chemistry and self-assembly. *Proceedings of the National Academy of Sciences of the United States of America* **2002**, 99 (8), 4818.
2. Hoffman, A. S., Hydrogels for biomedical applications. *Advanced Drug Delivery Reviews* **2012**, 64, 18-23.
3. Lee, S. C.; Kwon, I. K.; Park, K., Hydrogels for delivery of bioactive agents: a historical perspective. *Advanced Drug Delivery Reviews* **2013**, 65 (1), 17-20.
4. Peppas, N.; Bures, P.; Leobandung, W.; Ichikawa, H., Hydrogels in pharmaceutical formulations. *European Journal of Pharmaceutics and Biopharmaceutics* **2000**, 50 (1), 27-46.
5. Roy, S.; Banerjee, A., Amino acid based smart hydrogel: formation, characterization and fluorescence properties of silver nanoclusters within the hydrogel matrix. *Soft Matter* **2011**, 7 (11), 5300-5308.
6. Vashist, A.; Vashist, A.; Gupta, Y.; Ahmad, S., Recent advances in hydrogel based drug delivery systems for the human body. *Journal of Materials Chemistry B* **2014**, 2 (2), 147-166.
7. Everett, D., *Basic Principles of Colloid Science*. Royal Society of Chemistry: 1988.
8. Marr, P. C.; Marr, A. C., Ionic liquid gel materials: applications in green and sustainable chemistry. *Green Chemistry* **2016**, 18 (1), 105-128.
9. Bender, M., The colloidal state. *American Scientist* **1958**, 46 (4), 368-387.
10. Dorkoosh, F.; Brussee, J.; Verhoef, J. C.; Borchard, G.; Rafiee-Tehrani, M.; Junginger, H., Preparation and NMR characterization of superporous hydrogels (SPH) and SPH composites. *Polymer* **2000**, 41 (23), 8213-8220.
11. Wyss, H. M., Rheology of Soft Materials. *Fluids, Colloids, and Soft Materials: An Introduction to Soft Matter Physics* **2016**, 7, 149.
12. Yu, R.; Lin, N.; Yu, W.; Liu, X. Y., Crystal networks in supramolecular gels: formation kinetics and mesoscopic engineering principles. *CrystEngComm* **2015**, 17 (42), 7986-8010.
13. Zweep, N. Control of structure and function of organogels through self-assembly. University of Groningen, 2006.
14. Jeong, B.; Kim, S. W.; Bae, Y. H., Thermosensitive sol-gel reversible hydrogels. *Advanced Drug Delivery Reviews* **2012**, 64, 154-162.
15. Kaufmann, L.; Kennedy, S. R.; Jones, C. D.; Steed, J. W., Cavity-containing supramolecular gels as a crystallization tool for hydrophobic pharmaceuticals. *Chemical Communications* **2016**, 52 (66), 10113-10116.
16. Gonzatti, G. K.; Netz, P. A.; Fiel, L. A.; Pohlmann, A. R., Colloidal dispersion stability: kinetic modeling of agglomeration and aggregation. *Journal of the Brazilian Chemical Society* **2015**, 26 (2), 373-380.
17. Kumar, D. K.; Steed, J. W., Supramolecular gel phase crystallization: orthogonal self-assembly under non-equilibrium conditions. *Chemical Society Reviews* **2014**, 43 (7), 2080-2088.
18. Grove, C.; Jelinek, R. V.; Schoen, H. M., Crystallization from solution. *Advances in Chemical Engineering* **1962**, 3, 1-60.
19. Ramos Sasselli, I.; Halling, P. J.; Ulijn, R. V.; Tuttle, T., Supramolecular fibers in gels can be at thermodynamic equilibrium: a simple packing model reveals preferential fibril formation versus crystallization. *ACS Nano* **2016**, 10 (2), 2661-2668.
20. Borsos, A.; Gilányi, T., Transition from thermodynamically stable solution to colloid dispersion state. *Colloid and Polymer Science* **2012**, 290 (5), 473-479.
21. Kralchevsky, P. A.; Danov, K. D.; Denkov, N. D., *Chemical physics of colloid systems and interfaces*. CRC Press: 1997.
22. Dastidar, P., Supramolecular gelling agents: can they be designed? *Chemical Society Reviews* **2008**, 37 (12), 2699-2715.
23. Gupta, P.; Vermani, K.; Garg, S., Hydrogels: from controlled release to pH-responsive drug delivery. *Drug Discovery Today* **2002**, 7 (10), 569-579.
24. Branco, M. C.; Schneider, J. P., Self-assembling materials for therapeutic delivery. *Acta Biomaterialia* **2009**, 5 (3), 817-831.
25. Hoare, T. R.; Kohane, D. S., Hydrogels in drug delivery: Progress and challenges. *Polymer* **2008**, 49 (8), 1993-2007.
26. Gulrez, S. K.; Al-Assaf, S.; Phillips, G. O., Hydrogels: methods of preparation, characterisation and applications. In *Progress in molecular and environmental bioengineering-from analysis and modeling to technology applications*, InTech: 2011; pp 117-150.
27. Nishi, K.; Jayakrishnan, A., Self-Gelling Primaquine- Gum Arabic Conjugate: An Injectable Controlled Delivery System for Primaquine. *Biomacromolecules* **2007**, 8 (1), 84-90.

28. Raeburn, J.; Cardoso, A. Z.; Adams, D. J., The importance of the self-assembly process to control mechanical properties of low molecular weight hydrogels. *Chemical Society Reviews* **2013**, *42* (12), 5143-5156.

29. Cardoso, A. Z.; Alvarez, A. E. A.; Cattoz, B. N.; Griffiths, P. C.; King, S. M.; Frith, W. J.; Adams, D. J., The influence of the kinetics of self-assembly on the properties of dipeptide hydrogels. *Faraday Discussions* **2014**, *166*, 101-116.

30. Fairman, R.; Åkerfeldt, K. S., Peptides as novel smart materials. *Current Opinion in Structural Biology* **2005**, *15* (4), 453-463.

31. Qiu, Y.; Park, K., Environment-sensitive hydrogels for drug delivery. *Advanced Drug Delivery Reviews* **2012**, *53*, 321-339.

32. Segarra-Maset, M. D.; Nebot, V. J.; Miravet, J. F.; Escuder, B., Control of molecular gelation by chemical stimuli. *Chemical Society Reviews* **2013**, *42*, 7086-7098.

33. Morris, K. L.; Chen, L.; Raeburn, J.; Sellick, O. R.; Cotanda, P.; Paul, A.; Griffiths, P. C.; King, S. M.; O'Reilly, R. K.; Serpell, L. C., Chemically programmed self-sorting of gelator networks. *Nature communications* **2013**, *4*, 1480.

34. Gao, Y.; Ren, F.; Ding, B.; Sun, N.; Liu, X.; Ding, X.; Gao, S., A thermo-sensitive PLGA-PEG-PLGA hydrogel for sustained release of docetaxel. *Journal of drug targeting* **2011**, *19* (7), 516-527.

35. Schoener, C. A.; Peppas, N. A., pH-Responsive hydrogels containing PMMA nanoparticles: an analysis of controlled release of a chemotherapeutic conjugate and transport properties. *Journal of Biomaterials Science, Polymer Edition* **2013**, *24* (9), 1027-1040.

36. Pinhassi, R. I.; Assaraf, Y. G.; Farber, S.; Stark, M.; Ickowicz, D.; Drori, S.; Domb, A. J.; Livney, Y. D., Arabinogalactan- Folic Acid- Drug Conjugate for Targeted Delivery and Target-Activated Release of Anticancer Drugs to Folate Receptor-Overexpressing Cells. *Biomacromolecules* **2009**, *11* (1), 294-303.

37. Mao, L.; Wang, H.; Tan, M.; Ou, L.; Kong, D.; Yang, Z., Conjugation of two complementary anti-cancer drugs confers molecular hydrogels as a co-delivery system. *Chemical Communications* **2012**, *48* (3), 395-397.

38. Adams, D. J., Dipeptide and Tripeptide Conjugates as Low-Molecular-Weight Hydrogelators. *Macromolecular bioscience* **2011**, *11* (2), 160-173.

39. Lipowitz, V. A., Versuche und Resultate über die Löslichkeit der Harnsäure. *European Journal of Organic Chemistry* **1841**, *38* (3), 348-355.

40. Brenzinger, K., Zur Kenntniss des Cystins und des Cystëins.(Mitgetheilt von E. Baumann.). *Zeitschrift für physiologische Chemie* **1892**, *16* (6), 552-588.

41. Gortner, R.; Hoffman, W., An interesting colloidal gel. *Journal of the American Chemical Society* **1921**, *43*, 2199-2202.

42. Menger, F.; Venkatasubban, K., A carbon-13 nuclear magnetic resonance study of dibenzoylcystine gels. *The Journal of Organic Chemistry* **1978**, *43* (17), 3413-3414.

43. Menger, F. M.; Caran, K. L., Anatomy of a gel. Amino acid derivatives that rigidify water at submillimolar concentrations. *Journal of the American Chemical Society* **2000**, *122* (47), 11679-11691.

44. George, M.; Tan, G.; John, V. T.; Weiss, R. G., Urea and Thiourea Derivatives as Low Molecular-Mass Organogelators. *Chemistry-A European Journal* **2005**, *11* (11), 3243-3254.

45. Zurcher, D. M.; McNeil, A. J., Tools for Identifying Gelator Scaffolds and Solvents. *The Journal of Organic Chemistry* **2015**, *80* (5), 2473-2478.

46. Weiss, R. G., The past, present, and future of molecular gels. What is the status of the field, and where is it going? *Journal of the American Chemical Society* **2014**, *136* (21), 7519-7530.

47. Tomasini, C.; Castellucci, N., Peptides and peptidomimetics that behave as low molecular weight gelators. *Chemical Society Reviews* **2013**, *42* (1), 156-172.

48. Wang, J.; Liu, K.; Xing, R.; Yan, X., Peptide self-assembly: thermodynamics and kinetics. *Chemical Society Reviews* **2016**, *45* (20), 5589-5604.

49. Adams, D. J.; Morris, K.; Chen, L.; Serpell, L. C.; Bacsa, J.; Day, G. M., The delicate balance between gelation and crystallisation: structural and computational investigations. *Soft Matter* **2010**, *6* (17), 4144-4156.

50. Shapiro, Y. E., Structure and dynamics of hydrogels and organogels: An NMR spectroscopy approach. *Progress in Polymer Science* **2011**, *36* (9), 1184-1253.

51. Buerkle, L. E.; Rowan, S. J., Supramolecular gels formed from multi-component low molecular weight species. *Chemical Society Reviews* **2012**, *41* (18), 6089-6102.

52. Lan, Y.; Corradini, M.; Weiss, R.; Raghavan, S.; Rogers, M., To gel or not to gel: correlating molecular gelation with solvent parameters. *Chemical Society Reviews* **2015**, *44* (17), 6035-6058.

53. Dasgupta, A.; Mondal, J. H.; Das, D., Peptide hydrogels. *RSC Advances* **2013**, *3*, 9117-9149.

54. Johnson, E. K.; Adams, D. J.; Cameron, P. J., Peptide based low molecular weight gelators. *Journal of Materials Chemistry* **2011**, 21 (7), 2024-2027.

55. Perween, S.; Chandanshive, B.; Kotamarthi, H. C.; Khushalani, D., Single amino acid based self-assembled structure. *Soft Matter* **2013**, 9 (42), 10141-10145.

56. Fuhrhop, J. H.; Spiroski, D.; Boettcher, C., Molecular monolayer rods and tubules made of alpha-.(L-lysine), omega-.(amino) bolaamphiphiles. *Journal of the American Chemical Society* **1993**, 115 (4), 1600-1601.

57. Dudukovic, N. A.; Zukoski, C. F., Mechanical Properties of Self-Assembled Fmoc-Diphenylalanine Molecular Gels. *Langmuir* **2014**, 30 (15), 4493-4500.

58. Du, X.; Zhou, J.; Shi, J.; Xu, B., Supramolecular hydrogelators and hydrogels: from soft matter to molecular biomaterials. *Chemical Reviews* **2015**, 115 (24), 13165-13307.

59. Martin, A. D.; Robinson, A. B.; Thordarson, P., Biocompatible small peptide super-hydrogelators bearing carbazole functionalities. *Journal of Materials Chemistry B* **2015**, 3 (11), 2277-2280.

60. Birchall, L. S.; Roy, S.; Jayawarna, V.; Hughes, M.; Irvine, E.; Okorogheye, G. T.; Saudi, N.; De Santis, E.; Tuttle, T.; Edwards, A. A., Exploiting CH- π interactions in supramolecular hydrogels of aromatic carbohydrate amphiphiles. *Chemical Science* **2011**, 2 (7), 1349-1355.

61. Jayawarna, V.; Ali, M.; Jowitt, T. A.; Miller, A. F.; Saiani, A.; Gough, J. E.; Ulijn, R. V., Nanostructured hydrogels for three-dimensional cell culture through self-assembly of fluorenylmethoxycarbonyl-dipeptides. *Advanced Materials* **2006**, 18 (5), 611-614.

62. Snigdha, K.; Singh, B. K.; Mehta, A. S.; Tewari, R.; Dutta, P., Self-assembling N-(9-Fluorenylmethoxycarbonyl)-l-Phenylalanine hydrogel as novel drug carrier. *International Journal of Biological Macromolecules* **2016**, 93, 1639-1646.

63. Kumar, D.; Workman, V. L.; O'Brien, M.; McLaren, J.; White, L.; Ragunath, K.; Rose, F.; Saiani, A.; Gough, J. E., Peptide Hydrogels-A Tissue Engineering Strategy for the Prevention of Oesophageal Strictures. *Advanced Functional Materials* **2017**, 27, 1616-3028.

64. Zhang, S.; Marini, D. M.; Hwang, W.; Santoso, S., Design of nanostructured biological materials through self-assembly of peptides and proteins. *Current Opinion in Chemical Biology* **2002**, 6 (6), 865-871.

65. Tamamis, P.; Adler-Abramovich, L.; Reches, M.; Marshall, K.; Sikorski, P.; Serpell, L.; Gazit, E.; Archontis, G., Self-assembly of phenylalanine oligopeptides: insights from experiments and simulations. *Biophysical Journal* **2009**, 96 (12), 5020-5029.

66. Mossou, E.; Teixeira, S. C.; Mitchell, E. P.; Mason, S. A.; Adler-Abramovich, L.; Gazit, E.; Forsyth, V. T., The self-assembling zwitterionic form of l-phenylalanine at neutral pH. *Acta Crystallographica Section C: Structural Chemistry* **2014**, 70 (3), 326-331.

67. Frederix, P. W.; Scott, G. G.; Abul-Haija, Y. M.; Kalafatovic, D.; Pappas, C. G.; Javid, N.; Hunt, N. T.; Ulijn, R. V.; Tuttle, T., Exploring the sequence space for (tri-) peptide self-assembly to design and discover new hydrogels. *Nature chemistry* **2015**, 7 (1), 30-37.

68. Estroff, L. A.; Hamilton, A. D., Water gelation by small organic molecules. *Chemical Reviews* **2004**, 104 (3), 1201-1218.

69. Brittain, H., Thermodynamic vs. kinetic solubility: knowing which is which. *American Pharmaceutical Review* **2014**, 17 (3), 10-6.

70. Dixit, N. M.; Zukoski, C. F., Competition between crystallization and gelation: A local description. *Physical Review E* **2003**, 67 (6), 061501.

71. Chen, J.; Sarma, B.; Evans, J. M.; Myerson, A. S., Pharmaceutical crystallization. *Crystal Growth & Design* **2011**, 11 (4), 887-895.

72. Lan, Y.; Corradini, M. G.; Liu, X.; May, T. E.; Borondics, F.; Weiss, R. G.; Rogers, M. A., Comparing and correlating solubility parameters governing the self-assembly of molecular gels using 1, 3: 2, 4-dibenzylidene sorbitol as the gelator. *Langmuir* **2014**, 30 (47), 14128-14142.

73. Li, J.-L.; Liu, X.-Y.; Wang, R.-Y.; Xiong, J.-Y., Architecture of a biocompatible supramolecular material by supersaturation-driven fabrication of its fiber network. *The Journal of Physical Chemistry B* **2005**, 109 (51), 24231-24235.

74. German, H. W.; Uyaver, S.; Hansmann, a. U. H., Self-assembly of phenylalanine-based molecules. *The Journal of Physical Chemistry A* **2014**, 119 (9), 1609-1615.

75. Liu, X.; Fei, J.; Wang, A.; Cui, W.; Zhu, P.; Li, J., Transformation of Dipeptide-Based Organogels into Chiral Crystals by Cryogenic Treatment. *Angewandte Chemie International Edition* **2017**, 129 (10), 2704-2707.

76. Zhu, P.; Yan, X.; Su, Y.; Yang, Y.; Li, J., Solvent-Induced Structural Transition of Self-Assembled Dipeptide: From Organogels to Microcrystals. *Chemistry-A European Journal* **2010**, 16 (10), 3176-3183.

77. Terech, P., Metastability and sol phases: two keys for the future of molecular gels? *Langmuir* **2009**, 25 (15), 8370-8372.

78. Wang, Y.; Tang, L.; Yu, J., Investigation of spontaneous transition from low-molecular-weight hydrogel into macroscopic crystals. *Crystal Growth & Design* **2008**, *8* (3), 884-889.

79. Roy, B.; Bairi, P.; Nandi, A. K., Metastability in a bi-component hydrogel of thymine and 6-methyl-1, 3, 5-triazine-2, 4-diamine: ultrasound induced vs. thermo gelation. *Soft Matter* **2012**, *8* (8), 2366-2369.

80. Houton, K. A.; Morris, K. L.; Chen, L.; Schmidtmann, M.; Jones, J. T.; Serpell, L. C.; Lloyd, G. O.; Adams, D. J., On Crystal versus Fiber Formation in Dipeptide Hydrogelator Systems. *Langmuir* **2012**, *28* (25), 9797-9806.

81. Edwards, W.; Lagadec, C. A.; Smith, D. K., Solvent-gelator interactions—using empirical solvent parameters to better understand the self-assembly of gel-phase materials. *Soft Matter* **2011**, *7* (1), 110-117.

82. Nartowski, K. P.; Ramalhete, S. M.; Martin, P. C.; Foster, J. S.; Heinrich, M.; Eddleston, M. D.; Green, H. R.; Day, G. M.; Khimyak, Y. Z.; Lloyd, G. O., The Plot Thickens, Gelation by Phenylalanine in Water and Dimethyl Sulfoxide. *Crystal Growth & Design* **2017**, *17*, 4100-4109.

83. Barker, E. C.; Martin, A. D.; Garvey, C. J.; Goh, C. Y.; Jones, F.; Mocerino, M.; Skelton, B. W.; Ogden, M. I.; Becker, T., Thermal annealing behaviour and gel to crystal transition of a low molecular weight hydrogelator. *Soft Matter* **2017**, *13*, 1006-1011.

84. Tidhar, Y.; Weissman, H.; Wolf, S. G.; Gulino, A.; Rybtchinski, B., Pathway-Dependent Self-Assembly of Perylene Diimide/Peptide Conjugates in Aqueous Medium. *Chemistry-A European Journal* **2011**, *17* (22), 6068-6075.

85. Korevaar, P. A.; Newcomb, C. J.; Meijer, E.; Stupp, S. I., Pathway selection in peptide amphiphile assembly. *Journal of the American Chemical Society* **2014**, *136* (24), 8540-8543.

86. Mattia, E.; Otto, S., Supramolecular systems chemistry. *Nature Nanotechnology* **2015**, *10* (2), 111-119.

87. Wu, S.; Gao, J.; Emge, T.; Rogers, M., Influence of solvent on the supramolecular architectures in molecular gels. *Soft Matter* **2013**, *9* (25), 5942-5950.

88. Raynal, M.; Bouteiller, L., Organogel formation rationalized by Hansen solubility parameters. *Chemical Communications* **2011**, *47* (29), 8271-8273.

89. Fan, K.; Niu, L.; Li, J.; Feng, R.; Qu, R.; Liu, T.; Song, J., Application of solubility theory in bi-component hydrogels of melamine with di (2-ethylhexyl) phosphoric acid. *Soft Matter* **2013**, *9* (11), 3057-3062.

90. Niu, L.; Song, J.; Li, J.; Tao, N.; Lu, M.; Fan, K., Solvent effects on the gelation performance of melamine and 2-ethylhexylphosphoric acid mono-2-ethylhexyl ester in water-organic mixtures. *Soft Matter* **2013**, *9* (32), 7780-7786.

91. Diehn, K. K.; Oh, H.; Hashemipour, R.; Weiss, R. G.; Raghavan, S. R., Insights into organogelation and its kinetics from Hansen solubility parameters. Toward a priori predictions of molecular gelation. *Soft Matter* **2014**, *10* (15), 2632-2640.

92. Hirst, A. R.; Smith, D. K., Two-Component Gel-Phase Materials—Highly Tunable Self-Assembling Systems. *Chemistry-A European Journal* **2005**, *11* (19), 5496-5508.

93. Moffat, J. R.; Smith, D. K., Controlled self-sorting in the assembly of 'multi-gelator' gels. *Chemical Communications* **2009**, *(3)*, 316-318.

94. Foster, J. A.; Edkins, R. M.; Cameron, G. J.; Colgin, N.; Fucke, K.; Ridgeway, S.; Crawford, A. G.; Marder, T. B.; Beeby, A.; Cobb, S. L., Blending Gelators to Tune Gel Structure and Probe Anion-Induced Disassembly. *Chemistry-A European Journal* **2014**, *20* (1), 279-291.

95. Rodrigues, M.; Calpena, A. C.; Amabilino, D. B.; Garduño-Ramírez, M. L.; Pérez-García, L., Supramolecular gels based on a gemini imidazolium amphiphile as molecular material for drug delivery. *Journal of Materials Chemistry B* **2014**, *2* (33), 5419-5429.

96. Draper, E. R.; Adams, D. J., Supramolecular fibres: Self-sorting shows its true colours. *Nature Chemistry* **2016**, *8*, 737-738.

97. Yu, G.; Yan, X.; Han, C.; Huang, F., Characterization of supramolecular gels. *Chemical Society Reviews* **2013**, *42* (16), 6697-6722.

98. Ballabh, A.; Trivedi, D. R.; Dastidar, P., Structural studies of a new low molecular mass organic gelator for organic liquids based on simple salt. *Chemistry of Materials* **2003**, *15* (11), 2136-2140.

99. Piepenbrock, M.-O. M.; Lloyd, G. O.; Clarke, N.; Steed, J. W., Metal-and anion-binding supramolecular gels. *Chemical Reviews* **2009**, *110* (4), 1960-2004.

100. Almdal, K.; Dyre, J.; Hvidt, S.; Kramer, O., Towards a phenomenological definition of the term 'gel'. *Polymer Gels and Networks* **1993**, *1* (1), 5-17.

101. Weitz, D.; Wyss, H.; Larsen, R., Oscillatory rheology: Measuring the viscoelastic behaviour of soft materials. *G.I.T. Laboratory Journal Europe* **2007**, *11* (3-4), 68-70.

102. Shi, J. H.; Liu, X. Y.; Li, J. L.; Strom, C. S.; Xu, H. Y., Spherulitic networks: from structure to rheological property. *The Journal of Physical Chemistry B* **2009**, *113* (14), 4549-4554.

103. Terech, P., Fibers and wires in organogels from low-mass compounds: Typical structural and rheological properties. *Berichte der Bunsengesellschaft für physikalische Chemie* **1998**, *102* (11), 1630-1643.
104. Magill, J., A new technique for following rapid rates of crystallization. *Nature* **1960**, *187* (4739), 770-771.
105. Wang, R.; Geiger, C.; Chen, L.; Swanson, B.; Whitten, D. G., Direct observation of sol- gel conversion: the role of the solvent in organogel formation. *Journal of the American Chemical Society* **2000**, *122* (10), 2399-2400.
106. Usov, I.; Nyström, G.; Adamcik, J.; Handschin, S.; Schütz, C.; Fall, A.; Bergström, L.; Mezzenga, R., Understanding nanocellulose chirality and structure-properties relationship at the single fibril level. *Nature communications* **2015**, *6*, 7564.
107. Greenfield, N. J., Using circular dichroism spectra to estimate protein secondary structure. *Nature Protocols* **2006**, *1* (6), 2876-2890.
108. Piana, F.; Case, D. H.; Ramalhete, S. M.; Pileio, G.; Facciotti, M.; Day, G. M.; Khimyak, Y. Z.; Angulo, J.; Brown, R. C.; Gale, P. A., Substituent interference on supramolecular assembly in urea gelators: synthesis, structure prediction and NMR. *Soft Matter* **2016**, *12* (17), 4034-4043.
109. Lee, J. H.; Park, J.; Park, J.-W.; Ahn, H.-J.; Jaworski, J.; Jung, J. H., Supramolecular gels with high strength by tuning of calix [4] arene-derived networks. *Nature Communications* **2015**, *6*, 6650.
110. Ostuni, E.; Kamaras, P.; Weiss, R. G., Novel X-ray Method for In Situ Determination of Gelator Strand Structure: Polymorphism of Cholesteryl Anthraquinone-2-carboxylate. *Angewandte Chemie International Edition* **1996**, *35* (12), 1324-1326.
111. Cui, J.; Zheng, Y.; Shen, Z.; Wan, X., Alkoxy tail length dependence of gelation ability and supramolecular chirality of sugar-appended organogelators. *Langmuir* **2010**, *26* (19), 15508-15515.
112. Trivedi, D. R.; Ballabh, A.; Dastidar, P., Facile preparation and structure–property correlation of low molecular mass organic gelators derived from simple organic salts. *Journal of Materials Chemistry* **2005**, *15* (26), 2606-2614.
113. Martineau, C.; Taulelle, F., NMR crystallography. *EPJ Web of Conferences* **2012**, *30*, 02003.
114. Mu, X.; Eckes, K. M.; Nguyen, M. M.; Suggs, L. J.; Ren, P., Experimental and computational studies reveal an alternative supramolecular structure for Fmoc-dipeptide self-assembly. *Biomacromolecules* **2012**, *13* (11), 3562-3571.
115. Iqbal, S.; Rodríguez-LLansola, F.; Escuder, B.; Miravet, J. F.; Verbruggen, I.; Willem, R., HRMAS 1H NMR as a tool for the study of supramolecular gels. *Soft Matter* **2010**, *6* (9), 1875-1878.
116. Schaefer, J., High-Resolution Pulsed Carbon-13 Nuclear Magnetic Resonance Analysis of Some Cross-Linked Polymers. *Macromolecules* **1971**, *4* (1), 110-112.
117. Child, T.; Pryce, N., Steady-state and pulsed NMR studies of gelation in aqueous agarose. *Biopolymers* **1972**, *11* (2), 409-429.
118. Derbyshire, W.; Duff, I., NMR of agarose gels. *Faraday Discussions* **1974**, *57*, 243-254.
119. Yokota, K.; Abe, A.; Hosaka, S.; Sakai, I.; Saitô, H., A 13C nuclear magnetic resonance study of covalently cross-linked gels. Effect of chemical composition, degree of cross-linking, and temperature to chain mobility. *Macromolecules* **1978**, *11* (1), 95-100.
120. Schmitt, E. A.; Flanagan, D.; Linhardt, R. J., Importance of distinct water environments in the hydrolysis of poly (DL-lactide-co-glycolide). *Macromolecules* **1994**, *27* (3), 743-748.
121. Ford, W. T.; Mohanraj, S.; Hall, H.; O'Donnell, D. J., A sealed MAS rotor insert for liquid and air-sensitive samples. *Journal of Magnetic Resonance (1969)* **1985**, *65* (1), 156-158.
122. Kobayashi, M.; Ando, I.; Ishii, T.; Amiya, S., Structural study of poly (vinyl alcohol) in the gel state by high-resolution solid-state 13C NMR spectroscopy. *Macromolecules* **1995**, *28* (19), 6677-6679.
123. Schoonbeek, F. S.; van Esch, J. H.; Hulst, R.; Kellogg, R. M.; Feringa, B. L., Geminal Bis-ureas as Gelators for Organic Solvents: Gelation Properties and Structural Studies in Solution and in the Gel State. *Chemistry-A European Journal* **2000**, *6* (14), 2633-2643.
124. Behanna, H. A.; Donners, J. J.; Gordon, A. C.; Stupp, S. I., Coassembly of amphiphiles with opposite peptide polarities into nanofibers. *Journal of the American Chemical Society* **2005**, *127* (4), 1193-1200.
125. Mahajan, S. S.; Paranjpye, R.; Mehta, R.; Lyon, R. P.; Atkins, W. M., A glutathione-based hydrogel and its site-selective interactions with water. *Bioconjugate Chemistry* **2005**, *16* (4), 1019-1026.
126. Mathur, A.; Scranton, A. B., Characterization of hydrogels using nuclear magnetic resonance spectroscopy. *Biomaterials* **1996**, *17* (6), 547-557.
127. Andrasko, J., Water in agarose gels studied by nuclear magnetic resonance relaxation in the rotating frame. *Biophysical Journal* **1975**, *15* (12), 1235-1243.
128. McCall, D. W.; Douglass, D. C.; Blyler Jr, L. L.; Johnson, G. E.; Jelinski, L. W.; Bair, H. E., Solubility and diffusion of water in low-density polyethylene. *Macromolecules* **1984**, *17* (9), 1644-1649.

129. Lahtinen, M.; Behera, B.; Kolehmainen, E.; Maitra, U., Unraveling the packing pattern leading to gelation using SS NMR and X-ray diffraction: direct observation of the evolution of self-assembled fibers. *Soft Matter* **2010**, *6* (8), 1748-1757.

130. Doddrell, D.; Glushko, V.; Allerhand, A., Theory of nuclear overhauser enhancement and ¹³C-1H dipolar relaxation in proton-decoupled carbon-13 NMR spectra of macromolecules. *The Journal of Chemical Physics* **1972**, *56* (7), 3683-3689.

131. Ginter, D. M.; Bell, A. T.; Radke, C. J., Magic-angle-spinning NMR spectroscopy of gels. *Journal of Magnetic Resonance* (1969) **1989**, *81* (1), 217-219.

132. Kolehmainen, E., Solid state NMR studies of gels derived from low molecular mass gelators. *Soft Matter* **2016**, *12* (28), 6015-6026.

133. De Loos, M.; van Esch, J.; Stokroos, I.; Kellogg, R. M.; Feringa, B. L., Remarkable stabilization of self-assembled organogels by polymerization. *Journal of the American Chemical Society* **1997**, *119* (51), 12675-12676.

134. Hsu, S. M.; Lin, Y. C.; Chang, J. W.; Liu, Y. H.; Lin, H. C., Intramolecular interactions of a phenyl/perfluorophenyl pair in the formation of supramolecular nanofibers and hydrogels. *Angewandte Chemie International Edition* **2014**, *53* (7), 1921-1927.

135. Alam, T. M.; Jenkins, J. E., *HR-MAS NMR Spectroscopy in Material Science*. InTech ed.; 2012.

136. Brand, T.; Nolis, P.; Richter, S.; Berger, S., NMR study of the gelation of a designed gelator. *Magnetic Resonance in Chemistry* **2008**, *46* (6), 545-549.

137. Martineau, C., NMR crystallography: applications to inorganic materials. *Solid State Nuclear Magnetic Resonance* **2014**, *63*, 1-12.

138. Zhang, R.; Mroue, K. H.; Ramamoorthy, A., Hybridizing cross-polarization with NOE or refocused-INEPT enhances the sensitivity of MAS NMR spectroscopy. *Journal of Magnetic Resonance* **2016**, *266*, 59-66.

139. Grimmer, A. R.; Kretschmer, A.; Cajipe, V. B., Influence of magic angle spinning on sample temperature. *Magnetic Resonance in Chemistry* **1997**, *35* (2), 86-90.

140. Viel, S.; Ziarelli, F.; Pages, G.; Carrara, C.; Caldarelli, S., Pulsed field gradient magic angle spinning NMR self-diffusion measurements in liquids. *Journal of Magnetic Resonance* **2008**, *190* (1), 113-123.

141. Jochum, M.; Werner-Zwanziger, U.; Zwanziger, J., Observable effects of mechanical stress induced by sample spinning in solid state nuclear magnetic resonance. *The Journal of Chemical Physics* **2008**, *128* (5), 052304.

142. Asano, A.; Hori, S.; Kitamura, M.; Nakazawa, C. T.; Kurotsu, T., Influence of magic angle spinning on T1H of SBR studied by solid state 1H NMR. *Polymer Journal* **2012**, *44* (7), 706-712.

143. Bradley, S. A.; Paschal, J.; Kulanthaivel, P., DOSY of sample-limited mixtures: comparison of cold, nano and conventional probes. *Magnetic Resonance in Chemistry* **2005**, *43* (1), 31-35.

144. Gil, A.; Alberti, E., The effect of Magic Angle Spinning on proton spin-lattice relaxation times in some organic solids. *Solid State Nuclear Magnetic Resonance* **1998**, *11* (3), 203-209.

145. Shapiro, M. J.; Gounaris, J. S., High resolution MAS-NMR in combinatorial chemistry. *Biotechnology and Bioengineering* **2000**, *71* (2), 130-148.

146. Keifer, P. A., NMR tools for biotechnology. *Current opinion in biotechnology* **1999**, *10* (1), 34-41.

147. Escuder, B.; LLusar, M.; Miravet, J. F., Insight on the NMR study of supramolecular gels and its application to monitor molecular recognition on self-assembled fibers. *The Journal of Organic Chemistry* **2006**, *71* (20), 7747-7752.

148. Bouquet-Bonnet, S.; Yemloul, M.; Canet, D., New Application of Proton Nuclear Spin Relaxation Unraveling the Intermolecular Structural Features of Low-Molecular-Weight Organogel Fibers. *Journal of the American Chemical Society* **2012**, *134* (25), 10621-10627.

149. Ramalhete, S. M.; Nartowski, K. P.; Sarathchandra, N.; Foster, J. S.; Round, A. N.; Angulo, J.; Lloyd, G. O.; Khimyak, Y. Z., Supramolecular amino acid based hydrogels: probing the contribution of additive molecules using NMR spectroscopy. *Chemistry-A European Journal* **2017**, *23* (33), 8014-8024.

150. Hirst, A. R.; Coates, I. A.; Boucheteau, T. R.; Miravet, J. F.; Escuder, B.; Castelletto, V.; Hamley, I. W.; Smith, D. K., Low-molecular-weight gelators: elucidating the principles of gelation based on gelator solubility and a cooperative self-assembly model. *Journal of the American Chemical Society* **2008**, *130* (28), 9113-9121.

151. Song, J.; Wang, H.; Li, M., An NMR study on the gelation of N, N'-bis (4-N-alkylo-xybenzoyl) hydrazine (4D n) in two aromatic solvents. *New Journal of Chemistry* **2015**, *39* (4), 2711-2719.

152. Neuhaus, D.; Williamson, M. P., *The nuclear Overhauser effect in structural and conformational analysis*. VCH New York: 1989.

153. Butts, C. P.; Jones, C. R.; Towers, E. C.; Flynn, J. L.; Appleby, L.; Barron, N. J., Interproton distance determinations by NOE-surprising accuracy and precision in a rigid organic molecule. *Organic & Biomolecular Chemistry* **2011**, 9 (1), 177-184.

154. Mayer, M.; Meyer, B., Characterization of ligand binding by saturation transfer difference NMR spectroscopy. *Angewandte Chemie International Edition* **1999**, 38 (12), 1784-1788.

155. Segarra-Maset, M. D.; Escuder, B.; Miravet, J. F., Selective Interaction of Dopamine with the Self-Assembled Fibrillar Network of a Molecular Hydrogel Revealed by STD-NMR. *Chemistry-A European Journal* **2015**, 21 (40), 13925-13929.

156. Wallace, M.; Iggo, J. A.; Adams, D. J., Probing the surface chemistry of self-assembled peptide hydrogels using solution-state NMR spectroscopy. *Soft Matter* **2017**, 13 (8), 1716-1727.

157. Dalvit, C.; Fogliatto, G.; Stewart, A.; Veronesi, M.; Stockman, B., WaterLOGSY as a method for primary NMR screening: practical aspects and range of applicability. *Journal of Biomolecular NMR* **2001**, 21 (4), 349-359.

158. Lepre, C. A.; Moore, J. M.; Peng, J. W., Theory and applications of NMR-based screening in pharmaceutical research. *Chemical Reviews* **2004**, 104 (8), 3641-3676.

159. Harris, R. K.; E, W. R.; Duer, M. J., NMR Crystallography. Wiley: 2009.

160. Harris, R. K., NMR crystallography: The use of chemical shifts. *Solid State Sciences* **2004**, 6 (10), 1025-1037.

161. Bonhomme, C.; Coelho, C.; Baccile, N.; Gervais, C.; Azaïs, T.; Babonneau, F., Advanced solid state NMR techniques for the characterization of sol-gel-derived materials. *Accounts of Chemical Research* **2007**, 40 (9), 738-746.

162. Clark, S. J.; Segall, M. D.; Pickard, C. J.; Hasnip, P. J.; Probert, M. I.; Refson, K.; Payne, M. C., First principles methods using CASTEP. *Zeitschrift für Kristallographie-Crystalline Materials* **2005**, 220 (5/6), 567-570.

163. Chawla, K. K.; Meyers, M., *Mechanical behavior of materials*. Prentice Hall: 1999.

164. Dinnebier, R. E.; Billinge, S. J., Principles of powder diffraction. In *Powder Diffraction Theory and Practice*, 2008; p 19.

165. Pecharsky, V. K.; Zavalij, P. Y., *Fundamentals of powder diffraction and structural characterization of materials*. Springer: 2009; Vol. 69.

166. Fultz, B.; Howe, J., Diffraction and the X-ray powder diffractometer. In *Transmission Electron Microscopy and Diffractometry of Materials*, Springer: 2013.

167. Duer, M. J., The Basics of Solid-State NMR. In *Solid-State NMR Spectroscopy Principles and Applications*, Wiley: 2002; Vol. 33.

168. Keeler, J., *Understanding NMR Spectroscopy*. John Wiley & Sons: 2011.

169. Hore, P., *Nuclear Magnetic Resonance*. Oxford University Press, USA: 2015.

170. Levitt, M. H., *Spin dynamics: basics of nuclear magnetic resonance*. John Wiley & Sons: 2001.

171. Claridge, T. D., *High-resolution NMR techniques in organic chemistry*. Elsevier: 2016; Vol. 27.

172. Findeisen, M.; Berger, S., *50 and more essential NMR experiments: a detailed guide*. John Wiley & Sons: 2013.

173. Tubridy, N.; McKinstry, C., Neuroradiological history: Sir Joseph Larmor and the basis of MRI physics. *Neuroradiology* **2000**, 42 (11), 852-855.

174. Laws, D. D.; Bitter, H. M. L.; Jerschow, A., Solid-State NMR Spectroscopic Methods in Chemistry. *Angewandte Chemie International Edition* **2002**, 41 (17), 3096-3129.

175. Wider, G.; Riek, R.; Wüthrich, K., Diffusion filters for separation of solvent-protein and protein-protein nuclear overhauser effects (HYDRA). *Journal of the American Chemical Society* **1996**, 118 (46), 11629-11634.

176. Andrew, E. R.; Bradbury, A.; Eades, R., Nuclear magnetic resonance spectra from a crystal rotated at high speed. *Nature* **1958**, 182 (4650), 1659-1659.

177. Demers, J.-P.; Chevelkov, V.; Lange, A., Progress in correlation spectroscopy at ultra-fast magic-angle spinning: basic building blocks and complex experiments for the study of protein structure and dynamics. *Solid State Nuclear Magnetic Resonance* **2011**, 40 (3), 101-113.

178. Bennett, A. E.; Rienstra, C. M.; Auger, M.; Lakshmi, K.; Griffin, R. G., Heteronuclear decoupling in rotating solids. *The Journal of Chemical Physics* **1995**, 103 (16), 6951-6958.

179. Fung, B.; Khitrin, A.; Ermolaev, K., An improved broadband decoupling sequence for liquid crystals and solids. *Journal of Magnetic Resonance* **2000**, 142 (1), 97-101.

180. Alam, T.; Holland, G., ^1H - ^{13}C INEPT MAS NMR correlation experiments with ^1H - ^1H mediated magnetization exchange to probe organization in lipid biomembranes. *Journal of Magnetic Resonance* **2006**, 180 (2), 210-221.

181. Thieme, K.; Zech, G.; Kunz, H.; Spiess, H. W.; Schnell, I., Dipolar Recoupling in NOESY-Type 1H–1H NMR Experiments under HRMAS Conditions. *Organic letters* **2002**, *4* (9), 1559-1562.
182. Maas, W.; Laukien, F.; Cory, D., Gradient, high resolution, magic angle sample spinning NMR. *Journal of the American Chemical Society* **1996**, *118* (51), 13085-13086.
183. Ferreira, A. S.; Barreiros, S.; Cabrita, E. J., Probing sol-gel matrices microenvironments by PGSE HR-MAS NMR. *Magnetic Resonance in Chemistry* **2016**, *55*, 452-463.
184. D'Agostino, C.; Mitchell, J.; Gladden, L. F.; Mantle, M. D., Hydrogen bonding network disruption in mesoporous catalyst supports probed by PFG-NMR diffusometry and NMR relaxometry. *The Journal of Physical Chemistry C* **2012**, *116* (16), 8975-8982.
185. Waldeck, A. R.; Kuchel, P. W.; Lennon, A. J.; Chapman, B. E., NMR diffusion measurements to characterise membrane transport and solute binding. *Progress in Nuclear Magnetic Resonance Spectroscopy* **1997**, *30* (1), 39-68.
186. Brand, T.; Cabrita, E. J.; Berger, S., Intermolecular interaction as investigated by NOE and diffusion studies. *Progress in Nuclear Magnetic Resonance Spectroscopy* **2005**, *46* (4), 159-196.
187. von Meerwall, E., Self-diffusion in polymer systems, measured with field-gradient spin echo NMR methods. In *Spectroscopy: NMR, Fluorescence, FT-IR*, 1984; pp 1-29.
188. Price, W. S.; Kuchel, P. W., Restricted diffusion of bicarbonate and hypophosphite ions modulated by transport in suspensions of red blood cells. *Journal of Magnetic Resonance (1969)* **1990**, *90* (1), 100-110.
189. Larijani, B.; Rosser, C. A.; Woscholski, R., *Chemical Biology: Techniques and Applications*. John Wiley & Sons: 2006.
190. Palmer III, A. G., *Relaxation and dynamic processes*. Elsevier: 1996.
191. Angulo, J.; Nieto, P. M., STD-NMR: application to transient interactions between biomolecules—a quantitative approach. *European Biophysics Journal* **2011**, *40* (12), 1357-1369.
192. Angulo, J.; Ardá, A.; Cabrita, E. J.; Martín-Pastor, M.; Jiménez-Barbero, J.; Nieto, P. M., NMR Techniques for the Study of Transient Intermolecular Interactions. In *Structure Elucidation in Organic Chemistry: The Search for the Right Tools*, Wiley-VCH: 2014; pp 325-360.
193. Viegas, A.; Manso, J.; Nobrega, F. L.; Cabrita, E. J., Saturation-transfer difference (STD) NMR: a simple and fast method for ligand screening and characterization of protein binding. *Journal of Chemical Education* **2011**, *88* (7), 990-994.
194. Streiff, J. H.; Juranic, N. O.; Macura, S. I.; Warner, D. O.; Jones, K. A.; Perkins, W. J., Saturation transfer difference nuclear magnetic resonance spectroscopy as a method for screening proteins for anesthetic binding. *Molecular pharmacology* **2004**, *66* (4), 929-935.
195. Yan, J.; Kline, A. D.; Mo, H.; Shapiro, M. J.; Zartler, E. R., The effect of relaxation on the epitope mapping by saturation transfer difference NMR. *Journal of Magnetic Resonance* **2003**, *163* (2), 270-276.
196. Angulo, J.; Enríquez-Navas, P. M.; Nieto, P. M., Ligand-receptor binding affinities from saturation transfer difference (STD) NMR spectroscopy: the binding isotherm of STD initial growth rates. *Chemistry-A European Journal* **2010**, *16* (26), 7803-7812.
197. Bräuniger, T.; Wormald, P.; Hodgkinson, P., *Improved proton decoupling in NMR spectroscopy of crystalline solids using the SPINAL-64 sequence*. Springer: 2002.
198. Kelly, R. T. Investigating the structure of amyloid aggregates using solid-state nuclear magnetic resonance. University of Warwick, 2015.
199. Parella, T., *Pulse Program Catalogue*. Bruker: 2004.
200. Wu, D.; Chen, A.; Johnson, C. S., An improved diffusion-ordered spectroscopy experiment incorporating bipolar-gradient pulses. *Journal of Magnetic Resonance, Series A* **1995**, *115* (2), 260-264.
201. Hrabe, J.; Kaur, G.; Guilfoyle, D. N., Principles and limitations of NMR diffusion measurements. *Journal of Medical Physics* **2007**, *32* (1), 34.
202. Hwang, T.-L.; Shaka, A., Water suppression that works. Excitation sculpting using arbitrary waveforms and pulsed field gradients. *Journal of Magnetic Resonance Series A* **1995**, *112*, 275-275.
203. Vold, R.; Waugh, J.; Klein, M. P.; Phelps, D., Measurement of spin relaxation in complex systems. *The Journal of Chemical Physics* **1968**, *48* (8), 3831-3832.
204. Ernst, R. R.; Bodenhausen, G.; Wokaun, A., *Principles of nuclear magnetic resonance in one and two dimensions*. Clarendon Press Oxford: 1987; Vol. 14.
205. Piotto, M.; Saudek, V.; Sklenář, V., Gradient-tailored excitation for single-quantum NMR spectroscopy of aqueous solutions. *Journal of Biomolecular NMR* **1992**, *2* (6), 661-665.
206. Griesinger, C.; Ernst, R., Cross relaxation in time-dependent nuclear spin systems: Invariant trajectory approach. *Chemical Physics Letters* **1988**, *152* (2-3), 239-247.
207. Adler-Abramovich, L.; Vaks, L.; Carny, O.; Trudler, D.; Magno, A.; Caflisch, A.; Frenkel, D.; Gazit, E., Phenylalanine assembly into toxic fibrils suggests amyloid etiology in phenylketonuria. *Nature Chemical Biology* **2012**, *8* (8), 701-706.

208. Singh, V.; Rai, R. K.; Arora, A.; Sinha, N.; Thakur, A. K., Therapeutic implication of L-phenylalanine aggregation mechanism and its modulation by D-phenylalanine in phenylketonuria. *Scientific Reports* **2014**, *4*, 3875.

209. Do, T. D.; Kincannon, W. M.; Bowers, M. T., Phenylalanine oligomers and fibrils: the mechanism of assembly and the importance of tetramers and counterions. *Journal of the American Chemical Society* **2015**, *137* (32), 10080-10083.

210. Olszynska, S.; Dupuy, N.; Vrielynck, L.; Komorowska, M., Water evaporation analysis of L-phenylalanine from initial aqueous solutions to powder state by vibrational spectroscopy. *Applied Spectroscopy* **2006**, *60* (9), 1040-1053.

211. Kono, K.; Okano, Y.; Nakayama, K.; Hase, Y.; Minamikawa, S.; Ozawa, N.; Yokote, H.; Inoue, Y., Diffusion-weighted MR imaging in patients with phenylketonuria: relationship between serum phenylalanine levels and ADC values in cerebral white matter. *Radiology* **2005**, *236* (2), 630-636.

212. Hsu, W.-P.; Koo, K.-K.; Myerson, A. S., The gel-crystallization of 1-phenylalanine and aspartame from aqueous solutions. *Chemical Engineering Communications* **2002**, *189* (8), 1079-1090.

213. Williams, P. A.; Hughes, C. E.; Buanz, A. B.; Gaisford, S.; Harris, K. D., Expanding the solid-state landscape of L-phenylalanine: discovery of polymorphism and new hydrate phases, with rationalization of hydration/dehydration processes. *The Journal of Physical Chemistry C* **2013**, *117* (23), 12136-12145.

214. King, M. D.; Blanton, T. N.; Korter, T. M., Revealing the true crystal structure of L-phenylalanine using solid-state density functional theory. *Physical Chemistry Chemical Physics* **2012**, *14* (3), 1113-1116.

215. Ihlefeldt, F. S.; Pettersen, F. B.; von Bonin, A.; Zawadzka, M.; Görbitz, C. H., The Polymorphs of L-Phenylalanine. *Angewandte Chemie International Edition* **2014**, *53* (49), 13600-13604.

216. Pronk, S.; Páll, S.; Schulz, R.; Larsson, P.; Bjelkmar, P.; Apostolov, R.; Shirts, M. R.; Smith, J. C.; Kasson, P. M.; van der Spoel, D., GROMACS 4.5: a high-throughput and highly parallel open source molecular simulation toolkit. *Bioinformatics* **2013**, *29* (7), 845-854.

217. Griffith, E. C.; Perkins, R. J.; Telesford, D.-M.; Adams, E. M.; Cwiklik, L.; Allen, H. C.; Roeselová, M.; Vaida, V., Interaction of L-phenylalanine with a phospholipid monolayer at the water-air interface. *The Journal of Physical Chemistry B* **2014**, *119* (29), 9038-9048.

218. Weissbuch, I.; Frolow, F.; Addadi, L.; Lahav, M.; Leiserowitz, L., Oriented crystallization as a tool for detecting ordered aggregates of water-soluble hydrophobic alpha-amino acids at the air-solution interface. *Journal of the American Chemical Society* **1990**, *112* (21), 7718-7724.

219. Martin, A. D.; Robinson, A. B.; Mason, A. F.; Wojciechowski, J. P.; Thordarson, P., Exceptionally strong hydrogels through self-assembly of an indole-capped dipeptide. *Chemical Communications* **2014**, *50* (98), 15541-15544.

220. Moggach, S. A.; Marshall, W. G.; Rogers, D. M.; Parsons, S., How focussing on hydrogen bonding interactions in amino acids can miss the bigger picture: a high-pressure neutron powder diffraction study of ϵ -glycine. *CrystEngComm* **2015**, *17* (28), 5315-5328.

221. Dunitz, J. D., Intermolecular atom-atom bonds in crystals? *IUCrJ* **2015**, *2* (2), 157-158.

222. Dunitz, J.; Gavezzotti, A., Proteogenic amino acids: chiral and racemic crystal packings and stabilities. *The Journal of Physical Chemistry B* **2012**, *116* (23), 6740-6750.

223. Braga, D.; Bazzi, C.; Maini, L.; Grepioni, F., Supramolecular co-ordination networks constructed via pi-stacking interactions and charge-assisted hydrogen bonds. *CrystEngComm* **1999**, *1* (5), 15-20.

224. Duncan, D. C.; Whitten, D. G., ¹H NMR Investigation of the Composition, Structure, and Dynamics of Cholesterol-Stilbene Tethered Dyad Organogels. *Langmuir* **2000**, *16* (16), 6445-6452.

225. Lozano, V.; Hernández, R.; Ardá, A.; Jiménez-Barbero, J.; Mijangos, C.; Pérez-Pérez, M.-J., An asparagine/tryptophan organogel showing a selective response towards fluoride anions. *Journal of Materials Chemistry* **2011**, *21* (24), 8862-8870.

226. Pályi, G.; Zucchi, C.; Caglioti, L., *Progress in Biological Chirality*. Elsevier: 2004.

227. Weast, R. C.; Astle, M. J.; Beyer, W. H., *Handbook of Chemistry and Physics*. CRC Press: 1988; Vol. 69.

228. Abdallah, D. J.; Sirchio, S. A.; Weiss, R. G., Hexatriacontane organogels. The first determination of the conformation and molecular packing of a low-molecular-mass organogelator in its gelled state. *Langmuir* **2000**, *16* (20), 7558-7561.

229. Khawas, B.; Krishna Murti, G., On the unit-cell dimensions and space group of L-tyrosine and L-tryptophane. *Acta Crystallographica Section B: Structural Crystallography and Crystal Chemistry* **1969**, *25* (5), 1006-1009.

230. Šaman, D.; Kolehmainen, E., Studies on supramolecular gel formation using DOSY NMR. *Magnetic Resonance in Chemistry* **2015**, *53* (4), 256-260.

231. Lorenz, U. J.; Rizzo, T. R., Multiple isomers and protonation sites of the phenylalanine/serine dimer. *Journal of the American Chemical Society* **2012**, *134* (27), 11053-11055.

232. Ryan, D. M.; Anderson, S. B.; Nilsson, B. L., The influence of side-chain halogenation on the self-assembly and hydrogelation of Fmoc-phenylalanine derivatives. *Soft Matter* **2010**, *6* (14), 3220-3231.

233. Pizzi, A.; Lascialfari, L.; Demitri, N.; Bertolani, A.; Maiolo, D.; Carretti, E.; Metrangolo, P., Halogen bonding modulates hydrogel formation from Fmoc amino acids. *CrystEngComm* **2017**, *19* (14), 1870-1874.

234. Liyanage, W.; Nilsson, B. L., Substituent effects on the self-assembly/coassembly and hydrogelation of phenylalanine derivatives. *Langmuir* **2016**, *32* (3), 787-799.

235. Bertolani, A.; Pirrie, L.; Stefan, L.; Houbenov, N.; Haataja, J. S.; Catalano, L.; Terraneo, G.; Giancane, G.; Valli, L.; Milani, R., Supramolecular amplification of amyloid self-assembly by iodination. *Nature Communications* **2015**, *6*, 1-9.

236. Feng, Y.; Chen, H.; Liu, Z. X.; He, Y. M.; Fan, Q. H., A pronounced halogen effect on the organogelation properties of peripherally halogen functionalized poly (benzyl ether) dendrons. *Chemistry-A European Journal* **2016**, *22* (14), 4980-4990.

237. Meazza, L.; Foster, J. A.; Fucke, K.; Metrangolo, P.; Resnati, G.; Steed, J. W., Halogen-bonding-triggered supramolecular gel formation. *Nature Chemistry* **2013**, *5* (1), 42-47.

238. Desiraju, G. R.; Ho, P. S.; Kloo, L.; Legon, A. C.; Marquardt, R.; Metrangolo, P.; Politzer, P.; Resnati, G.; Rissanen, K., Definition of the halogen bond (IUPAC Recommendations 2013). *Pure and Applied Chemistry* **2013**, *85* (8), 1711-1713.

239. Takezawa, H.; Murase, T.; Resnati, G.; Metrangolo, P.; Fujita, M., Halogen-Bond-Assisted Guest Inclusion in a Synthetic Cavity. *Angewandte Chemie International Edition* **2015**, *54* (29), 8411-8414.

240. Amombo Noa, F. M.; Bourne, S. A.; Nassimbeni, L. R., Halogen Bonding in Host–Guest Compounds: Structures and Kinetics of Enclathration and Desolvation. *Crystal Growth & Design* **2015**, *15* (7), 3271-3279.

241. Priimagi, A.; Cavallo, G.; Metrangolo, P.; Resnati, G., The halogen bond in the design of functional supramolecular materials: recent advances. *Accounts of Chemical Research* **2013**, *46* (11), 2686-2695.

242. Mukherjee, A.; Tothadi, S.; Desiraju, G. R., Halogen bonds in crystal engineering: like hydrogen bonds yet different. *Accounts of Chemical Research* **2014**, *47* (8), 2514-2524.

243. Politzer, P.; Lane, P.; Concha, M. C.; Ma, Y.; Murray, J. S., An overview of halogen bonding. *Journal of Molecular Modeling* **2007**, *13* (2), 305-311.

244. Desiraju, G. R.; Parthasarathy, R., The nature of halogen. cndot.. cndot.. cndot. halogen interactions: are short halogen contacts due to specific attractive forces or due to close packing of nonspherical atoms? *Journal of the American Chemical Society* **1989**, *111* (23), 8725-8726.

245. Metrangolo, P.; Resnati, G., Type II halogen···halogen contacts are halogen bonds. *IUCrJ* **2014**, *1* (1), 5-7.

246. Jungbauer, S. H.; Bulfield, D.; Kniep, F.; Lehmann, C. W.; Herdtweck, E.; Huber, S. M., Toward molecular recognition: three-point halogen bonding in the solid state and in solution. *Journal of the American Chemical Society* **2014**, *136* (48), 16740-16743.

247. In, Y.; Kishima, S.; Minoura, K.; Nose, T.; Shimohigashi, Y.; Ishida, T., Aggregation Feature of Fluorine-Substituted Benzene Rings and Intermolecular C–H···F Interaction: Crystal Structure Analyses of Mono-and Trifluoro-L-phenylalanines. *Chemical and Pharmaceutical Bulletin* **2003**, *51* (11), 1258-1263.

248. Hiyama, Y.; Silverton, J. V.; Torchia, D. A.; Gerig, J.; Hammond, S., Molecular structure and dynamics of crystalline p-Fluoro-D, L-phenylalanine. A combined X-ray/NMR investigation. *Journal of the American Chemical Society* **1986**, *108* (10), 2715-2723.

249. Pawley, G., Unit-cell refinement from powder diffraction scans. *Journal of Applied Crystallography* **1981**, *14* (6), 357-361.

250. Schur, E.; Nauha, E.; Lusi, M.; Bernstein, J., Kitaigorodsky revisited: Polymorphism and mixed crystals of acridine/phenazine. *Chemistry-A European Journal* **2015**, *21* (4), 1735-1742.

251. Peumans, P.; Uchida, S.; Forrest, S. R., Efficient bulk heterojunction photovoltaic cells using small-molecular-weight organic thin films. *Nature* **2003**, *425* (6954), 158-162.

252. Walzer, K.; Maennig, B.; Pfeiffer, M.; Leo, K., Highly efficient organic devices based on electrically doped transport layers. *Chemical Reviews* **2007**, *107* (4), 1233-1271.

253. Kitaigorodsky, A. I., Inorganic solid solutions. In *Mixed Crystals*, Springer: 1984; pp 181-199.

254. Kitaigorodsky, A., *Molecular crystals and molecules*. Elsevier: 2012; Vol. 29.

255. Glazer, A., Variation of Physical properties with composition of phenazine-N-oxyphenazine mixed crystals. *Philosophical Transactions of the Royal Society of London A: Mathematical, Physical and Engineering Sciences* **1970**, *266* (1180), 623-634.

256. Hinderhofer, A.; Schreiber, F., Organic-organic heterostructures: concepts and applications. *ChemPhysChem* **2012**, *13* (3), 628-643.

257. Bag, P.; Itkis, M. E.; Stekovic, D.; Pal, S. K.; Tham, F. S.; Haddon, R. C., Band Structure Engineering by Substitutional Doping in Solid-State Solutions of [5-Me-PLY (O, O)] 2B (1-x) Be x Radical Crystals. *Journal of the American Chemical Society* **2015**, 137 (31), 10000-10008.

258. Nath, N. K.; Nangia, A., Isomorphous crystals by chloro-methyl exchange in polymorphic fuchsones. *Crystal Growth & Design* **2012**, 12 (11), 5411-5425.

259. Cordero-Borboa, A.; Mijangos, R.; Flores-Morales, L., Structural and textural characterization of a novel spatially coherent crystalline nanocomposite obtained from a melt of KBr, RbCl, RbBr, KI, RbI, and KCl salts. *Journal of Materials Science* **2008**, 43 (13), 4573.

260. Sada, K.; Inoue, K.; Tanaka, T.; Eperges, A.; Tanaka, A.; Tohnai, N.; Matsumoto, A.; Miyata, M., Multicomponent organic alloys based on organic layered crystals. *Angewandte Chemie International Edition* **2005**, 117 (43), 7221-7224.

261. Ramalhete, S.; Foster, J. S.; Green, H. R.; Nartowski, K. P.; Heinrich, M.; Martin, P.; Khimyak, Y. Z.; Lloyd, G. O., FDHALO17: Halogen effects on the solid-state packing of phenylalanine derivatives and the resultant gelation properties. *Faraday Discussions* **2017**, 203, 423-439.

262. Emsley, J. W.; Phillips, L., Fluorine chemical shifts. *Progress in Nuclear Magnetic Resonance Spectroscopy* **1971**, 7, 1-520.

263. Clore, G.; Gronenborn, A., Theory and applications of the transferred nuclear Overhauser effect to the study of the conformations of small ligands bound to proteins. *Journal of Magnetic Resonance* (1969) **1982**, 48 (3), 402-417.

264. Cherukuvada, S.; Kaur, R.; Row, T. N. G., Co-crystallization and small molecule crystal form diversity: from pharmaceutical to materials applications. *CrystEngComm* **2016**, 18 (44), 8528-8555.

265. Martin, G. J.; Martin, M. L.; Gouesnard, J.-P., *15N-NMR spectroscopy*. Springer Science & Business Media: 2012; Vol. 18.

266. Hanabusa, K.; Shimura, K.; Hirose, K.; Kimura, M.; Shirai, H., Formation of Organogels by Intermolecular Hydrogen Bonding between Ureylene Segment. *Chemistry Letters* **1996**, 10, 885-886.

267. van Esch, J.; Schoonbeek, F.; de Loos, M.; Kooijman, H.; Spek, A. L.; Kellogg, R. M.; Feringa, B. L., Cyclic bis-urea compounds as gelators for organic solvents. *Chemistry-A European Journal* **1999**, 5, 937-950.

268. Steed, J. W., Anion-tuned supramolecular gels: a natural evolution from urea supramolecular chemistry. *Chemical Society Reviews* **2010**, 39 (10), 3686-3699.

269. Lloyd, G. O.; Piepenbrock, M.-O. M.; Foster, J. A.; Clarke, N.; Steed, J. W., Anion tuning of chiral bis (urea) low molecular weight gels. *Soft Matter* **2012**, 8 (1), 204-216.

270. Day, G. M., Current approaches to predicting molecular organic crystal structures. *Crystallography Reviews* **2011**, 17 (1), 3-52.

271. Kazantsev, A. V.; Karamertzanis, P. G.; Adjiman, C. S.; Pantelides, C. C.; Price, S. L.; Galek, P. T.; Day, G. M.; Cruz-Cabeza, A. J., Successful prediction of a model pharmaceutical in the fifth blind test of crystal structure prediction. *International Journal of Pharmaceutics* **2011**, 418 (2), 168-178.

272. Neumann, M. A.; Leusen, F. J.; Kendrick, J., A major advance in crystal structure prediction. *Angewandte Chemie International Edition* **2008**, 47 (13), 2427-2430.

273. Sun, Z.; Li, Z.; He, Y.; Shen, R.; Deng, L.; Yang, M.; Liang, Y.; Zhang, Y., Ferrocenoyl phenylalanine: a new strategy toward supramolecular hydrogels with multistimuli responsive properties. *Journal of the American Chemical Society* **2013**, 135 (36), 13379-13386.

274. Vujičić, N. Š.; Glasovac, Z.; Zweep, N.; van Esch, J. H.; Vinković, M.; Popović, J.; Žinić, M., Chiral Hexa-and Nonamethylene-Bridged Bis (L-Leu-oxalamide) Gelators: The First Oxalamide Gels Containing Aggregates with a Chiral Morphology. *Chemistry-A European Journal* **2013**, 19 (26), 8558-8572.

275. Tanaka, M.; Ikeda, T.; Mack, J.; Kobayashi, N.; Haino, T., Self-assembly and gelation behavior of tris (phenylisoxazolyl) benzenes. *The Journal of Organic Chemistry* **2011**, 76 (12), 5082-5091.

276. Velichko, Y. S.; Stupp, S. I.; De La Cruz, M. O., Molecular simulation study of peptide amphiphile self-assembly. *The Journal of Physical Chemistry B* **2008**, 112 (8), 2326-2334.

277. Lee, O.-S.; Stupp, S. I.; Schatz, G. C., Atomistic molecular dynamics simulations of peptide amphiphile self-assembly into cylindrical nanofibers. *Journal of the American Chemical Society* **2011**, 133 (10), 3677-3683.

278. Wallace, M.; Iggo, J. A.; Adams, D. J., Using solution state NMR spectroscopy to probe NMR invisible gelators. *Soft Matter* **2015**, 11 (39), 7739-7747.

279. Steed, K. M.; Steed, J. W., Packing problems: high Z' crystal structures and their relationship to cocrystals, inclusion compounds, and polymorphism. *Chemical Reviews* **2015**, 115 (8), 2895-2933.

280. Pickard, C. J.; Mauri, F., All-electron magnetic response with pseudopotentials: NMR chemical shifts. *Physical Review B* **2001**, *63* (24), 245101.
281. Ménard-Moyon, C.; Venkatesh, V.; Krishna, K. V.; Bonachera, F.; Verma, S.; Bianco, A., Self-Assembly of Tyrosine into Controlled Supramolecular Nanostructures. *Chemistry-A European Journal* **2015**, *21* (33), 11681-11686.